

Theoretische Physik

Precise predictions for supersymmetric particle production at the LHC

Inaugural-Dissertation
zur Erlangung des Doktorgrades
der Naturwissenschaften im Fachbereich Physik
der Mathematisch-Naturwissenschaftlichen Fakultät
der Westfälischen Wilhelms-Universität Münster

vorgelegt von
Marcel Rothering
aus Vreden
-2016-

Dekan:	Prof. Dr. Christian Weinheimer
Erster Gutachter:	Prof. Dr. Michael Klasen
Zweite Gutachterin:	Jun. Prof. Dr. Anna Kulesza
Tag der mündlichen Prüfung:
Tag der Promotion:

Zusammenfassung

Eine der Hauptaufgaben des Large Hadron Colliders (LHC) ist die Suche nach Physik jenseits des Standardmodells (SM). Das minimale supersymmetrische Standardmodell (MSSM) ist einer der vielversprechendsten Kandidaten für eine Erweiterung des SMs und postuliert die Existenz neuer Teilchen. Jedoch wurde keines dieser Teilchen bisher entdeckt und somit werden ihre Massengrenzen immer größer. Mit der verfügbaren Energie des LHCs würden diese Teilchen immer in der Nähe ihrer Produktionsschwelle erzeugt werden. Dies führt zu Vorhersagen für die Wirkungsquerschnitte, die durch das Auftreten dominanter logarithmischer Terme charakterisiert sind, welche von der Emission zusätzlicher weicher Gluonen stammen. Dies hat zur Folge, dass die perturbative Störungsreihe nicht mehr konvergiert und erfordert eine Resummation um verlässliche Ergebnisse in diesen kritischen kinematischen Regionen vorherzusagen.

Aufgrund der Verlagerung des Fokus der experimentellen Suchen zu elektroschwachen supersymmetrischen Teilchenproduktionen aktualisieren wir in dieser Arbeit unsere Vorhersagen für die direkte Sleptonenproduktion am LHC durch die Berücksichtigung von Resummationsbeiträgen. Als Benchmark-Szenario verwenden wir vereinfachte supersymmetrische Modelle, welche nur wenige neue Parameter beinhalten und immer häufiger von den Experimentalphysikern für die Suche nach Sleptonen und elektroschwachen Gauginos benutzt werden. Die Berücksichtigung von nächst-führenden Logarithmen (NLL) durch Resummation führt zu einer drastischen Reduktion der Renormierungs- und Faktorisierungsskalenabhängigkeit des Wirkungsquerschnittes. Weiterhin geben wir einen Hinweis auf die Signifikanz der nächst-nächst-führenden logarithmischen (NNLL) Beiträge für steigende Sleptonmassen. Mit modernen Monte Carlo Methoden reanalysieren wir ATLAS und CMS Ergebnisse für Sleptonsuchen mit verschiedenen Annahmen für die Komposition der Sleptonen und deren Zerfallsprodukte, den Gauginos. Wir finden, dass linkshändige (rechtshändige) Selektrenen und Smuonen mit Massen bis zu 175 GeV (150 GeV) und 130 GeV (100 GeV) ausgeschlossen sind, wenn wir das leichteste Neutralino als masselos annehmen. Für ein sehr dichtes Massenspektrum der supersymmetrischen Teilchen können keine Massengrenzen abgeleitet werden. Außerdem zeigen wir auf, dass eine Unterscheidung des Flavors und der *Händigkeit* der Sleptonen für zukünftige Analysen berücksichtigt werden sollte, wohingegen die Mischung der Neutralinos die Massengrenzen nicht beeinflusst.

Im zweiten Teil der Arbeit untersuchen wir die gemeinsame Produktion von Gluinos und elektroschwachen Gauginos. Aufgrund der großen Gluinomassen kann es möglich sein, dass diese mit der verfügbaren Energie des LHCs nicht in der direkten Paarproduktion erzeugt werden können, jedoch in der verbundenen Produktion mit den relativ leichten Gauginos. Aus diesem Grund verallgemeinern wir die bisherigen Ergebnisse der nächst-führenden Ordnung (NLO) auf nichtentartete Squarks und berücksichtigen Resummationsbeiträge. Wir präsentieren Ergebnisse für die *soft anomalous dimension* und den *hard matching coefficient*. Für unser hier ausgewähltes Benchmark-Szenario finden wir Korrekturen zum NLO Wirkungsquerschnitt von 7% (20%) für eine Gluinomasse von 3 TeV (6 TeV) und eine Reduktion der Skalenabhängigkeit von $\pm 12\%$ zu Werten unter $\pm 3\%$.

Abstract

One of the main objectives of the Large Hadron Collider (LHC) is the search for physics beyond the Standard Model. Among the most promising candidates is the Minimal Supersymmetric Standard Model (MSSM) which postulates the existence of further particles. Since none of these supersymmetric particles have been found yet, their mass limits have been shifted to high values. Hence, with the available energy of the LHC they would always be produced close to their production threshold. This leads to predictions for cross sections which are characterized by the presence of dominant logarithmic terms stemming from multiple soft gluon emission. These contributions spoil the convergence of the perturbative series and require a resummation to predict reliable results in these critical kinematical phase space regions.

As the attention of experimental searches has been shifted towards electroweak supersymmetric particle production at the LHC, we update in this thesis our predictions for direct slepton pair production at proton-proton collision to next-to-leading order (NLO) matched to resummation at the next-to-leading logarithmic (NLL) accuracy. As a benchmark scenario we choose simplified models which have the advantage of only containing a few relevant physical parameters. They are now commonly adopted by the experimental collaborations for slepton and electroweak gaugino searches. We find that the scale dependence is drastically reduced by including NLL corrections, especially for large slepton masses. For increasing mass limits we hint towards the significance of next-to-next-to-leading logarithmic contributions to the cross section. By using modern Monte Carlo techniques we reanalyze ATLAS and CMS results for slepton searches for different assumptions about the compositions of the sleptons and their neutralino decay products. We observe similar mass limits for selectrons and smuons as both collaborations and find that masses for *left-handed* (*right-handed*) selectrons and smuons up to 175 GeV (150 GeV) and 130 GeV (100 GeV), respectively, are excluded for an almost massless lightest neutralino. For a compressed spectrum of the supersymmetric particles no limits can be derived as the signal electrons are too soft to be detected. In addition, we point out that a distinction between the flavor and the *left-* and *right-handed* components of the sleptons should be considered in future analyses, whereas the neutralino composition is irrelevant for our simplified models.

In the second part of this thesis we investigate the associated production of gluinos and electroweak gauginos. As the gluinos are required to be heavy due to the mass limits their direct pair production at the LHC could be beyond its reach. However, their associated production with the relatively light electroweak gauginos might be a possibility to produce gluinos at the LHC. For this reason, we generalize the previously obtained NLO results to non-degenerate squark masses and add NLL contributions. We present analytical results for the soft anomalous dimension and the hard matching coefficient function. For our chosen benchmark scenario NLL corrections increase the NLO cross section by 7 to 20% for central scale choices and gluino masses of 3 to 6 TeV, respectively, and reduce its scale dependence typically from up to $\pm 12\%$ to below $\pm 3\%$.

Contents

1	Introduction	1
2	Supersymmetry	3
2.1	Motivation for Supersymmetry	3
2.2	Theoretical concept and algebraic structure	6
2.2.1	Chiral superfields	9
2.2.2	Vector superfields	10
2.2.3	Supersymmetric Lagrangians	11
2.2.4	R-invariance and R-parity	14
2.3	The Minimal Supersymmetric Standard Model	15
2.3.1	MSSM Lagrangian and the superpotential	16
2.3.2	Supersymmetry breaking	18
2.3.3	The gaugino and higgsino sector	20
2.3.4	The sfermion sector	23
2.3.5	The gluino	24
3	Perturbative Quantum Chromodynamics	27
3.1	Asymptotic freedom	27
3.2	Parton distribution functions	29
3.2.1	The QCD improved parton model	30
3.3	Dipole subtraction formalism	35
3.4	Renormalization	37
3.4.1	Mass and field renormalization	37
3.4.2	Vertex renormalization	42
4	Threshold Resummation	43
4.1	The concept of resummation	44
4.2	Dynamical and kinematical factorization	46
4.2.1	Eikonal Feynman rules	46
4.2.2	Phase space factorization	47
4.3	Resummation for Drell-Yan-like processes	49
4.3.1	Refactorization	49
4.3.2	Exponentiation	52
4.4	Final results and incorporation of final state emission	56
4.5	The soft anomalous dimension	59
4.6	The hard matching coefficient	60
4.7	Matching and inverse Mellin transform	62
4.8	Improved threshold resummation	63

5	Revisiting Slepton Pair Production at the Large Hadron Collider	67
5.1	Fixed order computations	67
5.2	Simplified models for sleptons	71
5.2.1	First and second generation sleptons	72
5.2.2	Simplified models for staus	73
5.3	Precision predictions for slepton pair production at the LHC	74
5.3.1	Total cross section computations	74
5.3.2	Theoretical uncertainties	75
5.3.3	Comparison between NLL, improved NLL and NNLL	80
5.4	Sensitivity to slepton pair production at the LHC	85
5.4.1	Revisiting ATLAS searches for first and second generation sleptons . .	86
5.4.2	Revisiting CMS searches for first and second generation sleptons . . .	88
5.4.3	Conclusion and outlook	91
6	Associated Production of Gauginos and Gluinos	93
6.1	Leading order computations	94
6.2	Next-to-leading order computations	95
6.2.1	Virtual corrections	95
6.2.2	Real corrections	101
6.3	Soft gluon resummation	105
6.3.1	Soft anomalous dimension for gaugino-gluino production	105
6.3.2	The hard matching coefficient for gaugino-gluino production	108
6.4	Numerical results	109
6.4.1	SUSY benchmark scenario	110
6.4.2	Fixed order comparison	112
6.4.3	Total cross sections for benchmark point II	114
6.4.4	Invariant mass distribution	116
6.4.5	Scale uncertainty of the total cross section	117
6.4.6	Gluino mass dependence of the total cross section	117
6.4.7	Gaugino mass dependence of the total cross section	120
6.4.8	Parton density uncertainty of the total cross section	121
7	Conclusion	125
A	Feynman Rules	127
B	Virtual Corrections	131
C	Plus-Distribution	143
D	Mellin Transform of the PDFs	145
	Bibliography	147

1 Introduction

The interplay of theory and experiment makes physics a powerful science to study the laws of nature. Deriving mathematical models from observations allows to predict the outcome of future measurements. These developed models are capable of describing phenomena encompassing an immense scale range, from large structures like galaxies to the microscopic world of atoms and particles. Physics can also go the other way around by starting from a mathematical model and testing it against experimental results. This approach is used in the Standard Model (SM) of particle physics, which has been built by using concepts of symmetries and combines special relativity and quantum mechanics. After determining its 19 free parameters [1], the derived predictions lead to an astonishing agreement with experimental results, e.g. for the anomalous magnetic moment of the electron the agreement goes up to ten significant figures [2]. Since the discovery of the Higgs boson in 2012 [3] even the last missing ingredient of the SM has been found.

Another model using this approach is the Minimal Supersymmetric Standard Model (MSSM), which embeds the SM as an effective low-energy theory and relates fermions to bosons by imposing a new symmetry, called supersymmetry (SUSY). It tries to tackle the phenomena in particle and astroparticle physics, which cannot be explained by the SM alone. Among them are dark matter, the hierarchy problem, the origin of matter-antimatter asymmetry, neutrino masses, Grand Unification and the source of gravitation. In contrast to the SM, the MSSM contains a huge amount of free parameters because it postulates new particles. With the Large Hadron Collider (LHC) at CERN it is possible to search for these new particles. Yet, none of them have been found. For this reason, more precise predictions are needed to exclude parts of the large parameter space and hence narrow down the region where SUSY can possibly hide.

An effective and well established technique to compute predictions for observables such as production cross sections is perturbative Quantum Chromodynamics (QCD). However, in some phase space regions the convergence of the perturbative series is spoiled due to large logarithmic terms, e.g. close to the production threshold of heavy particles. It has been found out that these terms stem from the mismatch between real and virtual corrections including soft gluons. In order to make reliable predictions in this problematic phase space region another technique has been developed, the so called threshold resummation. It is capable of organizing the multiple emission of soft gluons in such a way that their dominant logarithmic terms are included up to all orders in perturbation theory. Therefore, it assures the predictive power even in the critical kinematical region. Resummation contributions to the production cross section of supersymmetric particles can become crucial, as the mass limits of the new postulated particles of the MSSM are shifted to high values and thus their available phase space at the LHC is restricted to the region close to their production threshold.

Among these new particles are the sleptons. As they only interact weakly, they are expected to be relatively light, compared to strongly interacting supersymmetric particles. They would

decay into the lightest supersymmetric particle (LSP), which in most scenarios of the MSSM is the lightest neutralino, and their corresponding superpartners, the leptons. This would result into a signal of highly energetic leptons together with missing energy and could be easily detected at the LHC. This signal allows for slepton searches and thus for narrowing down the corresponding parameter space. For this reason, we dedicate one part of this thesis to the sleptons, which we study in the light of simplified models. These are minimal extensions of the SM and hence only contain a minimal amount of new parameters. They are now commonly adopted for searches of electroweak SUSY particles by experimental collaborations as it makes the MSSM parameter space feasible. We study the inclusion of resummation effects and additionally derive new mass limits by a reanalysis of ATLAS and CMS data.

Another group of supersymmetric particles contains those carrying color charge. Therefore, they interact strongly, which can lead to large direct production cross sections. As no colored supersymmetric particle has been found yet, their corresponding model parameters entering the production cross sections need to be adapted in such a way that the predictions are in agreement with the current experimental limits on the visible cross section, i.e. the signal cross section, for new physics. Consequently, the masses of the colored sparticles have been shifted to values above 1 TeV. To this group belong the gluinos, which are the supersymmetric counterparts of the gluons. Due to their high mass limits their direct production at the LHC could be inaccessible. Hence, the associated production of gluinos together with the relatively light electroweak gauginos becomes phenomenologically relevant since it could be the only possibility to produce the heavy gluinos at the reach of the LHC. On this account, we dedicate the second part of this thesis to the associated gaugino-gluino¹ production. Our main goal is to generalize and update the current NLO predictions by recalculating the virtual and real corrections with non-degenerate squark masses and by including threshold resummation effects.

The structure of this thesis is as follows: we start with the presentation of the necessary background of SUSY and the MSSM in Chap. (2). This is followed by a review of some main concepts of perturbative QCD in Chap. (3). Chap. (4) is dedicated to threshold resummation, where we describe the general principle of resummation and present the basic steps needed to obtain the cross section in a resummed form. In Chap. (5) we focus on slepton pair production, where we discuss briefly the NLO computations, present and discuss numerical results including threshold resummation effects and derive mass limits for the sleptons in simplified SUSY models. Next, in Chap. (6), we address the associated production of gauginos and gluinos, where we first show the fixed order computations and present the necessary formulas to include resummation effects up to NLL and afterwards discuss the obtained numerical results. We conclude this thesis in Chap. (7).

¹For the associated production of gauginos and gluinos the name gaugino always refers to an electroweak gaugino.

2 Supersymmetry

The study of symmetries is one of the most important and successful concepts to examine nature. Especially in particle physics, with the study of external space-time symmetries in combination with internal gauge symmetries, a model has been developed with a tremendous predictive power, the Standard Model of particle physics.

Although being powerful, it still lacks some features. Therefore, a symmetry unlike all the others has been developed during the last four decades in particle physics. Being just a nice mathematical concept in the beginning, it is now one of the most promising candidates for an extension of the SM: supersymmetry, a theory relating fermionic to bosonic degrees of freedom.

In this chapter we give a brief overview of the concepts and ideas behind SUSY. First, in Sec. 2.1, we address the advantages coming along with this new kind of symmetry. Afterwards, in Sec. 2.2, we show its algebraic structure and the construction of supersymmetric field theories. We close this chapter in Sec. 2.3 with a discussion of the most important realization of a supersymmetric extension of the SM, the MSSM, which is the model of interest in this thesis.

2.1 Motivation for Supersymmetry

In the following we present some of the theoretical and experimental issues of the SM, which can be solved by SUSY.

Unnaturalness, hierarchy problem and fine-tuning: Loop corrections to the Higgs boson are an outstanding issue in the SM. Due to the scalar nature of the Higgs boson, its mass corrections exhibit quadratic divergences which lead to the question of unnaturalness and the accompanied hierarchy and fine-tuning problems.

To see these issues more clearly, let us have a look at a Lagrangian

$$\begin{aligned}\mathcal{L}(\Lambda) = & \mathcal{O}(\Lambda^4) + \mathcal{O}(\Lambda^2)\mathcal{L}_2 + \mathcal{O}(\Lambda)\mathcal{L}_3 + \mathcal{O}(1)\mathcal{L}_4 \\ & + \mathcal{O}\left(\frac{1}{\Lambda}\right)\mathcal{L}_5 + \mathcal{O}\left(\frac{1}{\Lambda^2}\right)\mathcal{L}_6 + \dots ,\end{aligned}\tag{2.1}$$

where the cutoff parameter Λ characterizes loop corrections and represents the energy scale at which new physics becomes important, e.g. the Planck scale where gravitation starts to be relevant. \mathcal{L}_D is a coupling operator of dimension D . For instance, $\mathcal{L}_2 = \phi^*\phi$ is a scalar mass term, \mathcal{L}_3 a fermion mass term and \mathcal{L}_4 describes gauge and Yukawa interactions. The complete first row of Eq. (2.1) is the Lagrangian of the SM, \mathcal{L}_5 is the Weinberg operator for neutrino masses and \mathcal{L}_6 includes four-fermion operators [4].

The baseline power of loop corrections is fixed by the dimension of \mathcal{L}_D and can only be suppressed by a natural symmetry. For the electron mass m_e we expect a linear growth with Λ , but due to the chiral symmetry in the massless limit the corrections grow like $m_e \ln \Lambda$ [5], which makes m_e naturally small. A small parameter in the theory is called natural if the symmetry of the system is enhanced by setting it to zero [6, 7]. The Higgs sector in the SM is not protected by any symmetry. For this reason, we call the Higgs mass unnatural. Hence, corrections to the mass are quadratic in Λ and for the top quark contribution we get $\delta m_h^2 \propto -(0.2\Lambda)^2$ as a correction to the Higgs mass. If we want a correction which does not exceed the light Higgs mass and if we want to avoid fine-tuning, Λ should be of $\mathcal{O}(1 \text{ TeV})$. Thus, new physics should be close, instead of being 16 orders of magnitude away at the Planck scale.

Interpreting Λ as a physical parameter is not mandatory. We can also think of it as a mathematical regulator of the divergences appearing in loop corrections and after renormalization no quadratic divergence is left. Still, a correction term proportional to the particle mass in the loop remains. Especially if the SM gives a way to a more fundamental theory like a Grand Unified one, corrections arising from new particles with a mass of $M_U \simeq 10^{16} \text{ GeV}$ can be large. A counterterm with an unnatural amount of fine-tuning is required in order to keep the Higgs mass at 125 GeV.

In a softly broken SUSY theory, like the MSSM, the quadratic divergences cancel due to the inclusion of the scalar superpartners of the fermions in the loop corrections. Only a logarithmic dependence on Λ remains, which is scaled by the mass splitting $\delta = m_f - m_{\tilde{f}}$ of the superpartners appearing in the radiative corrections. So there is a symmetry *shielding* the Higgs mass. Furthermore, the Higgs sector becomes natural, because if $\delta \rightarrow 0$ SUSY is unbroken and leads to an enhanced symmetry of the theory. The mass splitting should not be too large in order to avoid fine-tuning. Nevertheless, naturalness is one of the main motivations for finding new physics in the range of the LHC [4, 8, 7].

Dark matter: From observations of the cosmic microwave background (CMB) with experiments like the Wilkinson Microwave Anisotropy Probe [9] (WMAP) and Planck [10], and due to gravitational effects like gravitational lensing, we know that the universe consists of more than the ordinary atoms which account for only around 4% of the universe's total energy. It turned out that the two main constituents are dark energy, with 72% and dark matter (DM), with 24%.

The matter is called dark, because it does not interact with photons and gluons. Therefore, it must be electrically neutral and colorless and it can only interact weakly and gravitationally. The main part of it must also be non-baryonic and cold, i.e. non-relativistic, in order to explain the observations of the large-scale structures in the universe. One of the most promising explanations for DM is the concept of a weakly interacting massive particle (WIMP). Such a particle does not exist in the SM, but SUSY models can include proper candidates. For instance, the lightest stable (or long lived) particle (LSP) in the MSSM, which is the lightest neutralino in most SUSY scenarios, fulfills all the properties to be a DM particle [11]. Nowadays, these SUSY candidates are heavily tested in LHC searches and direct and indirect detection experiments.

Matter and antimatter asymmetry: The universe as we know it contains more particles than antiparticles. However, we assume an equilibrium of matter and antimatter in the early universe. Therefore, today's asymmetry must have been generated by some mechanism, where one of the most studied ones is baryogenesis. For this mechanism to work a model has to fulfill the so called Sakharov conditions [12]. The first and most obvious one is the baryon number (B) violation. Furthermore, the loss of thermal equilibrium is needed in order to prevent the inverse of the B -violating process from compensating the gained B -asymmetry. Last, we need charge (C) and charge parity (CP) violation, so that the rates of the B - and \bar{B} -process differ and that we do not only get an asymmetry between left- and right-handed quarks.

In the SM the first condition can be fulfilled by the Sphaleron process¹, but the other conditions are not or not sufficiently satisfied. For instance, the second condition could be achieved in an electroweak phase transition (EWPT) of first order, but would require a Higgs mass smaller than 114.4 GeV and is therefore ruled out. Besides, the CP -violating source of the SM, which is the complex phase of the Cabibbo-Kobayashi-Maskawa (CKM) matrix, is too small [13].

The MSSM introduces new sources for CP violation and offers also the possibility for the inclusion of additional B -violating processes². An EWPT of first order can be achieved because of additional particles which couple to the SM-like Higgs. It turns out that this requires a very light right-handed stop³ which should be lighter than the top quark. This option is called the *light stop window* and is still possible in the MSSM, although getting less likely [14, 15, 16].

There are also other explanation attempts like leptogenesis [17] or the Affleck-Dine mechanism [18]. These mechanisms can be successfully embedded in SUSY models, but cannot be realized in the SM alone.

Grand Unification: A Grand Unified Theory (GUT) embeds the gauge groups of the SM in a larger symmetry group like $SU(5)$ ⁴ or $SO(10)$. It reduces the three gauge couplings to only one by imposing the condition that they meet at one point at a higher scale, i.e. at the early universe. Solving the renormalization group equations (RGEs) and evolving the couplings to the GUT scale does not lead to a unification in the SM. By extending the particle content of the model we get additional loop corrections and hence the running coupling is modified. Interestingly, the MSSM seems to extend this content by the right amount. In Fig. 2.1 the evolution of the gauge couplings at two-loop order is shown. The couplings in the MSSM meet at around 1.5×10^{16} GeV. Increasing the masses of the sparticles would result in a decrease of the GUT scale. Note that the couplings do not match exactly, but the slight discrepancy can be repealed by minor threshold effects which arise close to the unification scale [8].

¹This is a non-perturbative process which for instance converts three baryons to three antileptons and thus violates baryon number (B) and lepton number (L) conservation, but preserves $B - L$.

²This means we would have to give up on R -symmetry (see Sec. 2.2.4). It is possible to allow certain B -violating processes and still impose L conservation, so that the proton decay channels $p \rightarrow \pi^+ \nu, \pi^0 e^+$ are forbidden [13].

³As the stop is a scalar particle it does not have any chirality. When we say left- or right-handed sfermion we actually refer to the chirality of their superpartners.

⁴This scenario is already ruled out, because it leads to an unstable proton which does not agree with its measured lifetime.

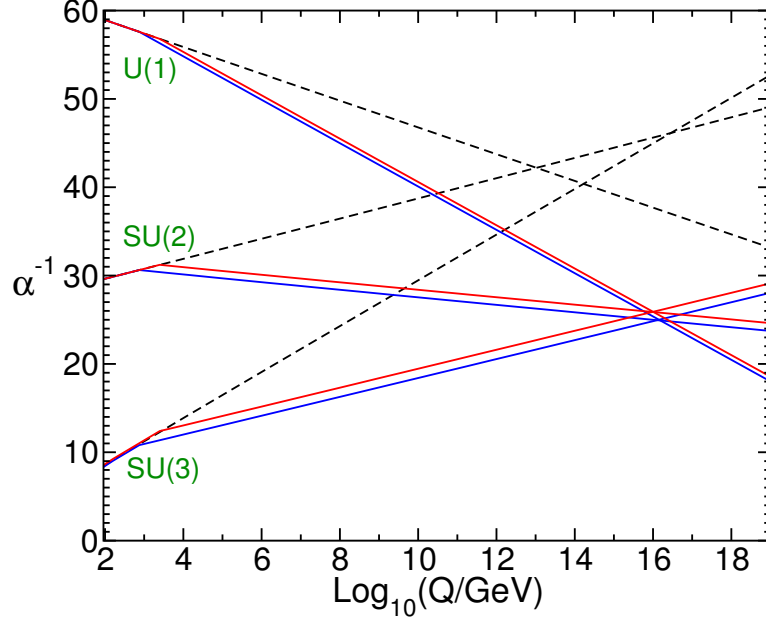


Figure 2.1: Comparison of the running gauge couplings in the SM (dashed lines) and the MSSM (solid lines). The RGEs have been solved at two-loop order. The particle masses in the MSSM have been varied in the range of 750 GeV (blue solid lines) and 2.5 TeV (red solid lines). Figure taken from Ref. [8].

2.2 Theoretical concept and algebraic structure

This section deals with the basic concepts needed to get a supersymmetric field theory. First, we discuss superfields defined on an enlarged space, the superspace. Next, we look at specific superfields which are used to build supersymmetric Lagrangians. Finally, we show an additional symmetry, called R -parity, which is conserved in many supersymmetric models.

Most of the following parts are based on Refs. [7, 8]. We advise the interested reader to have a look at these references in order to get a more detailed picture of the algebraic structure of SUSY.

The largest group of space-time transformations is the Poincaré group. It is defined by its Lie algebra, which is completely given by the following set of commutator relations:

$$[P_\mu, P_\nu] = 0, \quad (2.2a)$$

$$[M_{\mu\nu}, P_\rho] = i(g_{\nu\rho}P_\mu - g_{\mu\rho}P_\nu), \quad (2.2b)$$

$$[M_{\mu\nu}, M_{\rho\sigma}] = -i(g_{\mu\rho}M_{\nu\sigma} - g_{\mu\sigma}M_{\nu\rho} - g_{\nu\rho}M_{\mu\sigma} + g_{\nu\sigma}M_{\mu\rho}). \quad (2.2c)$$

Here, P_μ is the generator for space-time translations, $M_{\mu\nu}$ the one for space-time rotations, including the proper three-dimensional rotations and Lorentz boosts, and $g_{\mu\nu}$ is the metric tensor of the Minkowski-space.

The *Coleman-Mandula* theorem [19] states, that an extended Lie algebra, containing the Poincaré group and any other symmetry of the theory, must be a direct sum of the generators belonging to each subgroup. So, only trivial extensions, i.e. internal symmetries, are possible. SUSY goes beyond Lie algebras, which include only commutator relations, to graded Lie algebras, which now include anti-commutator relations as well. This extension is based on the *Haag-Lopuszanski-Sohnius* theorem [20] and brings us to the following Z_2 -graded Lie algebra for our supersymmetric model in the Weyl representation⁵:

$$\{Q_\alpha, Q_\beta\} = 0, \quad \{\bar{Q}^{\dot{\alpha}}, \bar{Q}^{\dot{\beta}}\} = 0, \quad (2.3a)$$

$$[Q_\alpha, P_\mu] = 0, \quad [\bar{Q}^{\dot{\alpha}}, P_\mu] = 0, \quad (2.3b)$$

$$\{Q_\alpha, \bar{Q}_{\dot{\beta}}\} = 2\sigma_{\alpha\dot{\beta}}^\mu P_\mu, \quad \{\bar{Q}^{\dot{\alpha}}, Q_\beta\} = 2\bar{\sigma}^{\dot{\alpha}\beta\mu} P_\mu, \quad (2.3c)$$

$$[M_{\mu\nu}, Q_\alpha] = -(\sigma_{\mu\nu})_\alpha^\beta Q_\beta, \quad [M_{\mu\nu}, \bar{Q}^{\dot{\alpha}}] = -(\bar{\sigma}_{\mu\nu})^{\dot{\alpha}}_{\dot{\beta}} \bar{Q}^{\dot{\beta}}, \quad (2.3d)$$

$$[Q_\alpha, R] = Q_\alpha, \quad [\bar{Q}^{\dot{\alpha}}, R] = -\bar{Q}^{\dot{\alpha}}. \quad (2.3e)$$

Here, Q_α and $\bar{Q}^{\dot{\alpha}}$ describe two-component Weyl spinor-like anti-commuting generators with $\alpha = \{1, 2\}$ being spinor indices⁶. Note that *unbared* spinor variables belong to the $(1/2, 0)$ representation of the Lorentz group, whereas the *bared* ones belong to the $(0, 1/2)$ representation⁷. The matrices σ^μ and $\bar{\sigma}^\mu$ are the left- and right-chiral 2×2 sub-matrices of the 4×4 γ -matrices of the Clifford algebra in the Weyl representation and $\sigma^{\mu\nu} = i(\sigma^\mu \bar{\sigma}^\nu - \sigma^\nu \bar{\sigma}^\mu)/4$. The generator R belongs to a global $U(1)$ group and describes chiral rotations (see Sec. 2.2.4). Eqs. 2.3 together with Eqs. 2.2 form the Super-Poincaré group.

An elegant way to build a supersymmetric theory is by enlarging space-time to superspace and by introducing superfields. Therefore, we need supercoordinates $z = (x^\mu, \theta^\alpha, \bar{\theta}_{\dot{\alpha}})$, which span the superspace and consist of space-time coordinates x^μ and two Grassmann-valued quantities⁸ θ_α and $\bar{\theta}^{\dot{\alpha}}$. We can write a general superfield \mathcal{F} as an expansion in θ and $\bar{\theta}$ as

$$\begin{aligned} \mathcal{F}(x^\mu, \theta, \bar{\theta}) = & f(x) + \sqrt{2}\xi^\alpha(x)\theta_\alpha + \sqrt{2}\bar{\chi}_{\dot{\alpha}}(x)\bar{\theta}^{\dot{\alpha}} + M(x)\theta\theta + N(x)\bar{\theta}\bar{\theta} \\ & + \alpha_\mu(x)\theta^\alpha\sigma_{\alpha\dot{\alpha}}^\mu\bar{\theta}^{\dot{\alpha}} + \bar{\lambda}_{\dot{\alpha}}(x)\bar{\theta}^{\dot{\alpha}}\theta\theta + \zeta^\alpha(x)\theta_\alpha\bar{\theta}\bar{\theta} + \frac{1}{2}D(x)\theta\theta\bar{\theta}\bar{\theta}, \end{aligned} \quad (2.4)$$

which terminates at order $\mathcal{O}(\theta^2)$ due to the anticommuting properties of the Grassmann variables. Here, ξ , ζ , $\bar{\chi}$ and $\bar{\lambda}$ are Weyl-fermions, f , M , N and D are complex scalar fields and a_μ is a complex vector field. In total, \mathcal{F} contains 16 bosonic and 16 fermionic real degrees of freedom.

⁵This is an irreducible representation of the Clifford algebra arising in spin $1/2$ representations of the Lorentz group. It is also called the chiral basis, because γ^5 is diagonal.

⁶The dotted indices refer to right-handed spinors, whereas the undotted indices refer to left-handed ones.

⁷For those who are unfamiliar with representations of the Lorentz group we recommend Refs. [7, 21].

⁸We recall that $\theta\theta = \theta^\alpha\theta_\alpha = \epsilon_{\alpha\beta}\theta^\alpha\theta^\beta$ with $\epsilon_{\alpha\beta} \neq 0$ only for $\alpha \neq \beta$. If the reader is not familiar with computations involving Grassmann variables, we recommend to have a look at Ref. [7].

For supersymmetric transformations of a superfield \mathcal{F} it is common to define the generators

$$Q_\alpha = -i \frac{\partial}{\partial \theta^\alpha} + (\sigma^\mu \bar{\theta})_\alpha \partial_\mu, \quad \bar{Q}^{\dot{\alpha}} = -i \frac{\partial}{\partial \bar{\theta}_{\dot{\alpha}}} + (\bar{\sigma}^\mu \theta)^{\dot{\alpha}} \partial_\mu, \quad (2.5)$$

leading to the following infinitesimal translation in superspace

$$\begin{aligned} \delta \mathcal{F} &:= i \left(\epsilon Q + \bar{\epsilon} \bar{Q} \right) \mathcal{F}(x^\mu, \theta, \bar{\theta}) \\ &= \mathcal{F} \left(x^\mu - i \theta \sigma^\mu \bar{\epsilon} + i \epsilon \sigma^\mu \bar{\theta}, \theta + \epsilon, \bar{\theta} + \bar{\epsilon} \right) - \mathcal{F}(x^\mu, \theta, \bar{\theta}), \end{aligned} \quad (2.6)$$

where ϵ and $\bar{\epsilon}$ are two-component spinor-like parameters. The transformation for each component-field yields

$$\delta f = \sqrt{2}(\epsilon \xi + \bar{\epsilon} \bar{\chi}), \quad \delta D = i \partial_\mu (\zeta \sigma^\mu \bar{\epsilon} + \bar{\lambda} \bar{\sigma}^\mu \epsilon), \quad (2.7a)$$

$$\delta M = \bar{\epsilon} \bar{\lambda} + \frac{i}{\sqrt{2}} \partial_\mu \xi \sigma^\mu \bar{\epsilon}, \quad \delta N = \epsilon \zeta - \frac{i}{\sqrt{2}} \epsilon \sigma^\mu \partial_\mu \bar{\chi}, \quad (2.7b)$$

$$\delta(\sqrt{2} \xi_\alpha) = 2 \epsilon_\alpha M + (\sigma^\mu \bar{\epsilon})_\alpha (-i \partial_\mu f + \alpha_\mu), \quad (2.7c)$$

$$\delta(\sqrt{2} \bar{\chi}^{\dot{\alpha}}) = 2 \bar{\epsilon}^{\dot{\alpha}} N - (\bar{\sigma}^\mu \epsilon)^{\dot{\alpha}} (i \partial_\mu f + \alpha_\mu), \quad (2.7d)$$

$$\begin{aligned} \delta \alpha_\mu &= \epsilon \sigma_\mu \bar{\lambda} + \zeta \sigma_\mu \bar{\epsilon} - \frac{i}{\sqrt{2}} \epsilon \partial_\mu \xi + \frac{i}{\sqrt{2}} \partial_\mu \bar{\chi} \bar{\epsilon} \\ &\quad + i \sqrt{2} \epsilon \sigma_{\mu\nu} \partial^\nu \xi - i \sqrt{2} \bar{\epsilon} \bar{\sigma}_{\mu\nu} \partial^\nu \bar{\chi}, \end{aligned} \quad (2.7e)$$

$$\delta \bar{\lambda}^{\dot{\alpha}} = \bar{\epsilon}^{\dot{\alpha}} D - \frac{i}{2} \bar{\epsilon}^{\dot{\alpha}} \partial^\mu \alpha_\mu - i (\bar{\sigma}^\mu \epsilon)^{\dot{\alpha}} \partial_\mu M + (\bar{\sigma}^{\mu\nu} \bar{\epsilon})^{\dot{\alpha}} \partial_\mu \alpha_\nu, \quad (2.7f)$$

$$\delta \zeta_\alpha = \epsilon_\alpha D + \frac{i}{2} \epsilon_\alpha \partial^\mu \alpha_\mu - i (\sigma^\mu \bar{\epsilon})_\alpha \partial_\mu N - (\sigma^{\mu\nu} \epsilon)_\alpha \partial_\mu \alpha_\nu, \quad (2.7g)$$

and illustrates a mixing between the fermionic and bosonic degrees of freedom.

The general superfield in Eq. (2.4) has too many degrees of freedom to match with any supermultiplet in the MSSM and is reducible by applying physical constraints. Next, we will state two different classes of physical superfields which are contained in the MSSM: the chiral and vector superfields⁹.

⁹Note that we only consider classical, not quantized fields.

2.2.1 Chiral superfields

We construct ordinary Lagrangians with the covariant derivative ∂_μ , fortunately already commuting with the generators Q and \bar{Q} . The derivative $\partial_\alpha := \partial/\partial\theta^\alpha$ is not supersymmetric covariant, but we can define supersymmetric covariant and contravariant derivatives as

$$\begin{aligned}\mathcal{D}_\alpha &= \partial_\alpha - i(\sigma^\mu\bar{\theta})_\alpha\partial_\mu, & \mathcal{D}^\alpha &= -\partial^\alpha + i(\bar{\theta}\bar{\sigma}^\mu)^\alpha\partial_\mu, \\ \bar{\mathcal{D}}^{\dot{\alpha}} &= \partial^{\dot{\alpha}} - i(\bar{\sigma}^\mu\theta)^{\dot{\alpha}}\partial_\mu, & \bar{\mathcal{D}}_{\dot{\alpha}} &= -\partial_{\dot{\alpha}} + i(\theta\sigma^\mu)_{\dot{\alpha}}\partial_\mu.\end{aligned}\tag{2.8}$$

A superfield fulfilling either of the conditions $\bar{\mathcal{D}}_{\dot{\alpha}}\Phi = 0$ or $\mathcal{D}_\alpha\Phi^\dagger = 0$ is called a left- or right-chiral superfield, respectively, and describes a complete irreducible chiral supermultiplet. By applying these constraints on the general superfield in Eq. (2.4) we get:

$$\begin{aligned}\Phi(x, \theta, \bar{\theta}) &= \phi(x) - i\theta\sigma^\mu\bar{\theta}\partial_\mu\phi(x) - \frac{1}{4}\theta\theta\bar{\theta}\bar{\theta}\partial^\mu\partial_\mu\phi(x) \\ &\quad + \sqrt{2}\theta\xi(x) + \frac{i}{\sqrt{2}}\theta\theta\partial_\mu\xi\sigma^\mu\bar{\theta} + \theta\theta F(x),\end{aligned}\tag{2.9}$$

$$\begin{aligned}\Phi^\dagger(x, \theta, \bar{\theta}) &= \phi^*(x) + i\theta\sigma^\mu\bar{\theta}\partial_\mu\phi^*(x) - \frac{1}{4}\theta\theta\bar{\theta}\bar{\theta}\partial^\mu\partial_\mu\phi^*(x) \\ &\quad + \sqrt{2}\bar{\theta}\bar{\xi}(x) - \frac{i}{\sqrt{2}}\bar{\theta}\bar{\theta}\partial_\mu\sigma^\mu\bar{\xi}(x) + \bar{\theta}\bar{\theta}F^*(x).\end{aligned}\tag{2.10}$$

Eq. (2.9) describes a left-chiral field, whereas Eq. (2.10) describes a right-chiral one. Both contain one Weyl spinor ξ or $\bar{\xi}$, hence having four fermionic degrees of freedom, and two complex scalar fields ϕ and F , leading also to four bosonic degrees of freedom. The field F is called auxiliary field and assures the matching of the bosonic and fermionic degrees of freedom on and off shell. It can be removed from supersymmetric Lagrangians by using its equation of motion.

By comparing the components of a left-chiral superfield with those of a general superfield in Eq. (2.4), we can read off the transformations of the component fields from Eq. (2.7), leading to

$$\delta\phi = \sqrt{2}\epsilon\xi,\tag{2.11}$$

$$\delta\xi_\alpha = \sqrt{2}\epsilon_\alpha F - \sqrt{2}i(\sigma^\mu\bar{\epsilon})_\alpha\partial_\mu\phi,\tag{2.12}$$

$$\delta F = i\partial_\mu(\sqrt{2}\xi\sigma^\mu\bar{\epsilon}).\tag{2.13}$$

The auxiliary field F transforms only to itself and a space-time derivative and thus plays an important role in constructing supersymmetric Lagrangians. We can isolate the F -term from a general superfield, e.g. with

$$[\Phi]_F := \frac{1}{4}\mathcal{D}\mathcal{D}\Phi(x, \theta, \bar{\theta})|_{(\theta=\bar{\theta}=0)} = F(x),\tag{2.14}$$

$$[\Phi^\dagger]_F := \frac{1}{4} \bar{\mathcal{D}} \bar{\mathcal{D}} \Phi^\dagger(x, \theta, \bar{\theta})|_{(\theta=\bar{\theta}=0)} = F^*(x). \quad (2.15)$$

Note that products of chiral superfields are chiral superfields themselves. Furthermore, the F -term in any polynomial of only left- or right-chiral superfields leads to an invariant action, but not if we combine left- and right-chiral fields like $\Phi^\dagger \Phi$. Instead, we can define the so called D -term¹⁰ leading also to an invariant action

$$\begin{aligned} [\Phi_i^\dagger \Phi_j]_D &:= \int d^2\theta d^2\bar{\theta} \Phi_i^\dagger \Phi_j \\ &= F_i^* F_j + \frac{1}{2} \partial_\mu \phi_i^* [\partial^\mu] \phi_j - \frac{1}{2} \phi_i^* [\partial_\mu] \partial^\mu \phi_j + i \xi_j \sigma^\mu [\partial_\mu] \bar{\xi}_i, \end{aligned} \quad (2.16)$$

where $X[\partial_\mu]Y := X\partial_\mu Y/2 - (\partial_\mu X)Y/2$ with X and Y being fields and the indices i and j referring to different types, e.g. flavor. Eq. (2.16) contains a kinetic energy term for a Weyl-fermion and for a complex scalar field, together with a term for the auxiliary field F .

2.2.2 Vector superfields

Another class of superfields are vector superfields, determined by the reality condition $V = V^\dagger$. Looking at the general superfield in Eq. (2.4) this condition leads to $f = f^* =: C, \bar{\chi} = \bar{\xi}, N = M^*, a_\mu = a_\mu^* =: A_\mu, \zeta = \lambda$ and $D = D^*$. Thereby, we can write

$$\begin{aligned} V(x, \theta, \bar{\theta}) &\propto C(x) + \sqrt{2}\theta\xi(x) + \sqrt{2}\bar{\theta}\bar{\xi}(x) + \theta\theta M(x) + \bar{\theta}\bar{\theta}M^*(x) + \theta\sigma^\mu\bar{\theta}A_\mu(x) \\ &\quad + \theta\theta\bar{\theta}\bar{\lambda}(x) + \bar{\theta}\bar{\theta}\theta\lambda(x) + \frac{1}{2}\theta\theta\bar{\theta}\bar{\theta}D(x), \end{aligned} \quad (2.17)$$

where C and D are real scalar fields, A_μ is a real vector field, M is a complex scalar field and ξ and λ are two-component spinor fields.

Vector superfields can be constructed out of chiral superfields, e.g. with $\Phi + \Phi^\dagger$ and $\Phi^\dagger \Phi$. It is also common to define a more general vector superfield, where the substitutions $\lambda \rightarrow \lambda - i\sigma^\mu \partial_\mu \bar{\xi}/\sqrt{2}$, $\bar{\lambda} \rightarrow \bar{\lambda} - i\bar{\sigma}^\mu \partial_\mu \xi/\sqrt{2}$ and $D \rightarrow D - \partial^\mu \partial_\mu C/2$ have been performed. This leads to

$$\begin{aligned} V(x, \theta, \bar{\theta}) &= C(x) + \sqrt{2}\theta\xi(x) + \sqrt{2}\bar{\theta}\bar{\xi}(x) + \theta\theta M(x) + \bar{\theta}\bar{\theta}M^*(x) + \theta\sigma^\mu\bar{\theta}A_\mu(x) \\ &\quad + \theta\theta\bar{\theta} \left(\bar{\lambda}(x) - \frac{i}{\sqrt{2}} \bar{\sigma}^\mu \partial_\mu \xi(x) \right) + \bar{\theta}\bar{\theta}\theta \left(\lambda(x) - \frac{i}{\sqrt{2}} \sigma^\mu \partial_\mu \bar{\xi} \right) \\ &\quad + \frac{1}{2} \theta\theta\bar{\theta}\bar{\theta} \left(D(x) - \frac{1}{2} \partial^\mu \partial_\mu C(x) \right). \end{aligned} \quad (2.18)$$

A local abelian supergauge transformation can be introduced by

$$V \rightarrow V + i\Lambda - i\Lambda^\dagger, \quad (2.19)$$

¹⁰The name refers to the D -coefficient in a general superfield decomposition in Eq. (2.4).

where Λ and Λ^\dagger are chiral superfields, but their sum results in a vector superfield. This leads to the specific transformations $C \rightarrow C + 2\text{Re}(\phi)$, $\xi \rightarrow \xi + \chi$, $M \rightarrow M + F$, $A_\mu \rightarrow A_\mu - 2\partial_\mu \text{Im}(\phi)$, $\lambda \rightarrow \lambda$ and $D \rightarrow D$ for the components of the vector superfield V .

The supergauge transformation in Eq. (2.19) contains the ordinary local U(1) gauge transformation for the real vector field A_μ . Furthermore, one can change the component fields of Λ and Λ^\dagger in such a way that the fields ξ , M and C can be eliminated. The U(1)-term $2\text{Im}(\phi)$ can still be chosen independently. This leads to a vector superfield in the so called Wess-Zumino gauge, which is given by

$$V_{WZ} = \theta\sigma^\mu\bar{\theta}A_\mu(x) + \theta\theta\bar{\theta}\bar{\lambda}(x) + \bar{\theta}\bar{\theta}\theta\lambda(x) + \frac{1}{2}\theta\theta\bar{\theta}\bar{\theta}D(x). \quad (2.20)$$

The remaining fields in Eq. (2.20) are the real vector field A_μ , the gaugino field λ and the auxiliary field D , which has a similar purpose as the F -field. Furthermore, the D -term of a vector field $[V]_D$ is supersymmetric and supergauge invariant.

The field strength tensor can be defined by

$$W_\alpha = -\frac{1}{4}\bar{D}\bar{D}D_\alpha V, \quad \bar{W}_{\dot{\alpha}} = -\frac{1}{4}\mathcal{D}\mathcal{D}\bar{\mathcal{D}}_{\dot{\alpha}}V, \quad (2.21)$$

leading to a useful result for

$$\frac{1}{4}\left[W^\alpha W_\alpha + \bar{W}_{\dot{\alpha}}\bar{W}^{\dot{\alpha}}\right]_F = \frac{1}{2}D^2(x) - \frac{1}{4}F_{\mu\nu}(x)F^{\mu\nu}(x) + i\lambda(x)\sigma^\mu[\partial_\mu]\bar{\lambda}(x), \quad (2.22)$$

where $F_{\mu\nu} = \partial_\mu A_\nu - \partial_\nu A_\mu$ is the common abelian field strength tensor. Eq. (2.22) contains kinetic energy terms for a real vector field A_μ and for a gaugino λ and a term for the auxiliary field D .

This concept can be generalized to non-abelian gauge theories [7, 8], but would go beyond the scope of this introduction.

2.2.3 Supersymmetric Lagrangians

After the introduction of the chiral and vector superfields, the supersymmetric invariant D - and F -terms and supergauge transformations, we can finally start to construct a supersymmetric Lagrangian out of these building blocks. In general we can write a supersymmetric action as

$$S = \int d^2\theta d^2\bar{\theta} d^4x \tilde{\mathcal{L}}_{SUSY}(\theta, \bar{\theta}, x) = \int d^4x \mathcal{L}_{SUSY}(x), \quad (2.23)$$

where we have integrated out the fermionic degrees of freedom. \mathcal{L}_{SUSY} should be Lorentz and supergauge invariant and supersymmetric, except for the surface terms which vanish after integration. The integral of a superfield \mathcal{F} over the total superspace is automatically invariant under SUSY transformations [8]. The reality condition of the action demands that this field must also be a real, i.e. a vector superfield.

For the chiral supermultiplet we can write a Lagrangian like

$$\mathcal{L}_{\text{chiral}}(x) = [\Phi_i^\dagger \Phi_i]_D + \left[\mathcal{W}(\Phi_i) + \mathcal{W}^\dagger(\Phi_i^\dagger) \right]_F, \quad (2.24)$$

including the kinematical parts of a scalar field and of a Weyl fermion, the auxiliary field F and a holomorphic function¹¹

$$\mathcal{W}(\Phi_i) = h_i \Phi_i + \frac{1}{2} M^{ij} \Phi_i \Phi_j + \frac{1}{3!} f^{ijk} \Phi_i \Phi_j \Phi_k, \quad (2.25)$$

comprising mass and Yukawa terms. By inserting all the components we get

$$\begin{aligned} \mathcal{L}_{\text{chiral}} = & i \xi_i [\partial_\mu] \bar{\xi}_i + \partial^\mu \phi_i^* \partial_\mu \phi_i + F_i^* F_i \\ & + \left[\left(h_i + m_{ik} \phi_i + \frac{1}{2} f_{ijk} \phi_i \phi_j \right) F_k - \frac{1}{2} \xi_i \xi_j (m_{ij} + f_{ijk} \phi_k) + \text{h.c.} \right], \end{aligned} \quad (2.26)$$

where the index i labels a specific flavor. Using the equations of motion $\partial \mathcal{L} / \partial F_i^* = 0$ and $\partial \mathcal{L} / \partial F_i = 0$ for the auxiliary fields leads to

$$F_i = -h_i^* - m_{ij}^* \phi_j^* - \frac{1}{2} f_{ijk}^* \phi_j^* \phi_k^*, \quad (2.27)$$

$$F_i^* = -h_i - m_{ij} \phi_j - \frac{1}{2} f_{ijk} \phi_j \phi_k \quad (2.28)$$

and we can rewrite the Lagrangian in terms of dynamical fields only. This yields

$$\mathcal{L}_{\text{chiral}} = i \xi_i \sigma^\mu [\partial_\mu] \bar{\xi}_i + \partial^\mu \phi_i^* \partial_\mu \phi_i - \left(\frac{1}{2} \xi_i \xi_j \mathcal{W}_{ij}(\phi) + \text{h.c.} \right) - V_{\text{scalar}}(\phi_i, \phi_j^*), \quad (2.29)$$

$$V_{\text{scalar}}(\phi_i, \phi_j^*) = \mathcal{W}_i(\phi) \bar{\mathcal{W}}^i(\bar{\phi}) = F_i^* F_i, \quad (2.30)$$

$$\mathcal{W}_{ij}(\phi) = \frac{\partial^2 \mathcal{W}}{\partial \Phi_i \partial \Phi_j} \Big|_{(\theta=\bar{\theta}=0)} \quad \text{and} \quad \mathcal{W}_i(\phi) = \frac{\partial \mathcal{W}}{\partial \Phi_i} \Big|_{(\theta=\bar{\theta}=0)}, \quad (2.31)$$

where the double derivative of the superpotential contains the Yukawa interactions and the fermion mass terms. Here, we see that the auxiliary fields can also be expressed in terms of a derivative of the superpotential. Note that $\bar{\mathcal{W}}^i(\bar{\phi})$ denotes the derivative of the superpotential with respect to the hermitian conjugate chiral superfield. The whole scalar potential of the theory is governed by $V_{\text{scalar}}(\phi_i, \phi_j^*)$ and the expectation value $\langle V_{\text{scalar}} \rangle$ defines the supersymmetric ground state.

¹¹It must be holomorphic to be invariant under SUSY transformations.

For the Wess-Zumino model [22], which is the first known example of a supersymmetric field theory in four dimensions consisting only of one chiral superfield, the on shell Lagrangian of Eq. (2.29) turns into

$$\begin{aligned}\mathcal{L}_{WZ} = & i\xi\sigma^\mu[\partial_\mu]\bar{\xi} - \phi^*\partial_\mu\partial^\mu\phi - \frac{1}{2}m(\xi\xi + \bar{\xi}\bar{\xi}) \\ & - \frac{f}{2}(\bar{\xi}\bar{\xi}\phi^* + \xi\xi\phi) - |h + m\phi + \frac{f}{2}\phi^2|^2.\end{aligned}\quad (2.32)$$

In the limit of vanishing couplings h and f we can derive the equations of motion

$$(i\gamma^\mu\partial_\mu - m)\lambda_M = 0, \quad \lambda_M = \begin{pmatrix} \xi \\ \bar{\xi}^T \end{pmatrix}, \quad (2.33)$$

$$(\partial_\mu\partial^\mu + m^2)\phi = 0, \quad (2.34)$$

which describe a free Majorana field and a free Klein-Gordon equation. In this model the scalar and the fermion have the same mass m .

Finally, we add gauge fields and the gauge interactions to the model. We can introduce a U(1) supergauge transformation as

$$\Phi'_i = e^{-2igt_i\Lambda(z)}\Phi_i, \quad \bar{D}^{\dot{\alpha}}\Lambda = 0, \quad (2.35)$$

$$\Phi_i^\dagger = \Phi_i^\dagger e^{2igt_i\Lambda(z)^\dagger}, \quad \mathcal{D}_\alpha\Lambda^\dagger = 0, \quad (2.36)$$

where g is a gauge coupling, t_i is the corresponding charge of the field Φ_i and Λ is a chiral superfunction in superspace. In general $\Lambda \neq \Lambda^\dagger$ and the kinetic energy D -term in Eq. (2.24) is not gauge invariant by itself, but we can introduce a gauge vector superfield V with the gauge transformation (see Eq. (2.19))

$$V' = V + i(\Lambda - \Lambda^\dagger) \quad (2.37)$$

and change the D -term to

$$\left[\Phi_i^\dagger e^{2gt_i V} \Phi_i\right]_D, \quad (2.38)$$

which is then gauge invariant. The vector field V can be exponentiated without any complications, because it is dimensionless and the series in θ and $\bar{\theta}$ terminates at third order, which makes the theory still renormalizable. For the expansion of the exponent we get

$$e^{2gt_i V} = 1 + 2gt_i \left(\theta\sigma^\mu\bar{\theta}A_\mu + \theta\theta\bar{\theta}\bar{\lambda} + \theta\bar{\theta}\theta\lambda + \frac{1}{2}\theta\theta\bar{\theta}\bar{\theta}D \right) + g^2t_i^2\theta\theta\bar{\theta}\bar{\theta}A_\mu A^\mu. \quad (2.39)$$

After inserting Eq. (2.39) in the kinetic energy term in Eq. (2.38) we get

$$\begin{aligned} \left[\Phi_i^\dagger e^{2gt_i V} \Phi_i \right]_D &= F_i^* F_i + D_\mu \phi_i^* D^\mu \phi_i + i \bar{\xi}_i \bar{\sigma}^\mu D_\mu \xi_i - \sqrt{2} g t_i (\phi_i^* \xi_i \lambda + \bar{\lambda} \bar{\xi}_i \phi_i) \\ &\quad + g t_i \phi_i^* \phi_i D, \end{aligned} \quad (2.40)$$

where we have introduced the covariant derivatives

$$D_\mu \phi_i = \partial_\mu \phi_i - i g t_i A_\mu \phi_i, \quad (2.41)$$

$$D_\mu \phi_i^* = \partial_\mu \phi_i^* + i g t_i A_\mu \phi_i^*, \quad (2.42)$$

$$D_\mu \xi_i = \partial_\mu \xi_i - i g t_i A_\mu \xi_i. \quad (2.43)$$

Here, we can see the ordinary U(1) gauge interaction, e.g. a photon field A_μ which couples to a fermion, and its supersymmetric counterpart, which for instance describes the coupling between an electron, a selectron and a photino. Similar to the F -field also the D -field can be eliminated by using its equation of motion $\partial \mathcal{L} / \partial D = 0$. Keep in mind that the particles in a chiral superfield have the same gauge representation, since SUSY transformations commute with internal gauge symmetries. The kinetic energy term for the vector superfield can be added by using the gauge invariant and supersymmetric field strengths (see Eq. (2.22)). In total, we can write a supersymmetric Lagrangian as

$$\mathcal{L} = \left[\Phi_i^\dagger e^{2gt_i V} \Phi_i \right]_D + ([\mathcal{W}(\Phi_i)]_F + \text{h.c.}) + \frac{1}{4} ([W^\alpha W_\alpha]_F + \text{h.c.}). \quad (2.44)$$

Let us recall that the first D -term contains the kinetic terms of the chiral fields and the U(1) gauge and supersymmetric gauge interactions. The F -term of the superpotential contains fermion mass terms, Yukawa interactions and the scalar potential. The last F -term comprises the kinetic terms of a real vector field and its superpartner, a gaugino field.

2.2.4 R-invariance and R-parity

In Eq. (2.3) we have already seen an additional generator for a global U(1) transformation. It describes a phase rotation of the Grassmann variables. For an arbitrary superfield we can define

$$\mathcal{F}(x, e^{i\varphi} \theta, e^{-i\varphi} \bar{\theta}) = e^{i\varphi R_{\mathcal{F}}} \mathcal{F}(x, \theta, \bar{\theta}), \quad (2.45)$$

where $R_{\mathcal{F}}$ is the R -charge of the field \mathcal{F} . One can show that the left- and right-chiral superfields have opposite R -charges, i.e. $R_\Phi = -R_{\Phi^\dagger}$, and for its components we get $R(\phi) = R_\Phi$, $R(\xi) = R_\Phi - 1$ and $R(F) = R_\Phi - 2$. Due to the reality condition of the vector superfield its R -charge is $R_V = 0$ and we get for its components in Wess-Zumino gauge $R(A_\mu) = 0$, $R(\lambda) = -R(\bar{\lambda}) = 1$ and $R(D) = 0$.

The kinetic energy term and the gauge interactions of a supersymmetric field theory are R -invariant, but not general Yukawa interactions and Majorana mass terms. We can abandon the continuous U(1) transformations and go to a discrete subgroup $Z_2(\varphi = \pi)$ which is an

exact symmetry in the MSSM and leads to $e^{i\pi R} = (-1)^R$. The value R for the charge of a superfield is called matter parity and of its components R -parity. R -parity is positive for all SM particles and negative for their SUSY partners. It can be expressed as [7]

$$R_p = (-1)^{3(B-L)+2S} \quad (2.46)$$

where B is the baryon number, L the lepton number and S the spin of the particle.

Imposing this symmetry leads to important consequences: first, each vertex must give $R_p = 1$ and hence there is always an even number of sparticles present in each vertex, leading to the observation that in collisions of SM particles, sparticles are always produced in pairs. Second, the LSP is stable and can for instance be a dark matter candidate [7].

2.3 The Minimal Supersymmetric Standard Model

In this section we discuss the minimal extension of the SM including SUSY, which is called the Minimal Supersymmetric Standard Model. We first address the particle content and the Lagrangian of the MSSM. Afterwards, we briefly discuss SUSY breaking terms. The end of this section is dedicated to the gaugino, sfermion and gluino sector of the MSSM, which are the most important particle sectors in this thesis.

First, we remark that it is impossible to construct a supersymmetric field theory with the SM fields alone. The SM gauge bosons and fermions cannot be combined into a supermultiplet. This is due to the fact that fields which are contained in the same supermultiplet must belong to the same representation of the gauge group. Fermions in the SM belong to the fundamental representation, whereas in a consistent field theory the spin one gauge bosons belong to the adjoint representation. Thus, they cannot be put into the same supermultiplet.

The MSSM is a softly broken $N = 1$ supersymmetric extension of the SM, which is called minimal, because it extends the particle content by the smallest possible amount in order to get a supersymmetric field theory. Here, N refers to the amount of the added SUSY-generators, which in the MSSM is only one, namely the four-component Majorana spinor $Q_A := (Q_\alpha, \bar{Q}^{\dot{\alpha}})$.

Next, we specify the different supermultiplets of the MSSM. Each SM vector field will be put in a vector superfield together with a Majorana fermion as its superpartner. The left- and right-handed fermions belong to different $SU(2)_L$ doublets in the SM, and therefore we have to put them into different chiral superfields together with new scalar superpartners, the sfermions. Since the superpotential \mathcal{W} can only contain left-chiral superfields in order to be a holomorphic function, we are forced to use the charge conjugates of the $SU(2)_L$ singlet right-chiral fermion fields, which are left-chiral. This means for instance $f_{uR}^C = (f_u^C)_L$ and its scalar superpartner f_{uR}^* , where C denotes charge conjugation, will be embedded in such a way in a left-chiral superfield with quantum numbers of the conjugate representations [7].

The Higgs sector differs from that in the SM and has to be extended. As the charge conjugated Higgs doublet cannot be put in a left-chiral superfield, but is needed to generate all fermion masses, we have to introduce an additional Higgs doublet. For this reason, we will have two left-chiral superfields denoted by \hat{H}_1 and \hat{H}_2 . From this it follows that we also get two vacuum expectation values (VEVs) after the electroweak symmetry breaking. They are denoted by v_1 and v_2 . Since both VEVs are connected to the W mass, they cannot be

determined explicitly and usually the ratio $v_2/v_1 := \tan \beta$ is taken as a free parameter.

All chiral supermultiplets of the MSSM and their gauge representations are shown in Tab. 2.1. Superfields are labeled with a *hat* and the new superpartners with a *tilde*. Neutrinos and the left-chiral leptons are comprised in the superfield \hat{L} , together with their superpartners, the sneutrinos and left-handed sleptons. $SU(2)_L$ singlet leptons and sleptons are contained in the superfield \hat{E} . The quark sector is very similar. Here, \hat{Q} denotes the $SU(2)_L$ doublets and \hat{U}_R and \hat{D}_R denote the singlets. The two Higgs superfields \hat{H}_1 and \hat{H}_2 consist of one neutral and one charged Higgs and their corresponding higgsino fields.

In Tab. 2.2 we show all the vector superfields of the MSSM. The field \hat{G} contains the gluon and the so called gluino as its superpartner. The superfields \hat{W} and \hat{B} comprise the W and B boson and their corresponding superpartners, the wino and bino fields.

Apart from the component fields which are listed here, each chiral and vector superfield also contains an auxiliary field. We recall that this field can be eliminated from the Lagrangian by using its equation of motion. This particle content is the minimal amount of new particles

Table 2.1: Chiral supermultiplets of the MSSM. The weak hypercharge has been defined as $Y = 2(Q - T_3)$, where Q denotes the electric charge and T_3 the third component of the weak isospin. The *bar* over the $SU(2)_L$ -singlet superfields is merely a label to emphasize the usage of the charge conjugate of the right-chiral fields. All the spin 1/2 fields are four-component spinors.

Names	Symbol	Spin 1/2	Spin 0	$SU(3)_c, SU(2)_L, U(1)_Y$
Leptons & Sleptons	\hat{L}	$L = (\nu_{eL}, e_L)$	$\tilde{L} = (\tilde{\nu}_{eL}, \tilde{e}_L)$	$(\mathbf{1}, \mathbf{2}, -1)$
(three generations)	\hat{E}	e_R^C	\tilde{e}_R^*	$(\mathbf{1}, \mathbf{1}, 2)$
Quarks & Squarks	\hat{Q}	$Q = (u_L, d_L)$	$\tilde{Q} = (\tilde{u}_L, \tilde{d}_L)$	$(\mathbf{3}, \mathbf{2}, 1/3)$
(three generations)	\hat{U}	u_R^C	\tilde{u}_R^*	$(\bar{\mathbf{3}}, \mathbf{1}, -4/3)$
	\hat{D}	d_R^C	\tilde{d}_R^*	$(\bar{\mathbf{3}}, \mathbf{1}, 2/3)$
Higgs & Higgsinos	\hat{H}_1	$\tilde{H}_1 = (\tilde{H}_1^0, \tilde{H}_1^-)$	$H_1 = (h_1, h_1^-)$	$(\mathbf{1}, \mathbf{2}, -1)$
	\hat{H}_2	$\tilde{H}_2 = (\tilde{H}_2^+, \tilde{H}_2^0)$	$H_2 = (h_2^+, h_2)$	$(\mathbf{1}, \mathbf{2}, 1)$

needed to achieve a supersymmetric extension of the SM. In general, there can be more particles depending on the specific SUSY scheme and SUSY breaking scenario. For instance, in minimal supergravity scenarios the graviton and the gravitino are embedded in the theory as well.

2.3.1 MSSM Lagrangian and the superpotential

The general Lagrangian for the MSSM can be written as a sum of two terms

$$\mathcal{L}_{\text{MSSM}} = \mathcal{L}_{\text{SUSY}} + \mathcal{L}_{\text{Soft}} , \quad (2.47)$$

Table 2.2: Same as in Tab. 2.1, but now showing the gauge supermultiplets of the MSSM.

Names	Symbol	Spin 1	Spin 1/2	$SU(3)_c, SU(2)_L, U(1)_Y$
Gluon & Gluino	\hat{G}	g	\tilde{g}	$(\mathbf{8}, \mathbf{1}, 0)$
W bosons & Winos	\hat{W}^\pm, \hat{W}^0	W^\pm, W^0	$\tilde{W}^\pm, \tilde{W}^0$	$(\mathbf{1}, \mathbf{3}, 0)$
B boson & Bino	\hat{B}	B	\tilde{B}	$(\mathbf{1}, \mathbf{1}, 0)$

where $\mathcal{L}_{\text{SUSY}}$ denotes the exact supersymmetric part and $\mathcal{L}_{\text{Soft}}$ governs the soft SUSY breaking terms which lead to different masses for the component fields of a supermultiplet. In this section we only address the first term and in the next section we discuss the terms included in $\mathcal{L}_{\text{Soft}}$.

$\mathcal{L}_{\text{SUSY}}$ is very similar to the SM Lagrangian and only differs significantly in the Higgs sector. We can write

$$\mathcal{L}_{\text{SUSY}} = \mathcal{L}_g + \mathcal{L}_M + \mathcal{L}_H, \quad (2.48)$$

where \mathcal{L}_g comprises the field strength tensors of the three gauge fields. Each of these tensors can be written in a similar way as shown in Eq. (2.22). The second term, \mathcal{L}_M , contains the chiral matter fields and the covariant derivatives (see Eq. (2.40)). \mathcal{L}_H includes the Higgs fields, their gauge couplings and the super potential, which is given by

$$\mathcal{W}_{\text{MSSM}} = \mu \hat{H}_1 \cdot \hat{H}_2 - f_{ij}^e \hat{H}_1 \cdot \hat{L}_i \hat{E}_j - f_{ij}^d \hat{H}_1 \cdot \hat{Q}_i \hat{D}_j - f_{ij}^u \hat{Q}_i \cdot \hat{H}_2 \hat{U}_j. \quad (2.49)$$

In Eq. (2.49) the first term denotes a supersymmetric generalization of the Higgs mass term, with μ being a parameter with the dimension of mass. It is also often referred to as the μ -term. The last three remaining terms are supersymmetric generalizations of the Yukawa couplings of the SM, where their strength is described by f_{ij} with i and j being generation indices. The Yukawa interactions are completely symmetric in a general SUSY theory. In addition to the common Higgs-lepton-lepton and Higgs-quark-quark couplings, we get the squark-higgsino-quark and slepton-higgsino-lepton couplings. For SUSY phenomenology these Yukawa interactions are actually not very important, since they are known to be very small, except for the particles of the third generation. Therefore, it is common to use an approximation where only the Yukawa couplings of the third generation are nonzero. The direct production of SUSY particles is usually dominated by the supersymmetric gauge interactions [8]. Since the MSSM preserves R -parity, no further terms in the superpotential are allowed.

In total, the MSSM contains 17 auxiliary F -fields coming from the chiral matter fields. Furthermore, we get three D -fields, namely D^Y coming from the $U(1)_Y$ -gauge group, a $SU(2)_L$ triplet \vec{D} and D^a which is contained in the vector superfield of the gluon. All together define the scalar potential

$$V_{\text{SUSY}} = F_k^* F_k + \frac{1}{2} \left[\vec{D}^2 + (D^Y)^2 + D^a D^a \right], \quad (2.50)$$

where a summation over the index k , describing the different chiral superfields, and the color index a is implied. In contrast to the SM, this scalar potential has not to be added *ad hoc*. Eq. (2.50) can be rewritten in terms of physical fields only (see e.g. [7]). Then this potential does not only include the famous *mexican hat* potential for electroweak symmetry breaking, but also further scalar couplings, like quartic slepton and squark interactions and interactions between the Higgs fields and the sfermions. Moreover, this scalar potential is the only possibility to break SUSY in the MSSM.

2.3.2 Supersymmetry breaking

We know that SUSY is not realized as an exact symmetry in nature, at least not nowadays. For instance, scalar superpartners of the electron with the same mass as the electron should have been already found. SUSY breaking terms must repeal the mass degeneracy of the supermultiplets and should lead to large masses for the sparticles as they have not been detected yet.

The term $\mathcal{L}_{\text{Soft}}$ breaks SUSY explicitly and hence Eq. (2.47) describes a SUSY theory at a low energy scale. We assume that the breaking occurred at a much higher energy scale which is unreachable for the LHC. It is impossible to break SUSY spontaneously only with the particle content of the MSSM¹². In order to achieve the SUSY breaking, we need additional fields which lead to a non-vanishing VEV for some of the scalar fields in the MSSM. For this reason, it is common to add a so called hidden sector to the theory which includes much heavier particles than those of the MSSM. The interaction with the MSSM takes place with so called messenger fields. It can for instance be gravitational (in supergravity models) or gauge mediated (in gauge mediated SUSY breaking models). Since the masses of the messenger fields are much larger than those of the MSSM fields, we obtain the Lagrangian $\mathcal{L}_{\text{MSSM}}$ as an effective theory by integrating out the additional messenger fields. For the spontaneous breakdown of SUSY, one of the auxiliary scalar fields has to get a nonzero VEV. These scenarios are then either called D -term breaking or F -term breaking, also referred to as the Fayet-Ilioupolis or O' Raifeartaigh breaking, respectively [7].

So far, we do not know how SUSY breaking has occurred. Fortunately, for phenomenological studies of the MSSM the details of the hidden and messenger sectors are not of great interest. However, in order to make predictions we need to parameterize the soft SUSY breaking terms of $\mathcal{L}_{\text{Soft}}$. Soft means that no additional divergences are introduced. A general soft breaking term for a theory with one chiral and one gauge field (see Eq. (2.44)) can be written as

$$\mathcal{L}_{\text{Soft}} = -\phi_i^*(m^2)_{ij}\phi_j + \left(\frac{1}{3!}\mathcal{A}_{ijk}\phi_i\phi_j\phi_k - \frac{1}{2}\mathcal{B}_{ij}\phi_i\phi_j + \mathcal{C}_i\phi_i - \frac{1}{2}M\lambda^a\lambda^a + \text{h.c.} \right). \quad (2.51)$$

Here, ϕ_i is the scalar component of the chiral supermultiplet Φ_i , where $(m^2)_{ij}$ is the matrix of the squared mass. The fields λ^a and $\bar{\lambda}^a$ correspond to the two two-component gaugino fields of the vector supermultiplet with mass M . Additionally, we have trilinear (\mathcal{A} -term) and bilinear (\mathcal{B} -term) scalar couplings. Finally, there is a term which is linear in the field ϕ_i (\mathcal{C} -term) and which is only nonzero if the field is gauge invariant by itself.

¹²We would need sleptons/squarks in each of the three generations which are lighter than their SM partner [7].

Similarly to Eq. (2.51), we can specify the explicit breaking terms of the MSSM. Due to all the new fields, many free parameters have to be introduced, leading to the following Lagrangian

$$\begin{aligned}
-\mathcal{L}_{\text{Soft}}^{\text{MSSM}} = & \tilde{q}_{iL}^* \left(\mathcal{M}_{\tilde{q}}^2 \right)_{ij} \tilde{q}_{jL} + \tilde{u}_{iR}^* \left(\mathcal{M}_{\tilde{u}}^2 \right)_{ij} \tilde{u}_{jR} + \tilde{d}_{iR}^* \left(\mathcal{M}_{\tilde{d}}^2 \right)_{ij} \tilde{d}_{jR} \\
& + \tilde{l}_{iL}^* \left(\mathcal{M}_{\tilde{l}}^2 \right)_{ij} \tilde{l}_{jL} + \tilde{e}_{iR}^* \left(\mathcal{M}_{\tilde{e}}^2 \right)_{ij} \tilde{e}_{jR} \\
& + \left[h_1 \cdot \tilde{l}_{iL} (f^e A^e)_{ij} \tilde{e}_{jR}^* + h_1 \cdot \tilde{q}_{iL} (f^d A^d)_{ij} \tilde{d}_{jR}^* + \tilde{q}_{iL} \cdot h_2 (f^u A^u)_{ij} \tilde{u}_{jR}^* + \text{h.c.} \right] \\
& + m_1^2 |h_1|^2 + m_2^2 |h_2|^2 + (B\mu h_1 \cdot h_2 + \text{h.c.}) \\
& + \frac{1}{2} \left(M_1 \tilde{B} P_L \tilde{B} + M_1^* \tilde{B} P_R \tilde{B} \right) + \frac{1}{2} \left(M_2 \vec{\tilde{W}} P_L \vec{\tilde{W}} + M_2^* \vec{\tilde{W}} P_R \vec{\tilde{W}} \right) \\
& + \frac{1}{2} \left(M_3 \tilde{g}^a P_L \tilde{g}^a + M_3^* \tilde{g}^a P_R \tilde{g}^a \right) \\
& := V_{\text{Soft}} + \text{gaugino mass terms.}
\end{aligned} \tag{2.52}$$

Here, (\mathcal{M}_{ij}^2) are squared mass matrix elements for the left- and right-handed squarks and sleptons, where i and j denote generation indices. The mass terms $M_{1,2,3}$ are (in general) complex gaugino mass parameters. Note that for the winos we use the notation $\vec{\tilde{W}} = (\tilde{W}_1, \tilde{W}_2, \tilde{W}_3)$ for the $\text{SU}(2)_L$ triplet. $m_{1,2}$ are the real Higgs scalar mass parameters and μ is the mass parameter for the higgsino field. The soft breaking mass terms also contain general trilinear couplings (fA) and bilinear couplings, where the latter is scaled by $B\mu$. In comparison to Eq. (2.51), we see the absence of a C -term, because the MSSM does not contain any scalar field which is invariant under the three SM gauge groups by itself [7]. Additionally, we remark that in Eq. (2.52) we have used a four-component notation for the gaugino fields.

In total the MSSM contains 124 real parameters, including 19 of the SM. Not all of the parameters are completely independent. Due to experiments some of them are highly constrained. For instance the minimal flavor violation observations or the minimal CP violation restrict this huge parameter space. By making additional assumptions, e.g. of the breaking mechanism and the hidden sector, we can break down the enormous amount of arbitrariness for the MSSM leading to a theory with a predictive power.

The model with the minimal number of free parameters is called minimal supergravity¹³ (mSUGRA) and makes the following assumptions: first, the soft SUSY breaking universality, i.e. all mass matrices are proportional to the unit matrix; second, the trilinear couplings are supposed to be proportional to the Yukawa couplings. Additionally, we assume the gaugino masses (M_1, M_2, M_3) and all the scalar masses unify to $m_{1/2}$ and m_0^2 , respectively, at a much higher scale, the unification scale. This scenario is depicted in Fig. 2.2. Using RGEs for the soft breaking parameters we can calculate the whole MSSM mass spectrum and the couplings at the electroweak scale. In mSUGRA the amount of free parameters can be reduced to

¹³Sometimes it is also referred to as the constrained MSSM (cMSSM).

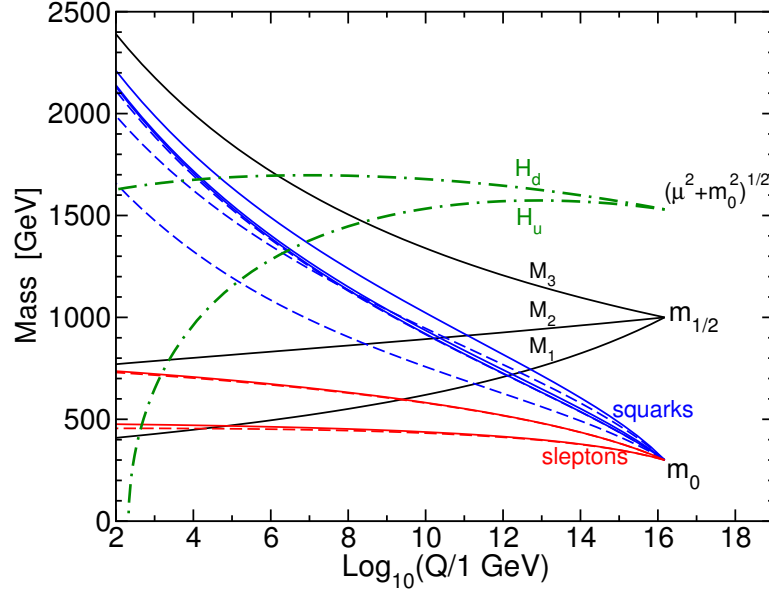


Figure 2.2: Running scalar and gaugino mass parameters in the MSSM for minimal supergravity models. The unification scale is considered as $Q_0 = 2 \times 10^{16}$ GeV. The running of the Higgs masses is assumed to be negative in order to provoke an electroweak symmetry breaking. The dashed lines represent the square roots of the third family parameters. Figure taken from Ref. [8].

only five. However, due to experimental data this model is already very challenging, if not even ruled out completely [23]. There are plenty of other models which reduce the parameter space of the MSSM to a manageable amount. It is also possible to investigate models with only *physical* parameters, which are often referred to as simplified models. In this thesis we investigate two models: for slepton pair production we use simplified models (see Sec. 5.2), whereas for the associated gaugino-gluino production we use a version of the phenomenological MSSM (pMSSM) which includes 13 parameters (see Sec. 6.4.1).

2.3.3 The gaugino and higgsino sector

The gauginos \tilde{B} and \tilde{W} are the spin 1/2 supersymmetric partners of the gauge bosons B and \tilde{W} and the higgsinos the partners of the Higgs fields in the MSSM. After electroweak symmetry breaking we are left with charged and neutral Higgs, higgsino and gauge fields. Fields carrying the same quantum numbers can mix. For this reason, the charged gaugino and higgsino fields mix to two charginos, whereas the neutral fields mix to four neutralinos. These mixing effects are completely determined by the parameters $M_{1,2}$, μ and $\tan \beta$. In the following we will use two-component Weyl spinors which will be denoted by lower case letters, instead of capital ones, e.g. $\tilde{B}^T = (\tilde{b}, \tilde{b}^T)$. The discussion presented here is based on Ref. [7].

For the charged sector we can write the mass term of the Lagrangian as

$$-\mathcal{L}_{\text{Mass}}^c = (\psi^-)^T \mathcal{M}^c \psi^+ + \text{h.c.}, \quad (2.53)$$

where

$$\mathcal{M}^c = \begin{pmatrix} M_2 & \sqrt{2}M_W \sin \beta \\ \sqrt{2}M_W \cos \beta & \mu \end{pmatrix}, \psi^+ = \begin{pmatrix} -i\tilde{w}^+ \\ \tilde{h}_2^+ \end{pmatrix} \text{ and } \psi^- = \begin{pmatrix} -i\tilde{w}^- \\ \tilde{h}_1^- \end{pmatrix}. \quad (2.54)$$

Here, \tilde{h}_1^- and \tilde{h}_2^+ are two-component spinorial higgsino fields. The gaugino fields are defined as $\tilde{w}^\pm = (\tilde{w}_1 \mp i\tilde{w}_2)/\sqrt{2}$. It is possible to find unitary matrices \mathcal{U} and \mathcal{V} so that the matrix \mathcal{M}^c can be diagonalized as $\mathcal{U}^* \mathcal{M}^c \mathcal{V}^{-1} = \mathcal{M}_D^c$. Then we can rewrite the Lagrangian as

$$-\mathcal{L}_{\text{Mass}}^c = \chi_k^- (\mathcal{M}_D^c)_{km} \chi_m^+ + \text{h.c.}, \quad (2.55)$$

where $\chi_k^+ = \mathcal{V}_{km} \psi_m^+$ and $\chi_k^- = \mathcal{U}_{km} \psi_m^-$ denote the mass eigenstates. If \mathcal{M}^c is only real-valued, i.e. if we ignore the complex phases of M_2 and μ , the mixing matrices can be parameterized by using one mixing angle. We define $\mathcal{U} =: O_u$ and $\mathcal{V} =: O_v$ (or $\mathcal{V} =: \sigma_3 O_v$ if the determinant of \mathcal{M}^c is smaller than zero) which allows us to write

$$O_{u,v} = \begin{pmatrix} \cos \phi_{u,v} & \sin \phi_{u,v} \\ -\sin \phi_{u,v} & \cos \phi_{u,v} \end{pmatrix}, \quad (2.56)$$

where the angles can be expressed as

$$\tan 2\phi_u = \frac{2\sqrt{2}M_W (\mu \sin \beta + M_2 \cos \beta)}{M_2^2 - \mu^2 - 2M_W^2 \cos 2\beta}, \quad (2.57)$$

$$\tan 2\phi_v = \frac{2\sqrt{2}M_W (\mu \cos \beta + M_2 \sin \beta)}{M_2^2 - \mu^2 + 2M_W^2 \cos 2\beta}. \quad (2.58)$$

Finally, we can write the mass eigenstates in terms of four-component Dirac spinors

$$\tilde{\chi}_{1,2}^\pm := \begin{pmatrix} \chi_{1,2}^\pm \\ \bar{\chi}_{1,2}^{\mp T} \end{pmatrix}, \quad (2.59)$$

where the $\bar{\chi} = \chi^\dagger$ denotes the hermitian conjugate¹⁴. The Lagrangian in terms of these Dirac chargino fields yields

$$-\mathcal{L}_{\text{Mass}}^c = M_{\tilde{\chi}_1^\pm} \bar{\tilde{\chi}}_1^+ \tilde{\chi}_1^+ + M_{\tilde{\chi}_2^\pm} \bar{\tilde{\chi}}_2^+ \tilde{\chi}_2^+ \quad (2.60)$$

where

$$M_{\tilde{\chi}_{1,2}^\pm}^2 = \frac{1}{2} \left[|M_2^2| + |\mu^2| + 2M_W^2 \mp \left\{ (|M_2^2| - |\mu^2|)^2 \right. \right]$$

¹⁴Note that for four-component Dirac spinors $\bar{\psi} = \psi^\dagger \gamma^0$.

$$+ 4M_W^4 \cos^2 2\beta + 4M_W^2 (|M_2^2| + |\mu^2| + 2 \operatorname{Re}(M_2 \mu) \sin 2\beta) \}^{1/2} \quad (2.61)$$

are the squared masses obeying the mass ordering $M_{\tilde{\chi}_1^\pm} < M_{\tilde{\chi}_2^\pm}$.

Next, we turn to the neutralinos. The Lagrangian for the neutral electroweak gauginos and higgsinos can be written as

$$\mathcal{L}_{\text{Mass}}^n = -\frac{1}{2} (\psi^0)^T \mathcal{M}^n \psi^0 + \text{h.c.}, \quad (2.62)$$

with

$$\mathcal{M}^n = \begin{pmatrix} M_1 & 0 & -M_Z c_\beta s_W & M_Z s_\beta s_W \\ 0 & M_2 & M_Z c_\beta c_W & -M_Z s_\beta c_W \\ -M_Z c_\beta s_W & M_Z c_\beta c_W & 0 & -\mu \\ M_Z s_\beta s_W & -M_Z s_\beta c_W & -\mu & 0 \end{pmatrix}, (\psi^0)^T = \begin{pmatrix} -i\tilde{b} \\ -i\tilde{w}_3 \\ \tilde{h}_1 \\ \tilde{h}_2 \end{pmatrix} \quad (2.63)$$

and $s_W = \sin \theta_W$, $c_W = \cos \theta_W$, $s_\beta = \sin \beta$ and $c_\beta = \cos \beta$, with θ_W being the Weinberg angle and $\tan \beta = v_2/v_1$ the relation of the two Higgs VEVs. The unitary transformation that diagonalizes the mass matrix is given by $N^* \mathcal{M}^n N^{-1} = \mathcal{M}_D^n$. After the diagonalization we get four two-component neutralino fields $\chi_l^0 = N_{ln} \psi_n^0$. Thereby, the Lagrangian can be written as

$$\mathcal{L}_{\text{Mass}}^n = -\frac{1}{2} \sum_l M_{\tilde{\chi}_l^0} \tilde{\chi}_l^0 \tilde{\chi}_l^0, \text{ where } \tilde{\chi}_l^0 = \begin{pmatrix} \chi_l^0 \\ \bar{\chi}_l^0 \end{pmatrix} \quad (2.64)$$

and $M_{\tilde{\chi}_l^0}$ are the mass eigenvalues. It is common to choose a real and orthogonal matrix N , although the eigenvalues of \mathcal{M}^n can be negative. The fields corresponding to the negative mass eigenvalue are then redefined by using a chiral rotation ($\tilde{\chi}_i^0 \rightarrow \tilde{\chi}_i^0 e^{i\pi/2}$) [24] to obtain the physical fields with a positive mass eigenvalue. In general the mass and the mixing matrix are obtained numerically. If all entries are real it is also possible to perform an analytical computation, but the result is too cumbersome to show here.

We label the neutralinos in a mass ordering $M_{\tilde{\chi}_1^0} > M_{\tilde{\chi}_2^0} > M_{\tilde{\chi}_3^0} > M_{\tilde{\chi}_4^0}$. As already mentioned, in most scenarios $\tilde{\chi}_1^0$ is the LSP and can be a proper DM candidate. In contrast to the chargino sector, the neutralino mixing depends additionally on M_1 , which is basically arbitrary. Nonetheless, GUT theories relate M_1 and M_2 in such a way that they unify at the GUT-scale. In order to satisfy this unification, the condition $M_1(M_Z) \approx M_2(M_Z)/2$ must hold at the electroweak scale [7].

Finally, let us make some remarks about the composition of the neutralinos and charginos with respect to the SUSY breaking parameters. If $|\mu| \gg |M_{1,2}| \gg M_Z$ the two lightest neutralinos $\tilde{\chi}_{1,2}^0$ are mostly dominated by their gaugino components. Furthermore, if the unification condition ($M_1 \approx M_2/2$) holds, the lightest neutralino $\tilde{\chi}_1^0$ is mostly the $U(1)_Y$ -bino field \tilde{B} , whereas $\tilde{\chi}_2^0$ is the $SU(2)_L$ -wino field \tilde{W}_3 . The two heavier neutralinos are then dominated by their higgsino component. This applies also to the charginos, where the lighter

one, χ_1^\pm , is dominantly the charged wino and χ_2^\pm the charged higgsino. There is also a relation between the magnitude of the μ parameter and the neutralino and chargino masses given by [7] $M_{\chi_1^\pm} \simeq M_{\tilde{\chi}_2^0} \simeq 2M_{\tilde{\chi}_1^0}$ and $|\mu| \simeq M_{\tilde{\chi}_3^0} \simeq M_{\tilde{\chi}_4^0} \simeq M_{\chi_2^\pm} \gg M_{\chi_1^\pm}$.

Considering the opposite limit ($|\mu| \ll |M_{1,2}|$) the composition changes. Then the lighter neutralinos and charginos are mostly made of the higgsino components and the heavier chargino is most likely the charged wino. If the parameters are set to $|\mu| \approx |M_1|$ or $|M_2|$ we obtain strong mixing between all the components. Moreover, if we assume $|\mu, M_2| \gg M_Z$ together with the GUT relation between M_1 and M_2 , the approximate relation $M_{\tilde{\chi}_2^0} \simeq M_{\tilde{\chi}_1^\pm}$ holds. It is worth mentioning that all these considerations are independent of $\tan \beta$ [7].

2.3.4 The sfermion sector

In general, the sfermion masses are affected by the supersymmetric scalar potential

$$V^{\tilde{f}} = V_{\text{Soft}}^{\tilde{f}} + V_F^{\tilde{f}} + V_D^{\tilde{f}}, \quad (2.65)$$

where the first term consists of explicit scalar mass terms and the trilinear couplings (see Eq. (2.52)). The second and third contributions come from the F - and D -terms in Eq. (2.50). Mixing of the left- and right-handed sfermions is driven by the trilinear scalar couplings and the term originating from the higgsino mass term in the superpotential [7]. There can also be additional flavor mixing, but due to experimental data this can, in a good approximation, be neglected. In contrast to the slepton sector, the squark sector is a bit more complicated, because it also includes the CKM mixing matrix.

Next, we discuss the left- and right-handed mixing of the sfermions explicitly. In general, the mass term can be written as

$$-\mathcal{L}_{\tilde{f}\text{-mass}} = \sum_{\tilde{f}} \tilde{f}^\dagger \mathcal{M}_{\tilde{f}}^2 \tilde{f}, \quad (2.66)$$

$$\text{where } \tilde{f} = \begin{pmatrix} \tilde{f}_L \\ \tilde{f}_R \end{pmatrix} \quad \text{and} \quad \mathcal{M}_{\tilde{f}}^2 = \begin{pmatrix} \mathcal{M}_{\tilde{f}LL}^2 & \mathcal{M}_{\tilde{f}LR}^2 \\ \mathcal{M}_{\tilde{f}LR}^{2*} & \mathcal{M}_{\tilde{f}RR}^2 \end{pmatrix}. \quad (2.67)$$

Note that the matrix elements of $\mathcal{M}_{\tilde{f}}^2$ in Eq. (2.67) are in general 3×3 matrices in flavor space. This is similar for the components $\tilde{f}_{L,R}$ which are three-component vectors in flavor space, e.g. $\tilde{f}_L = (\tilde{e}_L, \tilde{\mu}_L, \tilde{\tau}_L)^T$. The matrix elements can be written in a general form [25] as

$$\mathcal{M}_{\tilde{f}LL}^2 = \mathcal{M}_{\tilde{F}}^2 + M_Z^2 \cos 2\beta \left(T_3^f - Q_f \sin^2 \theta_W \right) + m_f^2, \quad (2.68)$$

$$\mathcal{M}_{\tilde{f}RR}^2 = \mathcal{M}_{\tilde{F}'}^2 + M_Z^2 \cos 2\beta Q_f \sin^2 \theta_W + m_f^2, \quad (2.69)$$

$$\mathcal{M}_{\tilde{f}LR}^2 = m_f \left(A_f^* - \mu (\tan \beta)^{-2T_3^f} \right), \quad (2.70)$$

where $\mathcal{M}_{\tilde{F}}$ and $\mathcal{M}_{\tilde{F}'}$ are soft breaking mass terms corresponding to the left- and right-handed sfermions, respectively (see Eq. (2.52)), A_f is the trilinear Higgs-sfermion-sfermion coupling, m_f , Q_f and T_3^f are the fermion mass, fraction of the electric charge and third component of the weak isospin, θ_W is the Weinberg angle, M_Z the mass of the Z boson and μ the higgsino mass parameter.

We find that the off-diagonal components are directly proportional to the masses of the fermionic partners. For this reason, it is common to take only the mixing of the heavy third generation into account, namely for the $\tilde{\tau}$, \tilde{b} and \tilde{t} . For the other two generations mixing effects can be neglected.

The mass eigenstates can be written as

$$\tilde{f}^m = S^{\tilde{f}} \tilde{f}, \quad (2.71)$$

where the matrix $S^{\tilde{f}}$ is used to diagonalize the mass matrix as

$$\mathcal{M}_{\tilde{f}}^{2(D)} = S^{\tilde{f}} \mathcal{M}_{\tilde{f}}^2 S^{\tilde{f}\dagger} \quad (2.72)$$

leading to the two squared mass eigenvalues

$$\mathcal{M}_{\tilde{f}_{1,2}}^2 = \frac{1}{2} \left[\mathcal{M}_{\tilde{f}_{LL}}^2 + \mathcal{M}_{\tilde{f}_{RR}}^2 \mp \sqrt{(\mathcal{M}_{\tilde{f}_{LL}}^2 - \mathcal{M}_{\tilde{f}_{RR}}^2)^2 + 4|\mathcal{M}_{\tilde{f}_{LR}}^2|^2} \right], \quad (2.73)$$

where by convention $\mathcal{M}_{\tilde{f}_1} < \mathcal{M}_{\tilde{f}_2}$. Similar to the chargino sector, the mixing matrix can be parameterized by a mixing angle as

$$S_{ii}^{\tilde{f}} = S_{(i+3)(i+3)} = \cos \theta_{\tilde{f}}, \quad (2.74)$$

$$S_{i(i+3)}^{\tilde{f}} = -S_{(i+3)i}^{\tilde{f}} = \sin \theta_{\tilde{f}}, \quad (2.75)$$

with the mixing angle [26]

$$\tan 2\theta_{\tilde{f}} = \frac{2\mathcal{M}_{\tilde{f}_{LR}}^2}{\mathcal{M}_{\tilde{f}_{LL}}^2 - \mathcal{M}_{\tilde{f}_{RR}}^2}. \quad (2.76)$$

All the other matrix elements are set to zero so that there is no mixing between the generations. The left- and right-handed mixing can be especially large in the stop sector due to the large top mass. It follows that in some MSSM scenarios \tilde{t}_1 will be the lightest sfermion [7].

2.3.5 The gluino

The gluino is the only color octet fermion in the MSSM and hence cannot mix with any other particle. For models with mass unification boundaries like mSUGRA the gluino mass parameter M_3 has to fulfill the condition

$$M_3 = \frac{\alpha_s}{\alpha} \sin^2 \theta_W M_2 = \frac{3}{5} \frac{\alpha_s}{\alpha} \cos^2 \theta_W M_1, \quad \text{with } \alpha = e^2/(4\pi) \quad (2.77)$$

at any renormalization scale (neglecting small two-loop corrections). Near the TeV scale this roughly gives $M_3 : M_2 : M_1 \approx 6 : 2 : 1$. It turns out that in those scenarios the gluino will be much heavier than the charginos and neutralinos at the electroweak scale. This is even true for many scenarios which do not imply a unification at the GUT scale. Moreover, we remark that M_3 is the LO mass of the gluino. Beyond LO the gluino mass receives further correction terms and differs from M_3 [8].

3 Perturbative Quantum Chromodynamics

The foundations of Quantum Chromodynamics, the theory of strong interactions between quarks and gluons, were laid more than 40 years ago, when several people helped to develop one of the cornerstones of today's SM. Among them Murray Gell-Mann, who introduced quarks as constituents of hadrons obeying a $SU(3)$ flavor symmetry in 1964 [27]. Later, in 1973, Gell-Mann, Fritzsch and Leutwyler established a local non-abelian $SU(3)$ gauge symmetry, not only including all the properties of the former quark model, but also leading to the gauge interactions of quarks and gluons carrying a color charge as a conserved quantum number [28]. This was one of the milestones leading to QCD as we know it nowadays.

There are two important consequences due to the non-abelian gauge group: asymptotic freedom [29, 30] and confinement, which we briefly address in this chapter.

We begin as follows: in Sec. 3.1 we describe the asymptotic freedom, followed by the phenomena of confinement accompanied by the parton distribution functions (PDFs) and the Dokshitzer–Gribov–Lipatov–Altarelli–Parisi [31, 32, 33] (DGLAP) equations in Sec. 3.2. Afterwards, in Sec. 3.3, we address a method for the treatment of soft and collinear divergences in QCD, the Catani-Seymour dipole subtraction formalism [34, 35], which is well suited for numerical phase space integration. Finally, we address the renormalization formulas in Sec. 3.4 which we use for our computations of the virtual corrections.

3.1 Asymptotic freedom

One of the key features of perturbative QCD (pQCD) is asymptotic freedom. It can be obtained by the analysis of the running coupling $\alpha_s = g_s^2/(4\pi)$, determined by the RGE

$$\mu^2 \frac{\partial \alpha_s}{\partial \mu^2} = \beta(\alpha_s), \quad (3.1)$$

which can be derived by using the fact that the unrenormalized (bare) coupling is independent of the renormalization scale μ [36]. The β -function in Eq. (3.1) can be computed perturbatively as a power series in α_s starting at $\mathcal{O}(\alpha_s^2)$:

$$\beta = - \left[\left(\frac{\alpha_s}{2\pi} \right)^2 \beta_0 + \left(\frac{\alpha_s}{2\pi} \right)^3 \beta_1 + \mathcal{O}(\alpha_s^4) \right], \quad (3.2)$$

with

$$\beta_0 = \frac{11C_A - 2n_f}{6}, \quad \beta_1 = \frac{17C_A^2 - n_f(5C_A + 3C_F)}{6}, \quad (3.3)$$

where n_f is the number of light quark flavors, $C_A = 3$ and $C_F = 4/3$ are the quadratic Casimir invariants of SU(3) in the adjoint and fundamental representation, respectively. We can solve this differential equation by integrating from μ_0^2 to μ^2 , yielding at one-loop order[37]:

$$\alpha_s(\mu^2) = \frac{\alpha_s(\mu_0^2)}{1 + \alpha_s(\mu_0^2)(\beta_0/2\pi) \ln(\mu^2/\mu_0^2)} . \quad (3.4)$$

Here, μ_0 is a reference scale at which α_s has to be measured and is often set to M_Z , the mass of the Z boson. The values of μ and μ_0 need to be in the perturbative regime of QCD. Eq. (3.4) describes the scaling behavior of α_s . For increasing μ the strong coupling α_s decreases due to the positive sign of β_0 . The running coupling in four-loop approximation is shown in Fig. 3.1. There is no easy explanation why the coupling constant scales this way¹. This is in contrast to Quantum Electrodynamics (QED), where the electromagnetic coupling gets smaller at larger distances, because it is screened by vacuum polarizations [38].

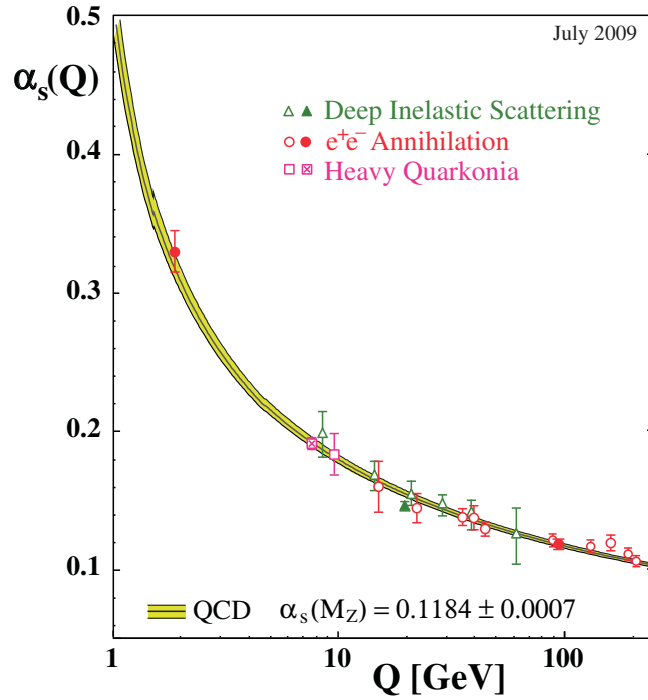


Figure 3.1: The yellow band shows theoretical QCD predictions for the running of α_s using the world average value of $\alpha_s(M_Z) = 0.1184 \pm 0.0007$ in four-loop approximation and three-loop threshold matching at the heavy quark pole mass. The crossed square is based on a Lattice-QCD computation, whereas the remaining points are measured values. Figure taken from [39].

Eq. (3.4) can be rewritten in a historically more convenient way as

$$\alpha_s(Q^2) = \frac{2\pi}{\beta_0 \ln(\mu^2/\Lambda^2)} , \quad (3.5)$$

¹The interested reader may have a look at Ref. [38] for a detailed discussion and explanation attempt.

where μ has been replaced by Q and $\Lambda^2 = \mu_0^2 \exp[-2\pi/(\beta_0\alpha_s(\mu_0^2))]$ is a scale *chosen by nature*, from which on QCD can be treated perturbatively. Its value is just below the GeV scale, but strongly depends on its definition, by means of the β -function and the renormalization scheme [38, 37]. With the knowledge of the RGE and the one-loop approximation of the β -function we have not only received the one-loop correction of α_s , but also resummed² all leading logarithmic contributions in $\ln(\mu^2/\mu_0^2)$ of the perturbative series, which can be potentially large for a considerable difference between the two scales μ and μ_0 . By including the β_1 coefficient to the β -function as well, we even resum all the subleading logarithmic terms [40].

Similar to the running coupling, we can derive a RGE for the quark masses m ,

$$\mu^2 \frac{\partial m}{\partial \mu^2} = -\gamma_m(\alpha_s)m(\mu^2), \quad (3.6)$$

where γ_m is the mass anomalous dimension and can be calculated perturbatively like the β -function. Integrating Eq. (3.6) and inserting γ_m up to a certain order leads to an equation showing the decrease of the quark masses m by increasing the scale μ . Therefore, the effect of the quark mass is suppressed at higher scales. For this reason, we can run into trouble for the derivation of the running coupling. We have to try matching the low scale region, taking masses into account, and the high scale region, where masses are negligible. Technically, the coupling of the full theory is matched to the one of an effective theory, both yielding different β -functions. An obvious approach is for instance to impose the scaling behavior of α_s to be continuous at $\mu = m$ [38].

The decrease of the coupling allows us to treat QCD perturbatively at huge momentum transfer and to neglect the quark masses, except for the top quark, which will be treated separately. When we look again at Fig. 3.1, we can see an increase of the coupling for very low scales. This leads to the concept of confinement, i.e. we cannot have free quarks or gluons. Hence we have to collide hadrons, which are low energy bound states and cannot be treated perturbatively. For all that, there is a way out: the parton model and parton distribution functions (PDFs).

3.2 Parton distribution functions

The name *parton* and the *parton model* have been introduced by Feynman in 1969 [41], the latter of which allows us to make predictions for scattering experiments involving hadrons at high energy scales. We assume the hadron with a four-momentum P^μ is made of point-like constituents, carrying the longitudinal momentum fraction x of the hadron. Hence, a hadronic cross section $\sigma^{(h)}$ involving two initial state hadrons A and B can be written as

$$\sigma^{(h)}(P_A, P_B) = \sum_{ab} \int_0^1 \int_0^1 dx_a dx_b f_{a/A}(x_a) f_{b/B}(x_b) \sigma_{ab}(x_a P_A, x_b P_B), \quad (3.7)$$

²The resummation of the leading logarithmic terms can be seen by expanding Eq. (3.4) for small α_s .

where σ_{ab} denotes the underlying partonic cross section, which can be calculated perturbatively. The functions $f_{i/h}(x_i)$ describe the probability³ of finding a parton i with a longitudinal momentum fraction $0 \leq x \leq 1$ in the hadron h [37]. Additionally, we sum over all possible partons $a(b)$ in the hadron $A(B)$.

The parton model with its probabilistic interpretation only holds for leading-order (LO) cross sections. At higher orders we have to abandon this *naive* model. Due to experiments of deep inelastic scattering (DIS) we know that the PDFs depend on the energy scale of the exchanged photon. Furthermore, in higher order computations we get confronted with collinear divergences which do not cancel without adjustments of the model, bringing us to the QCD improved parton model.

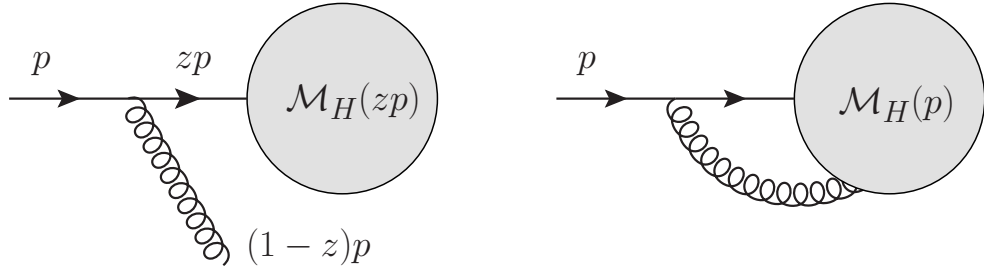


Figure 3.2: Schematic Feynman diagrams for real collinear emission (left) and for a virtual correction with a collinear emitted virtual gluon (right). After the real emission or virtual correction, the quark goes into a hard scattering process depicted by the gray filled circle. The virtual gluon couples to another colored particle inside the gray filled circle.

3.2.1 The QCD improved parton model

In NLO QCD calculations we encounter soft, collinear and soft-collinear divergences, for instance from the Feynman diagrams depicted in Fig. 3.2. The Kinoshita-Lee-Nauenberg (KLN) theorem [42] states that soft and collinear divergences cancel if we sum over all initial and final degenerate (experimentally indistinguishable) states. This means we have to add the soft and collinear real emission contributions to the corresponding virtual corrections. The reason for this is that we cannot distinguish between a single particle and a narrow jet of collinear particles and that we cannot detect soft gluons with an energy less than the detector resolution. Summing over all degenerate particles in the initial state is problematic, since we compute our diagrams by assuming a fixed amount of identified initial state partons carrying a fixed momentum. Thus, our partonic cross section in Eq. (3.7) containing identified partons in the initial state still suffers from collinear divergences, which have to be treated in a different manner.

³More specifically, they are defined as a number density since they are normalized to the number of partons in the hadron and not to one.

Let us have a look at the partonic cross section for a collinear real emission diagram as shown in Fig. 3.2. In the collinear limit it can be written as [43, 44]

$$d\sigma_{\text{Real}}(p) = \frac{\alpha_s}{2\pi} \int \frac{dk_T^2}{k_T^2} dz P_{qq}(z) d\sigma_B(zp), \quad (3.8)$$

where k_T is the transverse momentum of the emitted gluon with respect to the momentum p of the parent parton, $d\sigma_B(zp)$ is the underlying Born cross section, z is the longitudinal momentum fraction of the parent parton and $P_{qq}(z)$ is a LO Altarelli-Parisi (AP) splitting function (see Eq. (4.20)) which is divergent for $z \rightarrow 1$, i.e. for soft emitted gluons. By integrating over k_T we encounter a collinear divergence for $k_T \rightarrow 0$.

The corresponding virtual contribution of the NLO correction can be computed in the collinear limit in a similar way, giving

$$d\sigma_{\text{Virtual}}(p) = -\frac{\alpha_s}{2\pi} \int \frac{dk_T^2}{k_T^2} dz P_{qq}(z) d\sigma_B(p). \quad (3.9)$$

Both contributions factorize to the Born cross section multiplied by divergent pieces. Adding up both cross sections gives the full collinear correction to the Born cross section

$$\begin{aligned} d\sigma_{\text{Real}}(p) + d\sigma_{\text{Virtual}}(p) &= \frac{\alpha_s}{2\pi} \int \frac{dk_T^2}{k_T^2} dz P_{qq}(z) [d\sigma_B(zp) - d\sigma_B(p)] \\ &= \frac{\alpha_s}{2\pi} \int \frac{dk_T^2}{k_T^2} dz [P_{qq}(z)]_+ d\sigma_B(zp), \end{aligned} \quad (3.10)$$

where we have introduced the plus-distribution (see Appendix C) which regularizes the splitting function $P_{qq}(z)$. The soft and soft-collinear divergences cancel, but a collinear divergence remains⁴. Thus, we split the integral as

$$\int_{\mu_0^2}^{(k_T^{\text{max}})^2} \frac{dk_T^2}{k_T^2} = \int_{\mu_0^2}^{\mu_F^2} \frac{dk_T^2}{k_T^2} + \int_{\mu_F^2}^{(k_T^{\text{max}})^2} \frac{dk_T^2}{k_T^2}, \quad (3.11)$$

where we have introduced the factorization scale μ_F , separating the long and short distance behavior. By adding the collinear divergent part of Eq. (3.10) to the Born cross section, we get

$$d\sigma_B(p) + \frac{\alpha_s}{2\pi} \int_{\mu_0^2}^{\mu_F^2} \frac{dk_T^2}{k_T^2} \int_0^1 dz [P_{qq}(z)]_+ d\sigma_B(zp) = \int_0^1 dz \phi_{qq}(z, \mu_F^2) d\sigma_B(zp), \quad (3.12)$$

⁴Note that for an inclusive cross section and pure final state emission even the collinear divergences cancel, since we have the same momentum going into the hard process for the virtual and the real emission contributions. However, isolating a real gluon in the final state would lead to similar issues.

where we have defined

$$\phi_{qq}(z, \mu_F^2) := \delta(1 - z) + \frac{\alpha_s}{2\pi} \int_{\mu_0^2}^{\mu_F^2} \frac{dk_T^2}{k_T^2} [P_{qq}(z)]_+ \quad (3.13)$$

as a *parton-in-parton* distribution function. This function describes the density of a quark of resolution μ_F inside a quark of resolution μ_0 with momentum fraction z of the parent parton and exhibits the collinear divergence for $\mu_0 \rightarrow 0$.

Since Eq. (3.13) belongs to the long distance behavior ($k_T^2 \rightarrow 0$), we *absorb* it into the PDFs by means of the following *redefinition*⁵:

$$\begin{aligned} f_{q/H}(x, \mu_F^2) &:= \iint dy dz f_{q/H}(y) \phi_{qq}(z, \mu_F^2) \delta(x - yz) \\ &= \int_x^1 \frac{dz}{z} \phi_{qq}(z, \mu_F^2) f_{q/H}\left(\frac{x}{z}\right) =: [\phi_{qq} \otimes f_{q/H}](x, \mu_F^2). \end{aligned} \quad (3.14)$$

This procedure is shown schematically in Fig. 3.3. If a gluon is emitted with a transverse momentum $k_T^2 \leq \mu_f^2$ it belongs to the PDF, else it takes part in the hard scattering process and has to be taken into account in the perturbative corrections to the partonic cross section [38]. The hadronic cross section, expressed in terms of the new PDFs, can be written as

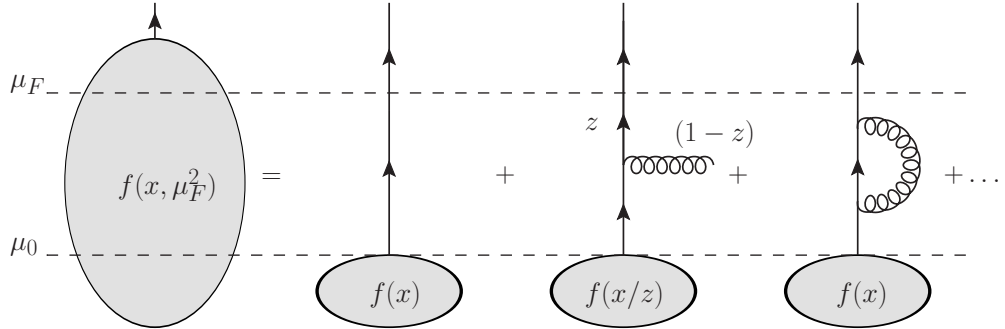


Figure 3.3: Schematic visualization of the factorization scale μ_F and the redefined PDF. All real and virtual emitted partons with a transverse momentum $k_T \leq \mu_F$ belong to the PDF pictured by the gray ellipse on the left hand side. The dots on the right hand side represent further real and virtual emission contributions.

$$d\sigma^{(h)}(P) = \sum_q \int_0^1 dx f_{q/H}(x) d\sigma_q(xP)$$

⁵Factorization is actually not a method for absorbing collinear divergences by a redefinition of the PDFs. Collinear divergences for parton densities defined by the *operator formalism* get canceled by needed subtraction terms to avoid double counting between NLO and LO hard scattering contributions. Also notice that for the computation of hard scattering processes we assume on shell partons, which is actually not true since they can be off shell up to $k_T^2 = \mu_F^2$. Nonetheless, we stick to the simpler illustration which makes no difference for most of the results of the hard scattering functions. For further information see Ref. [45].

$$= \sum_q \int_0^1 dx f_{q/H}(x, \mu_F^2) d\sigma_q(xP, \mu_F^2). \quad (3.15)$$

The redefined partonic cross section $d\sigma_q(xP, \mu_F^2)$ now consists only of the short distance behavior of the former partonic cross section and does no longer exhibit the collinear divergence. This was a first hint towards the famous *factorization theorem* [46].

Note that we have *absorbed* the whole collinear part up to μ_F into the PDFs. Furthermore, we have used a cutoff method⁶ for the regularization of the divergence which is not very practicable for higher order computations and also not mandatory [45]. Using techniques of dimensional regularization (DREG) we can isolate the collinear divergent pole. The real collinear emission cross section in Eq. (3.8) can then be written as [34]

$$d\sigma^C(p, \mu_F^2) = \frac{\alpha_s}{2\pi} \frac{1}{\Gamma(1-\epsilon)} \int_0^1 dz \left[-\frac{1}{\epsilon} \left(\frac{4\pi\mu^2}{\mu_F^2} \right)^\epsilon P_{qq}(z) \right] d\sigma^B(zp), \quad (3.16)$$

where the integral over k_T^2 has been performed in $D = 4 - 2\epsilon$ dimensions from zero to μ_F^2 . Here, Γ is the gamma function and μ is a scale to keep the dimension of the D -dimensional integral fixed. It is now possible to *absorb* only the divergent pole or also additional finite terms. This defines different factorization schemes. Since the collinear divergences are process independent it is possible to construct universal collinear counterterms by using DREG as it is done in the Catani-Seymour dipole formalism [34, 35] (see Sec. 3.3). Thereby, we can directly use the redefined PDFs in our computations and use the counterterms to subtract the divergent collinear terms which have been already *absorbed* into the PDFs. It is worth mentioning that we have to use the same factorization scheme for the PDFs and for the collinear counterterms.

In order to achieve the factorization, we had to introduce a new scale, the factorization scale μ_F , on which the PDFs and the partonic cross section depend. The PDFs cannot be computed perturbatively and have to be extracted from a comparison of the measurement of the left hand side (LHS) of Eq. (3.15) while we insert a theoretical computation for the partonic cross section on the right hand side (RHS), e.g. for DIS. Fortunately, we only have to perform the measurement at one scale $\mu_F = Q$, while the rest is determined by an evolution equation, which we can derive with Eq. (3.14). Taking the derivative with respect to μ_F and replacing $f(x)$ with $f(x, \mu_F^2)$ on the RHS, leading only to an error of $\mathcal{O}(\alpha_s^2)$, yields

$$\frac{df_{q/H}(x, \mu_F^2)}{d \ln \mu_F^2} = \frac{\alpha_s}{2\pi} \left[[P_{qq}(x)]_+ \otimes f_{q/H} \right] (x, \mu_F^2). \quad (3.17)$$

This whole procedure can be generalized to an arbitrary splitting at higher orders, because of the *factorization theorem* which has been proven up to all orders for DIS and for Drell-Yan-like processes [46]. The parton-in-parton distribution functions as well as the splitting kernels

⁶Here, it is also referred to as a *cutoff*-scheme as it defines the amount of finite terms which get *absorbed* by the PDFs.

can be computed in a perturbative series in α_s and can be generalized to different parton splittings:

$$\phi_{ik}(z) = \delta_{ik}\delta(1-z) + \sum_{n=1}^{\infty} \left(\frac{\alpha_s(\mu_F)}{2\pi} \right)^n \phi_{ik}^{(n)}(z), \quad (3.18)$$

$$\mathcal{P}_{ij} := \sum_{n=1}^{\infty} \left(\frac{\alpha_s(\mu_F)}{2\pi} \right)^n P_{ij}^{(n)}(z). \quad (3.19)$$

Actually, the usual way to derive the evolution equations is by using the fact that the hadronic cross section in Eq. (3.15) does not depend on μ_F ⁷, leading to an equivalent of an RGE. For the whole particle content of QCD we get

$$\frac{df_{i/H}(x, \mu_F^2)}{d \ln \mu_F^2} = \sum_j \left[\mathcal{P}_{ij}(\alpha_s(\mu_F^2)) \otimes f_{j/H} \right](x, \mu_F^2), \quad (3.20)$$

which are the so called DGLAP equations. The diagonal splitting kernels have been regularized using the plus-distribution, whereas the off-diagonal splitting functions are not infrared (IR) divergent. For the sake of simplicity we have set $\mu_R = \mu_F$ for the running of α_s .

Let us make some general remarks about PDFs: an important consequence is that parton densities cannot be formulated for a fixed final state, because they include the effects from any number of collinear emitted partons⁸. Therefore, only processes like $pp \rightarrow \mu^+ \mu^- + X$ can be evaluated, where X includes any number of collinear jets [43]. Furthermore, the PDFs are universal, i.e. we can measure them for one process, e.g. DIS, at one scale and use them for another process at another scale with the help of the evolution equations. This universality of the PDFs assures the predictive power of pQCD. In Fig. 3.4 we see a NLO PDF for two different resolution scales Q , where NLO refers to NLO splitting functions which have been used for solving the DGLAP equations. At higher resolution scales (right panel of the figure) the sea quarks become more important than for lower scales (left panel of the figure), where the valence quark and gluon contributions are dominant. For low scales the importance of the gluon PDF increases with respect to the valence quark PDFs. When Q^2 increases, the valence quark PDFs decrease at large x and increase at small x . This can be understood as an increase in the phase space of the additional emitted gluons by the quark as Q^2 increases and thus leads to a reduction of the quark momentum [38].

In this section we have seen that for the *naive* parton model the function $f(x)$ has a direct interpretation as the probability of finding a parton with a certain longitudinal momentum fraction x inside a hadron. In their core the PDFs have a similar interpretation, with the restriction that the parton can be off shell by no more than a transverse momentum μ_F^2 [37]. Beyond this limit a parton would not be considered as a part of the hadron. Instead it would be involved in the hard scattering process. Besides, we remark that the PDFs depend on the factorization scheme and can also become negative. From this follows that a pure probabilistic interpretation is not really correct.

⁷However, for a fixed order computation the hadronic cross section depends on μ_F (and μ_R).

⁸With regard to the KLN-theorem it can eventually be understood as the summation over all degenerate initial states.

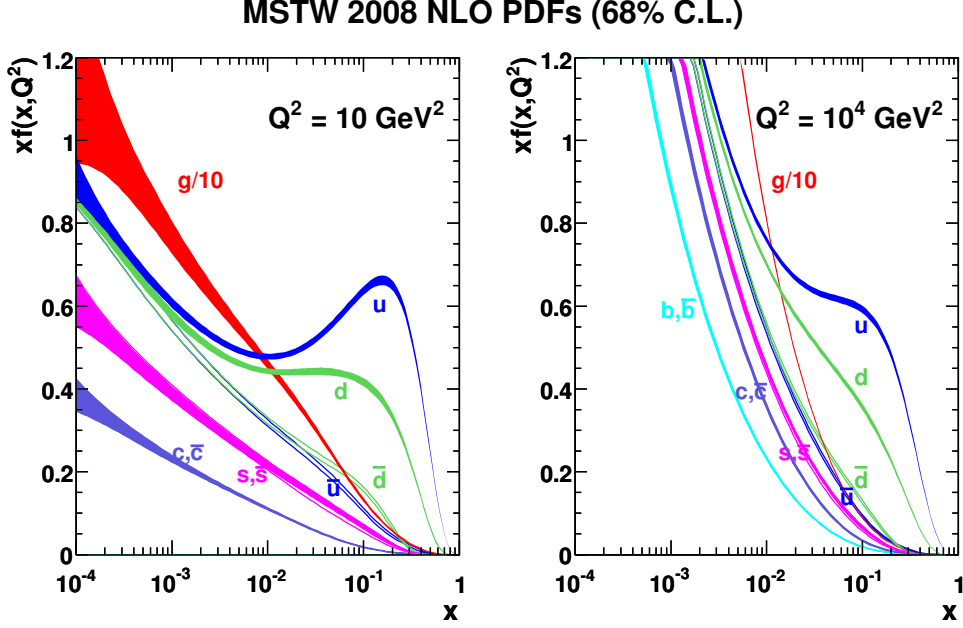


Figure 3.4: Momentum fraction distribution function $x f(x, Q^2)$ of the MSTW collaboration depicted for all partons at two different resolution scales $Q^2 = 10 \text{ GeV}^2$ (left) and $Q^2 = 10^4 \text{ GeV}^2$ (right). Figure taken from Ref. [47].

We have also mentioned the cancellation of the IR divergences among the virtual and real emission corrections. Usually, we perform the particle phase space integrals numerically, since they can become very cumbersome. For this reason, we need a good technique to assure the cancellation of the IR divergences, e.g. the Catani-Seymour dipole formalism [34, 35], which brings us to the next section.

3.3 Dipole subtraction formalism

In the previous section we have seen that we can write the hadronic cross section up to NLO, including two initial state hadrons, as a convolution of the PDFs with the partonic cross section:

$$\sigma^{(h)}(P_a, P_b) = \sum_{ab} \int_0^1 dx_a f_{a/A}(x_a, \mu_F^2) \int_0^1 dx_b f_{b/B}(x_b, \mu_F^2) \left[\sigma_{ab}^{\text{LO}}(x_a P_a, x_b P_b) + \sigma_{ab}^{\text{NLO}}(x_a P_a, x_b P_b, \mu_F^2) \right]. \quad (3.21)$$

The NLO part exhibits soft, collinear and soft-collinear divergences in the real and the virtual contributions. Their sum together with the redefined PDFs is finite. For the real emission diagrams we encounter the divergences after the phase space integration has been performed. Since it can be rather complicated to evaluate the three-particle phase space integral in

$D = 4 - 2\epsilon$ dimensions analytically we adopt the Catani-Seymour dipole subtraction formalism [34, 35] which is convenient for a numerical integration.

For this method a local counterterm $d\sigma^A$, which acts as a good approximation of the real emission cross section $d\sigma^R$ and exhibits the same singular structure, is subtracted from the real emission cross section. The finite NLO cross section can be written as

$$\sigma^{\text{NLO}} = \int_{m+1} \left[d\sigma^R - d\sigma^A \right] + \int_{m+1} d\sigma^A + \int_m d\sigma^V + \int_m d\sigma^C, \quad (3.22)$$

where also a collinear subtraction counterterm $d\sigma^C$ has been added, which is scheme dependent and cancels together with the integrated form of $d\sigma^A$ all the singularities of the virtual cross section, leaving a finite so called collinear remainder. The scheme of the counterterm needs to agree with the one of the used PDFs. The labels m and $m+1$ denote the number of particles in the final state.

As the two contributions in the square bracket are IR finite, the integral can be performed numerically in $D = 4$ dimensions. In order to cancel the divergences of the virtual contribution, the one-particle phase space integral over $d\sigma^A$ has to be evaluated analytically in $D = 4 - 2\epsilon$ dimensions. Therefore, we can write

$$\sigma^{\text{NLO}} = \int_{m+1} \left[(d\sigma^R)_{\epsilon=0} - (d\sigma^A)_{\epsilon=0} \right] + \int_m \left[\int_1 d\sigma^A + d\sigma^V + d\sigma^C \right]_{\epsilon=0}. \quad (3.23)$$

It can be shown that the divergent parts of the local counterterms, $d\sigma^A$ and $d\sigma^C$, are independent of the underlying hard scattering process and only depend on the different parton types that take part in the scattering process. The divergences completely factorize to a form

$$d\sigma^A = \sum_{\text{dipoles}} d\sigma^B \otimes \left(dV_{\text{dipole}} + dV'_{\text{dipole}} \right), \quad (3.24)$$

$$\int_m d\sigma^C(p) = \int_0^1 dx \int_m d\sigma^B(xp) \Gamma(x), \quad (3.25)$$

where the symbol \otimes denotes a properly defined phase space convolution and a summation over color and spin indices. The factor $d\sigma^B$ is an appropriate color and spin projection of the Born level exclusive cross section to which the divergent pieces factorize [34]. The dipoles dV_{dipole} and dV'_{dipole} are completely universal and the former cancels all the soft and soft-collinear poles of the real emission and the latter cancels the remaining collinear poles. The collinear subtraction counterterm $d\sigma^C$, arising from the redefinition of the PDFs, involves an additional integration with respect to the longitudinal momentum fraction x of the parent parton. It can be written as a convolution of $d\sigma^B$ with a divergent process independent function $\Gamma(x)$. The dipoles dV_{dipole} and dV'_{dipole} are fully integrable analytically over the one-particle phase space. Performing the integral of the counterterm $d\sigma^A$ in Eq. (3.24) analytically leads to the singular insertion operator \mathbf{I} , which cancels all the singularities in the virtual contribution $d\sigma^V$, and to additional collinear divergent terms which get canceled by the collinear subtraction

counterterm $d\sigma^C$ leaving the finite collinear remainder. This leads to the following expression for a general NLO contribution with two massless initial state partons:

$$\begin{aligned} \sigma^{\text{NLO}}(p_a, p_b) = & \int_{(m+1)} \left[\left(d\sigma^R(p_a, p_b) \right)_{\epsilon=0} - \left(\sum_{\text{dipoles}} d\sigma^B(p_a, p_b) \otimes (dV_{\text{dipole}} + dV'_{\text{dipole}}) \right)_{\epsilon=0} \right] \\ & + \int_0^1 dx \int_m \left[d\sigma^B(xp_a, p_b) \otimes (\mathbf{P} + \mathbf{K})(x) + (a \leftrightarrow b) \right]_{\epsilon=0} \\ & + \int_m \left[d\sigma^V(p) + d\sigma^B \otimes \mathbf{I} \right]_{\epsilon=0}. \end{aligned} \quad (3.26)$$

The operators \mathbf{P} and \mathbf{K} govern the collinear remainder and contain for instance the regularized AP splitting functions. They are referred to as insertion operators as well and can lead to sizable contributions for $x \rightarrow 1$, i.e. for soft emitted partons. All the dipoles and insertion operators are universal, only depending on the number and type of the identified partons. Eq. (3.26) is a suitable form for a numerical approach of the NLO cross section with two initial state hadrons.

So far, we have only considered the treatment of the soft and collinear divergences and assumed that the ultraviolet (UV) divergences have already been subtracted by the renormalization approach. In the next section we briefly discuss how we renormalize the virtual cross section $d\sigma^V$.

3.4 Renormalization

So far, no theory in physics describes all phenomena we observe, because all of them are only valid for a certain energy scale region. For instance, the SM which does not embed gravitation and hence cannot make reliable predictions close to the Planck scale, where gravitational effects start to play an important role.

When we compute Feynman diagrams including virtual corrections, we have to integrate over all possible momenta of the virtual particle, i.e. also going up to a scale which is not described by the theory. By reaching the limit of the valid region, our predictions get worse. The high scale corresponds to a short distance where new physics has to be taken into account. Arising fluctuations can add up coherently and lead to the so called UV divergences. The concept of renormalization can handle these fluctuations and restores the convergence of our perturbative series and assures the predictive power of our theory [40].

In this section we address the necessary renormalization formulas for NLO computations needed for this thesis. An introduction about the concepts and ideas behind renormalization can be found in Ref. [40]. Derivations of applicable formulas are given in Ref. [48].

3.4.1 Mass and field renormalization

First, we deal with the renormalization of the two-point Green's function, leading to renormalized fields and masses. In this thesis only the self-energies of chiral fermions (quarks and

gluinos) and squarks are relevant. Afterwards, we explain our treatment of the UV divergences arising in three-point Green's functions, i.e. in the vertex corrections.

Non-mixing chiral fermions

A general Lagrangian for free non-mixing chiral fermions ψ with mass m can be written as the sum of the kinetic and mass terms

$$\mathcal{L}_F = i\bar{\psi}_b^L \not{\partial} \psi_b^L - im_b \bar{\psi}_b^R \psi_b^L + (L \leftrightarrow R), \quad (3.27)$$

where the index b denotes the *bare* quantities and the labels L and R refer to the left- and right-handed components of the field.

We can define renormalized quantities m , ψ^L and ψ^R and expand multiplicative renormalization factors Z_m and $Z_\psi^{L,R}$ up to $\mathcal{O}(\alpha_s)$ as

$$m_b = Z_m m = (1 + \delta Z_m) m + \mathcal{O}(\alpha_s^2), \quad (3.28a)$$

$$\psi_b^L = \sqrt{Z_\psi^L} \psi^L = (1 + \frac{1}{2} \delta Z_\psi^L) \psi^L + \mathcal{O}(\alpha_s^2), \quad (3.28b)$$

$$\psi_b^R = \sqrt{Z_\psi^R} \psi^R = (1 + \frac{1}{2} \delta Z_\psi^R) \psi^R + \mathcal{O}(\alpha_s^2), \quad (3.28c)$$

where δZ_m and $\delta Z_\psi^{L,R}$ are the mass and field counterterms. By inserting Eqs. (3.28a) to (3.28c) in Eq. (3.27) and using $\psi^{L,R} = P_{L,R} \psi$, where $P_{L,R}$ are the common left- and right-handed projectors, we can extract a counterterm for the two-point Green's function

$$-i\Sigma^{(\times)} = i\delta_{ab} \left[\not{p} \text{Re}(\delta Z_\psi^L) - m \left(\delta Z_m + \frac{1}{2} (\delta Z_\psi^{R*} + \delta Z_\psi^L) \right) \right] P_L + (L \leftrightarrow R), \quad (3.29)$$

where a and b are color indices. The *bare* self-energy Σ is usually split in a component proportional to the momentum p , denoted by Σ_V , and the remaining part, called Σ_S . Furthermore, we treat the left- and right-handed parts separately so that we can write

$$-i\Sigma = -i\delta_{ab} (\not{p} \Sigma_V^L + \Sigma_S^L) P_L + (L \leftrightarrow R), \quad (3.30)$$

where we have additionally factored out the color structure. The renormalized self-energy $\hat{\Sigma}$ is gained by adding Eq. (3.30) and Eq. (3.29), which yields

$$\begin{aligned} \hat{\Sigma} &= \delta_{ab} \left[\not{p} \left(\Sigma_V^L - \text{Re}(\delta Z_\psi^L) \right) + m \left(\frac{\Sigma_S^L}{m} + \delta Z_m + \frac{1}{2} (\delta Z_\psi^{R*} + \delta Z_\psi^L) \right) \right] P_L + (L \leftrightarrow R) \\ &= \delta_{ab} \left(\not{p} \hat{\Sigma}_V^L + \hat{\Sigma}_S^L \right) P_L + (L \leftrightarrow R). \end{aligned} \quad (3.31)$$

Here, the *hat* denotes renormalized quantities. In order to specify the field and mass counterterms, we first take a look at the fermion propagator up to NLO. According to Fig. 3.5 we can write

$$\begin{aligned}\mathcal{P}_F^{\text{NLO}} &= \mathcal{P}_F^{\text{LO}} + \mathcal{P}_F^{\text{LO}}(-i\Sigma)\mathcal{P}_F^{\text{LO}} + \mathcal{P}_F^{\text{LO}}(-i\Sigma^{(\times)})\mathcal{P}_F^{\text{LO}} \\ &= \mathcal{P}_F^{\text{LO}} \left(1 + (-i\hat{\Sigma})\mathcal{P}_F^{\text{LO}} \right),\end{aligned}\quad (3.32)$$

where $\mathcal{P}_F^{\text{LO}} = i\delta_{ab}(\not{p} - m)^{-1}$ represents the LO propagator. We define the residue \mathcal{R}_F of the

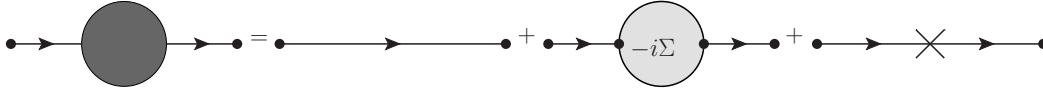


Figure 3.5: Fermion propagator including NLO corrections. The left hand side shows the renormalized propagator up to NLO. The parts on the right hand side are the LO, the self-energy and the counterterm contributions. The momentum, charge and fermion flows go from left to right.

complete fermion propagator \mathcal{P}_F as

$$\mathcal{R}_F u(p, m) \delta_{ab} = \lim_{p^2 \rightarrow m^2} -i(\not{p} - m) \mathcal{P}_F u(p, m), \quad (3.33)$$

where $u(p, m)$ denotes a Dirac spinor with momentum p and mass m .

For the on shell renormalization scheme there are two conditions: first, we impose the physical mass to be the real part of the propagator's pole; second, the real part of the propagator's residue should be one [49, 44]. This reads

$$\text{Re} \left(\left[\mathcal{P}_F^{-1} \right]_{p^2=m^2} \right) u(p, m) = 0, \quad (3.34)$$

$$\text{Re}(\mathcal{R}_F) = 1 \quad (3.35)$$

and can be translated into expressions for the renormalized self-energy by using Eq. (3.32):

$$\text{Re}(\hat{\Sigma}) \Big|_{(p^2=m^2)} u(p, m) = 0, \quad (3.36)$$

$$\lim_{p^2 \rightarrow m^2} \frac{\not{p} + m}{p^2 - m^2} \text{Re}(\hat{\Sigma}) u(p, m) = 0. \quad (3.37)$$

Thereby, we get four equations, because Eqs. (3.36) and (3.37) have to be fulfilled for the left- and right-handed part separately. They can be solved for the renormalization constants, yielding [49]

$$\delta Z_m = -\frac{1}{2} \text{Re} \left[\Sigma_V^L + \Sigma_V^R + \frac{\Sigma_S^L + \Sigma_S^R}{m} \right]_{p^2=m^2}, \quad (3.38)$$

$$\delta Z_{\psi}^{L,\text{ON}} = \text{Re} \left[\Sigma_V^L + m^2 \left(\Sigma_V^{L'} + \Sigma_V^{R'} + \frac{\Sigma_S^{L'} + \Sigma_S^{R'}}{m} \right) \right]_{p^2=m^2}, \quad (3.39)$$

$$\delta Z_{\psi}^{R,\text{ON}} = \text{Re} \left[\Sigma_V^R + m^2 \left(\Sigma_V^{R'} + \Sigma_V^{L'} + \frac{\Sigma_S^{R'} + \Sigma_S^{L'}}{m} \right) \right]_{p^2=m^2}, \quad (3.40)$$

with Σ' being the derivative of Σ with respect to p^2 .

Since we use the $\overline{\text{MS}}$ -scheme for the field renormalization we can extract $\overline{\text{MS}}$ counterterms from the on shell counterterms as

$$\delta Z_{\psi}^L = \overline{\text{UV}} \left[\delta Z_{\psi}^{L,\text{ON}} \right] \quad \text{and} \quad \delta Z_{\psi}^R = \overline{\text{UV}} \left[\delta Z_{\psi}^{R,\text{ON}} \right], \quad (3.41)$$

where $\overline{\text{UV}}$ denotes the UV divergent part together with the universal finite constants $(\ln 4\pi - \gamma_E)$, with γ_E being the Euler–Mascheroni constant. In the $\overline{\text{MS}}$ -scheme the real part of the propagator's residue is no longer renormalized to one. According to the Lehmann-Symanzik-Zimmermann (LSZ) formula [50], relating Green's functions to matrix elements, we have to multiply each external field by the square root of the propagator's residue \mathcal{R} [51]. For the $\overline{\text{MS}}$ -scheme it can be written as the $\overline{\text{UV}}$ finite part of the on shell field renormalization constant. Thus, we can write the expansion of the residue as

$$\sqrt{\mathcal{R}^L} = 1 + \frac{1}{2} \delta \tilde{Z}_{\psi}^{L,\text{ON}} + \mathcal{O}(\alpha_s^2) \quad \text{and} \quad \sqrt{\mathcal{R}^R} = 1 + \frac{1}{2} \delta \tilde{Z}_{\psi}^{R,\text{ON}} + \mathcal{O}(\alpha_s^2), \quad (3.42)$$

where the *tilde* denotes the $\overline{\text{UV}}$ finite part. Note that we renormalize left- and right-chiral fields separately.

Squarks

The Lagrangian for free left- and right-handed mixing squark fields of a given flavor can be written as

$$\mathcal{L}_{\tilde{q}} = \sum_{i=1}^2 \left(\partial_{\mu} \tilde{q}_i^{b\dagger} \partial^{\mu} \tilde{q}_i^b - (m_i^b)^2 \tilde{q}_i^{b\dagger} \tilde{q}_i^b \right), \quad (3.43)$$

where the index i refers to two different mass eigenstates with mass eigenvalues $(m_i^b)^2$. We can rewrite the *bare* quantities as⁹

$$\tilde{q}_i^b = \sqrt{Z_{ij}} \tilde{q}_j = (\delta_{ij} + \frac{1}{2} \delta Z_{ij}) \tilde{q}_j + \mathcal{O}(\alpha_s^2), \quad (3.44)$$

$$(m_i^b)^2 = Z_{m_i}^2 m_i^2 = (1 + \delta Z_{m_i}^2) m_i^2 + \mathcal{O}(\alpha_s^2), \quad (3.45)$$

where we have introduced multiplicative renormalization factors Z_{ij} and Z_{m_i} for the fields and masses, respectively, which have been expanded up to $\mathcal{O}(\alpha_s)$ resulting in additive counterterms δZ_{ij} and δZ_{m_i} . If we write Eq. (3.44) in a matrix form the field renormalization constants

⁹Note that if an index appears twice a summation over this index is implied.

would be elements of a 2×2 -matrix. This is due to the reason that by including loop corrections the two squark eigenstates can mix further. The mass renormalization constants δZ_{m_i} are diagonal per definition.

We can insert the new definitions in the Lagrangian and derive the Feynman rule for the counterterm of the squark self-energy, yielding

$$-i\Sigma_{ij}^{(\times)} = i\delta_{ab} \left(\frac{1}{2} (\delta Z_{ij} + \delta Z_{ji}^*) p^2 - \frac{1}{2} (m_i^2 \delta Z_{ij} + m_j^2 \delta Z_{ji}^*) - \delta Z_m^2 m_i^2 \delta_{ij} \right), \quad (3.46)$$

where δ_{ab} represents color conservation.



Figure 3.6: The left hand side shows the renormalized squark propagator up to NLO. On the right hand side the LO, the self-energy and the counterterm contributions are depicted. The momentum and charge flows go from left to right.

The residue $\mathcal{R}_{\tilde{q}_i}$ of a massive squark field can be defined as

$$\mathcal{R}_{\tilde{q}_i} \delta_{ij} \delta_{ab} = \lim_{p^2 \rightarrow m_i^2} i(p^2 - m_i^2) \mathcal{P}_{ij}, \quad (3.47)$$

where the propagator at NLO is given by

$$\mathcal{P}_{ij}^{\text{NLO}} = \mathcal{P}_{ij}^{\text{LO}} + \mathcal{P}_{ik}^{\text{LO}} (-i\Sigma_{kl} - i\Sigma_{kl}^{(\times)}) \mathcal{P}_{lj}^{\text{LO}}, \quad (3.48)$$

$$= \mathcal{P}_{ij}^{\text{LO}} + \mathcal{P}_{ik}^{\text{LO}} (-i\hat{\Sigma}_{kl}) \mathcal{P}_{lj}^{\text{LO}}, \quad (3.49)$$

with $\mathcal{P}_{ij}^{\text{LO}} = i\delta_{ab} \delta_{ij} (p^2 - m_i^2)$ being the LO propagator. Next, we specify the field and mass counterterms. First, we treat the case $i = j$. In the on shell scheme the pole of the propagator should be at the physical mass. So we impose

$$\text{Re} \left(\hat{\Sigma}_{ii}(m_i^2) \right) = 0. \quad (3.50)$$

Thereby, we can derive the mass counterterm

$$\delta Z_{m_i}^2 = - \frac{\text{Re} \left(\Sigma_{ii}(m_i^2) \right)}{m_i^2}. \quad (3.51)$$

Furthermore, we impose the real part of the residue to be one. This leads to

$$\text{Re} \left(\delta Z_{ii}^{\text{ON}} \right) = \text{Re} \left[\Sigma'_{ii}(m_i^2) \right]. \quad (3.52)$$

The imaginary part of the field renormalization constants can be set to zero, since the imaginary part of the self-energy does not contain a divergence [49]. Note that for both counterterms the color structure has been factorized out.

For $i \neq j$ the mass counterterm is zero. To get the field counterterms, we impose that no transition from a squark of type i to one of type j can occur through the propagator. This leads to

$$\text{Re} \left(\hat{\Sigma}_{12}(m_1^2) \right) = 0, \quad (3.53)$$

$$\text{Re} \left(\hat{\Sigma}_{12}(m_2^2) \right) = 0. \quad (3.54)$$

Thereby, we get

$$\delta Z_{12}^{\text{ON}} = -2 \frac{\text{Re}(\Sigma_{12}(m_2^2))}{(m_1^2 - m_2^2)}, \quad (3.55)$$

$$\delta Z_{21}^{\text{ON}} = 2 \frac{\text{Re}(\Sigma_{21}(m_1^2))}{(m_1^2 - m_2^2)}. \quad (3.56)$$

For the $\overline{\text{MS}}$ scheme, we take the $\overline{\text{UV}}$ divergent part of the on shell counterterm. Since we do not encounter external squarks in our computations, the LSZ factors are not required.

The interested reader may have a look at Ref. [49] for a more detailed discussion of the renormalization of squarks.

3.4.2 Vertex renormalization

The counterterms for the vertex correction are constructed in such a way to eliminate all the UV divergences together with the universal finite terms of the $\overline{\text{MS}}$ -scheme. Thus, we define

$$\Gamma_b := \bar{Z}_g \Gamma = (1 + \delta \bar{Z}_g) \Gamma, \quad (3.57)$$

$$\delta \bar{Z}_g \Gamma := \overline{\text{UV}} [\Gamma_b], \quad (3.58)$$

where Γ is a general interaction term of the Lagrangian, \bar{Z}_g a multiplicative renormalization factor and $\delta \bar{Z}_g$ a counterterm. We remark that in our treatment \bar{Z}_g is the only multiplicative renormalization constant in front of an interaction term in the Lagrangian. Alternatively, we could have added a multiplicative renormalization factor for the coupling constant g and each field contained in such an interaction term. The counterterm $\delta \bar{Z}_g$ can then be expressed in terms of these field and coupling counterterms.

4 Threshold Resummation

It is well known that cross sections for processes in perturbative QCD are characterized by the presence of large double logarithmic corrections near the boundary of the phase space, i.e. close to the production threshold for heavy particles. These potentially large logarithms emerge from a mismatch in the phase space between soft gluon emission in real and virtual contributions. Near the production threshold of massive particles the available phase space for real gluon emission is highly constrained and allows only for soft emission. However, for the virtual corrections we integrate over the full loop momentum of the virtual gluon. The outcome of this are large logarithmic remainders, which we encounter after the cancellation of the soft and soft-collinear divergences among the real and virtual corrections [52]. They exhibit the general structure

$$\alpha_s^n(\mu_R^2) \left[\frac{\ln^m(1-z)}{1-z} \right]_+, m \leq 2n-1, \quad (4.1)$$

where $z = M^2/s$, with M being the invariant mass of the final and s of the initial state, $1-z$ denotes the energy fraction of the emitted gluon with respect to its emitter and the subscript “+” denotes the plus-distribution (see Appendix C). Terms like in Eq. (4.1) arise at each order n of the perturbative series and increase drastically for soft emitted gluons, i.e. $z \rightarrow 1$, spoiling the convergence of the perturbative series and nullifying the truncation at fixed order of α_s . To make reliable predictions over the whole phase space region these logarithmic terms need to be resummed up to all orders [52].

Resummation requires a dynamical and kinematical factorization of the soft emitted gluons, where the former can be achieved through the eikonal approximation and the latter in a conjugate space, e.g. Mellin space. In this space the contributions in Eq. (4.1) transform to¹ $\alpha_s^n \ln^m N$, with $m \leq 2n$, and N being the Mellin moment of z . Here, the threshold region is now defined by $N \rightarrow \infty$.

The application of resummation techniques has been well established over the last three decades in particle physics. Especially for the production of supersymmetric heavy final state particles resummation is very important, because most of the available phase space at the LHC is restricted to the region close to their production threshold. Different precision levels are defined by the inclusion of next-to-dominant logarithmic terms in the resummed expression and are called leading logarithm (LL), next-to-leading logarithm (NLL) and so on. The achieved accuracy for electroweak SUSY particles, like sleptons [54] and gauginos [55], goes up to NLL+NLO, whereas for the, in most SUSY scenarios heavier, colored SUSY particles the accuracy goes up even to NNLL+NNLO² [56, 57, 58]. The searches for physics

¹The N -independent and threshold suppressed terms have been neglected here. Complete Mellin transforms of Eq. (4.1) up to $m = 3$ can be found in Ref. [53].

²We remark that the NNLL result is matched to an approximate NNLO computation.

beyond the SM do not only focus on SUSY, but also on new heavy electroweak gauge bosons, where resummation effects can be relevant [59, 60]. Due to the enormous experimental effort concerning the recently found Higgs boson, resummation techniques are also essential to narrow down theoretical uncertainties for Higgs production processes [61]. This follows from the fact that resummation does not only enlarge the cross section, but also decreases the scale dependencies on the renormalization scale μ_R and factorization scale μ_F , since more dominant scale dependent terms of the perturbative series are included.

It is worth mentioning that also other approaches exist which try to account for critical phase space regions. For instance, transverse momentum resummation (p_T -resummation) which resums large logarithmic terms which arise if the transverse momentum of an emitted parton goes to zero. Moreover, there are parton shower³ tools like PYTHIA [62] used in Monte-Carlo Event generators (see e.g. Refs. [63, 64]) or soft-collinear effective theories (see e.g. Refs. [65, 66]). Besides, there is also the so called absolute threshold resummation which uses another definition of the threshold. The threshold is reached if the velocities of the massive final state particles go to zero. It is also referred to as the β -threshold. In this thesis we focus on the threshold defined by $z \rightarrow 1$.

The aim of this chapter is to show the reader how we get to a resummed cross section which can then be applied to slepton pair and associated gaugino-gluino production. At the beginning, in Sec. 4.1, we discuss the basic ideas behind resummation. Next, we address the factorization of the soft emitted gluons from the underlying hard process in Sec. 4.2. The main part is the discussion of resummation for Drell-Yan-like processes in Sec. 4.3 for which we state the final results in Sec. 4.4. In Sec. 4.5 we extend this approach in order to include soft gluon emission contributions of the massive final state gluino in the associated production. Afterwards, we address the so called hard matching coefficient in Sec. 4.6 and discuss the matching procedure of the resummation result to a fixed order computation together with the inverse Mellin transform in Sec. 4.7. Finally, we show a collinear improved version for Drell-Yan-like processes up to NLL in Sec. 4.8.

4.1 The concept of resummation

Commonly, we make the assumption that a scattering process is characterized by one single scale M , which can be for instance the invariant mass of a lepton pair in case of the Drell-Yan (DY) process. Consequently, it is reasonable to set the renormalization scale μ_R and the factorization scale μ_F to M in order to keep the appearing logarithmic contributions small. In fact, however, we often have a *two scale problem* and due to the factorization of the short and long distance behavior and the cancellation of the soft and soft-collinear divergences, we introduce potentially large logarithmic contributions [67].

³Note that the parton shower approach does not lead to a shift in the total cross section, but ensures the correct shape in different distributions, like transverse momentum distributions. This is similar for p_T -resummation.

Imagine an infrared sensitive quantity $\mathcal{R}(M^2, m^2)$ depending on two scales, where M denotes a hard scale and m a scale measuring the distance to a critical region⁴. Due to the factorization theorem, we assume that our quantity can be written as

$$\mathcal{R}(M^2, m^2) = \mathcal{H}(M^2/\mu_F^2) \mathcal{S}(m^2/\mu_F^2), \quad (4.2)$$

where \mathcal{H} denotes the hard scattering and \mathcal{S} the long distance behavior. Note that this factorization can be highly nontrivial and is usually achieved in a conjugated space. As we know, both functions depend on logarithmic terms of their arguments. By setting $\mu_F = M$, we introduce potentially large logarithmic terms like $\ln(m^2/M^2)$ in the soft function \mathcal{S} ⁵. These logarithms can lead to very large corrections and the truncation of the perturbative series expanded in α_s is not justified, even if the value of α_s is small. Moreover, both scales satisfy the relation $M \gg m \gg \Lambda$, where Λ is a scale from which on QCD can be treated perturbatively. The first relation gives rise to the large logarithms in the soft function and the second one ensures that we can evolve the PDFs perturbatively and that $\alpha_s(M^2)$ is small [67]. For these reasons, we should try to resum the series in the soft limit, where we encounter the potentially large logarithms.

To obtain a resummed form of Eq. (4.2) we make use of the fact that the quantity \mathcal{R} is independent of the factorization scale:

$$\frac{d\mathcal{R}}{d \ln \mu_F^2} = 0 \implies \mu_F^2 \frac{d\mathcal{H}}{d\mu_F^2} \mathcal{S} = -\mu_F^2 \frac{d\mathcal{S}}{d\mu_F^2} \mathcal{H}. \quad (4.3)$$

Next, we define the soft anomalous dimension as

$$\gamma_S(\mu_F^2) := \frac{\mu_F^2}{\mathcal{H}} \frac{d\mathcal{H}}{d\mu_F^2} = -\frac{\mu_F^2}{\mathcal{S}} \frac{d\mathcal{S}}{d\mu_F^2} \quad (4.4)$$

and solve Eq. (4.3) by *separation of variables*. Thereby, we get

$$\mathcal{S}(m^2/\mu_F^2) = \mathcal{S}(1) \exp \left(- \int_{m^2}^{\mu_F^2} \frac{dk^2}{k^2} \gamma_s(k^2) \right). \quad (4.5)$$

Inserting this result in Eq. (4.2) leads to

$$\mathcal{R}(M^2, m^2) = \mathcal{H}(1) \mathcal{S}(1) \exp \left(- \int_{m^2}^{M^2} \frac{dk^2}{k^2} \gamma_s(k^2) \right), \quad (4.6)$$

where we have set $\mu_F = M$. The complete dependence on the two scales is now comprised in the exponent, the so called *Sudakov form factor*. The two functions $\mathcal{H}(1)$ and $\mathcal{S}(1)$ do not exhibit any large logarithmic terms of the two scales anymore. The exponent, or more explicit the soft anomalous dimension γ_s , can be computed perturbatively as an expansion in α_s , where its specific order defines the accuracy of the resummation.

⁴This can be something like $m \sim M/N$, where N is the Mellin moment and $N \rightarrow \infty$ in the critical region.

⁵An explicit example of the symbolic Eq. (4.2) is given in Eq. (4.32).

Here, we have only shown the basic concepts of resummation in a simplified manner. However, the main concepts which we use in the following are the same: factorization, renormalization group equations and the soft anomalous dimension. In addition, we make use of the gauge independence of the physical results.

4.2 Dynamical and kinematical factorization

4.2.1 Eikonal Feynman rules

In order to resum soft gluon emission up to all orders we need a dynamical factorization, i.e. a factorization of the multi-gluon QCD matrix element up to logarithmic accuracy [68]. This is achieved by the eikonal approximation, which we present for a single real gluon emission as shown in Fig. 4.1. The matrix element can be written as

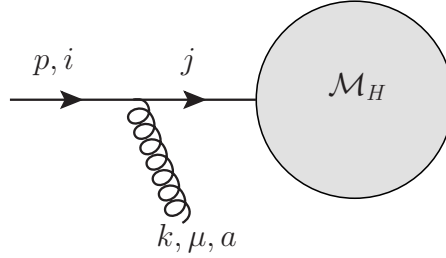


Figure 4.1: Feynman diagram for a quark with momentum p and color index i of the fundamental representation of SU(3) emitting a soft gluon with momentum k , color index a (adjoint representation) and Lorentz index μ . After the emission the quark goes into the hard scattering process \mathcal{M}_H depicted by the gray circle.

$$\begin{aligned}
 \mathcal{M}_{\text{Real}} &= \mathcal{M}_H \frac{i(\not{p} - \not{k} + m)}{(p - k)^2 - m^2 + i\epsilon} (-ig_s \gamma^\mu T_{ji}^a) u_i \epsilon_\mu^{a*} \\
 &\approx \mathcal{M}_H \frac{(\not{p} + m)}{-2p \cdot k + i\epsilon} (g_s \gamma^\mu T_{ji}^a) u_i \epsilon_\mu^{a*} \\
 &= \mathcal{M}_H \frac{2p^\mu}{-2p \cdot k + i\epsilon} (g_s T_{ji}^a) u_i \epsilon_\mu^{a*} \\
 &=: M_H \Gamma_{\text{eik.}}^\mu \epsilon_\mu^{a*}, \tag{4.7}
 \end{aligned}$$

where \mathcal{M}_H denotes the underlying hard scattering process, u_i the spinor of the incoming quark with momentum p and mass m , ϵ_μ^{a*} the polarization vector of the emitted gluon with momentum k and T_{ji}^a a color operator. Here, the matrix element has been factorized in the soft limit to the full hard scattering matrix element $M_H := \mathcal{M}_H u_i$ multiplied by an eikonal vertex

$$\Gamma_{\text{eik.}}^\mu := \frac{2p^\mu}{-2p \cdot k + i\epsilon} (g_s T_{ji}^a) \tag{4.8}$$

and the gluon polarization ϵ_μ^{a*} . For the derivation we have neglected the gluon momentum k in the numerator, because $k \ll p$, and used the fact that the gluon and the quark are on shell. Furthermore, we have used the anticommutator relation of the γ -matrices and the Dirac equation.

The eikonal vertex can be generalized for arbitrary emitter and absorber. It is common to write it as

$$\Gamma_{\text{eik.}}^\mu := g_s T^j \frac{\Delta_i v^\mu}{\delta_i v \cdot k + i\epsilon}, \quad (4.9)$$

where $v^\mu := p^\mu \sqrt{2/s}$ is a dimensionless vector, δ_i , Δ_i are different signs and T^j is a color operator (see Tab. 4.1). Thereby, we can distinguish between different possible scenarios. The same rules are applied to a soft emission or absorption for an exchange of a soft virtual

Type	in q	out q	in \bar{q}	out \bar{q}	in \tilde{g}/g	out \tilde{g}/g
Δ	+	+	-	-	+	+
δ	-	+	-	+	-	+
T^j	$T_{\beta\alpha}^a$	$T_{\alpha\beta}^a$	$T_{\alpha\beta}^a$	$T_{\beta\alpha}^a$	$-if^{abc}$	$-if^{abc}$

Table 4.1: Signs and color operator for the eikonal Feynman rules for soft emitted gluons by an incoming (in) and outgoing (out) quark, antiquark and gluino (gluon). For absorbing gluons the sign δ changes to $-\delta$.

gluon in loop corrections. For soft photon emission in Quantum Electrodynamics (QED) it is easy to show that for each additional emitted photon the *hard* matrix element M_H has to be multiplied just by another eikonal vertex and the photon polarization vector. This is in contrast to QCD, where it is much more complicated due to the non abelian gauge group and the thereby resulting gluon self interactions. However, it has been shown that the factorization holds in QCD as well and we can just multiply the underlying hard scattering process by eikonal vertices and gluon polarization vectors to include soft emitted gluons [52]. Nonetheless, care has to be taken to keep the correct order of the color operators. This is usually done by introducing additional color- or path-ordering operators [69].

4.2.2 Phase space factorization

By kinematical factorization we mean the factorization of the $2 + n$ -particle phase space into a two-particle phase space of the underlying Born process and n one-particle phase spaces for n soft emitted gluons. We can write the phase space of additional multiple gluon emissions as

$$\begin{aligned} d\text{PS}_{2+n} &= \frac{d^3 p_1}{(2\pi)^3 2E_1} \frac{d^3 p_2}{(2\pi)^3 2E_2} \prod_{i=1}^n \frac{d^3 k_i}{(2\pi)^3 2k_{i,0}} \\ &\times (2\pi)^4 \delta^{(4)} \left((p_a + p_b) - (p_1 + p_2) - \sum_{i=1}^n k_i \right) \end{aligned}$$

$$\times dM^2 \delta \left((p_a + p_b - \sum_{i=1}^n k_i)^2 - M^2 \right), \quad (4.10)$$

where p_1 and p_2 denote the momenta of the two final state particles of the Born process, p_a and p_b are the momenta of the two incoming partons, $M^2 = (p_1 + p_2)^2$ is the invariant mass of the final state system, k_i denotes the momenta of the soft emitted gluons and $k_{i,0}$ the zeroth component of k_i . If we neglect the soft gluon momenta k_i in the first δ -distribution, we are left with the task to show the factorization of the second δ -distribution in Eq. (4.10). We demonstrate this in the center-of-mass system, where $p_a = (\sqrt{s}/2, \vec{p}_a)$ and $p_b = (\sqrt{s}/2, -\vec{p}_a)$. Thereby, we get

$$\begin{aligned} \delta \left((p_a + p_b - \sum_{i=1}^n k_i)^2 - M^2 \right) &\approx \delta \left(s - 2\sqrt{s} \sum_{i=1}^n k_{i,0} - M^2 \right) \\ &= \frac{1}{s} \delta \left(1 - z - \sum_{i=1}^n z_i \right) \\ &\approx \frac{1}{s} \delta \left(\prod_{i=1}^n (1 - z_i) - z \right), \end{aligned} \quad (4.11)$$

where we have neglected $\mathcal{O}(k^2)$ terms and used the definitions $z = M^2/s$ and $z_i = 2k_{i,0}/\sqrt{s}$. The last line in Eq. (4.11) only holds in the limit $z \rightarrow 1$ and $z_i \rightarrow 0$, i.e. for soft emitted gluons. In order to achieve the factorization we perform a Mellin transform of the phase space with respect to the variable z , yielding

$$\int dz z^{N-1} \delta \left(\prod_{i=1}^n (1 - z_i) - z \right) = \prod_{i=1}^n (1 - z_i)^{N-1}. \quad (4.12)$$

For soft emitted gluons the limit $z \rightarrow 1$ turns into $N \rightarrow \infty$ due to the Mellin transform. In total we get

$$\int dz z^{N-1} d\text{PS}_{2+n}(z) \approx d\text{PS}_2 \times d\text{PS}_n(N), \quad (4.13)$$

where $d\text{PS}_2$ is the two-particle phase space and

$$d\text{PS}_n(N) := \frac{1}{s} \prod_{i=1}^n \frac{d^3 k_i}{(2\pi)^3 2k_{i,0}} (1 - z_i)^{N-1} \quad (4.14)$$

the one for n soft gluons. Note that it is not necessary to go into Mellin space. We could have also used a Laplace transformation leading to a similar result.

So far, we have shown the kinematical and dynamical factorization of multiple soft gluon emission. We are left with the task to get these isolated multiple gluon emissions in an exponential form. This is the topic of the next section.

4.3 Resummation for Drell-Yan-like processes

In this section, we describe the steps until we get a fully resummed result, which means that all the potentially large logarithms are contained in an exponential function multiplied by the underlying hard process. Therefore, we mainly follow the approaches presented in the Refs. [25, 69, 70, 71, 72]. Some of the steps are rather complicated and we recommend the interested reader to look at the original references, which are stated in each subsection.

4.3.1 Refactorization

Let us have a look at the single differential inclusive cross section for the process $p_A p_B \rightarrow l \bar{l} + X$, where p_A (p_B) denotes a proton, l and \bar{l} leptons with a large invariant mass M and X denotes an arbitrary amount of collinear and soft emitted partons, also including the remnant of the two protons. Due to the factorization theorem [46] we can write the hadronic cross section as a convolution of the two PDFs $f_{a/A}$ and $f_{b/B}$ with the partonic cross section $\hat{\sigma}_{ab}$ as

$$M^2 \frac{d\sigma_{AB}}{dM^2}(\tau, \alpha_s(\mu_R)) = \sum_{a,b} \int_0^1 dx_a dx_b dz \left[x_a f_{a/A}(x_a, \mu_F^2) \right] \left[x_b f_{b/B}(x_b, \mu_F^2) \right] \\ \times \left[z \hat{\sigma}_{ab}(z, M^2, \mu_F^2, \mu_R^2) \right] \delta(\tau - x_a x_b z), \quad (4.15)$$

where μ_F and μ_R are the factorization and renormalization scales, respectively, $\tau = M^2/S$ denotes the ratio of the final state center-of-mass energy to the hadronic one, $z = M^2/s = \tau/x_a x_b$ the ratio of the final state center-of-mass energy to the partonic one and $\hat{\sigma}_{ab}$ is the partonic hard scattering function⁶. For the sake of simplicity we set $\mu_F = \mu_R = \mu$ from now on and reintroduce the correct scale dependencies later again.

In order to resum soft gluon emission up to all orders in α_s we need a fully factorized form of the kinematical and dynamical parts of the cross section. The former can be achieved by using the eikonal approximation which has been discussed in Sec. 4.2.1, whereas for the latter (see. Sec. 4.2.2) we perform a Mellin transform

$$F(N) = \int_0^1 dy y^{N-1} F(y) \quad (4.16)$$

of the hadronic cross section with respect to the hadronic energy fraction $\tau = z x_a x_b$. This leads to three independent Mellin transformations⁷, two for the PDFs and one for the partonic cross section leading to the kinematical factorization mentioned in Sec. 4.2.2. In Mellin space the convolution of the PDFs and the partonic cross section in Eq. (4.15) turns into an ordinary product

$$M^2 \frac{d\sigma_{AB}}{dM^2}(N) = \sum_{ab} f_{a/A}(N, \mu^2) f_{b/B}(N, \mu^2) \hat{\sigma}_{ab}(N, M^2, \mu^2). \quad (4.17)$$

⁶We remark that the *hat* denotes a cross section differential in M^2 .

⁷The integrations over dz , dx_a and dx_b in Eq. (4.15) then turn into Mellin transformations.

We remark that the Mellin transform is only indicated by the change of the arguments to the Mellin moments N . In Sec. 3.2 we have seen that the partonic cross section factorizes in a long and in a short distance part. This result can be generalized to the partonic cross section $\hat{\sigma}_{ab}$ or in other words we can reinterpret Eq. (4.15) for the partonic cross section in Mellin space, leading to

$$M^2 \frac{d\sigma_{ab}}{dM^2}(N) = \sum_{cd} \phi_{ca}(N, \mu^2) \phi_{db}(N, \mu^2) \times \hat{\sigma}_{cd}(N, M^2, \mu^2), \quad (4.18)$$

where ϕ_{ij} are the already mentioned parton-in-parton functions (see Sec. 3.2), but now in Mellin space, and the cross section $\hat{\sigma}_{cd}$ is IR⁸ finite. The result in Eq. (4.18) is called refactorization. By demanding a renormalization and factorization scale independent hadronic cross section, we can derive the following DGLAP evolution equations for the parton-in-parton functions

$$\frac{d\phi_{ij}(N, \mu^2)}{d \ln \mu^2} = \sum_k \mathcal{P}_{ik}(N, \alpha_s(\mu^2)) \phi_{kj}(N, \mu^2), \quad (4.19)$$

where \mathcal{P}_{ik} are the splitting kernels in Mellin space, similar to Eq. (3.19). The corresponding AP splitting functions at LO in α_s are given by

$$P_{qq}^{(1)}(N) = C_F \left[\frac{3}{2} + \frac{1}{N(N+1)} - 2 \sum_{k=1}^N \frac{1}{k} \right], \quad (4.20)$$

$$P_{qg}^{(1)}(N) = \frac{1}{2} \left[\frac{2 + N + N^2}{N(N+1)(N+2)} \right], \quad (4.21)$$

$$P_{gq}^{(1)}(N) = C_F \left[\frac{2 + N + N^2}{N(N^2 - 1)} \right], \quad (4.22)$$

$$P_{gg}^{(1)}(N) = \beta_0 + 2C_A \left[\frac{1}{N(N-1)} + \frac{1}{(N+1)(N+2)} - \sum_{k=1}^N \frac{1}{k} \right], \quad (4.23)$$

where $C_F = 4/3$, $C_A = 3$ and β_0 is the first coefficient of the QCD β -function (see Eq. (3.2)). It is common to define the QCD evolution operator \mathcal{E} [73] by means of

$$\frac{d\mathcal{E}_{ij}(N, \mu^2, \mu_0^2)}{d \ln \mu^2} = \sum_k \mathcal{P}_{ik}(N, \alpha_s(\mu^2)) \mathcal{E}_{kj}(N, \mu^2, \mu_0^2), \quad (4.24)$$

⁸Note that IR refers to soft and collinear divergences.

in order to rewrite Eq. (4.19) as

$$\phi_{ij}(N, \mu^2) = \sum_k \mathcal{E}_{ik}(N, \mu^2, \mu_0^2) \phi_{kj}(N, \mu_0^2). \quad (4.25)$$

The evolution operator can be quite complicated depending on the order of the AP splitting functions. At LO the operator can be written in a closed exponential form [38].

The partonic cross section in Eq. (4.15) contains large logarithms for $z \rightarrow 1$. Their Mellin transformation leads to

$$\left[\frac{\ln^m(1-z)}{(1-z)} \right]_+ \rightarrow \ln^{m+1} N + \dots \quad (4.26)$$

Near threshold ($N \rightarrow \infty$) only the LO terms of the AP splitting functions are important. Expanding Eqs. (4.20) to (4.23) for large N yields

$$P_{qq}^{(1)}(N) = C_F \left[\frac{3}{2} - 2 \ln \bar{N} \right] + \mathcal{O}\left(\frac{1}{N}\right), \quad (4.27)$$

$$P_{gg}^{(1)}(N) \sim \frac{1}{2N}, \quad (4.28)$$

$$P_{gq}^{(1)}(N) \sim \frac{C_F}{N}, \quad (4.29)$$

$$P_{gg}^{(1)}(N) = \beta_0 - 2C_A \ln \bar{N} + \mathcal{O}\left(\frac{1}{N}\right), \quad (4.30)$$

where $\bar{N} := N \exp(\gamma_E)$ with γ_E being the Euler constant. The off-diagonal AP splitting functions are suppressed for large N which leads to a simplified evolution equation. Eq. (4.18) can now be rewritten by only keeping the dominant terms, leading to

$$\begin{aligned} M^2 \frac{d\sigma_{ab}}{dM^2}(N) &= \phi_{aa}(N, \mu^2) \phi_{bb}(N, \mu^2) \\ &\times \hat{\sigma}_{ab}(N, M^2, \mu^2) + \mathcal{O}\left(\frac{1}{N}\right), \end{aligned} \quad (4.31)$$

where we have neglected the parton mixing contributions. Thus, for DY-like processes as well as for the associated gaugino-gluino production only quark-antiquark initial states are relevant. The partonic cross section $\hat{\sigma}_{ab}$ is completely finite, but contains large logarithmic terms near threshold. The factorized result in Eq. (4.31) will be relevant later and should be kept in mind.

Next, we turn to another refactorization proposed by Sterman et. al. [74]. It allows us to separate the cross section in a hard IR safe part, denoted by H , and a soft part which includes the potentially large logarithms, denoted by S . Instead of using the light-cone parton-in-parton functions, we can refactorize the partonic cross section by making use of the so called jet functions. They are defined with respect to a certain energy fraction instead of a longitudinal momentum fraction and are more convenient for the treatment of the emission of collinear

particles near threshold. For a definition of such a jet function we advise the reader to have a look at Ref. [74, Eq. 2.1]. By using this refactorization the partonic cross section in Eq. (4.17) can be written as

$$M^2 \frac{d\sigma_{ab}}{dM^2}(N) = \psi_{aa} \left(\frac{p_a \cdot \zeta_a}{\mu}, \frac{M^2}{\mu N} \right) \psi_{bb} \left(\frac{p_b \cdot \zeta_b}{\mu}, \frac{M^2}{\mu N} \right) \\ \times H_{ab} \left(M^2, \frac{M^2}{\mu^2}, \zeta_a, \zeta_b \right) S_{ab} \left(\frac{M}{\mu N}, v_a, \zeta_a, v_b, \zeta_b \right) + \mathcal{O} \left(\frac{1}{N} \right). \quad (4.32)$$

Here, ψ_{aa} and ψ_{bb} are jet functions, ζ_a and ζ_b gauge vectors and v_a and v_b are dimensionless vectors, pointing to the direction of the momenta p_a and p_b of the incoming partons (cf. Eq. (4.9)). All threshold enhanced terms are now comprised in the soft function S , whereas the hard function H can be safely computed as an expansion in α_s .

The jet functions obey the evolution equations

$$\frac{\partial \psi_{ii}(N, \mu^2)}{\partial \ln \mu^2} = \gamma_{\psi_i}(\alpha_s(\mu^2)) \psi_{ii}(N, \mu^2), \quad (4.33)$$

where $\gamma_{\psi_i}(\alpha_s)$ is the anomalous dimension of the jet function, which can be computed perturbatively for a field i with renormalization constant Z_i as

$$\gamma_{\psi_i}(\alpha_s) = \frac{1}{Z_i} \frac{\partial Z_i}{\partial \ln \mu^2} = \sum_n \left(\frac{\alpha_s}{2\pi} \right)^n \gamma_{\psi_i}^{(n)} \quad (4.34)$$

and corresponds to the N -independent (virtual) parts of the AP splitting functions in the axial gauge [25]. The soft function S governs the soft wide-angle gluon emission.

So far, we have obtained two different factorized forms of the partonic cross section $\hat{\sigma}_{ab}$. The first one in Eq. (4.31) contains the standard parton-in-parton functions and a hard function which still exhibits potentially large logarithms. The second one in Eq. (4.32) uses the jet functions and the potentially large logarithmic terms are factorized into the soft function S .

4.3.2 Exponentiation

Next, we want to get an exponential form of Eq. (4.32). Therefore, we follow the steps presented in Refs. [69, 70, 72] and the original Ref. [71]. As this procedure is nontrivial, we strongly encourage the interested reader to study these references.

For the first step we make use of the so called *renormalization group approach to resummation*. We can define the following set of RGEs

$$\frac{\mu}{H} \frac{dH}{d\mu} = -\gamma_H(\alpha_s), \quad (4.35)$$

$$\frac{\mu}{S} \frac{dS}{d\mu} = -\gamma_S(\alpha_s), \quad (4.36)$$

$$\frac{\mu}{\psi_i} \frac{d\psi_i}{d\mu} = -\gamma_{\psi_i}(\alpha_s), \quad (i = a, b), \quad (4.37)$$

which describes the renormalization scale dependence of the hard, soft and jet functions. Here, γ_{ψ_i} and γ_H denote the anomalous dimensions of the jet and the hard function, respectively, and γ_S is the soft anomalous dimension. As Eq. (4.32) is independent of the renormalization scale μ , the relation

$$\gamma_H + \gamma_S + \sum_i \gamma_{\psi_i} = 0 \quad (4.38)$$

must hold [71]. We can solve Eqs. (4.36) and (4.37) [70], similarly to Eq. (4.5), by *separation of variables* leading to

$$S\left(\frac{Q}{\mu N}, v_a, \zeta_a, v_b, \zeta_b, \alpha_s(\mu^2)\right) = S\left(1, v_a, \zeta_a, v_b, \zeta_b, \alpha_s(M^2/N^2)\right) \times \exp\left[-\int_{M/N}^{\mu} \frac{d\lambda}{\lambda} \gamma_S(\alpha_s(\lambda^2))\right], \quad (4.39)$$

$$\psi_i\left(\frac{p_i \cdot \zeta_i}{\mu}, \frac{M}{\mu N}, \alpha_s(\mu^2)\right) = \psi_i\left(p_i \cdot \zeta_i \frac{N}{M}, 1, \alpha_s(M^2/N^2)\right) \times \exp\left[-\int_{M/N}^{\mu} \frac{d\lambda}{\lambda} \gamma_{\psi_i}(\alpha_s(\lambda^2))\right]. \quad (4.40)$$

The structure of the integrals in the exponents of Eqs. (4.39) and (4.40) indicates that we have only resummed single logarithmic terms. For the soft function S this is sufficient, since it governs the soft wide-angle emission and thus contains only single logarithmic terms of N . Soft-collinear emissions are contained in the jet function, leading to double logarithmic contributions. Still, the soft-collinear terms have not been resummed yet and an additional condition and further steps are required [69].

For this reason, we make use of the gauge independence of Eq. (4.32). As the specific choice of the gauge fixing vectors ζ_i should be irrelevant for the physical result, we know

$$p_i \cdot \zeta_i \frac{\partial \sigma_{ab}}{\partial (p_i \cdot \zeta_i)} = 0 \quad (4.41)$$

must be fulfilled. In the following we focus only on one of the two gauge fixing vectors, namely ζ_a . All steps for ζ_b are similar.

Eq. (4.41) can be converted into a relation between the hard, soft and jet functions. Inserting Eq. (4.32) in Eq. (4.41) and then dividing by Eq. (4.32) leads to

$$p_a \cdot \zeta_a \frac{\partial(\ln \psi_a)}{\partial (p_a \cdot \zeta_a)} = -p_a \cdot \zeta_a \frac{\partial(\ln H)}{\partial (p_a \cdot \zeta_a)} - p_a \cdot \zeta_a \frac{\partial(\ln S)}{\partial (p_a \cdot \zeta_a)}. \quad (4.42)$$

It is common to define two functions G and K by means of

$$G\left(\frac{p_a \cdot \zeta_a}{\mu}, \alpha_s(\mu^2)\right) := -p_a \cdot \zeta_a \frac{\partial(\ln H)}{\partial(p_a \cdot \zeta_a)}, \quad (4.43)$$

$$K\left(\frac{M}{\mu N}, \alpha_s(\mu^2)\right) := -p_a \cdot \zeta_a \frac{\partial(\ln S)}{\partial(p_a \cdot \zeta_a)}. \quad (4.44)$$

They describe the change of the hard and soft function with respect to a change of the gauge vector [71]. Next, we rewrite Eq. (4.42) by using these two newly defined functions, yielding

$$p_a \cdot \zeta_a \frac{\partial}{\partial(p_a \cdot \zeta_a)} \ln \psi_a\left(\frac{p_a \cdot \zeta_a}{\mu}, \frac{M}{\mu N}, \alpha_s(\mu^2)\right) = G\left(\frac{p_a \cdot \zeta_a}{\mu}, \alpha_s(\mu^2)\right) + K\left(\frac{M}{\mu N}, \alpha_s(\mu^2)\right). \quad (4.45)$$

Taking the derivative of Eq. (4.45) with respect to the renormalization scale, interchanging the two derivatives and making use of the anomalous dimension of the jet function yields

$$\begin{aligned} p_a \cdot \zeta_a \frac{d}{d p_a \cdot \zeta_a} \gamma_{\psi_a}(\alpha_s(\mu^2)) &= \mu \frac{d}{d \mu} \left[G\left(\frac{p_a \cdot \zeta_a}{\mu}, \alpha_s(\mu^2)\right) + K\left(\frac{M}{\mu N}, \alpha_s(\mu^2)\right) \right] \\ &= 0. \end{aligned} \quad (4.46)$$

This equation holds, since the jet function ψ_a is renormalized by a multiplicative factor and the anomalous dimension is independent of $p_a \cdot \zeta_a$ [70, 71]. Hence, the combination of $G + K$ is renormalization scale invariant [71]. We define the so called Sudakov anomalous dimension γ_K as

$$\mu \frac{d}{d \mu} K\left(\frac{M}{\mu N}, \alpha_s(\mu^2)\right) =: -\gamma_K, \quad (4.47)$$

$$\mu \frac{d}{d \mu} G\left(\frac{p_a \cdot \zeta_a}{\mu}, \alpha_s(\mu^2)\right) =: \gamma_K. \quad (4.48)$$

These two differential equations can be solved, again by using *separation of variables*, leading to the following solution for their sum [71, 69]:

$$\begin{aligned} G\left(\frac{p_a \cdot \zeta_a}{\mu}, \alpha_s(\mu^2)\right) + K\left(\frac{M}{\mu N}, \alpha_s(\mu^2)\right) &= G\left(1, \alpha_s\left((\zeta_a \cdot p_a)^2\right)\right) + K\left(1, \alpha_s\left(\frac{M^2}{N^2}\right)\right) \\ &\quad - \int_{M/N}^{p_a \cdot \zeta_a} \frac{d\xi}{\xi} \gamma_K\left(\alpha_s(\xi^2)\right). \end{aligned} \quad (4.49)$$

Eqs. (4.47) and (4.48) allow us to relate the two scales $p_a \cdot \zeta_a$ and M/N by

$$G\left(\frac{p_a \cdot \zeta_a}{\mu}, \alpha_s(\mu^2)\right) + K\left(\frac{M}{\mu N}, \alpha_s(\mu^2)\right) = A'\left(\alpha_s\left(p_a \cdot \zeta_a\right)^2\right) - \int_{M/N}^{p_a \cdot \zeta_a} \frac{d\xi}{\xi} A\left(\alpha_s(\xi^2)\right), \quad (4.50)$$

with the definitions

$$A'(\alpha_s(\mu^2)) := G(1, \alpha_s(\mu^2)) + K(1, \alpha_s(\mu^2)), \quad (4.51)$$

$$A(\alpha_s(\mu^2)) := \gamma_K(\alpha_s(\mu^2)) + 2\beta(\alpha_s) \frac{\partial K(1, \alpha_s)}{\partial \alpha_s}, \quad (4.52)$$

where we have used the QCD β -function [71, 70]. Now we can solve Eq. (4.45) by *separation of variables* and an integration over $p_a \cdot \zeta_a$, yielding

$$\begin{aligned} \psi_a\left(\frac{p_a \cdot \zeta_a}{\mu}, \frac{M}{\mu N}, \alpha_s(\mu^2)\right) &= \psi_a\left(1, \frac{M}{\mu N}, \alpha_s(\mu^2)\right) \\ &\times \exp\left[-\int_{\mu}^{p_a \cdot \zeta_a} \frac{d\lambda}{\lambda} \left(\int_{M/N}^{\lambda} \frac{d\xi}{\xi} A(\alpha_s(\xi^2)) - A'(\alpha_s(\lambda^2))\right)\right]. \end{aligned} \quad (4.53)$$

We can insert the scale dependence of the jet function by making use of the solution in Eq. (4.40):

$$\begin{aligned} \psi_a\left(\frac{p_a \cdot \zeta_a}{\mu}, \frac{M}{\mu N}, \alpha_s(\mu^2)\right) &= \psi_a\left(1, 1, \alpha_s(M^2/N^2)\right) \exp\left[-\int_{M/N}^{\mu} \frac{d\lambda}{\lambda} \gamma_{\psi_i}(\alpha_s(\lambda^2))\right] \\ &\times \exp\left[-\int_{M/N}^{p_a \cdot \zeta_a} \frac{d\lambda}{\lambda} \left(\int_{M/N}^{\lambda} \frac{d\xi}{\xi} A(\alpha_s(\xi^2)) - A'(\alpha_s(\lambda^2))\right)\right]. \end{aligned} \quad (4.54)$$

By inserting the expression for ψ_a given in Eq. (4.54), a similar one for ψ_b and the result in Eq. (4.39) for S in Eq. (4.32) we get our final resummed result [69]:

$$\begin{aligned} M^2 \frac{d\sigma_{ab}(N)}{dM^2} &= H_{ab}(1, 1, \alpha_s(M^2)) S_{ab}(1, \alpha_s(M^2/N^2)) \psi_a(1, 1, \alpha_s(M^2/N^2)) \psi_b(1, 1, \alpha_s(M^2/N^2)) \\ &\times \exp\left[-2 \int_{M/N}^M \frac{d\lambda}{\lambda} \left(\int_{M/N}^{\lambda} \frac{d\xi}{\xi} A(\alpha_s(\xi^2)) - B(\alpha_s(\lambda^2))\right)\right], \end{aligned} \quad (4.55)$$

with

$$B(\alpha_s(\mu^2)) = A'(\alpha_s(\mu^2)) - \frac{1}{2} \left[\gamma_{\psi_a}(\alpha_s(\mu^2)) + \gamma_{\psi_b}(\alpha_s(\mu^2)) + \gamma_S(\alpha_s(\mu^2)) \right] \quad (4.56)$$

and where $p_i \cdot \zeta_i$ and μ have been set to M . After the evaluation of the two integrals in the exponent of Eq. (4.55) it comprises double and single logarithmic terms of the Mellin moment N . By comparing an expansion of Eq. (4.55) in α_s to a fixed order calculation, we can determine the functions A and B up to a certain accuracy, depending on the order of the fixed order result [69].

The here obtained result is called basic Sudakov resummation [71, 75, 76] and contains all the potentially large logarithms up to all orders in perturbation theory. However, so far we have neglected that the jet functions contain collinear divergences due to the initial state emission. In order to cancel these divergences we can combine the two refactorized expressions in Eqs. (4.31) and (4.32). This is addressed in the next section.

4.4 Final results and incorporation of final state emission

By relating Eqs. (4.31) and (4.32) and setting $\mu = M$ we can solve for $\hat{\sigma}_{ab}$, leading to

$$\hat{\sigma}_{ab}(N, M^2) = H_{ab}(M^2) \frac{\psi_{aa}(N, M^2) \psi_{bb}(N, M^2)}{\phi_{aa}(N, M^2) \phi_{bb}(N, M^2)} S_{ab}(N, \alpha_s(M^2)), \quad (4.57)$$

where we have neglected terms of $\mathcal{O}(1/N)$ [71]. The jet and the parton-in-parton functions exhibit collinear divergences, which cancel exactly in the formula above, as the refactorized partonic cross section $\hat{\sigma}_{ab}$ is free from collinear divergences.

Next, we can insert the specific expression for the soft function of the previous section. It is common to write it as

$$S_{ab}(N, \alpha_s(M^2)) = S_{ab}(1, \alpha_s(M^2/N^2)) \exp \left[\int_0^1 dz \frac{z^{N-1} - 1}{1 - z} \Gamma_{ab}(\alpha_s((1 - z)^2 M^2)) \right], \quad (4.58)$$

where we have used the more common label Γ_{ab} for the soft anomalous dimension and where we have made the Mellin transform more explicit again.

Additionally, we need the ratio of the jet functions to the parton-in-parton functions. It can be extracted by a computation of a specific result for the DY process and reused for other processes, since the result is universal. For the DY process we can set $\psi_{aa} = \psi_{bb}$ and $\phi_{aa} = \phi_{bb}$ in Eq. (4.57). A specific result for the resummed form of the DY hard scattering function $\hat{\sigma}_{a\bar{a}}$ is given in Ref. [71]. By solving Eq. (4.57) for the ratio we can write [77]

$$\frac{\psi_{aa}(N, M^2)}{\phi_{aa}(N, M^2)} = R_a(\alpha_s(M^2)) \Delta_a(N, M^2, \alpha_s(M^2)) \left[S_{a\bar{a}}(N, \alpha_s(M^2)) \right]^{-\frac{1}{2}}, \quad (4.59)$$

where R_a denotes a hard function which is independent of N and

$$\begin{aligned} \ln \Delta_a(N, M^2, \alpha_s(M^2)) &= \int_0^1 dz \frac{z^{N-1} - 1}{1 - z} \int_1^{(1-z)^2} \frac{d\lambda}{\lambda} A_a(\alpha_s(\lambda M^2)) \\ &\quad + \int_0^1 dz \frac{z^{N-1} - 1}{1 - z} D_a(\alpha_s((1 - z)^2 M^2)), \end{aligned} \quad (4.60)$$

where D_i corresponds to the coefficient B in Eq. (4.55) [71, 69]. The first line in Eq. (4.60) contains the soft-collinear gluon emission, whereas the second line comprises the soft wide angle emission. The coefficients A_a and D_a can be computed perturbatively as mentioned above, leading for the so called one-loop coefficients to $A_q^{(1)} = A_{\bar{q}}^{(1)} = C_F$ and $D_a^{(1)} = 0$ [71].

By combining all the results obtained so far we get

$$\begin{aligned} \hat{\sigma}_{ab}(N, M^2, \alpha_s(M^2)) &= R_a(\alpha_s(M^2)) R_b(\alpha_s(M^2)) H_{ab}(\alpha_s(M^2)) \\ &\times \Delta_a(N, M^2, \alpha_s(M^2)) \Delta_b(N, M^2, \alpha_s(M^2)) . \end{aligned} \quad (4.61)$$

Our results are only valid for DY-like processes and thus not applicable for the associated gaugino-gluino production yet. We have to incorporate the final state emission from the massive gluino. Due to its mass, the collinear emission is screened and only soft wide-angle emissions are possible. Thus, we only have to modify the soft function S_{ab} , whereas the solutions for the jet functions ψ_a and ψ_b remain.

Before we start with this modification let us make some general remarks. If we had more massive colored final state particles the soft and hard functions would turn out to be matrices in color space, requiring a diagonalization procedure in order to achieve a resummed form [69, 70, 77]. For this reason, these functions are usually computed in an irreducible s-channel color basis with tensors c_J , which one obtains in general after decomposing the reducible initial state or final state multi-particle product representations and which has the advantage of rendering the anomalous dimension matrices diagonal at threshold [78, 79]. Fortunately, we have only one colored final state particle, the gluino with adjoint colour index i, i' . Hence, there is only one color basis tensor $c_J = \text{Tr}(T^i T^{i'}) = T_F \delta_{ii'}$ with $T_F = 1/2$, similarly to the case of prompt photon production with an associated gluon jet [80], and we can drop the associated indices I, J . For more details on resummation for more than one colored final state particle the interested reader may have a look at Refs. [69, 70, 77, 72].

Next, we focus on the modification of the soft function in order to incorporate the emission from the gluino. The soft wide-angle emission from the initial state is contained in Eq. (4.58). Since we want to maintain the previous result we define the so called modified soft function

$$\bar{S}_{ab \rightarrow ij} := \frac{S_{ab \rightarrow ij}}{\sqrt{S_{a\bar{a}}} \sqrt{S_{b\bar{b}}}} , \quad (4.62)$$

where the division prevents us from double counting the initial state soft wide-angle emission. This also leads to a modified soft anomalous dimension

$$\bar{\Gamma}_{ab \rightarrow ij} = \Gamma_{ab \rightarrow ij} - \Gamma_{ab} , \quad (4.63)$$

with Γ_{ab} being the soft anomalous dimension of the DY process (see Eq. (4.79)). The modified soft function can now be written as

$$\begin{aligned} \bar{S}_{ab \rightarrow ij}(N, \alpha_s(M^2)) &= S_{ab \rightarrow ij}(1, \alpha_s(M^2/N^2)) \\ &\times \exp \left[\int_0^1 dz \frac{z^{N-1} - 1}{1 - z} D_{ab \rightarrow ij}(\alpha_s((1-z)^2 M^2)) \right] \\ &:= S_{ab \rightarrow ij}(1, \alpha_s(M^2/N^2)) \Delta_{ab \rightarrow ij}^{(s)}(N, M^2, \alpha_s(M^2)) , \end{aligned} \quad (4.64)$$

where $D_{ab \rightarrow ij} = 2\pi/\alpha_s \operatorname{Re}(\bar{\Gamma}_{ab \rightarrow ij})$ is related to the soft anomalous dimension⁹. The modified result of Eq. (4.61) is now given by

$$\begin{aligned} \hat{\sigma}_{ab \rightarrow ij}(N, M^2, \alpha_s(M^2)) &= R_a(\alpha_s(M^2)) R_b(\alpha_s(M^2)) H_{ab \rightarrow ij}(\alpha_s(M^2)) S_{ab \rightarrow ij}(1, \alpha_s(M^2/N^2)) \\ &\quad \times \Delta_a(N, M^2, \alpha_s(M^2)) \Delta_b(N, M^2, \alpha_s(M^2)) \Delta_{ab \rightarrow ij}^{(s)}(N, M^2, \alpha_s(M^2)) \end{aligned} \quad (4.65)$$

and can be applied to processes which include one massive colored final state particle.

The former results have been computed for $\mu_F = \mu_R = M$. Correct scale dependence can be reinserted by exploiting the evolution equations for the jet and parton-in-parton functions in Eqs. (4.19) and (4.37), respectively. Therefore, we have replace μ by μ_R in Eq. (4.37) and by μ_F in Eq. (4.19). The hard function R and H will in general depend on μ_F and μ_R ¹⁰.

Finally, the integrals in Eqs. (4.60) and (4.64) can be evaluated. We can then write our final threshold resummation result as

$$\hat{\sigma}_{ab \rightarrow ij}(N, M^2, \mu_F^2, \mu_R^2) = \mathcal{H}_{ab \rightarrow ij}(M^2, M^2, \mu_F^2, \mu_R^2) \exp(\mathcal{G}_{ab \rightarrow ij}(N, M^2, \mu_F^2, \mu_R^2)). \quad (4.66)$$

The exponent $\mathcal{G}_{ab \rightarrow ij}$ is defined in such a way that it only contains the logarithmic contributions of the integrals. Therefore, the hard function $\mathcal{H}_{ab \rightarrow ij}$ is a redefinition of the former hard functions in Eq. (4.65) and has also absorbed the finite terms of the integrals. It is process dependent and will be discussed in Sec. 4.6 in more detail. $\mathcal{G}_{ab \rightarrow ij}$ is universal and takes the form

$$\mathcal{G}_{ab \rightarrow ij} = LG_{ab}^{(1)}(\lambda) + G_{ab \rightarrow ij}^{(2)}(\lambda, M^2, \mu_F^2, \mu_R^2) + \alpha_s G_{ab \rightarrow ij}^{(3)}(\lambda, M^2, \mu_F^2, \mu_R^2) + \dots, \quad (4.67)$$

where $\lambda = \alpha_s/(2\pi)\beta_0 L$ and $L = \ln \bar{N}$, with $\bar{N} := N \exp \gamma_E$. The first order term comprises the leading logarithms (LL) and depends only on $A_a^{(1)}$, the second one contains the next-to-leading logarithms (NLL) and includes the three functions $A_a^{(1)}$, $A_a^{(2)}$ and $D_{ab}^{(1)}$. Higher order logarithmic terms are governed by $G_{ab \rightarrow ij}^{(i)}$ for $i \geq 3$.

The functions up to NLL accuracy read [81, 82, 77]

$$G_{ab}^{(1)}(\lambda) = g_a^{(1)}(\lambda) + g_b^{(1)}(\lambda), \quad (4.68)$$

$$G_{ab \rightarrow ij}^{(2)}(\lambda) = g_a^{(2)}(\lambda, M^2, \mu_R^2, \mu_F^2) + g_b^{(2)}(\lambda, M^2, \mu_R^2, \mu_F^2) + h_{ab \rightarrow ij, I}^{(2)}(\lambda), \quad (4.69)$$

with

$$g_a^{(1)}(\lambda) = \frac{A_a^{(1)}}{2\beta_0\lambda} [2\lambda + (1 - 2\lambda) \ln(1 - 2\lambda)], \quad (4.70)$$

⁹For more than one colored final state particle $D_{ab \rightarrow ij}$ is related to the eigenvalues of the modified soft anomalous dimension [69].

¹⁰For further details you may have a look at Refs. [69, 70].

$$\begin{aligned}
g_a^{(2)}(\lambda) = & \frac{A_a^{(1)}\beta_1}{2\beta_0^3} \left[2\lambda + \ln(1-2\lambda) + \frac{1}{2} \ln^2(1-2\lambda) \right] , \\
& - \frac{A_a^{(2)}}{2\beta_0^2} [2\lambda + \ln(1-2\lambda)] \\
& + \frac{A_a^{(1)}}{2\beta_0} \left[\ln(1-2\lambda) \ln\left(\frac{M^2}{\mu_R^2}\right) + 2\lambda \ln\left(\frac{\mu_F^2}{\mu_R^2}\right) \right] , \tag{4.71}
\end{aligned}$$

$$h_{ab \rightarrow ij, I}^{(2)}(\lambda) = \frac{\ln(1-2\lambda)}{\beta_0} D_{ab \rightarrow ij, I}^{(1)} . \tag{4.72}$$

The coefficients in the equations above are

$$A_a^{(1)} = 2C_a , \tag{4.73}$$

$$A_a^{(2)} = 2C_a \left[\left(\frac{67}{18} - \frac{\pi^2}{6} \right) C_A - \frac{5}{9} n_f \right] , \tag{4.74}$$

$$D_{ab \rightarrow ij, I}^{(1)} = \frac{2\pi}{\alpha_s} \text{Re}(\bar{\Gamma}_{ab \rightarrow ij, II}) , \tag{4.75}$$

where $C_a = C_{F,A}$ for quarks and gluons and $\bar{\Gamma}_{ab \rightarrow ij, II}$ is the already mentioned modified diagonal soft anomalous dimension of the color representation I . The general formulas for NNLL resummation can be found in Ref. [81].

In this section we stated the full result for $\hat{\sigma}_{ab}$ up to NLL accuracy. It can be translated into a function for the hadronic cross section in Eq. (4.15), because the divergent parton-in-parton distribution functions appearing in Eq. (4.18) will be *absorbed* into the PDFs (cf. Eq. (3.14)).

4.5 The soft anomalous dimension

In the resummation formulas of the previous section we have encountered the soft anomalous dimension and its modified version, which is needed for the soft wide-angle emission. In this section we address its definition and show how it can be computed.

So far, we have assumed that all UV divergences appearing in the soft and hard function have been already removed by renormalization. Going one step back we can write the bare soft function as

$$S_{ab \rightarrow ij, IJ}^{\text{bare}} = \left(Z_{ab \rightarrow ij}^\dagger \right)_{JK} S_{ab \rightarrow ij, KL} \left(Z_{ab \rightarrow ij}^\dagger \right)_{LI} . \tag{4.76}$$

Here, a and b are labels for the initial and i and j for the final state particles, J , K , L and I denote a certain color representation and $Z_{ab \rightarrow ij}$ denotes a multiplicative renormalization constant for the soft function and is also referred to as the renormalization constant for

the Wilson-line (or eikonal line) operator. Since the bare function is independent of any renormalization scale we can derive a RGE given by

$$\mu \frac{d}{d\mu} S_{ab \rightarrow ij, IJ} = -\Gamma_{ab \rightarrow ij, IK}^\dagger S_{ab \rightarrow ij, KJ} - S_{ab \rightarrow ij, IK} \Gamma_{ab \rightarrow ij, KJ}, \quad (4.77)$$

where we have introduced the soft anomalous dimension $\Gamma_{ab \rightarrow ij, IJ}$ which can be computed from the renormalization constants by taking the residue of their ultraviolet poles in $\epsilon = 4 - D$ in D dimensions as

$$\Gamma_{ab \rightarrow ij, IJ} = -\alpha_s \frac{\partial}{\partial \alpha_s} \text{Res}_{\epsilon \rightarrow 0} Z_{ab \rightarrow ij, IJ}(\alpha_s, \epsilon). \quad (4.78)$$

In order to get the one-loop soft anomalous dimension for the DY process we have to compute the virtual correction where the two initial state quarks exchange a soft gluon via an eikonal line, leading to the so called eikonal integrals [78]. Solving these integrals in the axial gauge leads to

$$\Gamma_{ab} = \frac{\alpha_s}{2\pi} \sum_{k=\{a,b\}} C_k \left(1 - \ln \left(2 \frac{(v_k \cdot n)^2}{|n|^2} \right) - i\pi \right), \quad (4.79)$$

where we sum over the incoming particles k . Here, n is an axial gauge vector fulfilling $|n|^2 = -n^2 - i\epsilon$ [78, 79] and C_k is a color factor which is C_F for incoming quarks and C_A for incoming gluons. The dimensionless vector v_k is defined by the momentum of the incoming particle k divided by $\sqrt{2/s}$. To get NLL accuracy for the associated production means we have to compute

$$\bar{\Gamma}_{ab \rightarrow ij, IJ} = \Gamma_{ab \rightarrow ij, IJ} - \frac{\alpha_s}{2\pi} \sum_{k=\{a,b\}} C_k \left(1 - \ln \left(2 \frac{(v_k \cdot n)^2}{|n|^2} \right) - i\pi \right) \delta_{IJ} \quad (4.80)$$

at the one-loop level. We have subtracted the DY contribution to prevent double counting of the initial state soft wide-angle emission. For an example calculation of the one-loop modified soft anomalous dimension we refer to Sec. 6.3.1.

4.6 The hard matching coefficient

The final resummation formula in Eq. (4.66) contains the process dependent hard function $\mathcal{H}_{ab \rightarrow ij}$ which can be computed perturbatively in α_s . It is common to write it as

$$\begin{aligned} \mathcal{H}_{ab \rightarrow ij}(M^2, \mu^2) &= \sum_{n=0} \left(\frac{\alpha_s}{2\pi} \right)^n \mathcal{H}_{ab \rightarrow ij}^{(n)}(M^2, \mu^2) \\ &:= \tilde{\sigma}_{ab \rightarrow ij}^{(0)} \mathcal{C}_{ab \rightarrow ij}(M^2, \mu^2), \end{aligned} \quad (4.81)$$

where $\tilde{\sigma}_{ab \rightarrow ij}^{(0)}$ denotes the Mellin transform with respect to z of the LO differential cross section $d\sigma^{(0)}/dM^2$ and

$$\mathcal{C}_{ab \rightarrow ij}(M^2, \mu^2) = \sum_{n=0} \left(\frac{\alpha_s}{2\pi} \right)^n \mathcal{C}_{ab \rightarrow ij}^{(n)}(M^2, \mu^2) \quad (4.82)$$

is the so called hard matching coefficient function. Its coefficients are defined as

$$\mathcal{C}_{ab \rightarrow ij}^{(n)}(M^2, \mu^2) = \left(\frac{2\pi}{\alpha_s} \right)^n \left[\frac{\tilde{\sigma}_{ab \rightarrow ij}^{(n)}}{\tilde{\sigma}_{ab \rightarrow ij}^{(0)}} \right]_{N\text{-ind.}}. \quad (4.83)$$

Here, $N\text{-ind.}$ means that we only take the finite N -independent terms of the ratio of the n -th order cross section to the LO one. Hence, the first order hard matching coefficient is $\mathcal{C}_{ab \rightarrow ij}^{(0)} = 1$ and the LO hard function is $\mathcal{H}_{ab \rightarrow ij}^{(0)}(M^2, \mu^2) = \tilde{\sigma}_{ab \rightarrow ij}^{(0)}$. Before we specify the Mellin transform of the first order contribution it is worth noticing that

$$\hat{\sigma}_{ab \rightarrow ij}^{(0)} := \frac{d\sigma_{ab \rightarrow ij}^{(0)}}{dM^2} = \sigma_{ab \rightarrow ij}^{(0)}(s) \delta(s - M^2). \quad (4.84)$$

Then the Mellin transform leads to

$$\begin{aligned} \tilde{\sigma}_{ab \rightarrow ij}^{(0)} &= \int_0^1 dz z^{N-1} \sigma_{ab \rightarrow ij}^{(0)}(s) \delta(s - M^2) \\ &= \frac{\sigma_{ab \rightarrow ij}^{(0)}(M^2)}{M^2}, \end{aligned} \quad (4.85)$$

where we have used $z = M^2/s$. For the NLO hard matching coefficient we need the Mellin transform of the full NLO contribution. According to Eq. (3.22), it can be written as

$$\begin{aligned} \frac{d\sigma^{(1)}}{dM^2} &= \frac{d}{dM^2} \int_{(3)} \left[d\sigma^R - d\sigma^A \right] \\ &+ \frac{d}{dM^2} \int_0^1 dz \int_{(2)} d\sigma^{(0)}(zs) \otimes (\mathbf{P} + \mathbf{K})(z) \\ &+ \frac{d}{dM^2} \int_{(2)} \left[d\sigma^V + d\sigma^{(0)} \otimes \mathbf{I} \right], \end{aligned} \quad (4.86)$$

where the labels (1), (2) and (3) denote the one-particle, two-particle and three-particle phase spaces, respectively. In the relevant phase space region, i.e. $z \rightarrow 1$, the real emission cross section $d\sigma^R$ gets completely canceled by the Catani-Seymour dipole $d\sigma^A$. In the remaining phase space region the Mellin transform only leads to suppressed terms. Hence, the first line of Eq. (4.86) does not contribute to the hard matching coefficient. It turns out that the real emission near threshold is almost completely governed by $d\sigma^{(0)} \otimes \mathbf{I}$ and by the second line, the collinear remainder [79, 83, 81]. In the following we denote the second line of Eq. (4.86)

by $\hat{\sigma}^C$ and the third line by $\hat{\sigma}^{\text{virt.}}$. The Mellin transform of the virtual contribution can be obtained analog to the LO cross section, yielding

$$\tilde{\sigma}^{\text{virt.}} = \frac{\sigma^{\text{virt.}}(M^2)}{M^2}, \quad (4.87)$$

where for the sake of convenience we dropped the indices a, b, i and j labeling the initial and final states. The collinear remainder can be written in the following way [72]

$$\begin{aligned} \hat{\sigma}^C &= \frac{d}{dM^2} \int_0^1 dz \int_{(2)} d\sigma^{(0)}(zs) \otimes (\mathbf{P} + \mathbf{K})(z) \\ &= \frac{d}{dM^2} \int_{M_{\min}^2}^s dM^2 \frac{z}{M^2} \left(\sigma^{(0)}(M^2) \otimes (\mathbf{P} + \mathbf{K})(z) \right) \\ &= \frac{z}{M^2} \sigma^{(0)}(M^2) \otimes (\mathbf{P} + \mathbf{K})(z). \end{aligned} \quad (4.88)$$

Next, we can perform the Mellin transform leading to

$$\begin{aligned} \tilde{\sigma}^C &= \frac{\sigma^{(0)}(M^2)}{M^2} \otimes \int_0^1 dz z^N (\mathbf{P} + \mathbf{K})(z), \\ &:= \frac{\sigma^{(0)}(M^2)}{M^2} \otimes (\mathbf{P} + \mathbf{K})(N). \end{aligned} \quad (4.89)$$

Thus, we just need the Mellin moments of the insertion operators \mathbf{P} and \mathbf{K} . Finally, the NLO hard matching coefficient reads

$$\mathcal{C}_{ab \rightarrow ij}^{(1)} = \frac{2\pi}{\alpha_s} \left(\tilde{\sigma}_{ab \rightarrow ij}^{(0)} \right)^{-1} \left(\left[\tilde{\sigma}_{ab \rightarrow ij}^C \right]_{\text{N-ind.}} + \tilde{\sigma}_{ab \rightarrow ij}^{\text{virt.}} \right) \quad (4.90)$$

and the NLO contribution to the hard function is $\mathcal{H}_{ab \rightarrow ij}^{(1)} = \tilde{\sigma}_{ab \rightarrow ij}^{(0)} \mathcal{C}_{ab \rightarrow ij}^{(1)}$. By including this function the resummation of logarithmically enhanced contributions can be improved, because beyond NLO in α_s these finite terms are multiplied by threshold logarithms.

4.7 Matching and inverse Mellin transform

Threshold resummation is only a valid approximation near threshold and thus needs to be matched to the fixed order result in a consistent way in order to give a reliable prediction over the whole phase space region. This is obtained by

$$\sigma_{ab} = \sigma_{ab}^{(\text{res.})} + \sigma_{ab}^{(\text{f.o.})} - \sigma_{ab}^{(\text{exp.})}, \quad (4.91)$$

where the resummed cross section $\sigma_{ab}^{(\text{res.})}$ in Eq. (4.66) has been expanded to NLO, yielding $\sigma_{ab}^{(\text{exp.})}$, and subtracted from the fixed-order calculation $\sigma_{ab}^{(\text{f.o.})}$ in order to avoid the double counting of the logarithmically enhanced contributions. For the expansion we obtain

$$\begin{aligned} \sigma_{ab}^{(\text{exp.})} = & \mathcal{H}_{ab \rightarrow ij}^{(0)}(M^2, \mu^2) + \frac{\alpha_s}{2\pi} \mathcal{H}_{ab \rightarrow ij}^{(1)}(M^2, \mu^2) + \frac{\alpha_s}{2\pi} \mathcal{H}_{ab \rightarrow ij}^{(0)}(M^2, \mu^2) \\ & \times \left[(A_a^{(1)} + A_b^{(1)}) \ln^2 \bar{N} + \left((A_a^{(1)} + A_b^{(1)}) \ln \frac{\mu_F^2}{M^2} - 2D_{ab \rightarrow ij}^{(1)} \right) \ln \bar{N} \right], \end{aligned} \quad (4.92)$$

where $\mathcal{H}^{(0)}$ and $\mathcal{H}^{(1)}$ are the first and second order parts of the hard function. After the matching the resummed and the perturbatively expanded results in Mellin space must be multiplied by the N -moments of the PDFs according to Eq. (4.17). A technique to get the PDFs in Mellin space is shown in Appendix D. To get the final result of the hadronic cross section as a function of $\tau = M^2/S$ we have to perform an inverse Mellin transform:

$$M^2 \frac{d\sigma_{AB}}{dM^2}(\tau) = \frac{1}{2\pi i} \int_{\mathcal{C}_N} dN \tau^{-N} M^2 \frac{d\sigma_{AB}(N)}{dM^2}. \quad (4.93)$$

Special attention must be paid due to the singularities in the resummed exponents $G_{ab}^{(1,2)}$, which are located at $\lambda = 1/2$ and are related to the Landau pole of the perturbative coupling α_s . Furthermore, also the Mellin moments of the PDFs exhibit divergences (see Eq. (D.2)) which are related to the small- x (Regge) singularity $f_{a/A}(x, \mu_0^2) \propto x^\alpha (1-x)^\beta$ with $\alpha < 0$. Therefore, we choose an integration contour \mathcal{C}_N according to the *principal value* procedure proposed in Ref. [84] and the *minimal prescription*¹¹ proposed in Ref. [68]. We define two branches

$$\mathcal{C}_N : \quad N = C + ze^{\pm i\phi} \quad \text{with } z \in [0, \infty[, \quad (4.94)$$

where the constant C is chosen such that the singularities of the N -moments of the PDFs lie to the left and the Landau pole to the right of the integration contour. Formally, the angle ϕ can be chosen in the range $[\pi/2, \pi[$, but the integral converges faster if $\phi > \pi/2$.

4.8 Improved threshold resummation

For DY-like processes we use a collinear improved version of threshold resummation that allows us to resum additional subleading terms [25, 85] which have so far been neglected. Dominant $1/N$ -terms of the form $\alpha_s L^{2n-1}/N$ arise from the universal collinear radiation of the initial state partons [86] and are expected to exponentiate as well. This can be achieved by modifying the second order hard function for DY-like processes in the following way [86, 82]

$$\mathcal{H}_{ab}^{(1)} \rightarrow \mathcal{H}_{ab}^{(1)} + \mathcal{H}_{ab}^{(0)} \left(A_a^{(1)} + A_b^{(1)} \right) L/N. \quad (4.95)$$

¹¹For a pedagogical discussion see for instance Ref. [69, Ch. 4.6].

where we have included the corresponding subleading terms of the diagonal AP splitting functions (see Eqs. (4.20) and (4.23)). It has been shown that this can be further improved by including terms stemming from the off-diagonal splitting functions as well [87, 53]. This leads to a modified version of the resummation formula which explicitly contains the one-loop approximation of the QCD evolution operator \mathcal{E}_{ab} and has been defined in Eq. (4.24). It drives the parton-in-parton density functions with the energy and encompasses collinear radiation [73]. Incorporating the evolution operator leads to the following modification of our result in Eq. (4.66):

$$\begin{aligned} \hat{\sigma}_{ab}(N, M^2, \mu_F^2, \mu_R^2) &= \sum_{cd} \tilde{\mathcal{H}}_{cd}(M^2, M^2, \mu_F^2, \mu_R^2) \exp\left(\tilde{\mathcal{G}}_{cd}(N, M^2, \mu_F^2, \mu_R^2)\right) \\ &\times \mathcal{E}_{ca}^{(1)}(N, M^2/\bar{N}^2, \mu_F^2) \mathcal{E}_{db}^{(1)}(N, M^2/\bar{N}^2, \mu_F^2). \end{aligned} \quad (4.96)$$

The first two coefficients of the hard function are given by [25]

$$\tilde{\mathcal{H}}_{ab}^{(0)} = \tilde{\sigma}_{ab}^{(0)}, \quad (4.97)$$

$$\tilde{\mathcal{H}}_{ab}^{(1)} = \tilde{\sigma}_{ab}^{(0)} \left[\frac{\pi^2}{6} \left(A_a^{(1)} + A_b^{(1)} \right) \right] + \tilde{\sigma}_{ab}^{\text{virt.}}. \quad (4.98)$$

In contrast to the full NLO contribution to the hard matching coefficient (see Eq. (4.90)), the hard function for DY-like processes in Eq. (4.98) does not include factorization scale dependent terms. The expansion of the Sudakov exponential up to NLL accuracy is now given by

$$\tilde{g}_a^{(1)}(\lambda) = \frac{A_a^{(1)}}{2\lambda\beta_0} \left[2\lambda + \ln(1-2\lambda) \right], \quad (4.99)$$

$$\begin{aligned} \tilde{g}_a^{(2)}(\lambda) &= -\frac{A_a^{(2)}}{2\beta_0^2} \left[2\lambda + \ln(1-2\lambda) \right] + \frac{B_a^{(1)}}{\beta_0} \ln(1-2\lambda) \\ &+ \frac{A_a^{(1)}}{2\beta_0} \left[2\lambda + \ln(1-2\lambda) \right] \ln \frac{M^2}{\mu_R^2} \\ &+ \frac{\beta_1 A_a^{(1)}}{2\beta_0^3} \left[2\lambda + \ln(1-2\lambda) + \frac{1}{2} \ln^2(1-2\lambda) \right], \end{aligned} \quad (4.100)$$

where the coefficient $B_a^{(1)}$ has been introduced to avoid double counting of the NLL terms comprised in the one-loop approximation $\mathcal{E}_{ab}^{(1)}$ of the evolution operator. They are given by $B_q^{(1)} = 3C_F$ and $B_g^{(1)} = -2\beta_0$ [25]. In comparison to Eq. (4.72), the whole factorization scale dependence is now governed by the evolution operator. Due to this modification of the resummation formula, we get a different expansion:

$$\sigma_{ab}^{(\text{exp.})}(N, M^2, \mu_F^2, \mu_R^2) = \tilde{\mathcal{H}}_{ab}^{(0)}(M^2, \mu_R^2)$$

$$\begin{aligned}
& + \frac{\alpha_s}{2\pi} \tilde{\mathcal{H}}_{ab}^{(1)}(M^2, \mu_R^2) \\
& - \frac{\alpha_s}{2\pi} \ln \frac{\bar{N}^2 \mu_F^2}{M^2} \sum_c \left[P_{ac}^{(1)}(N) \tilde{\mathcal{H}}_{cb}^{(0)}(M^2, \mu_R^2) \right] \\
& - \frac{\alpha_s}{2\pi} \ln \frac{\bar{N}^2 \mu_F^2}{M^2} \sum_c \left[\tilde{\mathcal{H}}_{ac}^{(0)}(M^2, \mu_R^2) P_{bc}^{(1)}(N) \right] \\
& - \frac{\alpha_s}{2\pi} \tilde{\mathcal{H}}_{ab}^{(0)}(M^2, \mu_R^2) \left[(A_a^{(1)} + A_b^{(1)}) \ln^2 \bar{N} \right] \\
& + \frac{\alpha_s}{\pi} \tilde{\mathcal{H}}_{ab}^{(0)}(M^2, \mu_R^2) \left[(\gamma_a^{(1)} + \gamma_b^{(1)}) \ln \bar{N} \right], \tag{4.101}
\end{aligned}$$

where the quantities $P_{ab}^{(1)}$ are the full Mellin moments of the one-loop approximation of the AP splitting functions in four dimensions given in Eqs. (4.20) to (4.23). $\gamma_a^{(1)}$ is the field anomalous dimension corresponding, in axial gauge, to the virtual, N -independent, pieces of $P_{aa}^{(1)}$ [88]. For quarks and gluons they read

$$\gamma_q^{(1)} = \frac{3C_F}{2} \quad \text{and} \quad \gamma_g^{(1)} = \beta_0. \tag{4.102}$$

The additional subtracted terms stem from the expansion of the QCD evolution operator up to NLO.

5 Revisiting Slepton Pair Production at the Large Hadron Collider

Sleptons are considered to be among the lightest SUSY particles. Their masses are expected to be of $\mathcal{O}(100 \text{ GeV})$ and thus we assume that they can be discovered at the LHC. Finding appropriate mass limits for sleptons is not only relevant for slepton searches themselves, but is also crucial for the study of possible chargino and neutralino signals. The reason is the decay pattern of a low mass slepton, which most likely decays into its corresponding lepton and a gaugino. Vice versa, a gaugino can decay into a slepton and a lepton. Due to this connection of the decay patterns, slepton searches at the LHC are of great interest.

Most of the phenomenological and experimental studies for sleptons so far rely on either LO [89, 90, 91] or NLO [92] computations, which may lead to large theoretical uncertainties. For more accurate results we include threshold resummation effects of soft gluon emission matched to the NLO predictions. This has already been done in the past up to NLL+NLO accuracy [93, 94]. In this chapter we update these results for a center-of-mass energy of 7, 8 and 13 TeV and we discuss the effect and significance of the inclusion of NNLL terms. Furthermore, we derive new mass limits for sleptons in the light of simplified SUSY models with different benchmark scenarios.

This chapter is structured as follows: first, we briefly review the fixed order computations in Sec. 5.1, before we define the simplified models in Sec. 5.2. Afterwards, we show resummation predictions and study their scale and PDF uncertainties (see Sec. 5.3). Finally, we discuss the reanalysis of CMS and ATLAS results for the simplified models using our resummation predictions and considering different benchmark scenarios in Sec. 5.4.

Some of the analytical and numerical results presented in this chapter have been published in Ref. [54].

5.1 Fixed order computations

At the LHC, sleptons are most likely produced in pairs via the process $pp \rightarrow \tilde{l}\tilde{l}^* + X$, where p denotes a proton, \tilde{l} (\tilde{l}^*) a general slepton and X soft and collinear jets and the remnant of the protons. The underlying LO partonic process can only occur by an annihilation of an incoming quark and antiquark and only s -channel diagrams, as shown in Fig. 5.1, including different electroweak mediators are possible. A general solution for the Born matrix element can be written as

$$\mathcal{M}_B \mathcal{M}_{B_c}^* = \frac{4N_c e^2}{(s - m_V^2)(s - m_{V_c}^2)} \text{CC}_c (\text{LL}_c + \text{RR}_c) \left(tu - m_l^2 m_{\tilde{l}^*}^2 \right), \quad (5.1)$$

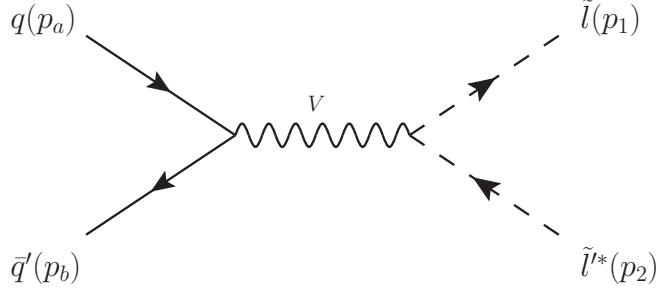


Figure 5.1: Leading order Feynman diagram for slepton pair production. The symbol \tilde{l} (\tilde{l}'^*) stands for any generation of sleptons, q (\bar{q}') for any of the five light quarks (antiquarks) and the symbol V for any electroweak vector boson.

where $N_c = 3$ is the number of quark colors, e the electromagnetic charge, $m_{\tilde{l}}$ ($m_{\tilde{l}'^*}$) the mass of the slepton (antislepton) and m_V denotes the mass of an electroweak vector boson V . The appearing coupling constants L, R and C can be found in Appendix A and the label c in the subscript of the couplings and the vector boson mass refers to those appearing in the complex conjugated diagram. Common Mandelstam variables s , t and u have been defined as

$$s = (p_a + p_b)^2 = 2p_a \cdot p_b, \quad (5.2)$$

$$t = (p_a - p_1)^2 = -2p_a \cdot p_1 + m_{\tilde{l}}^2, \quad (5.3)$$

$$u = (p_a - p_2)^2 = -2p_a \cdot p_2 + m_{\tilde{l}'^*}^2, \quad (5.4)$$

using the labeling of the momenta according to Fig. 5.1. Since we consider the incoming quarks as massless, the relation $s + t + u = m_{\tilde{l}}^2 + m_{\tilde{l}'^*}^2$ must hold. Finally, a summation over all spin and color degrees of freedom has been performed.

The partonic differential color and spin averaged Born cross section is given by

$$d\sigma_{ab}^B = \frac{1}{2s} \frac{1}{4N_c^2} \sum_{V, V_c} \mathcal{M}_B \mathcal{M}_{B_c}^* d\text{PS}^{(2)}, \quad (5.5)$$

where $1/(2s)$ is the flux factor, $1/(4N_c^2)$ the averaging term, $d\text{PS}^{(2)} = dt/(8\pi s)$ the common two-particle phase space and the labels a and b refer to the different incoming partons. The summation is performed over all possible electroweak gauge bosons V and V_c in the propagator.

NLO predictions include the virtual contributions depicted in Fig. 5.2, where the first row shows the contributions to the quark self-energy and the second row the vertex corrections. The corresponding analytical results can be found in Appendix B. Summing over all virtual contributions interfered with the Born diagrams leads to

$$d\sigma^V = \frac{1}{2s} \frac{1}{4N_c^2} \sum_{V, V_c} \sum_{\text{virtuals}} 2 \text{Re} (\mathcal{M}_v \mathcal{M}_{B_c}^*) d\text{PS}^{(2)}, \quad (5.6)$$

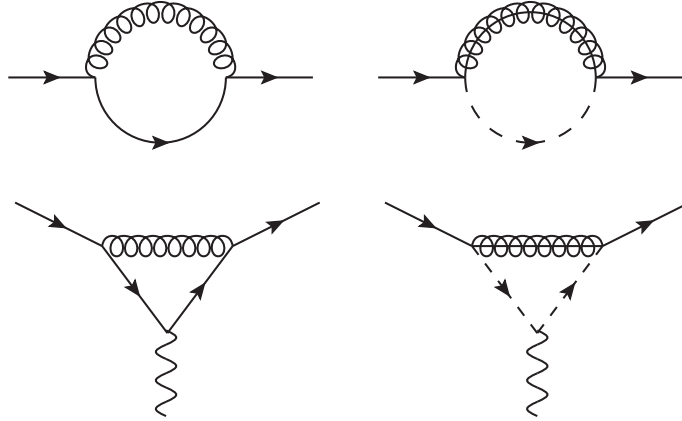


Figure 5.2: Feynman diagrams depicting the virtual corrections for slepton pair production. The first row shows the QCD (left) and SUSY-QCD (right) corrections to the quark self-energy and the second row the QCD (left) and SUSY-QCD (right) vertex corrections.

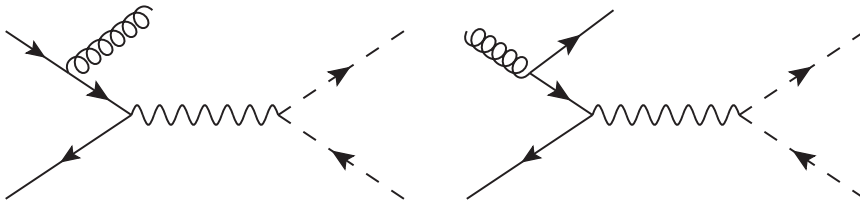


Figure 5.3: Feynman diagrams representing real gluon (left) and quark (right) emission which have to be taken into account for the NLO cross section.

where \mathcal{M}_v denotes a diagram including a virtual correction. To get an IR finite cross section real emission diagrams, as shown in Fig. 5.3, have to be taken into account as well. We distinguish between real gluon, quark and antiquark emission:

$$d\sigma^R = d\sigma_{\text{gluon}}^R + d\sigma_{\text{quark}}^R + d\sigma_{\text{antiquark}}^R. \quad (5.7)$$

After averaging over the initial state color, spins and polarizations we can write

$$d\sigma_{\text{gluon}}^R = \frac{1}{2s} \frac{1}{4N_c(N_c^2 - 1)} |\mathcal{M}_{\text{gluon}}^R|^2 d\text{PS}^{(3)}, \quad (5.8)$$

$$d\sigma_{\text{quark}}^R = \frac{1}{2s} \frac{1}{4N_c^2} |\mathcal{M}_{\text{quark}}^R|^2 d\text{PS}^{(3)}, \quad (5.9)$$

where $d\text{PS}^{(3)}$ is the three-particle phase space which is for instance given in Ref. [95]. To get the real antiquark emission cross section we just have to replace the matrix element in Eq. (5.9). The full NLO contribution to the partonic cross section can now be computed by employing Eq. (3.26). All the necessary dipoles, i.e. the insertion operators \mathbf{I} , \mathbf{P} and \mathbf{K} and the real emission dipole $d\sigma^A$, can be found in Ref. [34]. Finally, we perform a convolution of the partonic cross section with the PDFs of the two incoming protons according to Eq. (3.21) to obtain the hadronic cross section up to NLO accuracy.

Table 5.1: Total cross sections for $pp \rightarrow \tilde{l}l^*$ at $\sqrt{S} = 13$ TeV using CTEQ6L1 [96] and CT10NLO [97] as LO and NLO PDFs. We show a comparison between PROSPINO2.1 [98, 99] and RESUMMINO [85]. As the benchmark scenario we use BP II (see Sec. 6.4.1).

Final state	LO (10^{-4} fb)		NLO (10^{-4} fb)	
	RESUMMINO	PROSPINO	RESUMMINO	PROSPINO
$\tilde{e}_L \tilde{e}_L^*$	3.681	3.680	4.154	4.154
$\tilde{e}_R \tilde{e}_R^*$	1.567	1.567	1.789	1.790
$\tilde{\tau}_1 \tilde{\tau}_1^*$	1.671	1.671	1.915	1.915
$\tilde{\tau}_1 \tilde{\tau}_2^*$	0.726	0.726	0.805	0.806
$\tilde{\nu}_{\tilde{e}_L} \tilde{\nu}_{\tilde{e}_L}^*$	3.193	3.191	3.542	3.542

All matrix elements have been computed by employing a self-written FORM [100] script. UV and IR finiteness have been checked separately. In order to verify the fixed order results we perform a comparison between the public code PROSPINO2.1 [98, 99] and our code RESUMMINO using benchmark point (BP) II (see Sec. 6.4.1) as the benchmark scenario. For this scenario PROSPINO2.1 can only compute approximate NLO results, because it makes the assumption of degenerate squark masses¹. Only the LO result can be computed for non-degenerate squarks and is then scaled by the NLO K -factor of the degenerate computation in order to obtain an approximate NLO result. RESUMMINO [85] is able to use non-degenerate squark masses,

¹PROSPINO2.1 takes the average over the masses of all squarks, except the stops and sbottoms.

but for the comparison we also use averaged squark masses. The electroweak gauge couplings have been computed by using Fermi's coupling constant and the masses of the W and Z boson. For $\alpha_s(\mu_R)$ we use the evolution provided by the PDF sets, where for LO we use the CTEQ6L1 [96] and for NLO the CT10NLO [97] PDF. Factorization and renormalization scales are set to the average mass of the final state sleptons. The results² for different slepton final states are listed in Tab. 5.1 showing a perfect agreement.

5.2 Simplified models for sleptons

Due to the very large parameter space of the MSSM, simplified models only containing a few physical parameters are widely used for searches of SUSY particles. These models are extensions of the SM, where only a minimal content of new particles and interactions is included. This leads to a simplified production and decay scheme for the SUSY particles, but allows us to test some generic features possibly common to many other SUSY models. Furthermore, this framework aims for an easy comparison of theoretical prediction with data and a reinterpretation of the experimental results in case of more complete theories.

To develop such a model, we focus on a very specific final state topology as shown in Fig. 5.4. As sleptons are assumed to be among the lightest particles, we follow a very simple decay chain, where the slepton \tilde{l} decays into its corresponding lepton l with the same flavor and the lightest neutralino $\tilde{\chi}_1^0$. The decay pattern has motivated many different experimental searches, where the signal contains two leptons and missing energy, due to the undetectable neutralino. In our scenario the SM contains only two additional SUSY particles, the slepton \tilde{l}

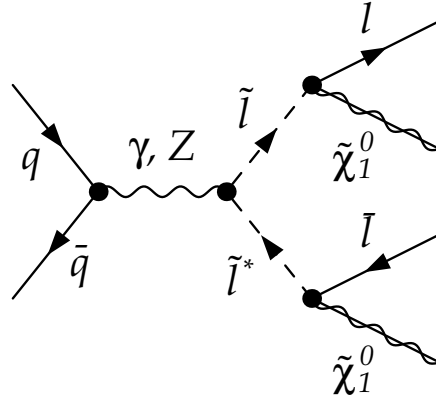


Figure 5.4: Leading-order Feynman diagram depicting slepton pair production and decay in the simplified models under consideration. The symbol \tilde{l} stands for any generation of (s)leptons.

and the LSP $\tilde{\chi}_1^0$. The whole colored SUSY sector has been decoupled from our model. This is

²Note that for this scenario the cross section for slepton pair production is actually too small to be observed. This BP is just used for a comparison and later for the associated production of gauginos and gluinos.

reasonable, because the mass limits of the colored sparticles are of $\mathcal{O}(1 \text{ TeV})$ and therefore SUSY-QCD loop-corrections are negligible compared to the ordinary QCD corrections. We consider the remaining electroweak sparticles to be heavier than the two included sparticles and hence they decouple from the decay chain. In this work we define different benchmark scenarios where we distinguish between the left- and right-handed³ nature of the sleptons and the gaugino or higgsino-nature of the LSP.

Next, we describe the simplified models in more detail. The third generation of sleptons will be treated separately, because left- and right-handed mixing effects have to be taken into account.

5.2.1 First and second generation sleptons

The two Lagrangians in Eqs. (5.10) and (5.11) describe a simplified model for L - and R -type sleptons. The first ingredient is the SM Lagrangian, denoted by \mathcal{L}_{SM} . Secondly, a four-component Majorana field Ψ_N has been added, representing the lightest neutralino $\tilde{\chi}_1^0$, together with a slepton field \tilde{l}_L (\tilde{l}_R), which can either be a selectron or a smuon. The subscripts L and R denote the chirality of the corresponding lepton Ψ_l .

$$\begin{aligned} \mathcal{L}^{(L)} = & \mathcal{L}_{\text{SM}} + \partial_\mu \tilde{\ell}_L^\dagger \partial^\mu \tilde{\ell}_L + \frac{i}{2} \bar{\Psi}_N \gamma^\mu \partial_\mu \Psi_N + ie \left[\partial_\mu \tilde{\ell}_L^\dagger \tilde{\ell}_L - \tilde{\ell}_L^\dagger \partial_\mu \tilde{\ell}_L \right] A_\mu \\ & - \frac{ie}{s_W c_W} \mathcal{C}_Z^{(L)} \left[\partial_\mu \tilde{\ell}_L^\dagger \tilde{\ell}_L - \tilde{\ell}_L^\dagger \partial_\mu \tilde{\ell}_L \right] Z_\mu + \left[\frac{1}{2c_W s_W} \bar{\Psi}_N \mathcal{C}_N^{(L)} P_L \Psi_\ell \tilde{\ell}_L^\dagger + \text{h.c.} \right], \end{aligned} \quad (5.10)$$

$$\begin{aligned} \mathcal{L}^{(R)} = & \mathcal{L}_{\text{SM}} + \partial_\mu \tilde{\ell}_R^\dagger \partial^\mu \tilde{\ell}_R + \frac{i}{2} \bar{\Psi}_N \gamma^\mu \partial_\mu \Psi_N + ie \left[\partial_\mu \tilde{\ell}_R^\dagger \tilde{\ell}_R - \tilde{\ell}_R^\dagger \partial_\mu \tilde{\ell}_R \right] A_\mu \\ & - \frac{ie}{s_W c_W} \mathcal{C}_Z^{(R)} \left[\partial_\mu \tilde{\ell}_R^\dagger \tilde{\ell}_R - \tilde{\ell}_R^\dagger \partial_\mu \tilde{\ell}_R \right] Z_\mu + \left[\frac{1}{2c_W s_W} \bar{\Psi}_N \mathcal{C}_N^{(R)} P_R \Psi_\ell \tilde{\ell}_R^\dagger + \text{h.c.} \right]. \end{aligned} \quad (5.11)$$

As interaction terms we have only added the gauge couplings between the sleptons and a photon A or a Z -boson and the coupling between the neutralino, slepton and lepton. The latter leads to the decay of the slepton if it is kinematically allowed. Additional interactions, such as four-scalar or neutralino-gauge interactions, are allowed by gauge invariance and supersymmetry. Moreover, contributions to the neutralino-lepton-slepton vertices proportional to the muon or electron Yukawa couplings are also present in the MSSM. However, in the context of the current work these couplings are either phenomenologically irrelevant or negligibly small and thus have been omitted for simplicity. The coupling constants in Eqs. (5.10) and (5.11) are given by

$$\mathcal{C}_Z^{(L)} = -\frac{1}{2} + s_W^2, \quad (5.12)$$

$$\mathcal{C}_N^{(L)} = \sqrt{2}e \left[s_W N_1^* + c_W N_2^* \right], \quad (5.13)$$

³As the slepton is a scalar particle it does not have any chirality. When we say left- or right-handed sleptons we actually refer to the chirality of their superpartners.

$$\mathcal{C}_Z^{(R)} = s_W^2 , \quad (5.14)$$

$$\mathcal{C}_N^{(R)} = -2\sqrt{2}es_W N_1 , \quad (5.15)$$

where N_i denotes an element of the neutralino mixing matrix (see Sec. 2.3.3), $s_W = \sin \theta_W$ and $c_W = \cos \theta_W$ with θ_W the Weinberg angle and e the electromagnetic charge. N_1 and N_2 denote the bino and wino components of the neutralino, whereas N_3 and N_4 refer to the two higgsino components. The unitarity condition for the mixing matrix leads to

$$|N_1|^2 + |N_2|^2 + |N_3|^2 + |N_4|^2 = 1 . \quad (5.16)$$

For a particular benchmark model we have to define the flavor and chirality of the slepton. Additionally, we have to fix three of the four elements of the neutralino mixing matrix, whereas the fourth one is given by the unitarity condition in Eq. (5.16). The remaining parameters are the slepton mass $M_{\tilde{l}}$ and the mass of the lightest neutralino, $M_{\tilde{\chi}_1^0}$, whereas the neutralino must be lighter than the slepton to allow the slepton decay.

5.2.2 Simplified models for staus

For the third generation of sleptons mixing effects between the left- and right-handed components are expected to be large. Therefore, our simplified model has to be slightly modified. We can parameterize the mixing matrix by one mixing angle $\theta_{\tilde{\tau}}$. Thereby, the transformation from interaction eigenstates $\tilde{\tau}_L$ and $\tilde{\tau}_R$ to mass eigenstates $\tilde{\tau}_1$ and $\tilde{\tau}_2$ can be written as

$$\begin{pmatrix} \tilde{\tau}_1 \\ \tilde{\tau}_2 \end{pmatrix} = \begin{pmatrix} \cos \theta_{\tilde{\tau}} & \sin \theta_{\tilde{\tau}} \\ -\sin \theta_{\tilde{\tau}} & \cos \theta_{\tilde{\tau}} \end{pmatrix} \begin{pmatrix} \tilde{\tau}_L \\ \tilde{\tau}_R \end{pmatrix} . \quad (5.17)$$

Incorporating these mixing effects in the previous simplified model leads to

$$\begin{aligned} \mathcal{L}^{(\tau)} = & \mathcal{L}_{\text{SM}} + \partial_\mu \tilde{\tau}_1^\dagger \partial^\mu \tilde{\tau}_1 + \frac{i}{2} \bar{\Psi}_N \gamma^\mu \partial_\mu \Psi_N \\ & + ie \left[\partial_\mu \tilde{\tau}_L^\dagger \tilde{\tau}_1 - \tilde{\tau}_1^\dagger \partial_\mu \tilde{\tau}_L \right] A_\mu - \frac{ie}{s_W c_W} \mathcal{C}_Z^{(\tau)} \left[\partial_\mu \tilde{\tau}_1^\dagger \tilde{\tau}_1 - \tilde{\tau}_1^\dagger \partial_\mu \tilde{\tau}_1 \right] Z_\mu \\ & + \frac{1}{2c_W s_W} \left[\bar{\Psi}_N \mathcal{C}_N^{(\tau,L)} P_L \Psi_\tau \tilde{\tau}_1^\dagger + \bar{\Psi}_N \mathcal{C}_N^{(\tau,R)} P_R \Psi_\tau \tilde{\tau}_1^\dagger + \text{h.c.} \right] . \end{aligned} \quad (5.18)$$

The coupling constants are now given by

$$\mathcal{C}_Z^{(\tau)} = \left[-\frac{1}{2} + s_W^2 \right] \cos^2 \theta_{\tilde{\tau}} + \left[s_W^2 \right] \sin^2 \theta_{\tilde{\tau}} , \quad (5.19)$$

$$\mathcal{C}_N^{(\tau,L)} = \sqrt{2}e \left[s_W N_1^* + c_W N_2^* \right] \cos \theta_{\tilde{\tau}} - \left[2c_W s_W N_3^* y_\tau \right] \sin \theta_{\tilde{\tau}} , \quad (5.20)$$

$$\mathcal{C}_N^{(\tau,R)} = \left[-2\sqrt{2}es_W N_1 \right] \sin \theta_{\tilde{\tau}} - \left[2c_W s_W N_3 y_\tau \right] \cos \theta_{\tilde{\tau}} , \quad (5.21)$$

where the Yukawa coupling y_τ is no longer negligible. Note that this is only a model for the lightest stau, namely $\tilde{\tau}_1$, whereas the heavier $\tilde{\tau}_2$ has been decoupled from the model.

Simplified models for the third generation of sleptons are now defined by two mass parameters, namely the mass of the lightest stau $M_{\tilde{\tau}_1}$ and the mass of the neutralino $M_{\tilde{\chi}_1^0}$, three of the four elements of the neutrino mixing matrix and the mixing angle $\theta_{\tilde{\tau}}$.

5.3 Precision predictions for slepton pair production at the LHC

In this section we present total cross sections for direct slepton pair production for the previous introduced simplified models. For the resummation predictions we employ the formulas given in Sec. 4.8. We focus on improved threshold resummation up to NLL accuracy and state results for both past LHC runs at center-of-mass energies of 7 TeV and 8 TeV.

5.3.1 Total cross section computations

This section is dedicated to an overview of the total cross sections for the three generations of sleptons. The electroweak gauge couplings have been computed by using Fermi's coupling constant and the masses of the W and Z boson, which additionally fix the Weinberg angle. For the LO predictions we use the LO PDF CTEQ6L1 [96], whereas for the NLO and NLL+NLO predictions we use the CT10NLO [97] fit. The strong coupling is provided by the PDF sets, where CT10NLO uses a two-loop computation for the β -function. For an easy access of the PDFs we make use of the LHAPDF6 [101] library. In all cases we fix the renormalization and factorization scale to $\mu_R = \mu_F = M_{\tilde{l}}$. The slepton mass region is chosen in such a way that the resulting cross sections together with the integrated luminosity of 5 fb^{-1} and 20 fb^{-1} for the 7 TeV and 8 TeV run of the LHC⁴, respectively, lead to an observable number of events.

In Fig. 5.5 we present results for a restricted mass range of $M_{\tilde{l}} \in [50, 450] \text{ GeV}$ at 7 TeV (upper panel) and 8 TeV (lower panel). We observe the common, approximately exponential, decrease of the cross section for larger masses. The maximal cross section is roughly 500 fb and the minimal value is 0.1 fb. This region leads to at least two possible events for the 8 TeV run, although these events are hidden in the overwhelming SM background. Light left-handed (right-handed) sleptons with a mass below 200 GeV (150 GeV) give rise to cross sections over 10 fb leading to a possibly feasible amount of events. Due to the reduced gauge couplings of the right-handed slepton compared to those of the left-handed one, the total cross section is significantly smaller.

Going from LO to NLO predictions we find a large K -factor going up to 1.25 in the low mass region ($M_{\tilde{l}} \lesssim 50 \text{ GeV}$) and 1.15 in the heavier mass region ($M_{\tilde{l}} \gtrsim 200 \text{ GeV}$). The difference between the NLO and NLO+NLL results for the total cross sections at the central scale is negligible. This is reasonable, since there is still plenty of phase space far from threshold available for the production of rather light sleptons. Together with the steeply falling PDFs close to the threshold region, we get only minor contributions by adding NLL corrections. However, by varying the scale by a factor of two around its central value we see a significant reduction of the scale uncertainty. This will be addressed in Sec. 5.3.2 in more detail.

⁴Looked up at <https://twiki.cern.ch/twiki/bin/view/AtlasPublic/LuminosityPublicResults>. (last visited: 2nd of October, 2016.)

Next, we investigate the production of the lighter $\tilde{\tau}_1$. In Fig. 5.6 we show the dependence of the total cross section for $\tilde{\tau}_1$ -pair production on the sine of the mixing angle $\theta_{\tilde{\tau}}$ and the stau mass $M_{\tilde{\tau}_1}$ for the center-of-mass energies of 7 TeV (upper panel) and 8 TeV (lower panel). As for the first and second generation of sleptons we set the factorization and renormalization scales to $M_{\tilde{\tau}_1}$. Total cross sections of 10 fb are expected for stau masses between 150 and 200 GeV, similarly to the previous results for selectrons and smuons. However, signals of staus are much more complicated to observe due to tau reconstruction efficiencies. If $\tilde{\tau}_1$ is constituted mostly of left-handed contributions ($\theta_{\tilde{\tau}} < \pi/4$), the cross section is larger than for mostly right-handed staus ($\theta_{\tilde{\tau}} > \pi/4$), which agrees with previous results for left- and right-handed sleptons of the first and second generation. For the rest of this work we choose a scenario with maximal mixing for staus, i.e. $\theta_{\tilde{\tau}} = \pi/4$. Thereby, a sizable cross section of 10 fb is found for $M_{\tilde{\tau}_1} \simeq 190$ GeV. For maximal mixing significant loop-induced contributions can appear for the production of staus with bottom-antibottom and gluon-pair initial states. This has not been included in this work and we advise to have a look at Ref. [102].

5.3.2 Theoretical uncertainties

We have already mentioned the reduction of the scale uncertainty by adding NLL contributions in the previous subsection. Here, we want to discuss this property in more detail. In Fig. 5.7 we show the scale dependence of the total cross section for three different processes, namely left-handed and right-handed first or second generation sleptons, and the lighter staus with a maximal mixing angle at a center-of-mass energy of 8 TeV. The slepton masses have been fixed to $M_{\tilde{l}} = 300$ GeV. We separately vary the renormalization and factorization scales by a factor of four around the central value.

In the upper panel of Fig. 5.7 we have kept the factorization scale fixed to the central value and only varied the renormalization scale by a factor of four around the central value. At LO the cross section does not include any renormalization scale dependence, since the strong coupling and loop corrections do not appear. By including QCD corrections, logarithms of the renormalization scale appear due to the strong coupling constant $\alpha_s(\mu_R)$ involved in the virtual and real emission diagrams. Thus, the total cross section at NLO decreases for larger renormalization scale values and shows a similar scaling behavior as the strong coupling itself. Matching the fixed order NLO results to NLL predictions, we find a reduction of the scale dependence. The inclusion of soft gluon emission attenuates the scaling behavior due to the inclusion of threshold enhanced logarithmic terms explicitly depending on μ_R (see Eq. (4.100)).

Next, we turn to the factorization scale dependence, shown in the lower panel of Fig. 5.7. The factorization scale behavior of the LO prediction is completely driven by the factorization scale dependence of the LO PDF. Using NLO PDFs instead this uncertainty is reduced. At NLO only the collinear remainder includes additional logarithms of the factorization scale, changing the scaling behavior as well. We achieve a further reduction of the factorization scale dependence by taking into account NLL contributions. Further logarithms of μ_F are contained in the one-loop approximation of the QCD evolution operator, which is used for the collinear improved NLL resummation formula (see Sec. 4.8).

As a second theoretical uncertainty we investigate the dependence of the cross section on different PDF fits. We compare uncertainties for three different PDF sets, namely CT10NLO,

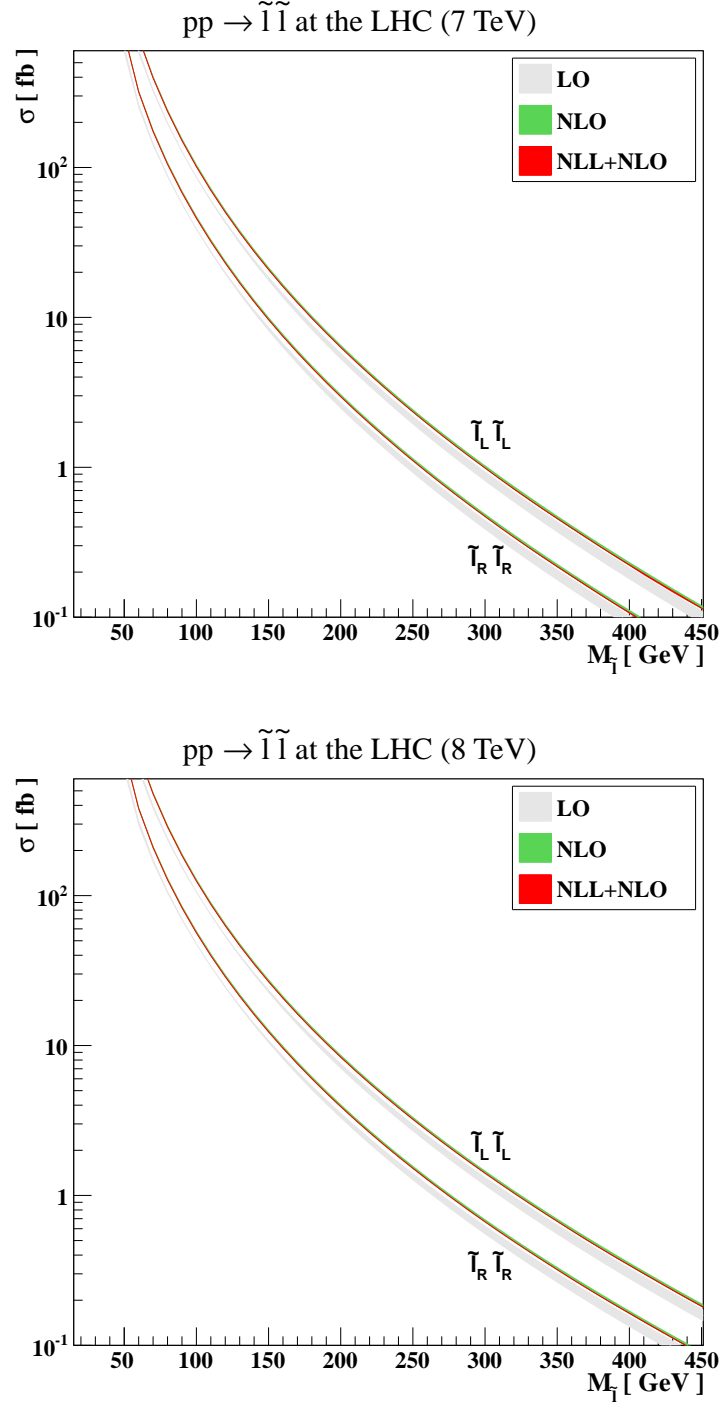


Figure 5.5: Total cross sections for slepton pair production at the LHC, running at center-of-mass energies of 7 TeV (upper panel) and 8 TeV (lower panel). We present predictions as functions of the slepton mass $M_{\tilde{l}}$ at LO (gray) and NLO (green) of pQCD and after matching the NLO results with threshold resummation at the NLL accuracy (red). The uncertainty bands correspond to variations induced by a change of the unphysical scales in the $[1/2M_{\tilde{l}}, 2M_{\tilde{l}}]$ range.

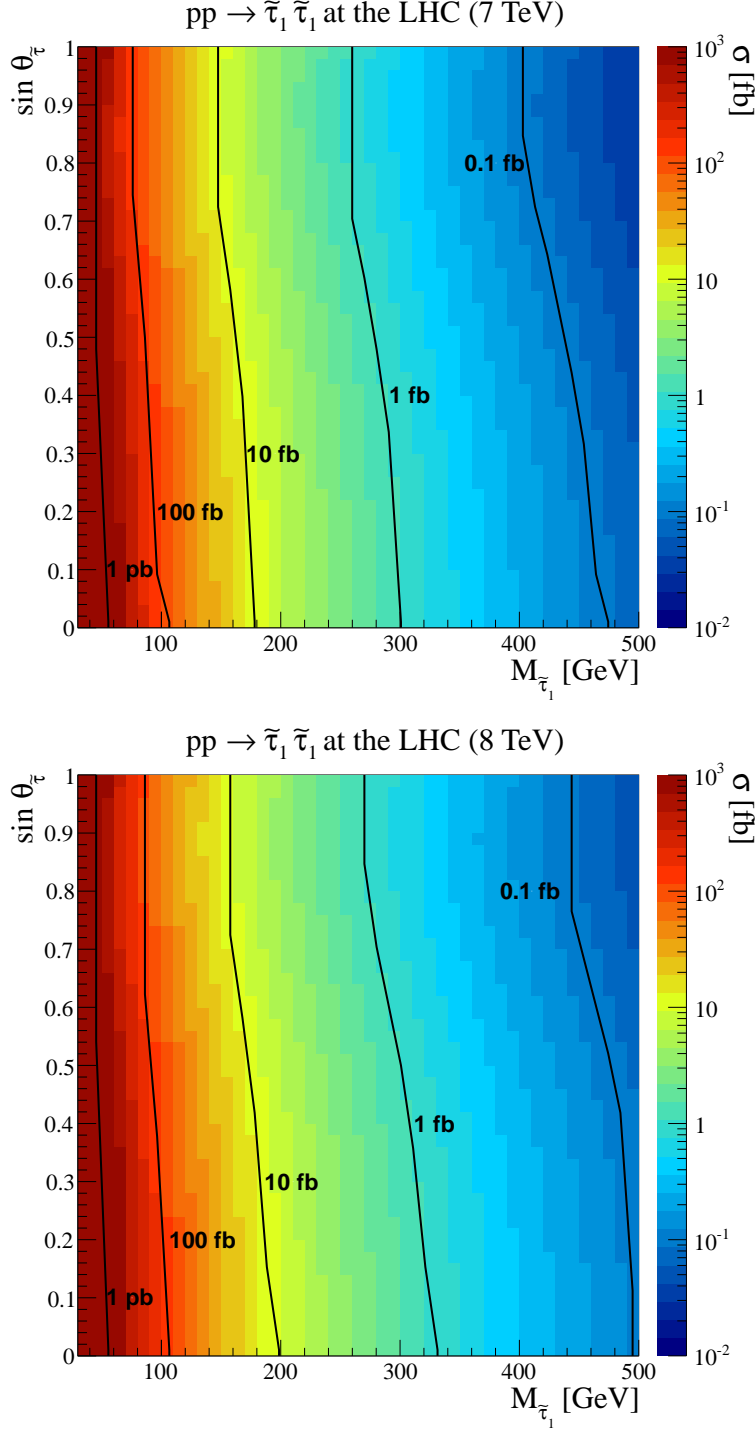


Figure 5.6: Total cross sections for stau pair production at the LHC, running at center-of-mass energies of 7 TeV (upper panel) and 8 TeV (lower panel). We present predictions as functions of the stau mass and the stau mixing angle after matching the NLO results with threshold resummation at the NLL accuracy.

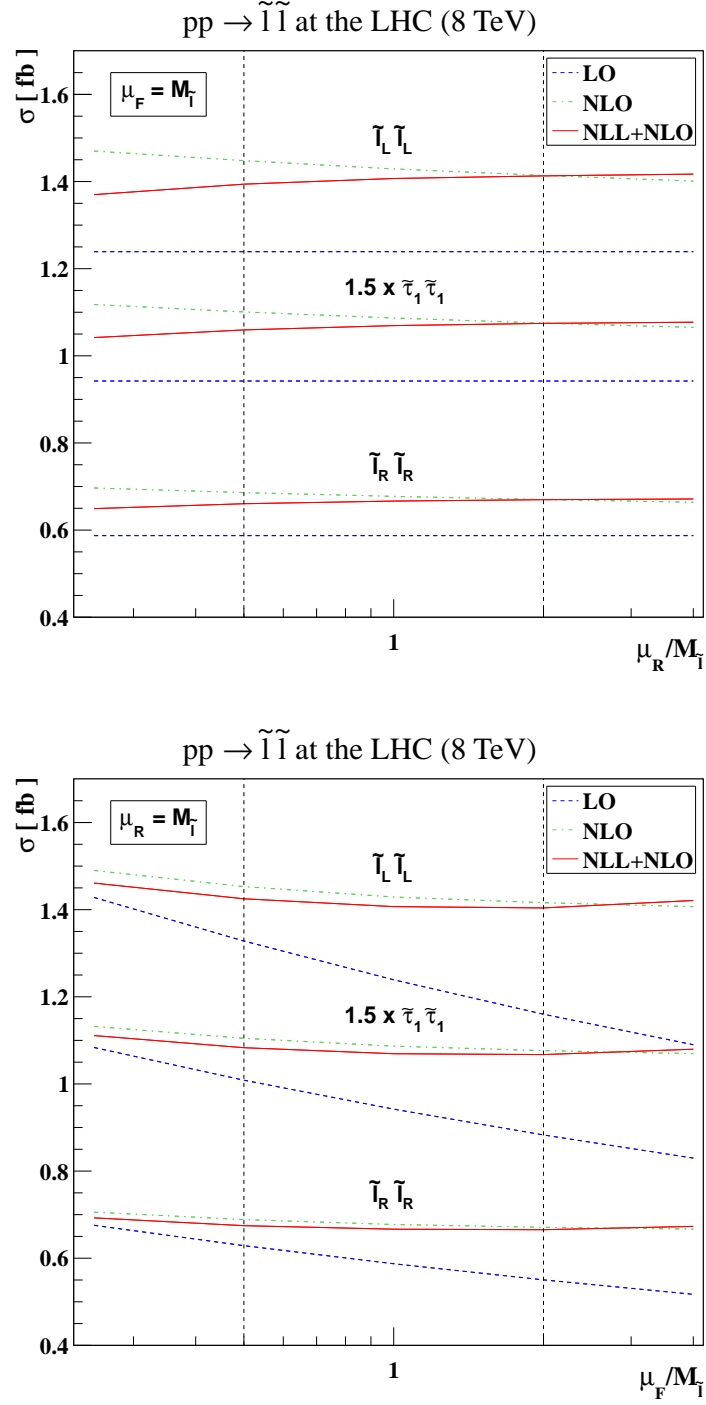


Figure 5.7: Total cross sections for the production of a pair of left-handed first or second generation sleptons, right-handed first or second generation sleptons and maximally mixing staus at the LHC, running at a center-of-mass energy of 8 TeV. We depict the dependence of the results on the renormalization (upper panel) and factorization (lower panel) scales at the LO (dashed blue), NLO (dashed-dotted green) and NLL+NLO (plain red) accuracy.

MSTW2008NLO90CL [103] and NNPDF23 [104]. Since the two former are Hessian-like PDF sets, the uncertainties are computed as

$$\Delta\sigma_{\text{up}} = \sqrt{\sum_{i=1}^n [\max(\sigma_{+i} - \sigma_0, \sigma_{-i} - \sigma_0)]}, \quad (5.22)$$

$$\Delta\sigma_{\text{down}} = \sqrt{\sum_{i=1}^n [\max(\sigma_0 - \sigma_{+i}, \sigma_0 - \sigma_{-i})]}, \quad (5.23)$$

where σ_{+i} and σ_{-i} denote predictions when employing a PDF set including a positive and negative variation along the i^{th} eigenvector of the covariance matrix, respectively. σ_0 is the cross section obtained by using the central fit. CT10NLO provides $n = 26$ eigenvectors of the parton density fit covariance matrix and $\alpha_s(M_Z) = 0.118001$, whereas MSTW2008nlo90cl includes $n = 20$ and $\alpha_s(M_Z) = 0.120179$. Applying Eqs. (5.22) and (5.23) on the different fits leads in both cases to a 90% confidence level for the PDF uncertainty.

For NNPDF23 the uncertainty is evaluated in a different manner. The NNPDF collaboration suggests to compute the standard deviation of the 100 replicas and multiply the result by the common factor of 1.645 in order to get the 90% confidence level [104, 105]. The value of the strong coupling at the reference scale is $\alpha_s(M_Z) = 0.118$.

Since it turned out that with our approach we could not get a proper Mellin transform of the NNPDF23 PDF set (for more details see Appendix D), which is needed for our resummation approach, we instead rely on the ratio κ of the NLL+NLO to NLO results which is expected to be largely independent of the parton density choice if the two calculations employ PDF sets evaluated at the same perturbative order. Therefore, the results for NNPDF23 are based on pure NLO results rescaled by the average κ -factor of MSTW2008NLO90CL and CT10NLO PDF sets. All PDF sets use a two-loop running of the strong coupling α_s .

Our obtained results in Fig. 5.8 show the three PDF uncertainty bands for the previously mentioned PDF sets, where all NLL+NLO predictions have been normalized to the one for the CT10NLO central PDF. We focus on the process for the production of left-handed sleptons at a center-of-mass energy of 8 TeV over a mass range $M_{\tilde{l}} \in [50, 500]$. First, we notice the difference in the symmetry of the upper and lower uncertainties. While the NNPDF23 band is completely symmetric around the central value due to the standard deviation method, the two other uncertainty bands are not symmetric due to the Hessian method. We further observe that up to these uncertainties, all predictions agree over the whole slepton mass range at the percent level. The PDF uncertainty for low slepton masses is about a few percent, whereas for larger masses it goes up to 10%, since the relevant regions of the (x, μ_F^2) parameter space lead to PDFs which are less constrained by data.

There is another source of theoretical uncertainty, namely the one on α_s . The value of the strong coupling is strongly correlated with the PDFs. PDF fits are performed with different values of $\alpha_s(M_Z)$ leading to additional provided PDF sets of the collaborations which have to be taken into account. However, this uncertainty has not been considered in this work and is left for further investigations. Finally, all three theoretical uncertainties should then be

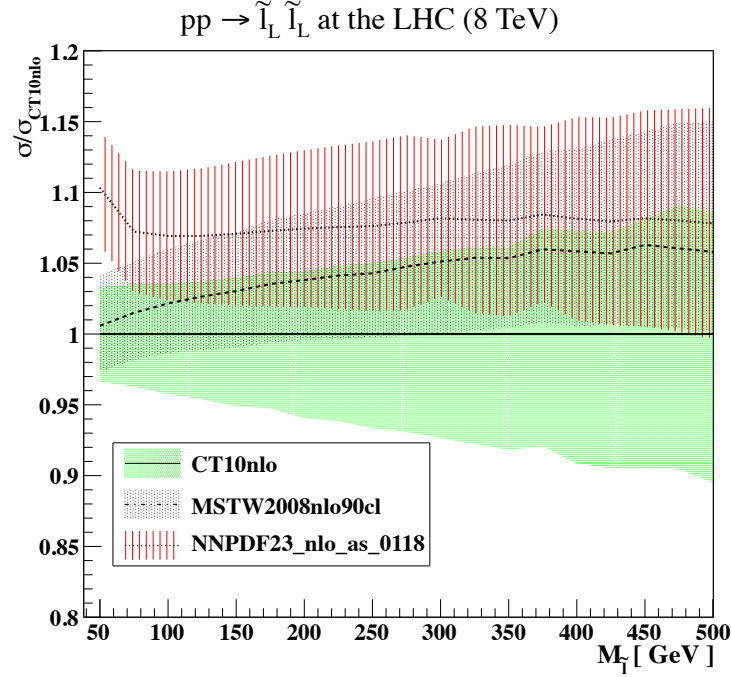


Figure 5.8: Total cross sections for the production of a pair of left-handed sleptons at the LHC, running at a center-of-mass energy of 8 TeV. We study the dependence of the results on the parton density fits by showing predictions obtained with the central PDF fits as provided by the CTEQ (plain), MSTW (dashed) and NNPDF (dotted) collaborations, normalized to results obtained when using the best CT10 NLO fit. We indicate additionally the associated theoretical uncertainties for all PDF choices.

added up in quadrature to give the full theoretical error [106]. For the significance of the α_s uncertainty we refer to [56]⁵.

5.3.3 Comparison between NLL, improved NLL and NNLL

Before closing this section about total cross sections for sleptons and discussing their uncertainties, we want to show a comparison between the improved NLL resummation formalism (see Sec. 4.8) and ordinary NLL and NNLL resummation. Formulas for the additional NNLL terms are stated for instance in Ref. [69]. For the collinear improved resummation we use the hard matching coefficient in Eqs. (4.97) and (4.98), whereas for the ordinary NLL and NNLL results we use the one discussed in Sec. 4.6. They only differ in the terms arising from the Mellin transform of the collinear remainder, which is given by

$$\langle P_{DY}(N) \rangle = \frac{\alpha_s}{2\pi} \left[-\frac{3}{2} C_F \ln \left(\frac{\mu_F^2}{M^2} \right) + 2 C_F \ln \left(\frac{\mu_F^2}{M^2} \right) \ln \bar{N} \right] + \mathcal{O}\left(\frac{1}{N}\right), \quad (5.24)$$

⁵In contrast to Ref. [56], which deals with the production of squarks and gluinos, the LO cross section for slepton pair production is independent of α_s and hence the uncertainty is expected to be less significant.

$$\langle \mathbf{K}_{DY}(N) \rangle = \frac{\alpha_s}{2\pi} \left[\frac{\pi^2}{2} C_F - (\gamma_q + K_q) + 2C_F \ln^2 \bar{N} \right] + \mathcal{O}\left(\frac{1}{N}\right), \quad (5.25)$$

with

$$\gamma_q = \frac{3}{2} C_F, \quad K_q = \left(\frac{7}{2} - \frac{\pi^2}{6} \right) C_F, \quad (5.26)$$

for the initial quark and the same result for the initial antiquark. Only the N -independent parts contribute to the hard matching coefficient. For the collinear improved version the factorization scale dependent term in Eq. (5.24) is comprised in the QCD evolution operator and hence not included in Eq. (4.98). Note that also for NNLL we use a NLO hard matching coefficient and match the result to the NLO predictions.

Since these results have been obtained relatively recently we focus on a center-of-mass energy of 13 TeV for left-handed slepton pair production and use the more recent PDF fit of the CTEQ-collaboration, namely CT14NLO [107].

In Fig. 5.9 we present the three different resummation predictions together with the NLO result for slepton masses of 500 GeV. First, we observe only a minor improvement of the NLL+NLO scale dependence compared to the NLO result. This is due to the still large amount of available phase space far from threshold. Going to the collinear improved NLL+NLO results we see a significant improvement which is due to the inclusion of the subleading terms contained in the one-loop approximation of the evolution operator. The evolution operator contains more μ_F dependent terms, leading to a difference especially for the variation of the factorization scale only. By adding NNLL terms to our result we observe an improvement compared to the ordinary NLL result and the typical behavior of an increase in the lower scale region. However, here the off-diagonal splitting terms contained in the improved resummation formula are more important than the NNLL corrections. Furthermore, we find for all three resummation predictions the typical inverse behavior for a variation of the renormalization scale compared to the variation of the factorization scale. The contributions for the separate variations compensate each other leading to a much smaller scale dependence for the simultaneous variation of the scales. The situation slightly changes when we increase the slepton masses to 1 TeV, which is shown in Fig. 5.10. The inclusion of the subleading terms in the evolution operator still leads to a significant improvement compared to the ordinary NLL+NLO predictions, whereas compared to NNLL+NLO the next-to-dominant logarithmic terms start to become more important, since the available phase space is restricted closer to the threshold region. As expected, we find that an increase of the slepton mass strengthens the effect of the NNLL results leading to the lowest scale dependence.

In Figs. 5.9 and 5.10 we find that the cross section predictions at the four precision levels leads to differences at the percent level for the central value. For slepton masses of 500 GeV the four results agree at one point, whereas for heavier slepton masses all results except the one of the improved resummation agree at one point which has now been shifted closer to the central scale. The improved resummation result is a bit smaller due to the included off-diagonal splitting terms. However, the shift of the intersection towards the central scale indicates that the choice of the central scale reduces the contributions of the appearing scale dependent logarithms at higher orders.

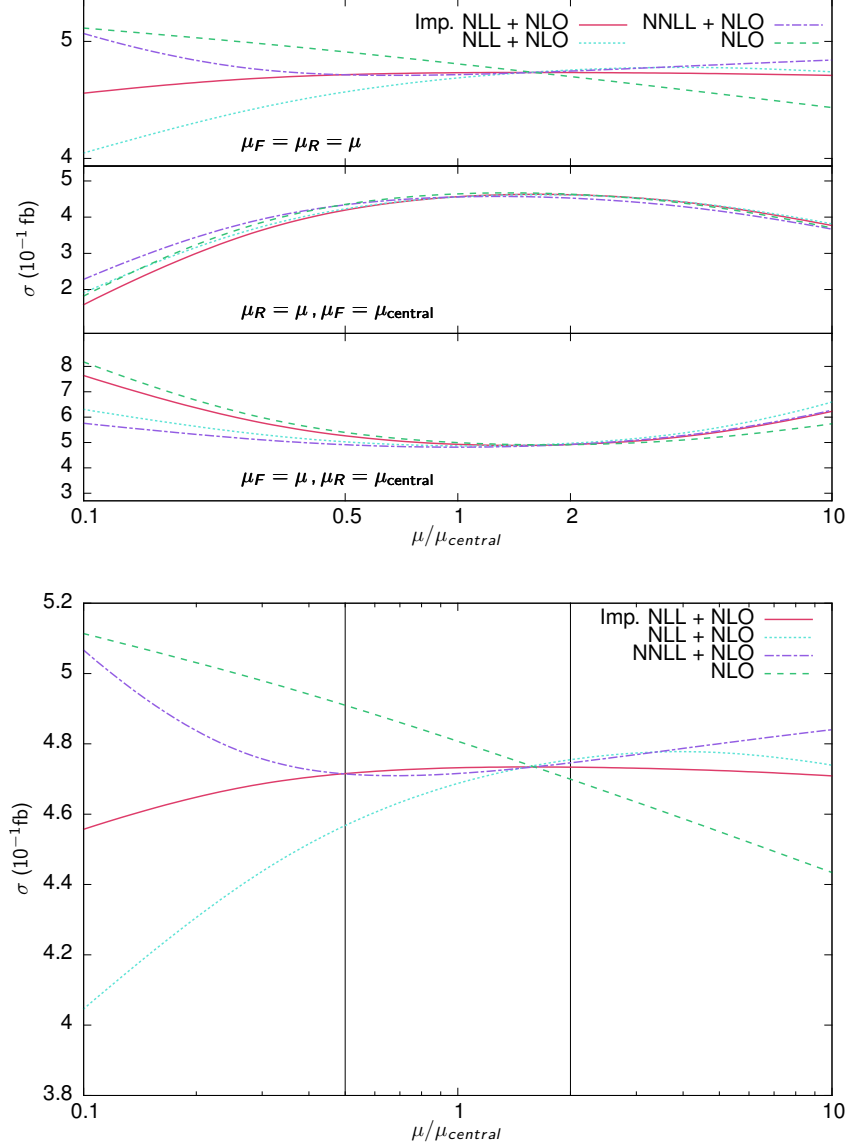


Figure 5.9: Analysis of the scale dependence for the process $pp \rightarrow \tilde{l}_L \tilde{l}_L^*$ at a center-of-mass energy of 13 TeV. The upper panel shows the total cross sections for NLO (blue), NLL+NLO (green), NNLL+NLO (orange) and collinear improved NLL+NLO (violet) while varying the factorization and renormalization scale simultaneously (top), only the renormalization scale (central) and only the factorization scale (bottom). The lower panel is a close-up of the simultaneous variation of the two scales. Vertical lines mark the usual variation region of a factor of two. For the benchmark scenario the simplified model with decoupled squarks has been chosen with slepton masses of 500 GeV.

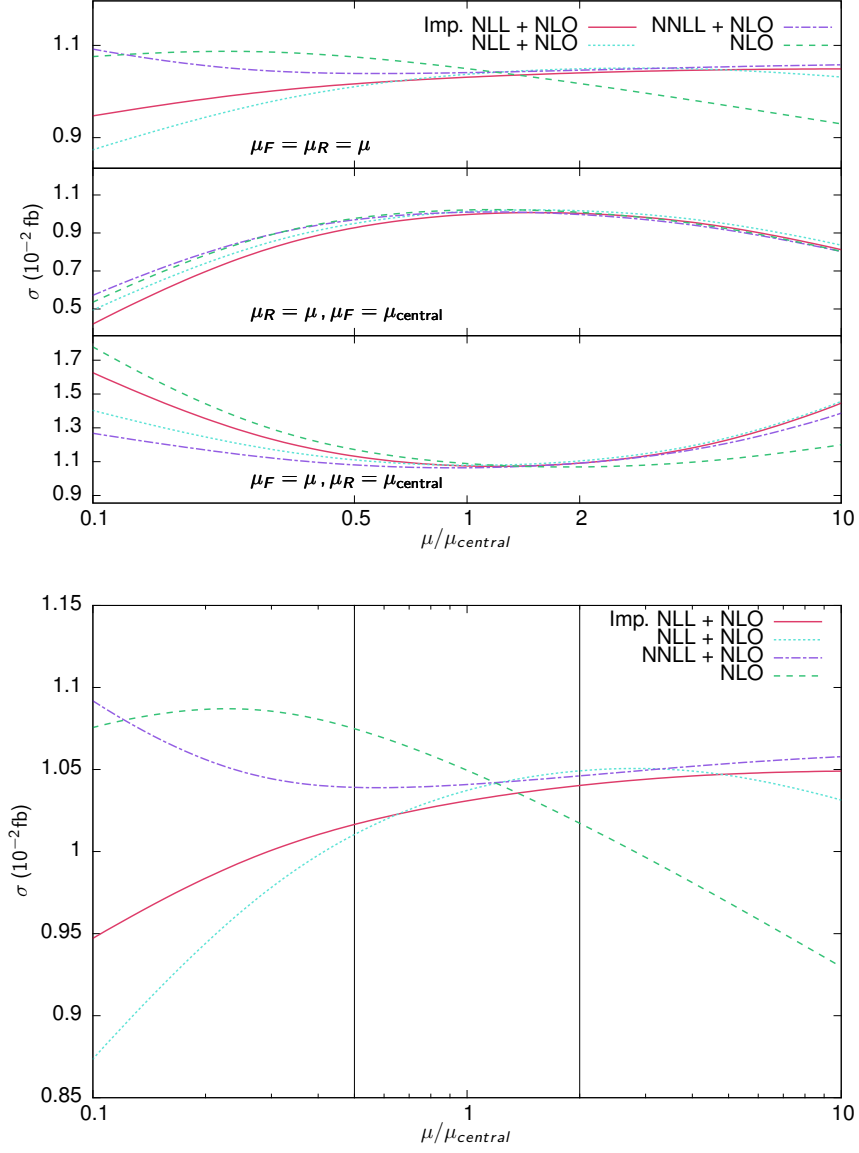


Figure 5.10: Same as in Fig. 5.9, but with slepton masses of 1000 GeV.

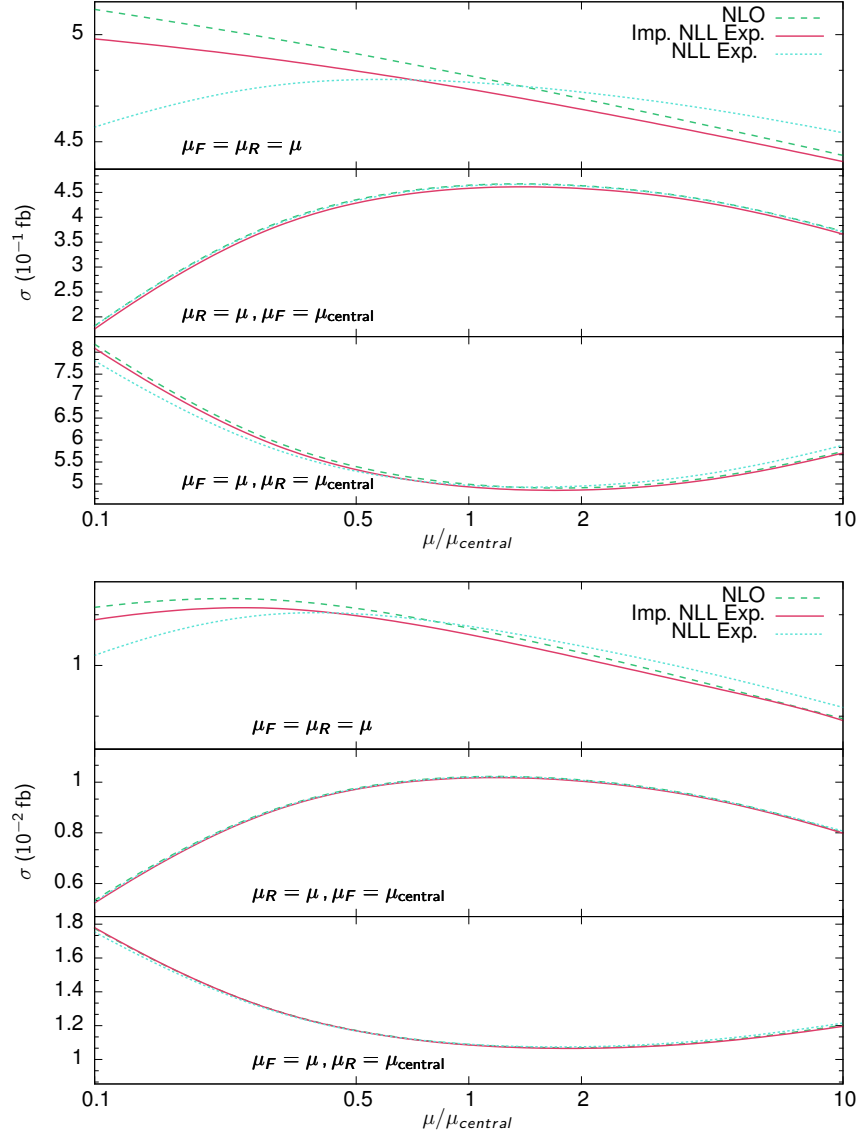


Figure 5.11: Total cross sections for NLO (blue), NLL expansion (green) and collinear improved NLL expansion (red). Slepton masses have been set to 500 GeV (upper panel) and 1000 GeV (lower panel). Rest is the same as in Fig. 5.9.

Finally, we compare the expansion of the NLL and improved NLL predictions up to NLO in Fig. 5.11. We remark that the resummation result contains the complete IR finite virtual correction and the threshold enhanced terms of the collinear remainder due to the hard matching coefficient. Hence, by an increase of the mass, which shifts the available phase space closer to the threshold, the expanded resummation results are expected to be a good approximation of the NLO predictions, since the threshold logarithms constitute the major part of the NLO corrections. For the variation of the renormalization scale only, we find a very good agreement between the ordinary NLL expansion, the improved version and the NLO results, whereas for the pure factorization scale dependence we do not. This is due to the improved NLL formula including subleading terms. Since these terms are proportional to logarithms of μ_F they mainly improve the dependence on the factorization scale. Thus, the agreement between NLO and the expansion of the improved NLL version is distinguished, especially for the factorization scale dependence. Furthermore, we see that the agreement between the expansion of the ordinary NLL result gets worse especially in the region of small factorization scales, where the off-diagonal splitting becomes more important due to the increase of the importance of the gluon PDFs.

It turns out that, for the current low mass limits of sleptons (and also gauginos), the improved NLL resummation formula leads to the best improvement regarding the scale dependence. Nevertheless, if the mass limits are shifted to higher values, NNLL corrections can lead to significant corrections, especially for scales different from the central one.

5.4 Sensitivity to slepton pair production at the LHC

Prior LHC searches for SUSY particles were mostly focused on the colored sector, i.e. on the production of squarks and gluinos. As a consequence of the negative search results and mass limits driven to very high values of $\mathcal{O}(1 \text{ TeV})$, the interest in searches for the possibly lighter electroweak SUSY particles has increased.

This section deals with a reinterpretation of ATLAS [108] and CMS [109] results for direct slepton searches at the LHC with center-of-mass energies of 7 and 8 TeV. For their analyses both collaborations have focused on signal regions with two final state leptons, electron-positron or muon-antimuon, in association with missing energy. Thus, these signal regions can be used to extract mass limits for the first and second generation of sleptons from their direct production and subsequent decay into the corresponding leptons and missing energy. For these searches simplified models, as introduced in Sec. 5.2, have been investigated [108, 109], but with a very specific scenario in terms of sleptons and neutralinos. Here, we want to extend these results and distinguish between different compositions of neutralinos (bino, wino or mixed bino-wino⁶) and sleptons (left- and right-handed). Additionally, we study the dependence of the mass bounds on different slepton flavors. For the analysis of stau pair production it turned out that it was not possible to find mass limits due to the complicated tau reconstruction together with the small signal cross section and the former luminosities.

To simulate the signal events, we employed the Monte-Carlo event generator MADGRAPH5 [110] together with its interface to PYTHIA6 [62] for the hadronization of the parton-level events,

⁶For the first and second generation of sleptons we have neglected the Yukawa coupling and hence there is no coupling to the higgsino-component of the neutralino-field. Therefore, this scenario has not been considered.

which contain up to two hard jets. For the decay of the tau we employed the package TAUOLA [111] and for the detector simulation we used DELPHES [112], using the CMS detector description explained in Ref. [113] and the built-in ATLAS detector setup. The simplified models have been designed with FEYNRULES [114] and added to MADGRAPH via the UFO [115] interface. RESUMMINO has been used for the reweighting of the events to the NLL+NLO results. Before analyzing the events with MADANALYSIS 5 [116], we reconstructed the jets with the anti- k_T algorithm (using a radius parameter set to $R = 0.5$) as implemented in the FASTJET [117] package.

Since our original publication of this work dates back roughly two years [54], new analyses have been performed in the meantime with the complete data of the 8 TeV run and some of the new data of the 13 TeV run. For this reason, we will briefly state updated results and mass limits at the very end of this section. Newer results can for instance be found in Refs. [118, 119, 120].

5.4.1 Revisiting ATLAS searches for first and second generation sleptons

This section deals with the recasting of the ATLAS results [108] for the first and second generation of sleptons at a center-of-mass energy of 7 TeV. Signal events have been generated as stated above. Afterwards, we apply the following selection criteria designed by the ATLAS collaboration [108]:

- Final state events must contain exactly two isolated leptons of the same flavor. Their transverse momentum is required to be larger than 10 GeV and their pseudorapidity has to fulfill $|\eta| \leq 2.47$ ($|\eta| \leq 2.4$) for electrons (muons). The isolation is enforced by constraining the transverse activity in a cone of a radius $R = \sqrt{\Delta\varphi^2 + \Delta\eta^2} = 0.2$ centered on the lepton to be less than 10% of the p_T for electrons and less than 1.8 GeV for muons, where φ is the azimuthal angle with respect to the beam direction.
- Events including at least one jet with a transverse momentum $p_T \geq 30$ GeV and a pseudorapidity $|\eta| \leq 2.5$ are discarded.
- The invariant mass m_{ll} of the lepton pair is constrained to be off the Z boson peak, $m_{ll} \notin [80, 100]$ GeV in order not to be compatible with a Z boson.
- We demand the final state to contain a significant amount of relative missing transverse energy $\cancel{E}_T^{\text{rel}} \geq 40$ GeV, where it is defined as the missing transverse energy \cancel{E}_T when the azimuthal angle $\tilde{\varphi}$ between the direction of the missing momentum and that of the nearest reconstructed jet object is larger than $\pi/2$ and by $\cancel{E}_T^{\text{rel}} = \cancel{E}_T \sin \tilde{\varphi}$ otherwise.
- Finally we exploit the properties of the m_{T2} variable [121] and select events for which $m_{T2} \geq 90$ GeV.

In Fig. 5.12 we present results for the production of left-handed selectrons decaying into an electron-positron pair and two neutralinos leading to missing transverse energy. We have defined three different scenarios for the composition of the neutralino. The panel on the left shows the results for a bino-like neutralino ($N_1 = 1, N_2 = N_3 = N_4 = 0$), whereas for the results of the central panel we use a pure wino state of the neutralino ($N_2 = 1, N_1 = N_3 = N_4 = 0$)

and for the panel on the right we consider a mixed state ($N_1 = N_2 = 1/\sqrt{2}$, $N_3 = N_4 = 0$). We show the visible cross section σ^{vis} for the $(M_{\tilde{L}}, M_{\tilde{\chi}_1^0})$ parameter space at a center-of-mass energy of 7 TeV, defined as the fraction of the cross section leading to events that can be observed by ATLAS when using the analysis described above. Furthermore, contour lines have been added for the 95% confidence level which can be extracted from the ATLAS limits by requiring a visible cross section $\sigma^{\text{vis}} \leq 1.5 \text{ fb}$. Due to the scalar nature of the selectron, we expect its decay

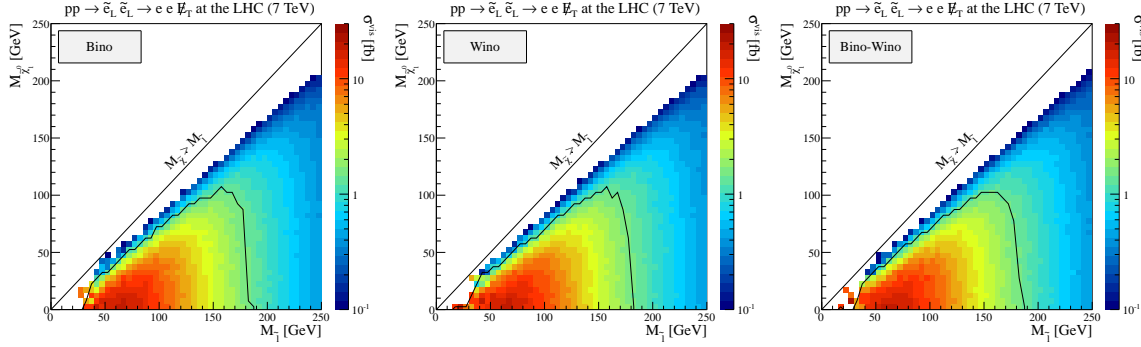


Figure 5.12: 95% confidence exclusion limit for left-handed selectron pair production, given in the $(M_{\tilde{L}}, M_{\tilde{\chi}_1^0})$ mass plane of the simplified model of Sec. 5.2 for different choices of the neutralino nature taken as bino (left), wino (center) and mixed (right). We present the visible cross section after applying the ATLAS selection describes in the text. The limits are extracted for an integrated luminosity of 4.7 fb^{-1} of LHC collisions at a center-of-mass energy of 7 TeV.

into an electron and a neutralino not to be sensitive to the composition of the latter. The outcome of the three panels of Fig. 5.12 is in agreement with these expectations. Selectrons with masses ranging up to about 175 GeV are excluded for almost massless neutralinos by 4.7 fb^{-1} of the 7 TeV LHC data. This exclusion limit holds for a neutralino mass going up to 100 GeV, whereas for larger neutralino masses the sensitivity drops so that no constraints can be derived. It can be seen that SUSY with a compressed spectrum, i.e. the selectron mass being slightly heavier than the neutralino mass, evades these limits. For such a spectrum the signal electrons are too soft to be detected.

The independence of the neutralino nature on the mass limits is supported by Fig. 5.14, where we show different kinematical observables for the bino, wino and mixed state of the neutralino. We present the transverse momentum distribution of the two final state leptons l_1 and l_2 (first row of the figure), the missing transverse energy distribution (left panel of the second row of the figure), the transverse mass of the lepton pair $M_T(l_1 l_2)$ (right panel of the second row), the angular distance in the azimuthal plane between the two leptons $\Delta\Phi(l_1 l_2)$ (left panel of the third row of the figure), the angular distance in the azimuthal plane of the missing momentum with the lepton pair $\Delta\Phi(l_1 l_2, \cancel{E}_T)$ as well as the one with the hardest lepton $\Delta\Phi(l_1, \cancel{E}_T)$ (last row of the figure). Slepton and neutralino masses have been set to 100 GeV and 60 GeV, respectively. Different mass values lead to similar results. We observe that all distributions are independent of the neutralino nature. From now on we only consider mixed wino-bino states of the neutralino.

Next, we analyze the dependence of the mass limits on the left- and right-handed nature of the sleptons as well as on their flavor. Hence, we show the visible cross section σ^{vis} in

Fig. 5.13 for left-handed smuons (left panel), right-handed selectrons (central panel) and right-handed smuons (right panel) for a center-of-mass energy of 7 TeV and a mixed wino-bino neutralino composition. Due to the larger production cross sections for left-handed sleptons compared to the right-handed ones, we observe a significant difference for the exclusion limits. It follows that the masses of the right-handed sleptons are less constrained. For almost massless neutralinos, we find right-handed selectrons of masses up to 150 GeV to be excluded. This holds for neutralino masses up to 60 GeV, whereas for larger neutralino masses we again lose the sensitivity, because the leptons carry too little energy in order to be detected. Turning

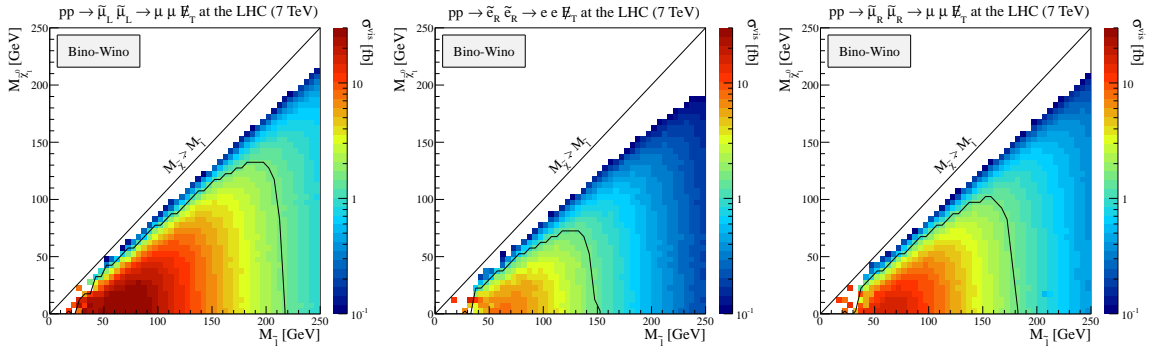


Figure 5.13: Same as in Figure 5.12, but for the production of a pair of left-handed smuons (left), right-handed selectrons (center) and right-handed smuons (right).

to the direct production of smuons, decaying into muons and neutralinos, visible cross sections larger than 1.6 fb are excluded by the ATLAS collaboration. Exclusion limits in the neutralino and smuon mass plane are shown in the left and right panel of Fig. 5.13. Different selections of muon and electron candidates together with a slightly different detector acceptance lead to a significant difference for the exclusion limits of selectrons and smuons. For almost massless neutralinos, masses ranging up to 220 GeV and 180 GeV are found to be excluded for left- and right-handed smuons, respectively. Similar as before, we lose all sensitivity for a neutralino mass going up to 130 GeV for left-handed and 100 GeV for right-handed smuons.

The properties found here are illustrated by the series of distributions shown in Fig. 5.15. The kinematical observables are the same as in Fig. 5.14, but this time we investigate the results for different flavors and chiralities of the sleptons with a fixed neutralino composition. We find that the shapes of these distributions differ for the electron and muon spectra. These figures have been obtained prior to the application of the event selection criteria for the Z boson veto, missing energy selection and the m_{T2} selection steps.

5.4.2 Revisiting CMS searches for first and second generation sleptons

This section is dedicated to the recasting of the CMS analysis [109] for the direct production of first and second generation sleptons at a center-of-mass energy of 8 TeV. Several signal regions are contained in their analysis, where one of them is expected to be sensitive to direct slepton pair production followed by their decay into the corresponding SM leptons and neutralinos. The applied selection criteria are the following:

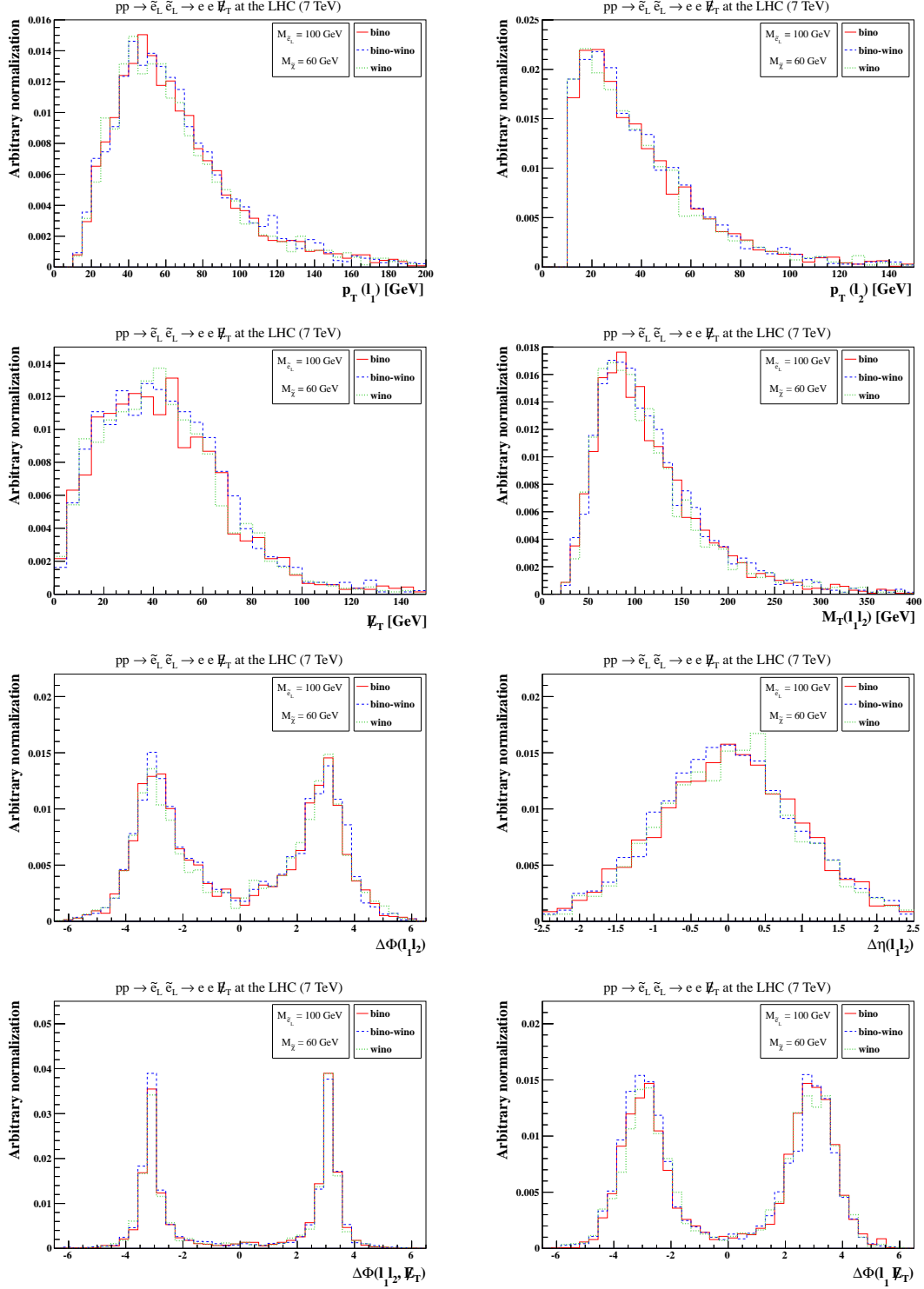


Figure 5.14: Properties of the dilepton plus missing energy final state arising from the production and decay of a pair of left-handed selectrons, for a benchmark scenario where the neutralino mass is set to 60 GeV and the left-handed selectron mass to 100 GeV. The distributions are shown for different choices of the neutralino nature.

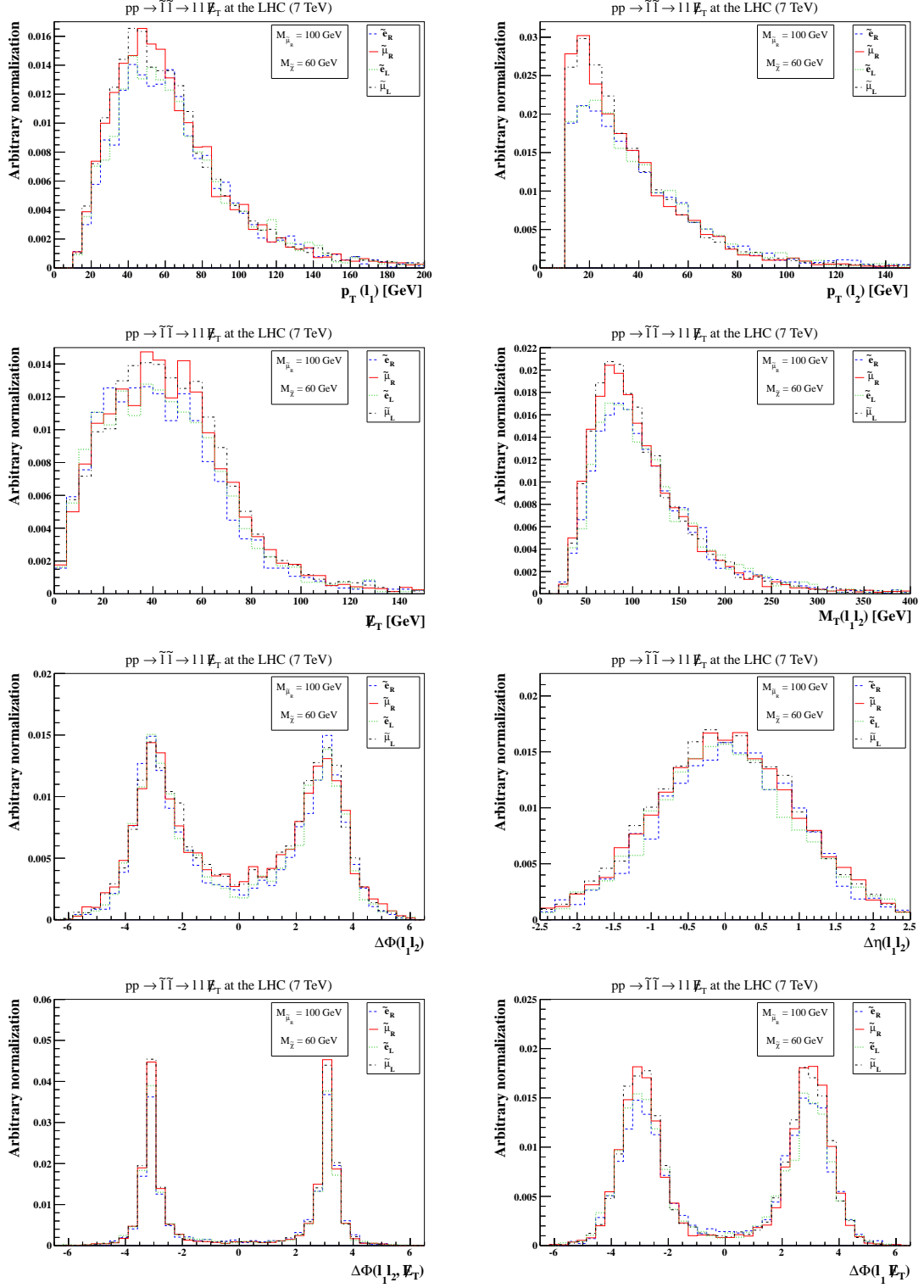


Figure 5.15: Same as in Fig. 5.14 but with the neutralino nature fixed to a bino-wino mixed state and for the production of different types of sleptons.

- Jets are required to have a transverse momentum larger than 30 GeV and a pseudorapidity $|\eta| \leq 2.5$. Events containing at least one b -tagged jet are discarded. The b -tagging efficiency and mistagging rates are described in Ref. [113].
- Isolated signal electrons (muons) are defined with a transverse momentum larger than 20 GeV and a pseudorapidity fulfilling $|\eta| \leq 2.4$. For the isolation criteria we additionally require the activity in a cone of a radius $R = 0.3$ around the lepton to be smaller than 15% of the lepton p_T .
- Signal leptons are required to have the same flavor and opposite electric charge. Moreover, we demand the dilepton invariant mass to be larger than 12 GeV (to discard events with a leptonically-decaying hadronic resonance) and not to be compatible with the mass of the Z boson, $m_{ll} \notin [75, 105]$ GeV.
- We remove each jet lying within a cone of radius $R = 0.4$ around an electron from the analysis.
- Final state signals should at least contain a missing transverse energy of 60 GeV and a transverse contranverse mass $M_{CT\perp}$ [122] larger than 100 GeV.

Results of our reanalysis are shown in Fig. 5.16 for the production of left-handed (left panel) and right-handed (right panel) sleptons after summing over both selectron and smuon channels, where the sleptons have been considered as degenerate in mass. For the predictions we have used an integrated luminosity of 9.2 fb^{-1} of LHC collisions with a center-of-mass energy of 8 TeV. As for the ATLAS analysis we show the visible cross section in the $(M_{\tilde{l}}, M_{\tilde{\chi}_1^0})$ parameter space, which is the fraction of the cross section after employing the above stated selection criteria. The exclusion contour with a 95% confidence level is obtained by the CMS observations of six data events. We compare this number with our predictions of the signal contribution, summed to the SM background, which has been computed by the CMS collaboration and is 14.2 ± 4.5 events.

For almost massless neutralinos we find left-handed (right-handed) sleptons being excluded for masses up to 310 GeV (250 GeV). For neutralino masses beyond 150 GeV (100 GeV) we lose all sensitivity due to the leptons being too soft. The CMS analysis is insensitive for mass differences $M_{\tilde{l}} - M_{\tilde{\chi}_1^0} \leq 70 \text{ GeV}$ and hence a compressed SUSY spectrum of the electroweak SUSY sector is still allowed.

5.4.3 Conclusion and outlook

The ATLAS collaboration was able to derive mass limits for simplified models for staus in a more recent analysis [120], by using the full data set of the 8 TeV run. In their scenario mixing effects of left- and right-handed components of the stau have been neglected. They have excluded a scenario for combined $\tilde{\tau}_L \tilde{\tau}_L^*$ and $\tilde{\tau}_R \tilde{\tau}_R^*$ production, with an almost massless neutralino and a mass of the τ_R of 109 GeV. No further constraints could be made since the theoretical predictions were nearly always below the observed limits [120].

For the first and second generations of sleptons new limits have been derived by ATLAS in Ref. [123] by using an integrated luminosity of 20.3 fb^{-1} of proton-proton collisions with

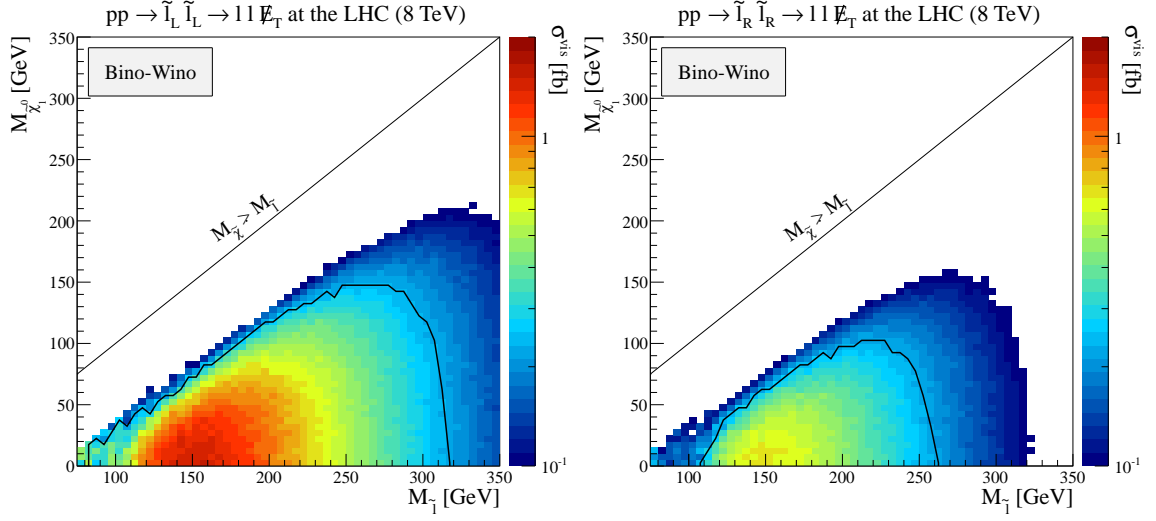


Figure 5.16: 95% confidence exclusion limit for left-handed (left) and right-handed (right) slepton pair production, given in the $(M_{\tilde{\ell}}, M_{\tilde{\chi}^0_1})$ mass plane of the simplified model of Sec. 5.2.1, for a mixed bino-wino neutralino and after summing over both first and second slepton generations. We present signal cross sections σ^{vis} that are obtained after having applied the CMS selection strategy described in the text. The limits are extracted for an integrated luminosity of 9.2 fb^{-1} of LHC collisions at a center-of-mass energy of 8 TeV.

a center-of-mass energy of 8 TeV. The selectron and smuon have been considered as mass-degenerate and there has not been an analysis distinguishing the two different flavors. For almost massless neutralinos they found left-handed (right-handed) sleptons to be excluded for a mass range of 90 GeV to 250 GeV (325 GeV). They lose all sensitivity for neutralino masses beyond 90 GeV (150 GeV) allowing for a compressed spectrum.

We conclude from our results that for future analyses it might be useful to distinguish between direct smuon and slepton production and hence not to sum over both signal events. Due to the larger production cross section of left-handed sleptons we were able to exclude a larger parameter space in the slepton-neutralino mass plane. With the data of the 13 TeV run we expect that stronger constraints can be made in the future.

6 Associated Production of Gauginos and Gluinos

The recent searches for SUSY particles have shifted the mass limits of the colored sparticles to higher and higher values. For instance, in the constrained MSSM (cMSSM) gluinos and squarks are excluded with masses up to 1.85 TeV with an integrated luminosity of 20.3 fb^{-1} of the 8 TeV LHC run [124]. In simplified SUSY models gluinos are ruled out with masses heavier than 1.52 TeV by 3.2 fb^{-1} of Run II, assuming the lightest neutralino as massless [125]. These limits vary slightly for different simplified benchmark scenarios and different signal searches, but they all point to the same direction: shifting the mass bounds of colored sparticles to values beyond 1 TeV. This stands in contrast to the neutralinos and charginos, which are still allowed to be light due to the weaker electroweak coupling involved in their direct production. Direct electroweak searches in the light of simplified models still allow the gaugino masses to be in the range of a few hundred GeV in most of the considered scenarios [123, 126].

As a result of the high mass limits for the gluinos, their direct pair production could be beyond the current reach of the LHC. For this reason, the associated production of gluinos together with the relatively light electroweak gauginos becomes phenomenologically relevant because it could be a possibility to produce gluinos at the LHC. Such a scenario could very well be realized in nature. For example, in GUTs the gaugino mass parameters M_i are expected to unify at the GUT-scale. After employing the RGEs, to evolve the masses to the electroweak scale, the relation $M_3 \simeq 6M_1$ follows. Therefore, the gluino with a mass of $m_{\tilde{g}} \simeq M_3$ is typically much heavier than the gauginos with masses of the order of the bino (M_1), wino ($M_2 \simeq 2M_1$) or higgsino (μ) mass parameters.

For these reasons, we dedicate this chapter to the associated production of gauginos and gluinos at the LHC. Cross sections at NLO have already been computed in the past [127, 128, 129, 130]. We perform an independent NLO computation and compare the numerical results with those previously obtained. Due to the expected large mass of the gluino, threshold effects of soft gluon emission may become crucial. Hence, we go beyond the pure fixed order computations and compute cross sections at the NLL+NLO accuracy level, which has not been done for this process yet.

The outline of this chapter is as follows: first, we review the fixed order computation of the cross section up to LO in Sec. 6.1 and NLO in Sec. 6.2. Second, we address the relevant parts needed to compute NLL+NLO resummation predictions in Sec. 6.3, i.e. the soft anomalous dimension and the hard matching coefficient. Finally, we present numerical results in Sec. 6.4, where we start by defining the chosen benchmark scenario followed by the discussion of the resummation predictions.

Some of the analytical and numerical results presented in this chapter have been published in Ref. [131].

6.1 Leading order computations

At the LHC the process for the associated production of a gluino \tilde{g} and a gaugino $\tilde{\chi}_j^{0,\pm}$ occurs on the partonic level at LO through an annihilation of a quark q and an antiquark \bar{q}' . This can be written as

$$q(p_a)\bar{q}'(p_b) \rightarrow \tilde{g}(p_1)\tilde{\chi}_j^{0,\pm}(p_2), \quad (6.1)$$

where the subscript j ($j = 1, \dots, 4$ for neutralinos and $j = 1, 2$ for charginos) labels the mass eigenstate of the gaugino and the prime at the antiquark label distinguishes between possible different flavors of the incoming quarks. The corresponding Feynman diagrams are shown in Fig. 6.1 and the squared matrix elements and interference terms are stated in Eqs. (6.2) to (6.4), where we have summed over all spin and color degrees of freedom.

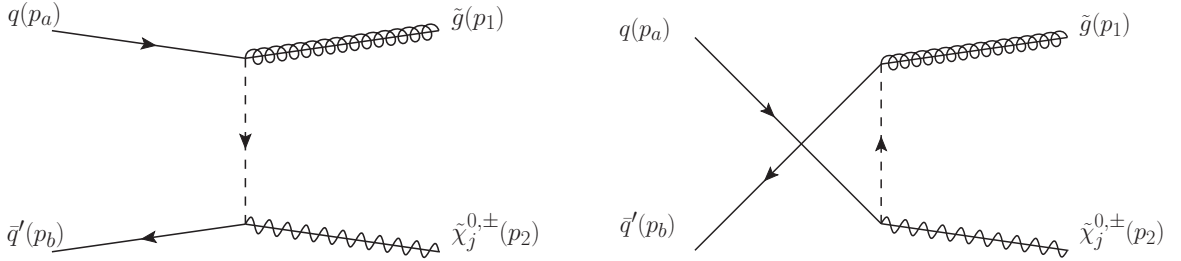


Figure 6.1: Tree-level t- (left) and u-channel (right) Feynman diagrams for the associated production of a gluino and a gaugino at hadron colliders. The dashed line represents squark exchanges.

$$\mathcal{M}_t \mathcal{M}_{t_c}^* = \frac{C_A C_F g_s(\mu_R) e}{(m_{\tilde{q}}^2 - t)(m_{\tilde{q}_c}^2 - t)} (\mathcal{L}' \mathcal{L}'_c + \mathcal{R}' \mathcal{R}'_c) (L L_c + R R_c) (m_{\tilde{g}}^2 - t)(m_{\tilde{\chi}}^2 - t) \quad (6.2)$$

$$\mathcal{M}_u \mathcal{M}_{u_c}^* = \frac{C_A C_F g_s(\mu_R) e}{(m_{\tilde{q}}^2 - u)(m_{\tilde{q}_c}^2 - u)} (\mathcal{L} \mathcal{L}_c + \mathcal{R} \mathcal{R}_c) (L' L'_c + R' R'_c) (m_{\tilde{g}}^2 - u)(m_{\tilde{\chi}}^2 - u) \quad (6.3)$$

$$\begin{aligned} \mathcal{M}_t \mathcal{M}_{u_c}^* = & \frac{C_A C_F g_s(\mu_R) e}{(m_{\tilde{q}}^2 - t)(m_{\tilde{q}_c}^2 - u)} \left[(-s^2 + t^2 + u^2 + (m_{\tilde{\chi}}^2 + m_{\tilde{g}}^2)(s - t - u) + 2m_{\tilde{g}}^2 m_{\tilde{\chi}}^2) \right. \\ & \left. (L L_c \mathcal{L}' \mathcal{L}'_c + R R_c \mathcal{R}' \mathcal{R}'_c) + 2m_{\tilde{g}} m_{\tilde{\chi}} s (\mathcal{R} \mathcal{R}_c \mathcal{L}' L'_c + \mathcal{L} L_c \mathcal{R}' R'_c) \right] \end{aligned} \quad (6.4)$$

Here, $\mathcal{L}^{(\prime)}, \mathcal{R}^{(\prime)}, L^{(\prime)}$ and $R^{(\prime)}$ are coupling constants specified in Appendix A, $m_{\tilde{g}}$ and $m_{\tilde{\chi}}$ are the gluino and gaugino mass, respectively, $m_{\tilde{q}}$ denotes the squark mass and the label c refers to the squark masses and couplings appearing in the complex conjugated diagram. We have used the common Mandelstam variables $s = (p_a + p_b)^2 = (p_1 + p_2)^2$, $t = (p_a - p_1)^2 = (p_b - p_2)^2$ and $u = (p_a - p_2)^2 = (p_b - p_1)^2$ satisfying $s + t + u = m_{\tilde{g}}^2 + m_{\tilde{\chi}}^2$ for massless incoming quarks using the labeling of the momenta according to Fig. 6.1. The SU(3) color factors are $C_A = 3$

and $C_F = 4/3$, e is the elementary charge and g_s is the strong coupling, where its scale dependence¹ is indicated by its argument, the renormalization scale μ_R .

Adding all contributions accordingly and averaging over the initial state color and spin degrees of freedom leads to the total squared amplitude

$$|\mathcal{M}|^2 = \frac{1}{4C_A^2} \sum_{\tilde{q}\tilde{q}_c} (\mathcal{M}_t \mathcal{M}_{t_c}^* + \mathcal{M}_u \mathcal{M}_{u_c}^* - 2 \operatorname{Re}(\mathcal{M}_t \mathcal{M}_{u_c}^*)) , \quad (6.5)$$

where we have inserted a relative minus sign between the t - and u -channel for the crossing of a fermion line. The differential cross section is given by

$$\sigma_{ab}^{\text{LO}}(s) = \int d\sigma_{ab}^{\text{LO}} = \int \frac{1}{2s} |\mathcal{M}|^2 d\text{PS}^{(2)} , \quad (6.6)$$

where $d\text{PS}^{(2)} = dt/(8\pi s)$ denotes the two-particle phase space and $1/(2s)$ is the flux factor. In order to get the hadronic cross section at LO we have to perform a convolution between the partonic cross section and the PDFs according to Eq. (3.21).

6.2 Next-to-leading order computations

To include the NLO corrections we need all the contributions of Eq. (3.26). These are the virtual corrections comprised in $d\sigma^V$, the cross section $d\sigma^R$, which contains an additional gluon, quark or antiquark in the final state, and all the corresponding Catani-Seymour dipoles. The latter are the insertion operators \mathbf{I} , \mathbf{P} and \mathbf{K} and the dipole $d\sigma^A$ which are listed in Ref. [35]. A useful tool to generate all dipoles for a specific process is SUPER AUTODIPOLE [133]. In the following two sections, we address the relevant pieces of the virtual and real emission corrections.

6.2.1 Virtual corrections

The virtual corrections for the associated gaugino-gluino production include self-energies of quarks, squarks and gluinos as shown in Fig. 6.2, vertex corrections for the quark-squark-gaugino and quark-squark-gluino vertex depicted in Fig. B.4 and box-diagrams for the t - and u -channel, where the former are shown in Fig. 6.4. Here, we briefly summarize the results for the self-energies, which have been computed in Appendix B and where we have used the mass and field counterterms of Sec. 3.4. We remark that we use field counterterms in the $\overline{\text{MS}}$ -scheme and mass counterterms in the on shell scheme. For the vertex corrections we refer to the analytical results in Appendix B and for the construction of their counterterms to Sec. 3.4. However, further finite counterterms are needed for these vertices, which we address in this section. The box diagrams do not need counterterms, because they are UV finite. All results are written in terms of tensor or scalar integrals according to LOOPTOOLS' [134] conventions. The complete virtual contribution is then obtained by employing Eq. (5.6).

¹For the electroweak couplings we use fixed values. Their change in the interesting scale region is rather small. To be specific, in a scale range of 1 GeV^2 to 10^4 GeV^2 the value of $1/\alpha_{\text{em}}$ changes only from 135 to 127 [132].

Self-energies

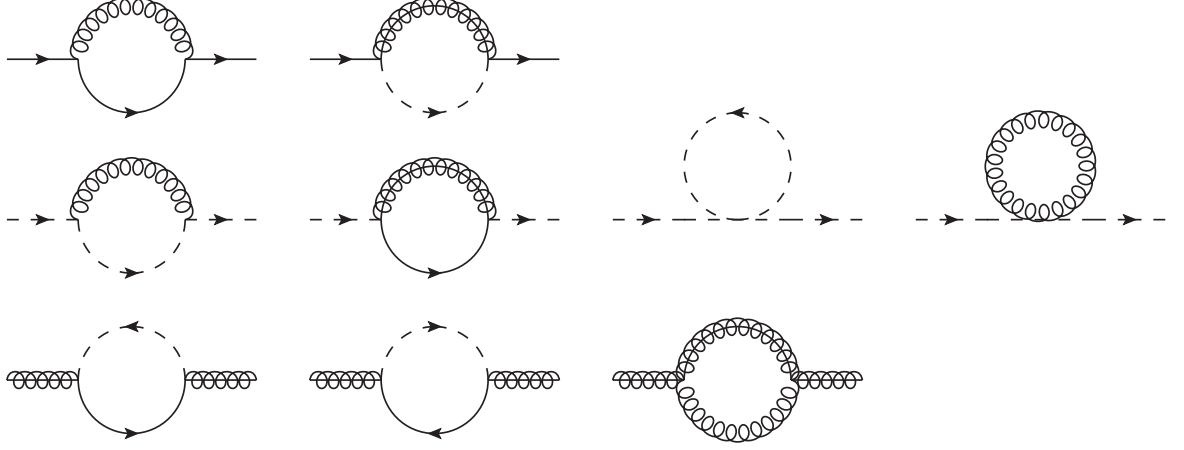


Figure 6.2: Self-energy diagrams for the quark (top row), the squark (central row) and the gluino (bottom row). The arrows describe the charge flow.

Self-energies of massless quarks: Here, we state the analytical results for the pure QCD self-energy contribution $\Sigma^{(qq)}$ and the SUSY-QCD correction $\Sigma^{(\tilde{g}\tilde{q})}$ together with their corresponding counterterms. Their labels in the exponent denote the particles which are involved in the loop correction. Both Feynman diagrams are depicted in the upper row of Fig. 6.2.

In general the self-energy of massless quarks can be written as

$$\Sigma = \delta_{ab} \not{p} \Sigma_V = \delta_{ab} \not{p} \left(\Sigma_V^L P_L + \Sigma_V^R P_R \right), \quad (6.7)$$

where P_L and P_R are the common left- and right-handed projectors and a and b are color indices of the fundamental representation. This leads to

$$\Sigma_V^{(qq)} = \frac{g_s^2 C_F}{8\pi^2} (1 - \epsilon) B_1(p^2, 0, 0), \quad (6.8)$$

$$\Sigma_V^{L(\tilde{g}\tilde{q})} = \frac{g_s^2 C_F}{16\pi^2} \sum_{\tilde{q}_i} B_1(p^2, m_{\tilde{g}}^2, m_{\tilde{q}_i}^2) \mathcal{R}_{Ii} \mathcal{L}'_{Ii}, \quad (6.9)$$

$$\Sigma_V^{R(\tilde{g}\tilde{q})} = \frac{g_s^2 C_F}{16\pi^2} \sum_{\tilde{q}_i} B_1(p^2, m_{\tilde{g}}^2, m_{\tilde{q}_i}^2) \mathcal{L}_{Ii} \mathcal{R}'_{Ii}, \quad (6.10)$$

where $m_{\tilde{g}}$ denotes the gluino mass and $m_{\tilde{q}_i}$ the squark mass of the squark mass eigenstates \tilde{q}_i . The coupling constants $\mathcal{L}^{(\prime)}$ and $\mathcal{R}^{(\prime)}$ are specified in Appendix A. B_1 is a scalar integral

²These states are either left- or right-handed since the squark mixing matrix is diagonal for the superpartners of massless quarks (see Sec. 2.3.4).

and $\epsilon = (4 - D)/2$, with D being the dimension of the Minkowski-space. The corresponding field counterterms are

$$\delta Z_q^{(gq)} = -\frac{g_s^2 C_F}{16\pi^2} \Delta, \quad (6.11)$$

$$\delta Z_q^{L(\tilde{g}\tilde{q})} = -\frac{g_s^2 C_F}{16\pi^2} \Delta, \quad (6.12)$$

$$\delta Z_q^{R(\tilde{g}\tilde{q})} = \delta Z_q^{L(\tilde{g}\tilde{q})}, \quad (6.13)$$

with $\Delta = \epsilon^{-1} + \ln 4\pi - \gamma_E$, where γ_E is the Euler-Mascheroni constant. For the associated gaugino-gluino production the quarks are external particles and hence we have to multiply their external spinors by the square root of the propagator's residue $\sqrt{\mathcal{R}} \simeq 1 + 1/2\delta\mathcal{R}$, as defined in Eq. (3.42). It yields

$$\delta \mathcal{R}_q^{(gq)} = \frac{g_s^2 C_F}{16\pi^2} \Delta_{\text{IR}}, \quad (6.14)$$

$$\delta R_L^{(\tilde{g}\tilde{q})} = \hat{\Sigma}_V^{L(\tilde{g}\tilde{q})}|_{p^2=0}, \quad (6.15)$$

$$\delta R_R^{(\tilde{g}\tilde{q})} = \hat{\Sigma}_V^{R(\tilde{g}\tilde{q})}|_{p^2=0}. \quad (6.16)$$

We remark that Eq. (6.14) is a pure IR divergent term, indicated by the subscript IR, and has to be kept for a check of IR finiteness. The results in Eqs. (6.15) and (6.16) are IR finite, because only massive particles appear in the loop correction.

Squark self-energy: Next, we state the self-energies of the squarks which enter the squark propagators (see Fig. 6.1). Due to flavor conservation, only scalar superpartners of massless quarks appear in the propagator. Hence, there will be no left- and right-handed squark mixing and the self-energies for $i \neq j$ vanish. The result of the first contribution reads

$$\Sigma_{ij}^{(g\tilde{q}_i)}(p^2, 0, m_{\tilde{q}_i}^2) = \frac{g_s^2 C_F}{16\pi^2} \left(p^2 B_{11} + DB_{00} + 4p^2(B_1 + B_0) \right) \delta_{ij}, \quad (6.17)$$

where the arguments of the scalar B -integrals are the same as those of the self-energy. The corresponding field and mass counterterms are

$$(\delta Z_m^{(g\tilde{q}_i)})^2 m_{\tilde{q}_i}^2 = -\frac{g_s^2 C_F}{16\pi^2} \text{Re} \left(m_{\tilde{q}_i}^2 B_{11} + DB_{00} + 4m_{\tilde{q}_i}^2(B_1 + B_0) \right) \Big|_{p^2=m_{\tilde{q}_i}^2}, \quad (6.18)$$

$$\delta Z_{ii}^{(g\tilde{q}_i)} = \frac{g_s^2 C_F}{8\pi^2} \Delta, \quad \delta Z_{ij}^{(g\tilde{q}_i)} = 0 \quad (\text{for } i \neq j). \quad (6.19)$$

For the second self-energy contribution we get

$$\Sigma_{ij}^{(\tilde{g}q)}(p^2, m_{\tilde{g}}^2, 0) = \frac{g_s^2 C_F}{8\pi^2} \sum_{q_I} (\mathcal{R}_{Ii} \mathcal{L}'_{Ij} + \mathcal{L}_{Ii} \mathcal{R}'_{Ij}) (p^2 (B_{11} + B_1) + DB_{00}), \quad (6.20)$$

where we have summed over all possible internal quarks q_I . The corresponding mass and field counterterms are

$$\left(\delta Z_m^{(\tilde{g}q)} \right)^2 m_{\tilde{q}_i}^2 = -\frac{g_s^2 C_F}{4\pi^2} \operatorname{Re} \left(p^2 (B_{11} + B_1) + DB_{00} \right) \Big|_{p^2=m_{\tilde{q}_i}^2}, \quad (6.21)$$

$$\delta Z_{ii}^{(\tilde{g}q)} = -\frac{g_s^2 C_F}{8\pi^2} \Delta, \quad \delta Z_{ij}^{(\tilde{g}q)} = 0 \quad (\text{for } i \neq j). \quad (6.22)$$

For the two field counterterms we find the relation $\delta Z_{ii}^{(\tilde{g}q)} = -\delta Z_{ii}^{(g\tilde{q})}$. The two last self-energy contributions in the central row of Fig. 6.2 vanish (see Appendix B). Since the self-energy corrections appear only for virtual squarks, i.e. inside the propagators of the LO Feynman diagrams, they do not lead to any IR divergences.

Gluino self-energy: The remaining self-energy diagrams are those for the gluino shown in the bottom row of Fig. 6.2. Here, we state the solutions in terms of the following decomposition

$$\Sigma = \delta_{ab} (\not{p} \Sigma_V^L + \Sigma_S^L) P_L + (L \leftrightarrow R), \quad (6.23)$$

where, in contrast to the quark self-energy, a and b are color indices of the adjoint representation. Furthermore, we have the additional terms $\Sigma_S^{L,R}$.

Due to the Majorana nature of the gluino, we have to take the first and the second self-energy contribution of the last row in Fig. 6.2 into account. Their sum yields

$$\Sigma_V^{L(\tilde{q}q)} = \frac{g_s^2}{32\pi^2} \sum_{\tilde{q}_i, q_I} (\mathcal{R}'_{Ii} \mathcal{L}_{Ii} + \mathcal{R}_{Ii} \mathcal{L}'_{Ii}) B_1(p^2, m_{q_I}^2, m_{\tilde{q}_i}^2), \quad (6.24)$$

$$\Sigma_V^{R(\tilde{q}q)} = \Sigma_V^{L(\tilde{q}q)}, \quad (6.25)$$

$$\Sigma_S^{L(\tilde{q}q)} = -\frac{g_s^2}{16\pi^2} \sum_{\tilde{q}_i, q_I} m_{q_I} \mathcal{L}'_{Ii} \mathcal{L}_{Ii} B_0(p^2, m_{q_I}^2, m_{\tilde{q}_i}^2), \quad (6.26)$$

$$\Sigma_S^{R(\tilde{q}q)} = \Sigma_S^{L(\tilde{q}q)*}. \quad (6.27)$$

Thereby, we get

$$\delta Z_{\tilde{g}}^{(q\tilde{q})L} = -\frac{g_s^2}{16\pi^2} (n_f + 1) \Delta, \quad \delta Z_{\tilde{g}}^{(q\tilde{q})R} = \delta Z_{\tilde{g}}^{(q\tilde{q})L} \quad (6.28)$$

for the field counterterms and the mass counterterm yields

$$\begin{aligned} \delta Z_m^{(\tilde{q}q)} = & - \sum_{\tilde{q}_I, q_I} \frac{g_s^2}{64\pi^2} \text{Re} \left[B_1 (\mathcal{R}'_{Ii} \mathcal{L}_{Ii} + \mathcal{R}_{Ii} \mathcal{L}'_{Ii} + \mathcal{L}'_{Ii} \mathcal{R}_{Ii} + \mathcal{L}_{Ii} \mathcal{R}'_{Ii}) \right. \\ & \left. - 2B_0 \frac{m_{q_I}}{m_{\tilde{g}}} (\mathcal{L}'_{Ii} \mathcal{L}_{Ii} + \mathcal{R}'_{Ii} \mathcal{R}_{Ii}) \right]_{p^2=m_{\tilde{g}}^2}. \end{aligned} \quad (6.29)$$

Here, $n_f = 5$ and m_{q_I} denotes the quark mass and is only non-zero for the top quark, which can be created in the loop together with a stop, where mixing effects between the left- and right-handed stop will then be taken into account. The last self-energy contribution yields

$$\Sigma_V^{(g\tilde{g})} = -\frac{g_s^2 C_A}{8\pi^2} (\epsilon - 1) B_1(p^2, m_{\tilde{g}}^2, 0), \quad (6.30)$$

$$\Sigma_S^{(g\tilde{g})} = \frac{g_s^2 C_A}{8\pi^2} (2 - \epsilon) m_{\tilde{g}} B_0(p^2, m_{\tilde{g}}^2, 0), \quad (6.31)$$

leading to the following counterterms

$$\delta Z_m^{(g\tilde{g})} = \frac{g_s^2 C_A}{8\pi^2} \text{Re} [(\epsilon - 1) B_1 + (\epsilon - 2) B_0]_{p^2=m_{\tilde{g}}^2}, \quad (6.32)$$

$$\delta Z_{\tilde{g}}^{(g\tilde{g})} = -\frac{g_s^2 C_A}{16\pi^2} \Delta. \quad (6.33)$$

Similar to the quarks, we have to multiply the external gluino field by the square root of the residuum \mathcal{R} according to Eq. (3.42). The residuum of the third contribution (see bottom row of Fig. 6.2) is IR divergent.

Vertex corrections

The coupling counterterms for the vertex corrections depicted in Fig. B.4 are connected via supersymmetric Ward identities to the gaugino and gluino self-energies [135]. As the gaugino is a non-colored particle it does not receive any QCD or SUSY-QCD self-energy corrections at NLO. Hence, the gaugino-quark-squark vertex does not require any further renormalization and only the squark and quark field renormalization counterterms will enter the vertex counterterm. The gluino-quark-squark vertex is connected to the self-energy of the gluino which does receive corrections at NLO and therefore leads to a non-zero coupling counterterm.

We construct the vertex counterterms as discussed in Sec. 3.4.2. Yet, our vertex corrections need further finite counterterms which we address now.

Dimensional reduction and finite shift: Using techniques of dimensional regularization (DREG) for the computations of the vertex corrections followed by the renormalization in the $\overline{\text{MS}}$ -scheme leads to complications in SUSY theories. For $D \neq 4$ dimensions DREG introduces a mismatch between the $(D - 2)$ gluon and two gluino degrees of freedom. Thus,

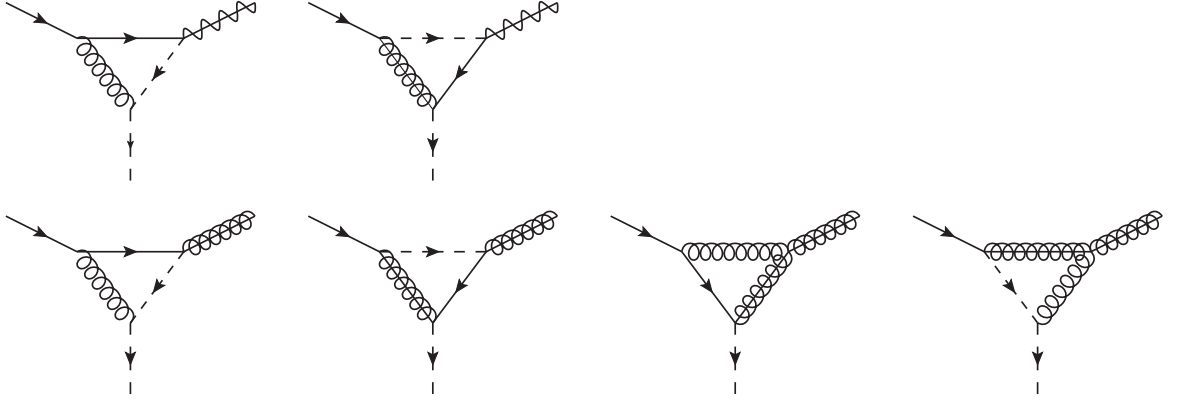


Figure 6.3: Virtual correction diagrams for the gaugino-quark-squark (top row) and gluino-quark-squark vertex (bottom row).

this regularization technique breaks SUSY. One way to overcome this problem is to use the modified dimensional reduction scheme ($\overline{\text{DR}}$). It is closely related to the ordinary dimensional reduction (DRED), where all the four-momenta are defined in D dimensions, but the γ -matrices and gauge fields are kept in four dimensions. It has been shown that also those two schemes are mathematically inconsistent. Especially the combination of the four-dimensional γ -matrices and the ϵ -tensor with the D -dimensional metric tensor $g^{\mu\nu}$ leads to inconsistent results with non-integer values for D . Fortunately, it turned out that by making slight modifications, e.g. by dropping the Fierz identities, DRED and the related $\overline{\text{DR}}$ -schemes can be used in a consistent way [136].

As it is more feasible to use DREG and besides the Catani-Seymour dipoles have been regulated by using DREG, we stick to this regularization technique and convert our result to the $\overline{\text{DR}}$ -scheme. The relevant mismatch is encountered in the two Yukawa-like couplings between a gaugino-squark-quark and a gluino-squark-quark, which we denote by \hat{g} and \hat{g}_s , respectively³. SUSY requires that these couplings are equal to the associated SU(2) and SU(3) gauge couplings up to all orders in perturbation theory, which is not valid in DREG in combination with the $\overline{\text{MS}}$ -scheme. Finite counterterms have to be introduced which remove the non-supersymmetric contributions. They are given by [137, 138]

$$\hat{g}_s = g_s \left[1 + \frac{\alpha_s}{4\pi} \left(\frac{2}{3}C_A - \frac{1}{2}C_F \right) \right] = g_s \left[1 + \frac{\alpha_s}{3\pi} \right], \quad (6.34)$$

$$\hat{g} = g \left[1 - \frac{\alpha_s}{8\pi}C_F \right]. \quad (6.35)$$

Decoupling heavy (s)quarks from the running coupling: The counterterm δg_s can be computed by the transverse part of the gluon self-energy and is also connected via SUSY Ward identities to the gluino self-energy. Hence, in SUSY theories it receives contributions from SM and SUSY particles. However, we use a SM QCD running coupling g_s which has been obtained by including only the contributions of the five light quark flavors and the gluon.

³Note that in Appendix A we do not make these distinctions since the couplings coincide at LO anyway.

To assure that only these particles contribute in our computation and to avoid artificial large logarithms a finite counterterm has to be added. Implementing this subtraction term assures that only the gluon and the five light quarks contribute to the running of α_s [139, 137]. It removes the contributions arising from the heavy colored particles, namely the squarks, gluino and top quark, and can be written as

$$\delta g_s^{(\text{heavy})} = \frac{\alpha_s}{8\pi} \left[-2 \ln \frac{m_{\tilde{g}}^2}{\mu_R^2} - \frac{3}{2} \ln \frac{m_t^2}{\mu_R^2} - \sum_{i=1}^{12} \frac{1}{6} \ln \frac{m_{\tilde{q}_i}^2}{\mu_R^2} \right], \quad (6.36)$$

where μ_R is the renormalization scale and m_t , $m_{\tilde{g}}$ and $m_{\tilde{q}_i}$ are the masses of the top quark, gluino and squarks, respectively [137].

Box diagrams

The last remaining virtual contributions are the box diagrams depicted in Fig. 6.4. Analytical expressions can be found in Ref. [130]. These diagrams do not exhibit any UV divergence and hence no counterterm is needed. However, the first and the last diagram suffer from IR divergences, which cancel by the inclusion of the insertion operator \mathbf{I} .

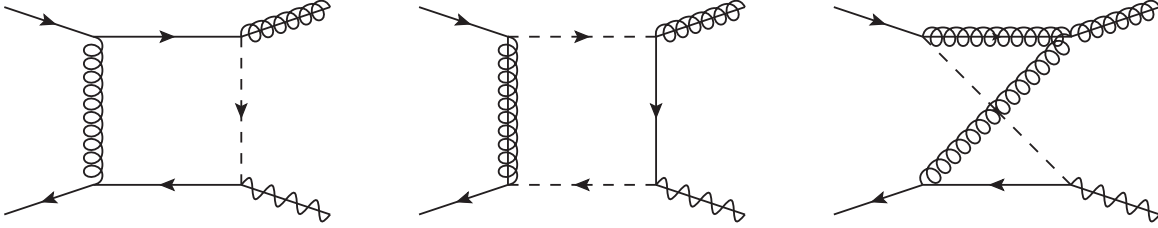


Figure 6.4: Box diagrams for the t-channel. Diagrams for the u-channel are similar and can be obtained by crossing the external quark legs.

6.2.2 Real corrections

Next, we have to include the real corrections in order to obtain the full inclusive NLO cross section. Similar to the real emission diagrams for sleptons, we split the contributions in real gluon, quark and antiquark emission. For the partonic cross section we can then apply Eq. (5.9).

A selection of Feynman diagrams for real gluon emission is depicted in Fig. 6.5. The diagrams in the first row suffer from soft, collinear and soft-collinear divergences. For the emission of the gluon by the final state gluino (second diagram of the last row) we encounter only soft divergences, because the collinear divergence is screened by the mass of the emitter. No divergence occurs if the gluon is emitted by an internal virtual particle (first diagram in second row). All divergences cancel by subtracting the corresponding Catani-Seymour dipoles [35].

We illustrate the cancellation of these divergences in Fig. 6.6, where we show a transverse momentum distribution for the process $pp \rightarrow \tilde{g}\tilde{\chi}_2^0$ at a center-of-mass energy of 13 TeV using CT10NLO as the PDF and the SUSY benchmark scenario BP II (see Sec. 6.4.1).

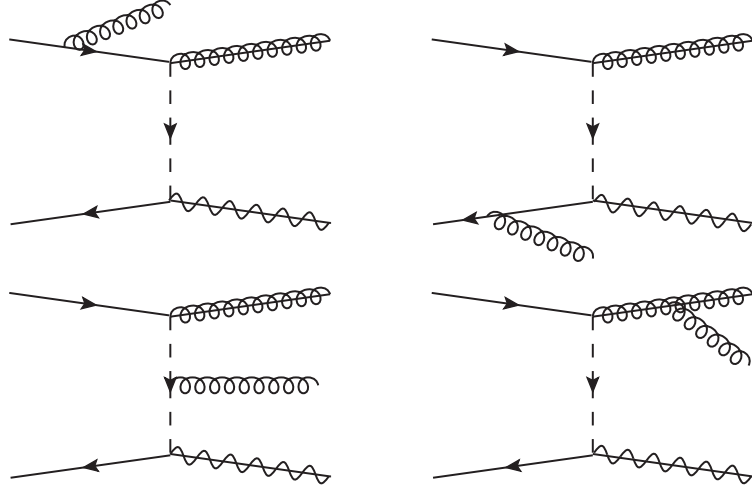


Figure 6.5: Selection of Feynman diagrams showing real corrections to the associated gaugino-gluino production with an additional gluon in the final state.

Here, p_T denotes the transverse momentum of the emitted gluon. Additionally, we show the corresponding dipole term. First, we observe an increase of the cross section for decreasing p_T which indicates the divergence for $p_T \rightarrow 0$. Furthermore, the corresponding dipole reproduces the cross section of the real gluon emission over the here shown p_T -range with a maximal deviation of 1% at a transverse momentum of 50 GeV. In particular in the collinear region ($p_T \rightarrow 0$), the ratio of the dipole to the real gluon emission cross section approaches one. Hence, by subtracting this dipole from the total cross section of the real gluon emission, we achieve a cancellation of the IR divergences.

The IR divergences of the real quark and antiquark emission cancel in the same manner. Sample diagrams for the real quark emission are shown in Fig. 6.7, where diagram a) suffers from IR divergences and the diagrams b), c) and d) are IR finite. Still, the gluon initiated channels c) and d) give rise to another kind of divergence. If $m_{\tilde{q}} \geq m_{\tilde{\chi}} + m_q$ and $s \geq (m_{\tilde{q}} + m_{\tilde{g}})^2$ the squark in diagram d) can be on shell leading to a resonance in the squark propagator. Similar for diagram c), where $m_{\tilde{q}} \geq m_{\tilde{g}} + m_q$ and $s \geq (m_{\tilde{q}} + m_{\tilde{\chi}})^2$ has to be fulfilled in order to possibly produce the intermediate squark on shell. These divergences can be regularized by introducing a finite width $\Gamma_{\tilde{q}}$ in the squark propagator. For this reason, we replace

$$\frac{1}{s_{\tilde{\chi}q} - m_{\tilde{q}}^2} \rightarrow \frac{1}{s_{\tilde{\chi}q} - m_{\tilde{q}}^2 + im_{\tilde{q}}\Gamma_{\tilde{q}}} \quad (6.37)$$

in the matrix element of diagram d), where $s_{\tilde{\chi}q} = (p_{\tilde{\chi}} + p_q)^2$ and proceed analogously for diagram c) with the replacement $s_{\tilde{\chi}q} \rightarrow s_{\tilde{g}q}$.

Considering all SUSY production processes, the resonance of the diagrams c) and d) correspond to the LO cross section for squark-gaugino or squark-gluino production with a subsequent decay of the squark to a gluino and quark or to a gaugino and quark, respectively. As a result, these resonant contributions have to be subtracted in order to avoid double counting. To achieve the subtraction in a consistent way, we follow a similar approach as

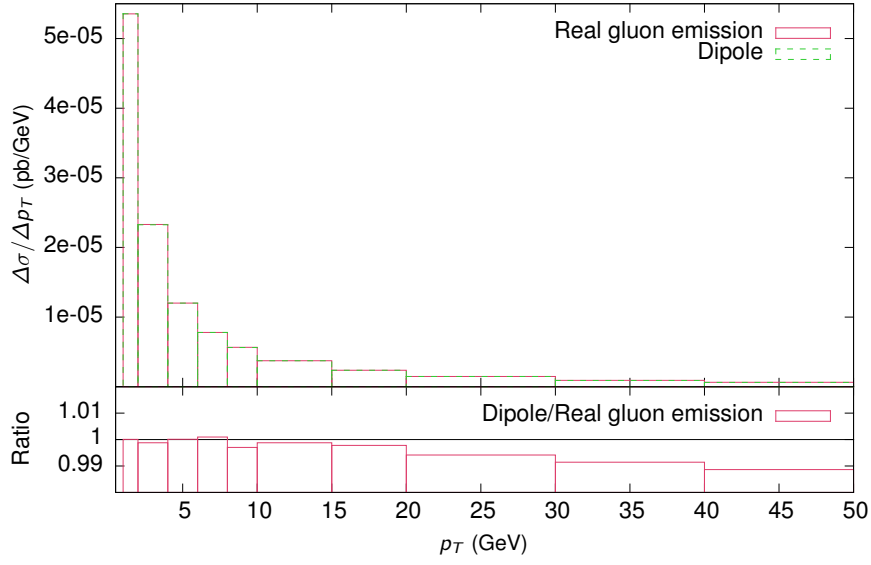


Figure 6.6: Transverse momentum distribution for real corrections to the associated gaugino-gluino production with an additional gluon in the final state and for the corresponding Catani-Seymour dipole term.

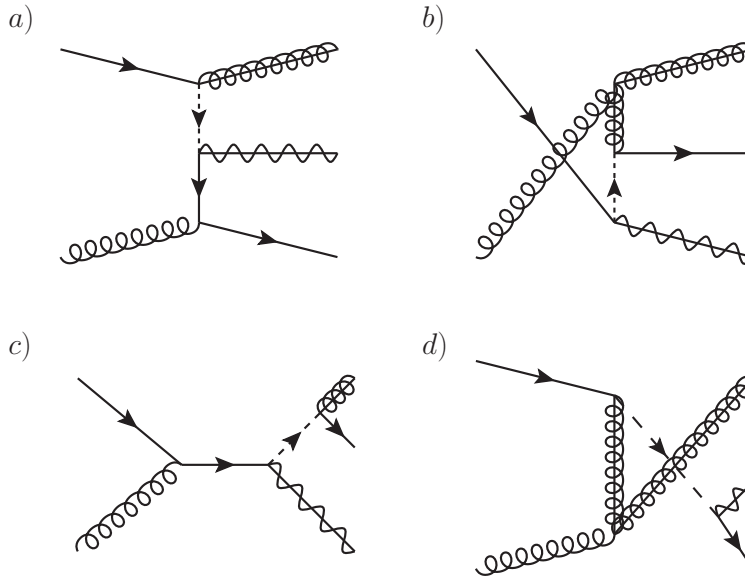


Figure 6.7: Selection of Feynman diagrams showing real corrections to the associated gaugino-gluino production with an additional quark in the final state.

presented in Ref. [139] which is called diagram subtraction (DS). First, we split the squared matrix elements in regular, resonant and interference terms:

$$|\mathcal{M}_{\text{quark}}|^2 = |\mathcal{M}_{\text{nonres}}|^2 + |\mathcal{M}_{\text{res},1}|^2 + |\mathcal{M}_{\text{res},2}|^2 + 2 \operatorname{Re} \left(\mathcal{M}_{\text{res},1} \mathcal{M}_{\text{res},2}^* \right) \\ + 2 \operatorname{Re} \left(\mathcal{M}_{\text{nonres}} \mathcal{M}_{\text{res},1}^* \right) + 2 \operatorname{Re} \left(\mathcal{M}_{\text{nonres}} \mathcal{M}_{\text{res},2}^* \right). \quad (6.38)$$

Here, $\mathcal{M}_{\text{nonres}}$ refers to the diagrams a) and b), whereas $\mathcal{M}_{\text{res},1}$ and $\mathcal{M}_{\text{res},2}$ represent the diagrams of type c) and d). The subscript 1 and 2 distinguishes between the two different resonant regions, i.e. $s_{\tilde{\chi}q} \rightarrow m_{\tilde{q}}^2$ and $s_{\tilde{g}q} \rightarrow m_{\tilde{q}}^2$. The inclusion of the squark width is only used for the resonant propagators in order not to spoil the cancellation of the IR divergences. Similar to the Catani-Seymour dipoles, a local counterterm

$$d\sigma^{\text{OS}} = \Theta(\sqrt{s} - m_{\tilde{q}} - m_{\tilde{g}}) \Theta(m_{\tilde{q}} - m_{\tilde{\chi}}) \frac{m_{\tilde{q}}^2 \Gamma_{\tilde{q}}^2}{(s_{\tilde{\chi}q} - m_{\tilde{q}}^2)^2 + m_{\tilde{q}}^2 \Gamma_{\tilde{q}}^2} |\hat{\mathcal{M}}_{\text{res}}|^2 d\hat{\text{PS}}^{(3)} \quad (6.39)$$

can be constructed, where for the sake of convenience we only focus on one resonant region. Here, $\hat{\mathcal{M}}_{\text{res}}$ denotes the squared resonant matrix element with reshuffled momenta. The reshuffling sets the intermediate squark on shell. Furthermore, momentum conservation should be preserved and the reshuffling should be an identity transformation for $s_{\tilde{\chi}q} = m_{\tilde{q}}^2$. The phase space $d\hat{\text{PS}}^{(3)}$ is the restricted on shell phase space. If all integrations have been mapped to the interval $[0,1]$ it can be computed by

$$d\hat{\text{PS}}^{(3)} = \frac{\hat{\mathcal{J}}}{\mathcal{J}} d\text{PS}^{(3)}, \quad (6.40)$$

where $\hat{\mathcal{J}}$ and \mathcal{J} denote the Jacobians of the restricted and complete three-particle phase space, respectively. Note that this approach is only gauge invariant in the limit for $\Gamma_{\tilde{q}} \rightarrow 0$ for which the local counterterm in Eq. (6.39) will turn into

$$\lim_{\Gamma_{\tilde{q}} \rightarrow 0} d\sigma^{\text{OS}} = d\sigma_{\tilde{q}\tilde{g}} BR(\tilde{q} \rightarrow q\tilde{\chi}). \quad (6.41)$$

Nonetheless, the width should not be too small in order to avoid numerical instabilities, especially for the interference of the IR divergent and resonant diagrams and for the interference diagrams of the two different resonant regions. Therefore, we choose a value of $\Gamma_{\tilde{q}} = 10^{-3} m_{\tilde{q}}$. It could also be set to the physical width of the squarks, but here it acts solely as a mathematical regulator of the divergence. We call the remnant of the on shell contributions the on shell remainder. We remark that the same treatment has to be performed for the real emission of antiquarks.

Finally, we can apply Eq. (3.26) together with the on shell subtraction counterterms and convolute the results with the PDFs to obtain the finite NLO corrections to the hadronic cross section.

6.3 Soft gluon resummation

So far, Eq. (4.66) cannot be employed for the associated gaugino-gluino production. First, we have to compute the missing process dependent ingredients. For this reason, we dedicate this section to the modified soft anomalous dimension and the hard matching coefficient.

6.3.1 Soft anomalous dimension for gaugino-gluino production

In order to achieve the NLL accuracy for the associated production we have to compute the diagonal modified soft anomalous dimension ($\bar{\Gamma}_{ab \rightarrow ij, I}$) (see Eq. (4.80)). The result for the Drell-Yan part is given in Eq. (4.79). In Fig. 6.8 we show the one-loop corrections from which the soft anomalous dimension can be extracted by rewriting the definition in Eq. (4.78) as

$$\bar{\Gamma}_{ab \rightarrow ij, I} = - \sum_{kl} C^{kl} \lim_{\epsilon \rightarrow 0} \epsilon \omega^{kl}, \quad (6.42)$$

where k and l denote eikonal lines, between which the virtual gluon is exchanged, C_{IJ}^{kl} are color mixing factors and ω^{kl} denotes the kinematical parts of the virtual corrections. These Feynman diagrams are in general computed in an irreducible s-channel color basis with tensors c_J (see e.g. Refs. [72, 83, 69, 70]). For only one colored final state particle there is only one tensor $c_J = \text{Tr}(T^i T^{i'}) = T_F \delta_{ii'}$, where i and i' are adjoint color indices of the gluino and $T_F = 1/2$. Hence, we drop the associated index. In the eikonal approximation the LO contribution factorizes (see Sec. 4.2.1) and the color mixing factors C^{kl} are thus defined as the color factors of the loop diagrams divided by the LO color factor $\text{Tr}(T^i T^i) = T_F \delta_{ii} = C_A C_F$. Here, the needed color factors are given by

$$\begin{aligned} C^{ab} &= \frac{\text{Tr}(T^i T^j T^i T^j)}{\text{Tr}(T^i T^i)} = C_F - \frac{C_A}{2}, & C^{a1} &= \frac{\text{Tr}(T^i T^{i'} T^j) f^{ii'j}(-i)}{\text{Tr}(T^i T^i)} = \frac{C_A}{2}, \\ C^{b1} &= \frac{\text{Tr}(T^i T^j T^{i'}) f^{ii'j}(-i)}{\text{Tr}(T^i T^i)} = -\frac{C_A}{2}, & C^{11} &= \frac{\text{Tr}(T^i T^{i'}) f^{ii''j} f^{i''i'j}(-i)^2}{\text{Tr}(T^i T^i)} = C_A, \end{aligned} \quad (6.43)$$

where we have used the color operators stated in Tab. 4.1 for the eikonal vertices. The kinematical parts of the loop corrections, the so called eikonal integrals, can be written in a general way as

$$\begin{aligned} \omega^{kl} = g_s^2 \int \frac{d^D q}{(2\pi)^D} \frac{-i}{q^2 + i\epsilon} &\left[\frac{\Delta_k \Delta_l v_k \cdot v_l}{(\delta_k v_k \cdot q + i\epsilon)(\delta_l v_l \cdot q + i\epsilon)} \right. \\ &\left. - \frac{\Delta_k v_k \cdot n}{(\delta_k v_k \cdot q + i\epsilon)} \frac{P}{(n \cdot q)} - \frac{\Delta_l v_l \cdot n}{(\delta_l v_l \cdot q + i\epsilon)} \frac{P}{(n \cdot q)} + n^2 \frac{P}{(n \cdot q)^2} \right], \end{aligned} \quad (6.44)$$

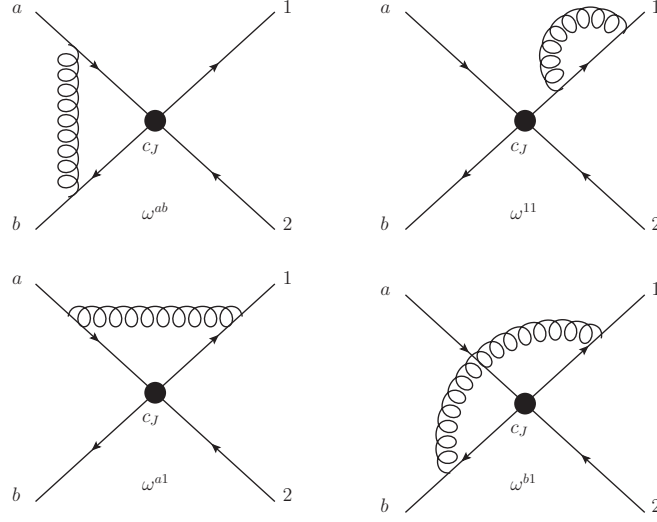


Figure 6.8: Generic diagrams for the virtual corrections including a gluon exchange. The final state particles (1,2) are considered as massive and the initial state particles (a,b) as massless and therefore their gluon self-exchange diagrams (quark self-energy) vanish (due to the scalar product $v \cdot v = 0$ for massless particles in the integrand which is therefore zero). The arrows on the lines represent the chosen fermion flow.

where q is the loop momentum, $v_i^\mu = p_i^\mu \sqrt{2/s}$ is the rescaled momentum of particle i , $\Delta_{k,l}$ and $\delta_{k,l}$ are signs associated with the eikonal Feynman rules (see Tab. 4.1) and P stands for the principal value [78, 79]:

$$\frac{P}{(n \cdot q)^\beta} = \frac{1}{2} \left(\frac{1}{(n \cdot q + i\epsilon)^\beta} + (-1)^\beta \frac{1}{(-n \cdot q + i\epsilon)^\beta} \right). \quad (6.45)$$

The integrals can be solved [78, 72] (also for two colored final state particles with unequal masses [79]) leading to

$$\omega^{ab} = S_{ab} \frac{\alpha_s}{\pi\epsilon} \left[-\ln \left(\frac{v_a \cdot v_b}{2} \right) + \frac{1}{2} \ln \left(\frac{(v_a \cdot n)^2 (v_b \cdot n)^2}{|n|^2 |n|^2} \right) + i\pi - 1 \right], \quad (6.46)$$

$$\omega^{a1} = S_{a1} \frac{\alpha_s}{\pi\epsilon} \left[-\frac{1}{2} \ln \left(\frac{(v_a \cdot v_1)^2 s}{2m_g^2} \right) + L_1 + \frac{1}{2} \ln \left(\frac{(v_a \cdot n)^2}{|n|^2} \right) - 1 \right], \quad (6.47)$$

$$\omega^{b1} = S_{b1} \frac{\alpha_s}{\pi\epsilon} \left[-\frac{1}{2} \ln \left(\frac{(v_b \cdot v_1)^2 s}{2m_g^2} \right) + L_1 + \frac{1}{2} \ln \left(\frac{(v_b \cdot n)^2}{|n|^2} \right) - 1 \right], \quad (6.48)$$

$$\omega^{11} = S_{11} \frac{\alpha_s}{\pi\epsilon} [2L_1 - 2]. \quad (6.49)$$

Here, the signs have been combined to $S_{kl} = \Delta_k \Delta_l \delta_k \delta_l$, so that $S_{ab} = 1$, $S_{a1} = 1$, $S_{b1} = -1$, and $S_{11} = -1$. The double poles in ϵ in the first three integrals involving at least one massless particle have canceled among themselves. As one can easily see, the scalar products are

$$v_a \cdot v_b = \frac{2p_a \cdot p_b}{s} = 1, \quad (6.50)$$

$$v_a \cdot v_1 = \frac{2p_a \cdot p_1}{s} = \frac{m_{\tilde{g}}^2 - t}{s}, \quad (6.51)$$

$$v_b \cdot v_1 = \frac{2p_b \cdot p_1}{s} = \frac{m_{\tilde{g}}^2 - u}{s}. \quad (6.52)$$

The function $L_k = [L_k(+n) + L_k(-n)]/2$ depends in a rather complicated way on the gauge vector n [78, 72]. However, all gauge-dependent terms disappear after the inclusion of the self-energies of the two incoming Wilson lines. Combining color factors, signs and soft integrals and simplifying the result leads to

$$\begin{aligned} \bar{\Gamma}_{q\bar{q} \rightarrow \tilde{g}\tilde{\chi}} &= \frac{\alpha_s}{2\pi} C_A \left[\ln 2 + i\pi - 1 + \ln \left(\frac{m_{\tilde{g}}^2 - t}{\sqrt{2}m_{\tilde{g}}\sqrt{s}} \right) + \ln \left(\frac{m_{\tilde{g}}^2 - u}{\sqrt{2}m_{\tilde{g}}\sqrt{s}} \right) \right] \\ &= \frac{\alpha_s}{2\pi} C_A (T_{a1} + T_{b1}), \end{aligned} \quad (6.53)$$

with

$$T_{a1} = \ln \left(\frac{m_{\tilde{g}}^2 - t}{m_{\tilde{g}}\sqrt{s}} \right) + \frac{i\pi - 1}{2}, \quad T_{b1} = \ln \left(\frac{m_{\tilde{g}}^2 - u}{m_{\tilde{g}}\sqrt{s}} \right) + \frac{i\pi - 1}{2}. \quad (6.54)$$

Due to the LSZ reduction formula, only half of the self-energy contribution ω^{11} has been taken into account. All terms proportional to C_F have vanished, so that only terms proportional to C_A remain. In the massless limit and before subtracting the initial state self-energies, one recovers the well-known result for associated gluon-photon production, i.e. the C_A -term in Eq. (2.26) of Ref. [80]. Our modified soft anomalous dimension can also be compared to the one obtained for associated top quark and W boson production in Eq. (3.8) of Ref. [140] after adjustments of the color factors.

The final result for the one-loop coefficient, which governs the soft wide-angle gluon emission for the associated gaugino-gluino production, is therefore

$$D_{q\bar{q} \rightarrow \tilde{g}\tilde{\chi}} = \text{Re} [C_A (T_{a1} + T_{b1})]. \quad (6.55)$$

At the production threshold, where the final state particle velocities vanish and

$$\beta = \sqrt{1 - \frac{(m_{\tilde{g}} + m_{\tilde{\chi}})^2}{s}} \rightarrow 0, \quad (6.56)$$

we find $D_{q\bar{q} \rightarrow \tilde{g}\tilde{\chi}} = -C_A$, in accordance with Ref. [79].

6.3.2 The hard matching coefficient for gaugino-gluino production

In Sec. 4.6 we discussed that the resummation of logarithmically enhanced contributions at threshold can be improved by including in the hard function $\mathcal{H}_{ab \rightarrow ij, I}(M^2, \mu^2)$ in Eq. (4.66) not only the Mellin transform of the LO cross section

$$\mathcal{H}_{ab \rightarrow ij}^{(0)}(M^2, \mu^2) = \tilde{\sigma}_{ab \rightarrow ij}^{(0)}(M^2), \quad (6.57)$$

but also the N -independent contributions of the NLO cross section

$$\mathcal{H}_{ab \rightarrow ij}^{(1)}(M^2, \mu^2) = \tilde{\sigma}_{ab \rightarrow ij}^{(0)}(M^2) \mathcal{C}_{ab \rightarrow ij}^{(1)}(M^2, \mu^2), \quad (6.58)$$

which beyond NLO are multiplied by threshold logarithms. Just as a reminder, the hard matching coefficient function $\mathcal{C}_{ab \rightarrow ij}^{(1)}(M^2, \mu^2)$ is obtained by computing the Mellin transform of the full NLO corrections $\tilde{\sigma}_{ab \rightarrow ij}^{(1)}(M^2, \mu^2)$ and dividing it by the LO contribution $\tilde{\sigma}_{ab \rightarrow ij}^{(0)}(M^2)$. As shown in Sec. 4.6, the Mellin transform of the virtual correction and the insertion operator \mathbf{I} are straightforward, since they are proportional to $\delta(1-z)$ and thus constant in N . The corresponding analytical results can be found in Refs. [130] and [35], respectively. The remaining ingredients are the Mellin transforms of the \mathbf{P} and \mathbf{K} operators. We recall that they belong to the so called collinear remainder, which can be written as

$$\sigma_{ab}^C = \sum_{a'} \int_0^1 dz \int_2 \left[d\sigma_{a'b}^{(0)}(zp_a, p_b) \otimes \langle a' | \mathbf{P} + \mathbf{K} | a \rangle(z) + (a \leftrightarrow b) \right]_{\epsilon=0}, \quad (6.59)$$

with a , a' and b denoting different parton types. For the initial quark a , after evaluating the color factors and transforming to Mellin space we obtain

$$\langle \mathbf{P}(N) \rangle = \frac{\alpha_s}{2\pi} \left[(2C_F - C_A) \ln \frac{\mu_F^2}{M^2} + C_A \ln \frac{\mu_F^2}{m_g^2 - t} \right] \left[\ln \bar{N} - \frac{3}{4} \right] + \mathcal{O}\left(\frac{1}{N}\right) \quad (6.60)$$

and

$$\begin{aligned} \langle \mathbf{K}(N) \rangle = & \frac{\alpha_s}{2\pi} \left\{ 2C_F \ln^2 \bar{N} + C_A \left[\ln \frac{m_g^2}{m_g^2 - t} + 1 \right] \ln \bar{N} + \frac{\pi^2}{2} C_F - \gamma_q - K_q \right. \\ & + \frac{C_A}{4} \left[1 + 4 \text{Li}_2 \frac{2m_g^2 - t}{m_g^2} + \left(1 + 4 \ln \frac{m_g^2}{m_g^2 - t} + 2 \frac{m_g^2}{m_g^2 - t} \right) \ln \frac{m_g^2}{2m_g^2 - t} \right. \\ & \left. \left. + 3 \ln \left(1 + \frac{2m_g}{m_g^2 - t} (m_g - \sqrt{2m_g^2 - t}) \right) + 6 \frac{m_g}{m_g + \sqrt{2m_g^2 - t}} - 3 \right] \right\} + \mathcal{O}\left(\frac{1}{N}\right), \end{aligned} \quad (6.61)$$

with

$$\gamma_q = \frac{3}{2} C_F, \quad K_q = \left(\frac{7}{2} - \frac{\pi^2}{6} \right) C_F \quad (6.62)$$

and similarly for the incoming antiquark b with $t \rightarrow u$. Non-diagonal operators give only $1/N$ -suppressed contributions, and there are no initial state gluons at LO. In the limit of $C_A \rightarrow 0$, one recovers the well-known results for Drell-Yan like processes [141].

For the hard matching coefficient, only the N -independent parts of the above results are needed. Still, we can use the N -dependent terms to check the resummed cross section when expanded to NLO. As the potentially large logarithms in the exponent of the resummation formula in Eq. (4.66) emerge from the soft and soft-collinear regions, we can compare the threshold enhanced terms of the Mellin transform of the insertion operators \mathbf{P} and \mathbf{K} with the expansion of the resummation result up to $\mathcal{O}(\alpha_s)$, which gives

$$\begin{aligned} \sigma_{ab}^{(\text{exp.})} &= \mathcal{H}_{ab \rightarrow ij}^{(0)}(M^2, \mu^2) + \frac{\alpha_s}{2\pi} \mathcal{H}_{ab \rightarrow ij}^{(1)}(M^2, \mu^2) + \frac{\alpha_s}{2\pi} \mathcal{H}_{ab \rightarrow ij}^{(0)}(M^2, \mu^2) \\ &\times \left[(A_a^{(1)} + A_b^{(1)}) \ln^2 \bar{N} + \left((A_a^{(1)} + A_b^{(1)}) \ln \frac{\mu_F^2}{s} - 2D_{ab \rightarrow ij}^{(1)} \right) \ln \bar{N} \right], \end{aligned} \quad (6.63)$$

where $\mathcal{H}_{ab \rightarrow ij}^{(0)}$ and $\mathcal{H}_{ab \rightarrow ij}^{(1)}$ are the first and second order parts of the hard function, respectively. Inserting $A_a^{(1)} = A_b^{(1)} = 2C_F$ (cf. Eq. (4.73)), the leading logarithms $\alpha_s/(2\pi) \ln^2 \bar{N}$ have the coefficient $4C_F$. This agrees with the leading logarithmic contribution to the hard matching coefficient arising exclusively from the \mathbf{K} -operators in the collinear remainder in Eq. (6.61). The coefficient $4C_F$ also governs the scale- and more precisely the $\ln(\mu_F^2/s)$ -dependent part of the next-to-leading logarithms $\alpha_s/(2\pi) \ln \bar{N}$, which agrees with the corresponding parts of the quark and antiquark \mathbf{P} -operator expectation values in the collinear remainder in Eq. (6.60). As expected, the C_A -terms depending on μ_F cancel since they are proportional to soft wide-angle contributions and hence no factorization scale-dependent term should be left over. The remaining NLL terms are

$$C_A \left[\ln \frac{s}{m_g^2 - t} + \ln \frac{s}{m_g^2 - u} \right]. \quad (6.64)$$

From the \mathbf{K} -operators in Eq. (6.61), we get in addition the NLL contributions

$$C_A \left[\ln \frac{m_g^2}{m_g^2 - t} + \ln \frac{m_g^2}{m_g^2 - u} + 2 \right], \quad (6.65)$$

which together correctly reproduce the contribution from the soft anomalous dimension in Eq. (6.55) and Eq. (6.63).

6.4 Numerical results

In this section we present the numerical results for the associated gaugino-gluino production at a center-of-mass energy of $\sqrt{S} = 13$ TeV. All matrix elements have been computed by employing a self-written FORM [100] script. For the numerical calculations we use the following setup (if not mentioned otherwise): the SM parameters are set to the values of the Particle Data Group (PDG) [142]. The running of the strong coupling is provided by the

PDF data sets. As our central PDF for the LO calculations we use CTEQ6L1 [96] which uses one-loop approximations for α_s and for the DGLAP evolution equations. For NLO and NLL+NLO predictions we use CT10NLO [97] which uses two-loop approximations. To be consistent with the PDFs, we take all light quarks including the bottom quark as massless. The top quark is decoupled. Its (pole) mass enters only in the gluino self-energy and has little numerical influence on the production cross sections. Moreover, the CKM matrix, which enters in the production cross section of charginos, is assumed to be diagonal. As our central values for the factorization and renormalization scale we use the average mass of the two final state particles, i.e. $\mu = (m_{\tilde{g}} + m_{\tilde{\chi}})/2$. The remaining parameters of the SUSY sector are fixed by the SUSY benchmark scenario which we address in the following section.

6.4.1 SUSY benchmark scenario

Our chosen benchmark scenario is inspired by the benchmark point II (BP II) of Ref. [143], that has been obtained with a Markov Chain Monte Carlo (MCMC) scan using also PDG values for the Standard Model parameters. Originally, this scan included 19 parameters with a focus on non-minimal flavor violation (NMFV) which has been described by flavor violation parameters. They checked in particular the most stringent flavour-changing neutral current (FCNC) constraints from rare B - and K -decays. As we are not interested in NMFV, we set these parameters all to zero. Moreover, we have changed the sign and increased the absolute value of the trilinear coupling A_f to obtain a Higgs boson mass compatible with the measured value. For the bino and wino mass parameters we impose the GUT relation $M_1 \simeq M_2/2$, whereas we allow the gluino mass parameter M_3 to vary independently. This brings us to $19 - 7 + 1 = 13$ free parameters listed in Tab. 6.1. Still, our default scenario imposes the GUT relation for $M_3 \simeq 6M_1$.

Table 6.1: Higgs sector and soft SUSY breaking parameters in our pMSSM-13 benchmark model. All values except the one for $\tan\beta$ are in GeV.

$\tan\beta$	μ	m_A	M_1	M_3	$M_{Q_{1,2}}$	M_{Q_3}	$M_{U_{1,2}}$	M_{U_3}	$M_{D_{12}}$	M_{D_3}	M_L	A_f
21	773	1300	315	1892	2288	425	1758	2754	552	714	1553	-2200

The SUSY mass spectrum is then obtained by employing SPHENO 3.37 [144] and is schematically shown in Fig. 6.9. The exact mass values are listed in Tab. 6.2. In our scenario the neutralino $\tilde{\chi}_1^0$ with a mass of 314 GeV is the LSP. Together with a light top squark this benchmark leads to a viable dark matter candidate and allows in general for sufficient stop coannihilation to reproduce the observed dark matter relic density [145, 146, 147, 148]. Moreover, this scenario reproduces the observed value of the anomalous magnetic moment of the muon, which is unaffected by the gluino mass. In addition, it satisfies the increasingly stringent constraints that are imposed on the masses of the SUSY particles from direct search results at the LHC. For example, with the 2015 data from Run II, ATLAS and CMS exclude gluino masses up to 1400 and 1280 GeV, assuming masses of the lightest neutralino of up to 600 and 800 GeV, respectively [149, 150]. Mass-degenerate light charginos and second-lightest neutralinos produced electroweakly have been excluded at Run I up to 465 and 720 GeV in the case of massless lightest neutralinos [123, 151]. These exclusion limits are, however, not

valid within the general pMSSM, as they have been obtained assuming direct production cross sections and simplified decay scenarios.

The SUSY parameters at the electroweak scale which affect the cross section for the associated gaugino-gluino production are the masses of the gauginos and the gluino, the neutralino and chargino mixing matrices, the squark masses and the squark mixing matrices⁴. In Eqs. (6.66) and (6.67) we show the neutralino and chargino mixing matrices. From these we can deduce the following compositions of the neutralinos and charginos: $\tilde{\chi}_1^0$ is mainly the bino, $\tilde{\chi}_2^0$ is wino-like and $\tilde{\chi}_3^0$ and $\tilde{\chi}_4^0$ consist mostly of higgsino components. $\tilde{\chi}_1^\pm$ and $\tilde{\chi}_2^\pm$ are mainly made of wino and charged higgsino components, respectively.

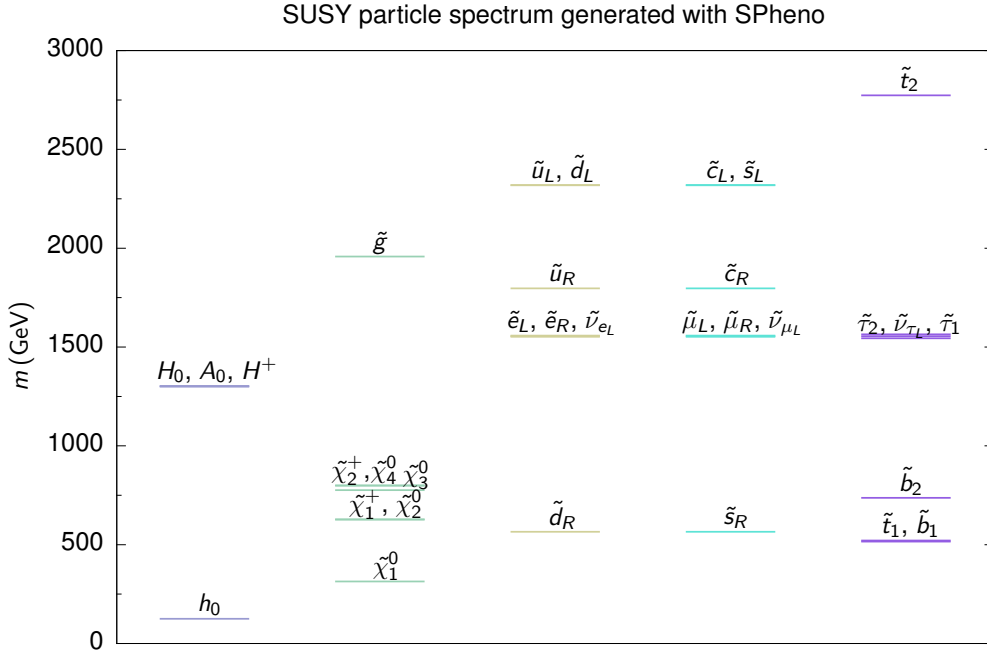


Figure 6.9: Visualised mass spectrum for the benchmark point defined in Tab. 6.1. Particles are grouped in Higgs particles, gauginos, first-, second- and third-generation sfermions (left to right).

$$N = \begin{pmatrix} -0.9972 & 0.0083 & -0.0681 & 0.0306 \\ -0.0343 & -0.9292 & 0.2841 & -0.2337 \\ -0.0261 & 0.0384 & 0.7048 & 0.7079 \\ -0.0615 & 0.3674 & 0.6465 & -0.6658 \end{pmatrix}, \quad (6.66)$$

$$V = \begin{pmatrix} -0.9394 & 0.3427 \\ 0.3427 & 0.9394 \end{pmatrix}, \quad U = \begin{pmatrix} -0.9099 & 0.4147 \\ 0.4147 & 0.9099 \end{pmatrix}. \quad (6.67)$$

We remark that the squark masses span a wide range from about 500 GeV for the light

⁴The stop contribution is actually negligible, since the stop takes only part in the gluino self-energy correction.

Table 6.2: SUSY mass spectrum for the benchmark point defined in Tab. 6.1.

Particle	m (GeV)	Particle	m (GeV)	Particle	m (GeV)
\tilde{e}_L	1558	\tilde{u}_L	2318	\tilde{g}	1958
\tilde{e}_R	1552	\tilde{u}_R	1797	$\tilde{\chi}_1^0$	314
$\tilde{\nu}_{\tilde{e}_L}$	1555	\tilde{d}_L	2319	$\tilde{\chi}_2^0$	627
$\tilde{\mu}_L$	1558	\tilde{d}_R	565	$\tilde{\chi}_3^0$	776
$\tilde{\mu}_R$	1552	\tilde{c}_L	2318	$\tilde{\chi}_4^0$	799
$\tilde{\nu}_{\tilde{\mu}_L}$	1555	\tilde{c}_R	1797	$\tilde{\chi}_1^+$	628
$\tilde{\tau}_1$	1544	\tilde{s}_L	2319	$\tilde{\chi}_2^+$	800
$\tilde{\tau}_2$	1564	\tilde{s}_R	565	h_0	125
$\tilde{\nu}_{\tilde{\tau}_L}$	1555	\tilde{b}_L	515	H_0	1300
		\tilde{b}_R	736	A_0	1300
		\tilde{t}_1	521	H^+	1303
		\tilde{t}_2	2774		

squarks to 2.8 TeV for the heavier ones. By neglecting the sbottoms and stops we obtain the averaged squark mass $\bar{m}_{\tilde{q}} = 1.75$ TeV.

6.4.2 Fixed order comparison

For the validation of the fixed order computation we compare our results with those obtained by employing the public code PROSPINO2.1 [152, 98, 99]. We compute the cross sections for all the different gaugino-gluino final states at 13 TeV using CTEQ6L1 [96] and CTEQ66 [153] for the LO and NLO PDFs, since these two are the default PDFs implemented in the public version of PROSPINO2.1. For the SUSY spectrum we use BP II with averaged squark masses $\bar{m}_{\tilde{q}} = 1.75$ TeV. This is due to the reason that PROSPINO2.1 only allows for NLO results with degenerate squark masses. Still, the code is able to compute approximate NLO results for a non-degenerate mass spectrum. Therefore, the LO cross section is computed by using free⁵ squark masses and then scaled by the NLO/LO K -factor obtained by using degenerate squark masses.

Results for the mass-degenerate squarks are presented in Tab. 6.3. Additionally, we show scale uncertainties which have been calculated by varying the central values simultaneously by a factor of two. First, we observe that for the LO cross section the discrepancy is below 1%. As expected, the results for the scale variation agree, since at LO the scale dependence is completely driven by the PDFs and the strong coupling. At NLO the difference is a bit larger, but still around the one percent level. By setting the gluon PDFs to zero we found

⁵Here, free means non-averaged squark masses.

Table 6.3: Total cross sections for $pp \rightarrow \tilde{g} \tilde{\chi}_j^{0,\pm}$ at $\sqrt{S} = 13$ TeV using CTEQ6L1 [96] and CTEQ66 [153] as LO and NLO PDFs, respectively, and BP II (see Sec. 6.4.1) with averaged squark masses for the SUSY spectrum. We show a comparison between PROSPINO2.1 and RESUMMINO.

Gaugino	LO ^{+scale} _{-scale} (10^{-1} fb)		NLO ^{+scale} _{-scale} (10^{-1} fb)	
	Resummino	Prospino	Resummino	Prospino
$\tilde{\chi}_1^0$	$1.4703^{+0.327}_{-0.251}$	$1.4681^{+0.327}_{-0.251}$	$1.4560^{+0.025}_{-0.065}$	$1.4741^{+0.030}_{-0.071}$
$\tilde{\chi}_2^0$	$1.2336^{+0.289}_{-0.220}$	$1.2316^{+0.288}_{-0.219}$	$1.2548^{+0.041}_{-0.073}$	$1.2642^{+0.045}_{-0.075}$
$\tilde{\chi}_3^0$	$0.0089^{+0.0020}_{-0.0015}$	$0.0089^{+0.0020}_{-0.0016}$	$0.0085^{+0.0001}_{-0.0004}$	$0.0086^{+0.0002}_{-0.0002}$
$\tilde{\chi}_4^0$	$0.1170^{+0.028}_{-0.021}$	$0.1168^{+0.0280}_{-0.0211}$	$0.1211^{+0.048}_{-0.075}$	$0.1220^{+0.050}_{-0.079}$
$\tilde{\chi}_1^+$	$2.2483^{+0.534}_{-0.405}$	$2.2453^{+0.533}_{-0.404}$	$1.9682^{+0.065}_{-0.121}$	$1.9791^{+0.074}_{-0.122}$
$\tilde{\chi}_1^-$	$0.5609^{+0.133}_{-0.101}$	$0.5599^{+0.132}_{-0.101}$	$0.6324^{+0.022}_{-0.037}$	$0.6380^{+0.024}_{-0.038}$
$\tilde{\chi}_2^+$	$0.2450^{+0.060}_{-0.048}$	$0.2449^{+0.059}_{-0.045}$	$0.2137^{+0.009}_{-0.013}$	$0.2155^{+0.009}_{-0.014}$
$\tilde{\chi}_2^-$	$0.0603^{+0.0146}_{-0.0110}$	$0.0603^{+0.0145}_{-0.0110}$	$0.0703^{+0.0026}_{-0.0046}$	$0.0706^{+0.0031}_{-0.0045}$

a perfect agreement, similar to the agreement of the LO results. Hence, we follow that the discrepancy originates mainly from the slightly different on shell subtraction approaches and their implementations. Furthermore, the agreement gets better for higher scales, since the gluon initiated channels become less dominant. If the spectrum gets harder, i.e. the SUSY particles become heavier, the discrepancy decreases. This is due to the decrease of the on shell remainder. We remark that we had to increase the number of evaluations of the integrals in PROSPINO2.1, in particular those of the gluon initiated processes in order to obtain a more stable result. All numerical errors for the cross sections presented here are slightly below 1%.

Next, we investigate the difference between degenerate and non-degenerate squark masses. Moreover, we compare both results with PROSPINO2.1. It is only able to compute approximate NLO cross sections for free squarks, as stated above. We use again BP II, but vary the gluino mass from 500 GeV up to 3 TeV. The results are shown in Fig. 6.10 for the specific process $pp \rightarrow \tilde{\chi}_2^0 \tilde{g}$ at $\sqrt{S} = 13$ TeV using CT10NLO as the PDF⁶. First, we observe a very good agreement (below 1%) over the whole gluino mass range for degenerate squarks. The slight differences originate from the on shell remainder. The total cross section for free squarks is significantly lower than the one for mass-degenerate squarks. This is already the case at LO (not shown here) and is due to the reason that especially the most relevant left-handed up and down squarks are much lighter (600 GeV) than the average of the squark masses. For the free squark scenario we find a larger discrepancy, where our result exceeds the approximate PROSPINO2.1 result by almost 5% at a gluino mass of roughly 1.8 TeV. One reason is the wide range of the squark masses for BP II going from roughly 500 GeV to 2.8 TeV. Computing the

⁶Therefore, we used a modified version of PROSPINO2.1, which has been interfaced to the LHAPDF [101] library.

K -factor by using degenerate squark masses ($m_{\tilde{q}} \approx 1.75$ TeV) neglects the possibility of those produced on shell and subsequently decay into a gluino and a quark or antiquark. The on shell remainder of these resonant squared diagrams can be sizable. Thus, K -factors for free and degenerate squark masses differ. This is the main reason for the here observed discrepancy.

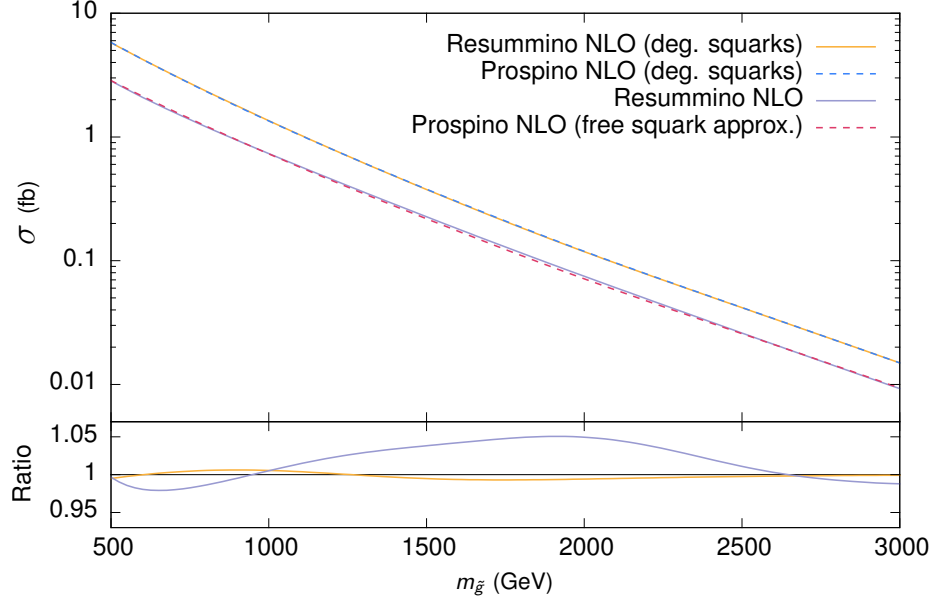


Figure 6.10: Gluino mass dependence on the total cross sections for the process $pp \rightarrow \tilde{\chi}_2^0 \tilde{g}$ at $\sqrt{S} = 13$ TeV using CT10NLO as the PDF, central scale values for the renormalization and factorization scale and BP II for the SUSY spectrum. We show the results for averaged and free squark masses obtained with RESUMMINO and PROSPINO2.1. For free squark masses PROSPINO2.1 can only compute approximate NLO results (see main text of Sec. 6.4.2). The lower panel shows the ratio of the RESUMMINO results to the corresponding PROSPINO2.1 results.

After the successful verification of the fixed order result we can now move on to include threshold resummation effects.

6.4.3 Total cross sections for benchmark point II

In this section we present total cross sections for all possible gauginos in the final state. In contrast to Tab. 6.3 we use free squark masses, include resummation effects and use the 7-point method for the scale uncertainties, i.e. we vary the central scale value for the factorization and renormalization scale independently by a factor of two, excluding relative factors of four. Additionally, we include PDF uncertainties for the NLO predictions. They will be discussed in more detail in Sec. 6.4.8. Our results for the LO, NLO and NLL+NLO cross sections are shown in Tab. 6.4. The cross section for $\tilde{\chi}_1^0$ is the largest one due to its low mass and mostly bino composition. The $\tilde{\chi}_2^0$ is mostly a wino and hence the strength of the couplings appearing in the LO diagram is smaller compared to those appearing in the production of $\tilde{\chi}_1^0$. Furthermore, the mass of $\tilde{\chi}_2^0$ is twice the mass of $\tilde{\chi}_1^0$. This results in a cross section which is roughly three times smaller. The cross sections for $\tilde{\chi}_3^0$ and $\tilde{\chi}_4^0$ are much smaller, since they are

Table 6.4: Total cross sections for $pp \rightarrow \tilde{\chi}_i^{0,\pm} \tilde{g}$ at $\sqrt{S} = 13$ TeV using CTEQ6L1 as the LO and CT10NLO as the NLO PDF. The SUSY scenario is BP II. We show the scale uncertainties obtained by using the 7-point method (see text) and the PDF uncertainties according to Eqs. (5.22) and (5.23) for the NLO cross sections.

Gaugino	LO ^{+scale} _{-scale} (fb)	NLO ^{+scale+PDF} _{-scale-PDF} (fb)	NLL + NLO ^{+scale} _{-scale} (fb)
$\tilde{\chi}_1^0$	$0.1924^{+22.2\%}_{-17.2\%}$	$0.2108^{+4.6\%+14.2\%}_{-6.7\%-12.4\%}$	$0.2171^{+0.5\%}_{-1.6\%}$
$\tilde{\chi}_2^0$	$0.0740^{+23.8\%}_{-17.9\%}$	$0.08121^{+4.9\%+17.2\%}_{-7.0\%-15.2\%}$	$0.0835^{+0.3\%}_{-1.9\%}$
$\tilde{\chi}_3^0$	$0.000730^{+20.4\%}_{-15.9\%}$	$0.000908^{+1.5\%+35.9\%}_{-3.2\%-18.6\%}$	$0.000959^{+3.9\%}_{-4.3\%}$
$\tilde{\chi}_4^0$	$0.00744^{+24.0\%}_{-18.0\%}$	$0.00841^{+5.9\%+19.9\%}_{-7.1\%-15.7\%}$	$0.00870^{+0.8\%}_{-1.5\%}$
$\tilde{\chi}_1^+$	$0.1339^{+24.5\%}_{-18.1\%}$	$0.1270^{+5.2\%+23.7\%}_{-7.3\%-24.8\%}$	$0.1308^{+0.7\%}_{-2.0\%}$
$\tilde{\chi}_1^-$	$0.0333^{+23.9\%}_{-18.1\%}$	$0.0403^{+5.5\%+29.0\%}_{-7.1\%-20.2\%}$	$0.0415^{+1.1\%}_{-1.9\%}$
$\tilde{\chi}_2^+$	$0.0150^{+24.3\%}_{-18.4\%}$	$0.0141^{+5.8\%+26.4\%}_{-7.6\%-26.7\%}$	$0.0147^{+0.6\%}_{-2.1\%}$
$\tilde{\chi}_2^-$	$0.00368^{+24.2\%}_{-18.3\%}$	$0.00460^{+6.2\%+30.1\%}_{-7.7\%-22.6\%}$	$0.00475^{+1.5\%}_{-2.2\%}$

mostly higgsino-like and the Yukawa couplings are small compared to the gauge couplings⁷. The cross section for $\tilde{\chi}_4^0$ is roughly ten times larger than for $\tilde{\chi}_3^0$, although both have similar masses. However, $\tilde{\chi}_4^0$ has a larger wino component leading to a larger cross section. This is similar for the charginos, where the cross section for $\tilde{\chi}_1^\pm$ is larger than the one for $\tilde{\chi}_2^\pm$, since the former has a larger wino component and additionally a smaller mass. Furthermore, the production of the positive charged final state is more likely than the production of the negative charged counterpart, since we have two protons in the initial state.

Going from LO to NLO we do not only observe a difference to the LO central value, but also a reduction of the scale uncertainties to values below $\pm 8\%$. This is further reduced by including threshold resummation effects to values below $\pm 2.2\%$, except for the production of $\tilde{\chi}_3^0$. Nonetheless, we find that the scale uncertainty for the production of $\tilde{\chi}_3^0$ is reduced if we consider a wider scale range. For this process the resummation result changes less in the higher scale region, compared to the NLO result. We address the scale uncertainties in more detail in Sec. 6.4.5. The resummation contributions to the central value are around 2.5% to 5%. Finally, let us mention that cross sections below 0.01 fb are too small to be observed with the current luminosity of the 13 TeV run of the LHC. Hence, the cross sections for $\tilde{\chi}_3^0$, $\tilde{\chi}_4^0$ and $\tilde{\chi}_2^-$ would not be observable. In addition, the associated production of a gluino and the lightest neutralino will be difficult to observe at the LHC, as the latter escapes directly undetected. It is therefore more promising to study the associated production of a gluino with the second-lightest neutralino (or the lightest chargino of often equal mass), since it will

⁷We recall that the Yukawa couplings are proportional to the quark masses and the PDFs for the heavier quarks are rather small.

decay into an additional Z (or W) boson, whose leptonic decay products will then lead to an identifiable signal and better background suppression. For these reasons, we focus on the associated production of a gluino together with the second lightest neutralino in the following section.

6.4.4 Invariant mass distribution

In the upper panel of Fig. 6.11, we show the invariant-mass distribution given for the production of a gluino with a mass of 1958 GeV and a second-lightest neutralino with a mass of 627 GeV. We find that the cross sections peak at about 3.2 TeV and then fall off toward higher invariant masses M . The maximum is shifted from LO (blue) to NLO (green) and NLL+NLO (red) towards slightly smaller values of M , due to the additional radiation of gluons, quarks and antiquarks. At the same time we observe a significant reduction of the scale dependence from LO to NLO. We obtain a further reduction of the scale dependence for NLL+NLO which is more clearly visible in the lower panel of Fig. 6.11. In particular for high invariant masses, for which most of the available phase space is close to the threshold, we find a change from $\pm 12\%$ to $\pm 3\%$ by including threshold effects. Here, the scale errors have been obtained by using the 7-point method, but using the invariant mass as the central scale value. In the high-mass region, the NLL+NLO cross section is roughly 10% larger than the one for NLO.

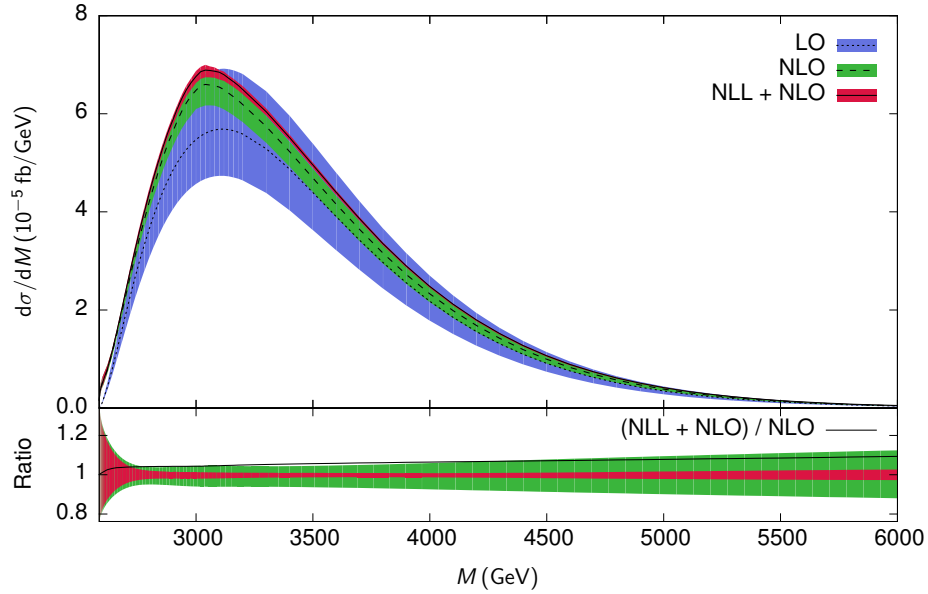


Figure 6.11: Upper panel: Invariant mass distribution for the process $pp \rightarrow \tilde{g}\tilde{\chi}_2^0$ at the LHC with a center-of-mass energy of $\sqrt{S} = 13$ TeV at the LO (blue), NLO (green) and NLL+NLO (red) accuracy. Lower panel: Corresponding relative scale uncertainties and the NLL+NLO/NLO κ -factor (black line).

6.4.5 Scale uncertainty of the total cross section

This section is dedicated to the scale uncertainties of the process $pp \rightarrow \tilde{g}\tilde{\chi}_2^0$. In Fig. 6.12 we show the total cross section while varying the factorization and renormalization scale simultaneously (upper panel), only the renormalization scale with fixed factorization scale (central panel) and vice versa (lower panel) around the average mass of the final state. For a process that depends already at LO on the strong coupling constant, one expects the significant (approximately logarithmic) scale dependence to be already reduced at NLO. This has already been seen in the invariant mass distribution. Here, the NLO result (green dashed curve) shows the characteristic maximum at approximately half the central renormalization and factorization scale (upper panel). Including resummation effects (red full curve) the scale dependence is further reduced. This is due to the inclusion of dominant scale dependent terms belonging to higher orders of the perturbative series. When the resummed result is expanded to NLO (blue dotted curve), it becomes a good approximation to the full NLO result especially for large scale choices, when the logarithmic terms dominate the cross section. One major difference between NLO and the expansion is that the former includes gluon initiated channels and hence can receive large corrections from the on shell remainder. This leads to the larger discrepancy for low factorization scales (lower panel) due to the more relevant gluon PDF for lower scale values. For the individual scale dependence (two lower panels) the expansion is also a good approximation. The two lower panels demonstrate the interplay of the renormalization and factorization scale dependence in the NLO and NLL+NLO cross sections, that together produce the stabilized scale behavior in the upper panel with a large plateau in particular at NLL+NLO.

We observe similar results in Fig. 6.13, where the gluino mass has been set to 3 TeV. For this reason, most of the available phase space is close to the production threshold which leads to a larger κ -factor at central scale and to a reduction of the scale dependence for the cross section at NLL+NLO accuracy. In addition, the expansion of the resummed cross section to NLO approximates the full NLO cross section better compared to the results shown in Fig. 6.12, since the NLO cross section is now dominated by large logarithmic contributions which explicitly depend on the factorization and renormalization scale. In particular for higher scale values we observe a perfect agreement, whereas for decreasing scale values the discrepancy increases. This mainly originates from the factorization scale dependent terms (see lower panel), since the independent renormalization scale variation shows a perfect agreement over the whole scale range. Here, the reason is again mostly the gluon initiated processes, which become more dominant for lower factorization scale values due to the then increasing relevance of the gluon PDF.

6.4.6 Gluino mass dependence of the total cross section

Since the gluino mass is unknown, it is interesting to compute the total cross section for associated gluino-neutralino production as a function of the gaugino or gluino mass. In this section we focus on the latter, whereas the former will be addressed in the following section.

The total cross section for the gluino mass dependence is shown in the upper panel of Fig. 6.14. As expected, the cross section falls steeply with the gluino mass from 3 to 0.01 fb in the range $m_{\tilde{g}} \in [500, 3000]$ GeV. With integrated LHC luminosities of currently a few

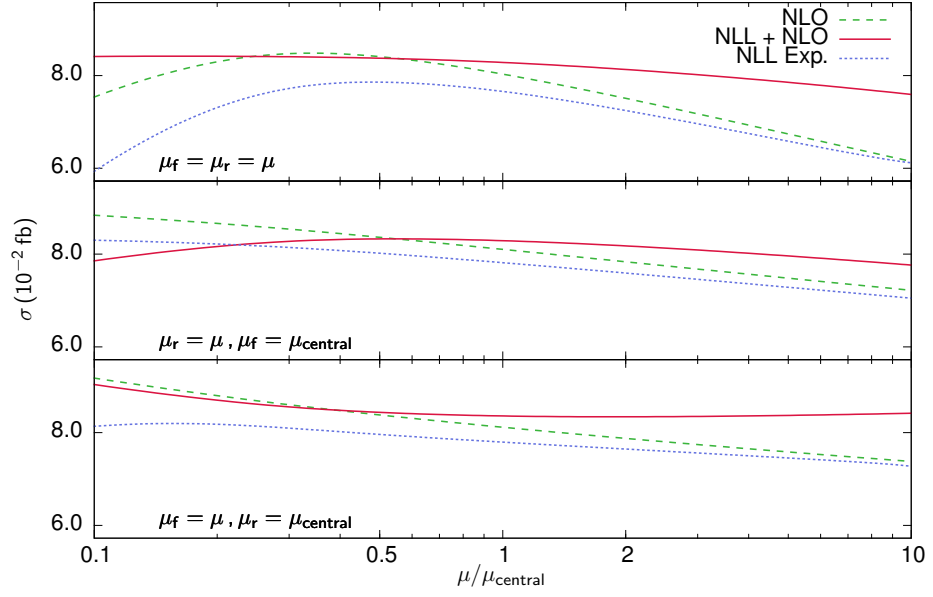


Figure 6.12: Total cross section for the process $pp \rightarrow \tilde{g}\tilde{\chi}_2^0$ at the LHC with a center-of-mass energy of $\sqrt{S} = 13$ TeV at NLO (green dashed curve), NLL+NLO (red full curve) and after the re-expansion of the NLL result to NLO (blue dotted curve). We vary the renormalization and factorization scale together (upper panel), only the renormalization scale with fixed factorization scale (central panel) and *vice versa* (lower panel) around the central scale $\mu_{\text{central}} = (m_{\tilde{g}} + m_{\tilde{\chi}_2^0})/2$. For the PDF we use CT10NLO and for the benchmark scenario BP II.

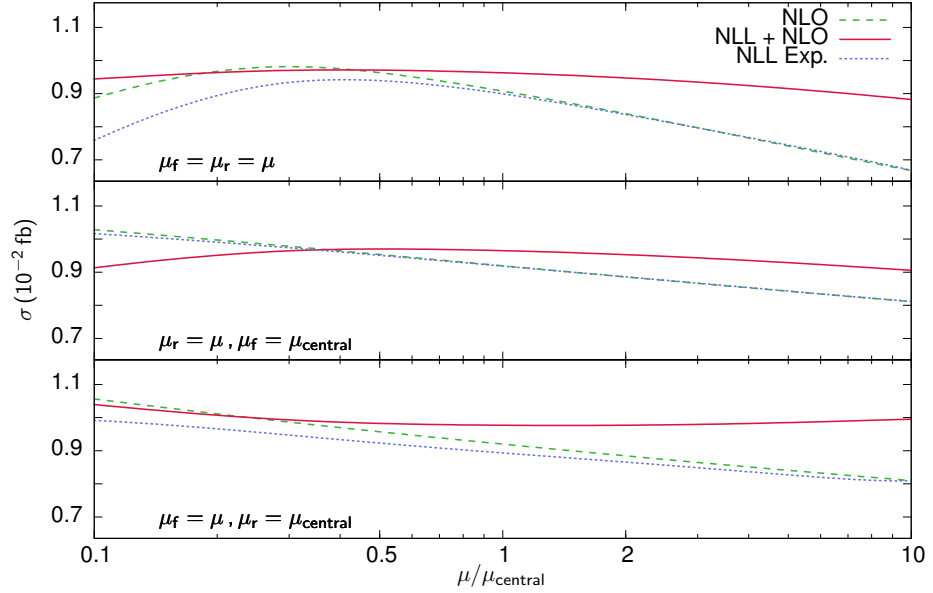


Figure 6.13: Same as in Fig. 6.12, but with $m_{\tilde{g}} = 3.0$ TeV.

fb^{-1} and in the near future of a few 100 fb^{-1} at $\sqrt{S} = 13 \text{ TeV}$, these cross sections will soon be observable. It is expected that in the high luminosity phase of the LHC an integrated luminosity of 3000 fb^{-1} can be reached and even larger gluino masses can possibly lead to observable events, whereas the direct strong production of gluino pairs may kinematically no longer be accessible.

As the lower panel of Fig. 6.14 shows, the NLO scale uncertainty (green band) on the total cross section of $\pm 10\%$ at 500 GeV decreases only slightly towards higher gluino masses. This is in sharp contrast to the NLL+NLO prediction (red band), that has already a smaller scale error of $\pm 7\%$ at 500 GeV and that becomes much more reliable with an error of only a few percent at large gluino masses. At the same time, the NLO cross section is increased at NLL+NLO by 7 (black line) to 20% for gluino masses of 3 to 6 TeV (not shown here), respectively.

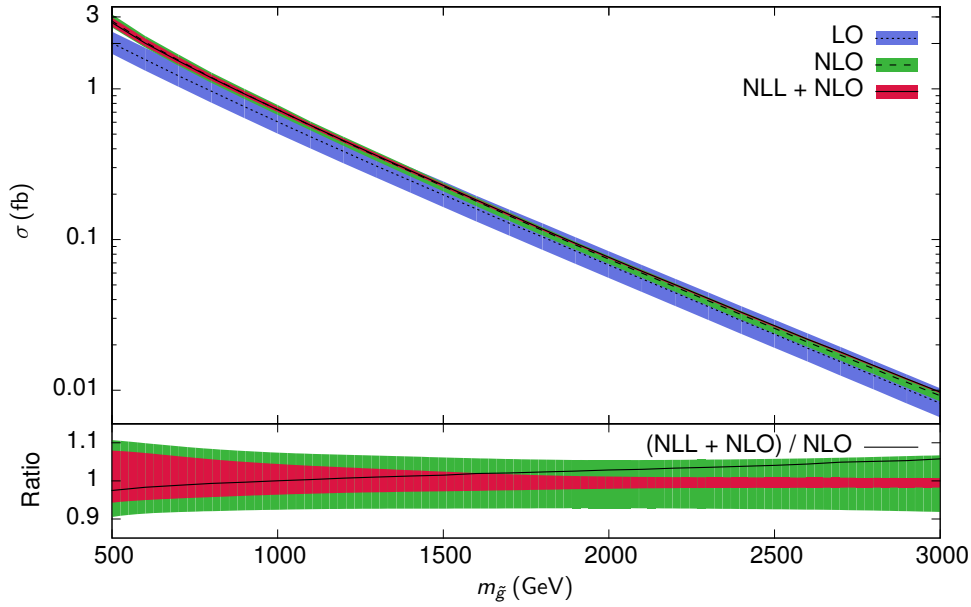


Figure 6.14: Upper panel: Total cross section for the process $pp \rightarrow \tilde{g}\tilde{\chi}_2^0$ at the LHC with a center-of-mass energy of $\sqrt{S} = 13 \text{ TeV}$ in LO (blue), NLO (green) and NLL+NLO (red) as a function of the gluino mass. Lower panel: Corresponding relative scale uncertainties and the NLL+NLO/NLO κ -factor (black line).

In the previous section we have observed that for heavier gluinos the relevance of the threshold enhanced terms is increased and the expansion of the resummed result up to NLO leads to a good approximation of the NLO cross section. This behavior is substantiated in Fig. 6.15, where we compare the gluino mass dependence of the expansion to the full NLO cross section. At a gluino mass of 500 GeV the discrepancy is still 20% since the threshold enhanced terms are not dominant yet. Here, the difference originates mainly from the gluon initiated channels. Due to the lower mass of the gluino compared to most of the squarks, the latter can be produced on shell leading to a sizable contribution to the on shell remainder.

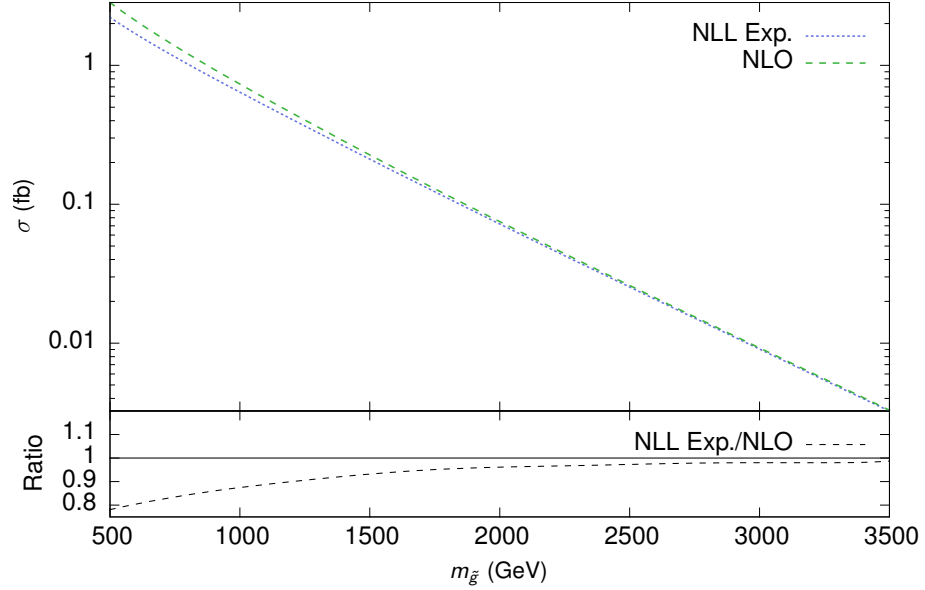


Figure 6.15: Upper panel: Total cross section for the process $pp \rightarrow \tilde{g}\tilde{\chi}_2^0$ at the LHC with a center-of-mass energy of $\sqrt{S} = 13$ TeV in NLO (green dashed) and the resummation result expanded to NLO (blue dotted) as a function of the gluino mass. Lower panel: Ratio of resummation result expanded to NLO to the full NLO cross section.

This changes at a gluino mass of 2.5 TeV, where this resonant region is now kinematically forbidden⁸ and furthermore the distance to the production threshold is reduced. By increasing the gluino mass the discrepancy decreases further to 1.2% at 3.5 TeV.

6.4.7 Gaugino mass dependence of the total cross section

Similarly to the gluino mass dependence, the total cross section falls steeply by increasing the gaugino mass. The mass of the second lightest neutralino does depend on the SUSY breaking parameters M_1 , M_2 , μ and $\tan\beta$. Only after a diagonalisation of the neutralino mass matrix with the mixing matrix N one obtains its physical mass. Hence, we vary the bino mass parameter M_1 instead, which fixes immediately also the wino mass parameter M_2 through the GUT relation $M_2 \simeq 2 M_1$ (see Sec. 2.3.3).

In the upper panel of Fig. 6.16 we show the dependence of the neutralino mass eigenvalues on the gaugino mass parameter M_2 . The mass eigenvalue of the second-lightest neutralino increases linearly with M_2 up to $M_2 = \mu = 773$ GeV, where a typical avoided crossing occurs. At higher values for M_2 its eigenvalue remains constant and the mass eigenvalue of $\tilde{\chi}_4^0$ depends linearly on M_2 . The mass eigenvalue of the lightest neutralino increases linearly over the whole M_2 range, whereas the mass eigenvalue for $\tilde{\chi}_3^0$ does not change. Accordingly, the decomposition of $\tilde{\chi}_2^0$ (lower panel) changes from wino-type (large mixing matrix element N_{22} , red curve) to

⁸Note that the other resonant region, where the squark decays into the neutralino and a quark or antiquark, is still kinematically allowed.

higgsino-type (large mixing matrix elements N_{23} and N_{24} , yellow and blue curves). Both features will of course influence the production cross section of the process $pp \rightarrow \tilde{g}\tilde{\chi}_2^0$.

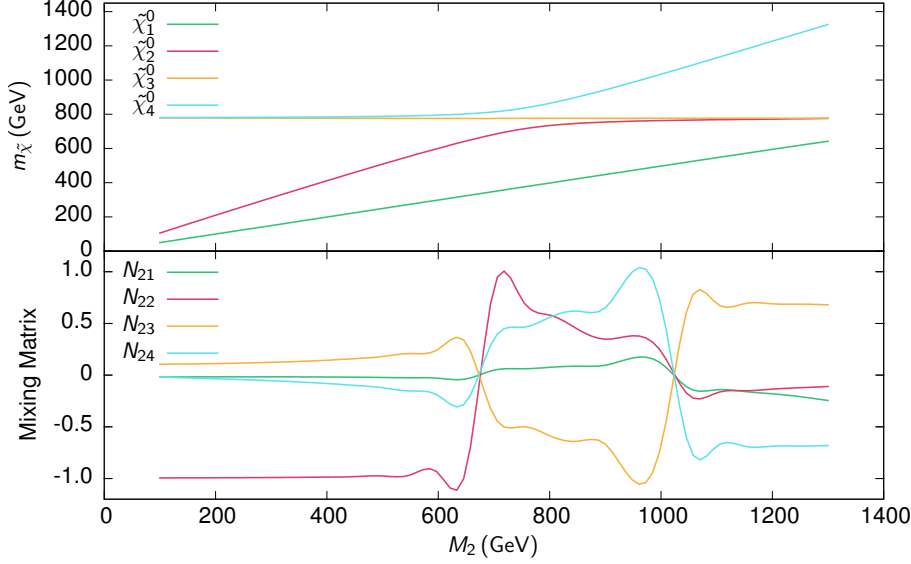


Figure 6.16: Dependence of the neutralino mass eigenvalues (upper panel) and mixing matrix elements of the second-lightest neutralino (lower panel) on the wino and bino mass parameters $M_2 \simeq 2 M_1$. All other Higgs and soft SUSY-breaking parameters have been kept fixed and set to the values of our benchmark scenario.

In Fig. 6.17 we show the dependence of the cross section on the wino mass parameter M_2 . As expected, it falls exponentially as long as the physical mass of $\tilde{\chi}_2^0$ changes. For $M_2 > \mu$, the neutralino becomes higgsino-like and couples mostly via quark Yukawa couplings, hence the cross section falls even faster than before, despite the fact that the gaugino mass remains constant. Interestingly, for $M_2 > 1150$ GeV the cross section starts to increase which is due to the slightly increasing bino component (see Fig. 6.16). The scale uncertainty is drastically reduced by going from LO (blue shaded band) to NLO (green shaded band). As long as the mass of the neutralino increases, i.e. until $M_2 = \mu = 773$ GeV, the scale uncertainty of the NLO result increases due to the rising contribution of the large logarithms. Beyond this value of M_2 the scale uncertainty remains constant, as expected, since the distance to the threshold does not change. Going from NLO to NLL+NLO (red) results we observe a similar trend of the scale dependence, but on a much lower level. To be specific, it rises only from ± 1 to $\pm 3\%$ compared to a scale dependence at NLO that rises from ± 3 to $\pm 6\%$. The κ -factor (black line) increases also with M_2 from 1.02 to 1.07.

6.4.8 Parton density uncertainty of the total cross section

Finally, we analyze the PDF uncertainty. In contrast to the scale uncertainty which is expected to reduce due to the resummation of large logarithms, the PDF uncertainty is normally not improved by this procedure. For the computations of the PDF uncertainties we employ

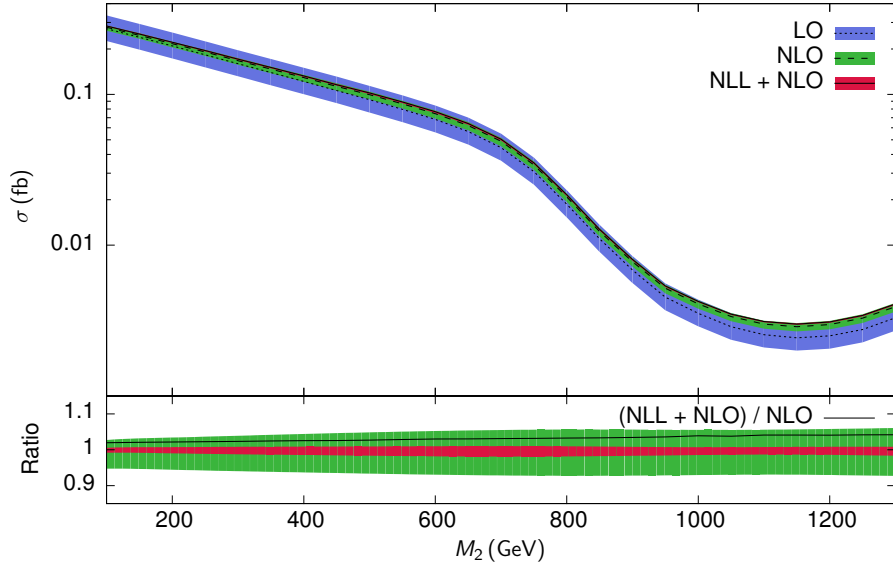


Figure 6.17: Upper panel: Total cross section for the process $pp \rightarrow \tilde{g}\tilde{\chi}_2^0$ at the LHC with a center-of-mass energy of $\sqrt{S} = 13$ TeV in LO (blue), NLO (green) and NLL+NLO (red) as a function of the wino mass parameter M_2 . The bino mass parameter has been varied simultaneously using the GUT relation $M_1 \simeq M_2/2$. Lower panel: Corresponding relative scale uncertainties and the NLL+NLO/NLO κ -factor (black line).

Eqs. (5.22) and (5.23) for the Hessian-like PDFs and compute the standard deviation as explained in Sec. 5.3.2 for the NNPDF-like PDFs. We remark that we observed no significant difference between the PDF uncertainties for the NLO and NLL+NLO results. We compute the PDF uncertainties for the NLO cross sections and study them together with the NLL+NLO results obtained with the central fit. As our method for the transformation of the PDFs to Mellin space is not yet satisfying for NNPDF-like PDFs, we estimate the NLL+NLO result using the κ -factor method explained in Appendix D.

In Fig. 6.18 we show the dependence of the PDF uncertainties for NNPDF30 [105], CT10NLO [97] and MSTW2008NLO90CL [103] on the gluino mass. All results have been normalized to the cross section obtained by the central fit of CT10NLO. As one can see, the estimates by the three groups overlap to a large extent. The central cross section for MSTW is the largest, which is due to the larger value of the strong coupling. To be specific, $\alpha_s(M_Z) \simeq 0.120$ for MSTW and $\alpha_s(M_Z) \simeq 0.118$ for the two other PDFs. For the two Hessian-like PDFs we find an asymmetric uncertainty band, whereas for NNPDF30 it is symmetric due to the symmetric standard deviation. At low masses of the gluino the three individual PDF uncertainties are still relatively small and comparable to the scale uncertainties with about $\pm 5\%$. In contrast to the scale uncertainties, they increase rather than decrease with the gluino mass and reach an uncertainty of $\pm 20\%$ at 3 TeV. This is due the fact that the PDFs are much less constrained at large than at intermediate values of the parton momentum fraction x . The increase of the uncertainty towards larger x is less pronounced in MSTW2008

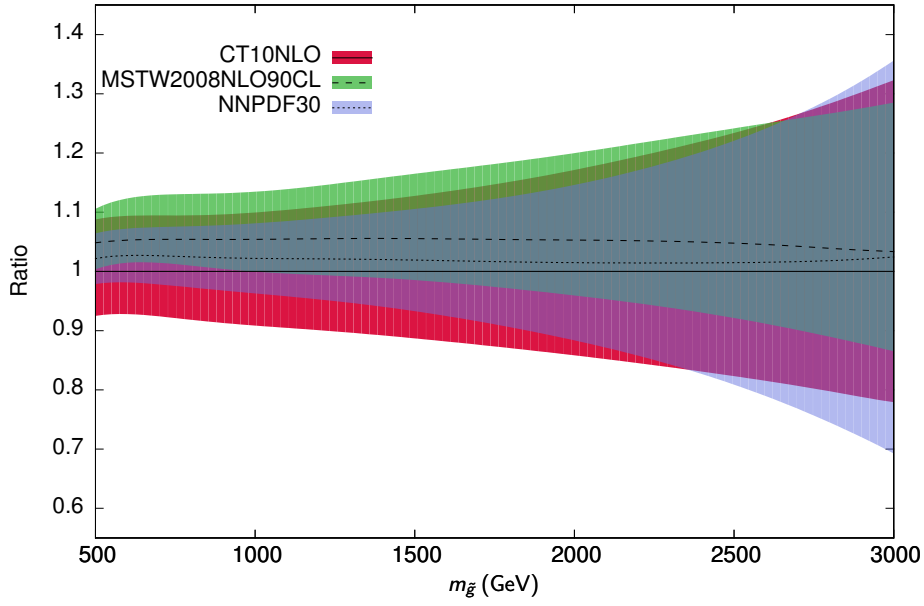


Figure 6.18: Relative PDF uncertainties of the total cross section for the process $pp \rightarrow g\tilde{\chi}_2^0$ at the LHC with a center-of-mass energy of $\sqrt{S} = 13$ TeV in NLL+NLO. The uncertainties are shown for three different PDFs, CT10NLO (red), MSTW2008NLO90CL (green) and NNPDF30 (blue), as a function of the gluino mass $m_{\tilde{g}}$.

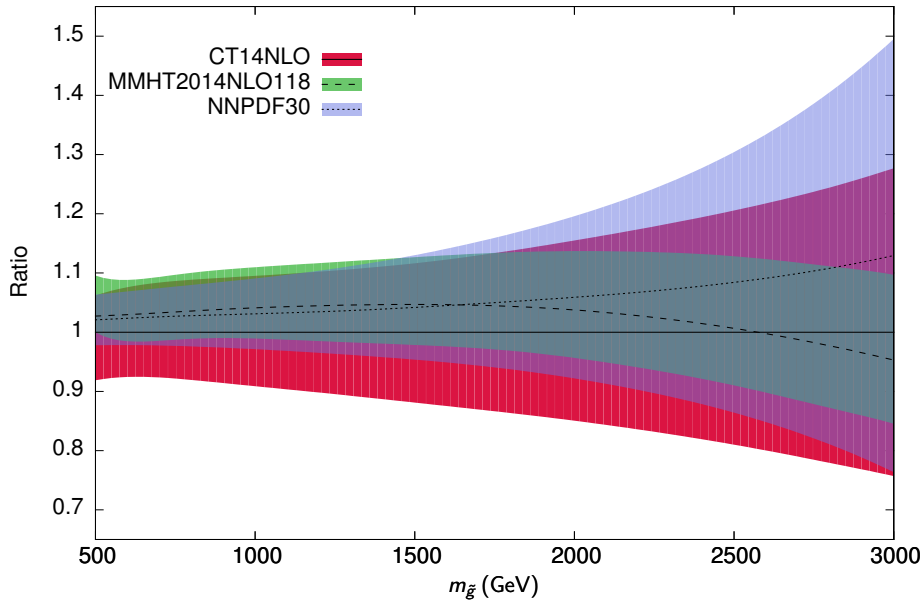


Figure 6.19: Same as in Fig. 6.18, but uncertainties are shown for CT14NLO (red), MMHT2014NLO118 (green) and NNPDF30 (blue).

and more pronounced in NNPDF30. It will therefore be interesting to study the impact of threshold-improved PDFs in future work, as it was done for squark and gluino production [154, 57].

We show similar results in Fig. 6.19, but for two newer PDF fits, namely CT14NLO [107] and MMHT2014NLO118 [155]. As the MMHT2014NLO118 PDF set is only available for a 68% and not for a 90% confidence level, the corresponding error must be multiplied by the standard factor of 1.645 for compatibility. By comparing the results of CT10NLO and CT14NLO, we find only a small reduction of the PDF uncertainty, if at all. While the PDF uncertainty of MMHT compared to MSTW is rather similar in the low gluino mass region, it changes drastically in the high mass region. To be specific, the PDF error is reduced by a factor of two. The possible reason is that scaling the 68% confidence level band by the standard factor of 1.645 underestimates the PDF uncertainty, especially in the high x -region, where the PDFs are much less constrained. Moreover, the central value of the MMHT gets smaller in the high x -region, compared to CT14NLO, NNPDF30 and MSTW.

We remark that the scale uncertainties computed in the previous sections and the PDF uncertainties computed in this section are independent and therefore usually added in quadrature. Besides, the uncertainty on α_s should be taken into account as well to get a reliable estimate of the total theoretical uncertainty.

7 Conclusion

In this work we have updated the precision predictions for slepton pair production and associated gaugino-gluino production at the LHC by including resummation effects. First, we have discussed the theoretical background of perturbative QCD, the MSSM and of resummation in order to apply resummation techniques to these two processes.

Simplified models, which are now widely used by the experimental collaborations, have been used as the benchmark scenario for our predictions of direct slepton pair production. These models allow for a more feasible parameter space of the corresponding SUSY sector of the MSSM and the production cross section depends only on a few physical parameters. The inclusion of dominant logarithmic terms reduced the renormalization and factorization scale uncertainties of the total cross sections. For slepton masses of the $\mathcal{O}(1 \text{ TeV})$ we pointed out that NNLL terms should be considered in the future. To study the impact at full NNLL accuracy the second order hard matching coefficient of the direct slepton pair production should be added and the complete NNLL result should be matched to a full (or approximate) NNLO computation. As in our simplified models SUSY-QCD corrections are negligible, these computations will be very similar to those of the DY process. Investigated PDF uncertainties for the PDF sets CT10NLO, MSTW2008NLO90CL and NNPDF23 overlapped to a large extent. For slepton masses of 500 GeV we found a PDF error slightly below $\pm 10\%$ at a center-of-mass energy of $\sqrt{S} = 8 \text{ TeV}$. When increasing the slepton masses, the PDF uncertainties increase due to the fact that PDFs are much less constrained at large values of the parton momentum fraction x . The updated results were then employed in a combination with modern Monte Carlo techniques in order to reanalyze ATLAS and CMS searches for direct slepton pair production in the light of simplified models. We focused on a signal of two high energetic leptons and missing energy. For our analysis we made different assumptions for the composition of the sleptons and their decay products, the lightest neutralino. As expected, the visible cross section is independent of the neutralino nature. By reanalyzing ATLAS results we derived mass limits for left-handed (right-handed) selectrons of 175 GeV (150 GeV) for almost massless neutralinos by an integrated luminosity of 4.7 fb^{-1} of the 7 TeV LHC data. The difference for the limits in the left- and right-handed case originates from the larger production cross section of left-handed sleptons. Due to different detector acceptances for different lepton flavors we found different exclusion limits for the second generation of sleptons. Left-handed (right-handed) smuons are excluded for masses below 220 GeV (180 GeV) for massless neutralinos. No mass limits have been derived for the third generation of sleptons, because of the complicated tau reconstruction together with small signal cross sections. In contrast to the ATLAS searches, CMS did not distinguish between selectrons and smuons. In our reanalysis we found that left-handed (right-handed) first and second generation sleptons are excluded for masses up to 310 GeV (250 GeV). For a compressed SUSY spectrum we lost all sensitivity due to too soft and therefore undetectable leptons and no exclusion limits could

be derived. With the data of the 13 TeV run of the LHC we expect that stronger constraints can be made in the future.

Furthermore, we have presented a threshold resummation calculation at the NLL+NLO accuracy level for the associated production of gluinos and gauginos at the LHC at a center-of-mass energy of 13 TeV. In contrast to the direct slepton pair production, this process is of intermediate strength, since both the electroweak and strong couplings are involved in the computation of the Born cross section. This process might become phenomenologically relevant should the gluinos prove to be too heavy to be produced in direct pair production at the LHC. This scenario is not unexpected, if one imposes the GUT relation for the gaugino mass parameters which predicts $M_1 = M_2/2 = M_3/6$ after renormalization group running at the weak scale. We performed an independent recalculation of the full NLO corrections, which we generalized to the case of non-universal squark masses. For our benchmark scenario, where the squark masses span a wide range, we found a maximal discrepancy of 5% compared to the approximate NLO computations obtained by PROSPINO2.1 for non-degenerate squark masses. Our update of the fixed order computation matched to resummation at the NLL accuracy required the computation of the process-dependent soft anomalous dimension and the hard matching coefficient function, which we could show to be consistent with each other. The then obtained resummation of NLL contributions increased the NLO cross section at large invariant mass by up to 10%. The total cross sections at central scale values have been increased due to threshold resummation by 7 to 20% for gluino masses of 3 to 6 TeV. Similar to the sleptons, we found a stabilization of the factorization and renormalization scale dependence. While the scale uncertainties reduce at higher masses, the PDF uncertainties increase, as expected. It would therefore be interesting to study threshold improved PDFs in the future.

A Feynman Rules

In this chapter we list the Feynman rules which have been used for the computations of the associated gaugino-gluino and direct slepton pair production up to NLO in α_s . The couplings have been generalized as shown in Fig. A.1. The explicit expressions for the coefficients are stated below and are based on Refs. [156, 7]. We remark that we have adapted these couplings

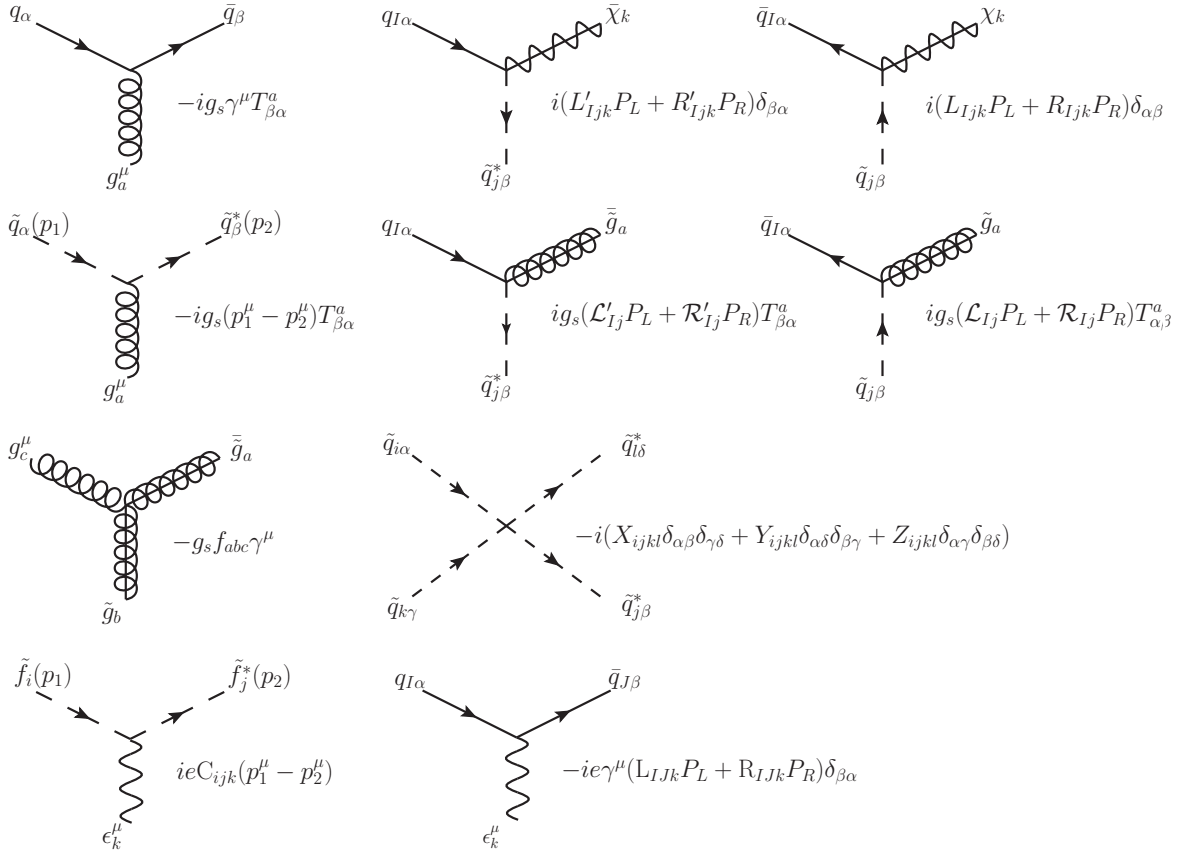


Figure A.1: Generalized Feynman rules for the vertices. All momenta are directed into the vertex. The arrows describe charge and fermion flows. Greek letters α, β, γ and δ denote color indices of the fundamental representation, whereas μ denotes a Lorentz index. Latin letters a, b and c denote color indices of the adjoint representation, I and J are generation indices, i and j label different sfermion states and k labels different neutralinos, charginos or electroweak gauge bosons.

to Refs. [24, 157] in order to read the needed parameters directly from input files in the SUSY

Les Houches Accord (SLHA) format. The *primed* and *unprimed* couplings are related to each other, e.g. $\mathcal{L}'_{Ij} = \mathcal{R}^*_{Ij}, \mathcal{R}'_{Ij} = \mathcal{L}^*_{Ij}$.

Quark-antisquark-gluino

The coefficients for the coupling between a quark of generation I , an antisquark j and a gluino are given by

$$\mathcal{R}'_{qI\tilde{q}_j^*} = \sqrt{2}S_{j(I+3)}^{\tilde{q}}, \quad \mathcal{L}'_{qI\tilde{q}_j^*} = -\sqrt{2}S_{jI}^{\tilde{q}}, \quad (\text{A.1})$$

where $q = u, d$ denotes the quark type and $S^{\tilde{q}}$ is the squark mixing matrix rotating the mass eigenstates to interaction eigenstates (see Sec. 2.3.4). We recall that these are in general matrices in generation and *left*- and *right-handed* space which act on mass eigenstates like $\tilde{f}^{\tilde{u}} := (\tilde{u}_1, \tilde{c}_1, \tilde{t}_1, \tilde{u}_2, \tilde{c}_2, \tilde{t}_2)^T$ (see Eq. (2.71)).

Quark-antisquark-neutralino/chargino

The coefficients for the coupling between a quark q_I , an antisquark \tilde{q}_j^* and a neutralino $\tilde{\chi}_k^0$ are

$$L'_{uI\tilde{u}_j^*\tilde{\chi}_k^0} = \frac{-e}{\sqrt{2}c_W s_W} S_{jI}^{\tilde{u}} \left(\frac{1}{3} N_{k1}^* s_W + N_{k2}^* c_W \right) - Y_u^I S_{j(I+3)}^{\tilde{u}} N_{k4}^*, \quad (\text{A.2})$$

$$R'_{uI\tilde{u}_j^*\tilde{\chi}_k^0} = \frac{2\sqrt{2}e}{3c_W} S_{j(I+3)}^{\tilde{u}} N_{k1} - Y_u^I S_{jI}^{\tilde{u}} N_{k4}, \quad (\text{A.3})$$

$$L'_{dI\tilde{d}_j^*\tilde{\chi}_k^0} = \frac{-e}{\sqrt{2}c_W s_W} S_{jI}^{\tilde{d}} \left(\frac{1}{3} N_{k1}^* s_W - N_{k2}^* c_W \right) - Y_d^I S_{j(I+3)}^{\tilde{d}} N_{k3}^*, \quad (\text{A.4})$$

$$R'_{dI\tilde{d}_j^*\tilde{\chi}_k^0} = \frac{-\sqrt{2}e}{3c_W} S_{j(I+3)}^{\tilde{d}} N_{k1} - Y_d^I S_{jI}^{\tilde{d}} N_{k3}, \quad (\text{A.5})$$

where $c_W = \cos \theta_W$ and $s_W = \sin \theta_W$ with θ_W being the Weinberg angle, $S^{\tilde{q}}$ is the squark mixing matrix, N the neutralino mixing matrix (see Sec. 2.3.3) and Y_q^I are the diagonal Yukawa couplings

$$Y_u^I = \frac{em_u^I}{\sqrt{2}s_W M_W \sin \beta}, \quad Y_d^I = \frac{em_d^I}{\sqrt{2}s_W M_W \cos \beta}, \quad (\text{A.6})$$

with $\tan \beta = v_2/v_1$. For the charginos the coefficients read

$$L'_{uI\tilde{d}_j^*\chi_k^-} = \left(\frac{-e}{s_W} S_{jJ}^{\tilde{d}} \mathcal{U}_{k1}^* + Y_d^I S_{j(J+3)}^{\tilde{d}} \mathcal{U}_{k2}^* \right) K_{JI}^*, \quad R'_{uI\tilde{d}_j^*\chi_k^-} = Y_u^I S_{jJ}^{\tilde{d}} \mathcal{V}_{k2} K_{JI}^*, \quad (\text{A.7})$$

$$L'_{dI\tilde{u}_j^*\chi_k^+} = \left(\frac{-e}{s_W} S_{jJ}^{\tilde{u}} \mathcal{V}_{k1}^* + Y_u^I S_{j(J+3)}^{\tilde{u}} \mathcal{V}_{k2}^* \right) K_{JI}, \quad R'_{dI\tilde{u}_j^*\chi_k^+} = Y_d^I S_{jJ}^{\tilde{u}} \mathcal{U}_{k2}^* K_{JI}, \quad (\text{A.8})$$

where \mathcal{V} and \mathcal{U} are the chargino mixing matrices (see Sec. 2.3.3) and K is the CKM matrix.

Sfermion-antifermion-electroweak vector boson

The coefficients for the coupling between a slepton i (I), an antislepton j (J) and an electroweak gauge boson k are

$$C_{\tilde{l}_i \tilde{l}_j^* \gamma} = \delta_{ij}, \quad C_{\tilde{l}_i \tilde{l}_j^* Z} = \frac{1}{2s_W c_W} \left(S_{iI}^{\tilde{l}*} S_{jI}^{\tilde{l}} - 2s_W^2 \delta_{ij} \right), \quad (\text{A.9})$$

$$C_{\tilde{\nu}_I \tilde{\nu}_J Z} = \frac{-1}{2s_W c_W} \delta_{IJ}, \quad C_{\tilde{l}_i \tilde{\nu}_J W} = \frac{-1}{\sqrt{2}s_W} S_{jI}^{\tilde{l}*} \delta_{IJ}. \quad (\text{A.10})$$

Here, $S^{\tilde{l}}$ is the left- and-right handed mixing matrix for charged sleptons. For the squarks we get

$$C_{\tilde{q}_i \tilde{q}_j^* \gamma} = -Q_f \delta_{ij} \delta_{\alpha\beta}, \quad C_{\tilde{u}_i \tilde{u}_j^* Z} = \frac{-\delta_{\alpha\beta}}{2s_W c_W} \left(S_{iI}^{\tilde{u}*} S_{jI}^{\tilde{u}} - \frac{4}{3} s_W^2 \delta_{ij} \right), \quad (\text{A.11})$$

$$C_{\tilde{u}_i \tilde{d}_j^* W} = \frac{-\delta_{\alpha\beta}}{\sqrt{2}s_W} S_{iI}^{\tilde{u}*} S_{jJ}^{\tilde{d}} K_{IJ}^*, \quad C_{\tilde{d}_i \tilde{d}_j^* Z} = \frac{\delta_{\alpha\beta}}{2s_W c_W} \left(S_{iI}^{\tilde{d}*} S_{jI}^{\tilde{d}} - \frac{2}{3} s_W^2 \delta_{ij} \right), \quad (\text{A.12})$$

where α and β are color indices of the fundamental representation for the antisquark and squark, respectively, $S^{\tilde{q}}$ is the left- and right-handed squark mixing matrix and Q_f is the fraction of the electric charge of the squarks with flavor f .

Quark-antiquark-electroweak vector boson

For the coupling between a quark q_I , an antiquark \bar{q}_J and an electroweak vector boson k we get the following coefficients:

$$L_{q_I \bar{q}_J \gamma} = Q_f \delta_{IJ}, \quad R_{q_I \bar{q}_J \gamma} = Q_f \delta_{IJ}, \quad (\text{A.13})$$

$$L_{u_I \bar{u}_J Z} = \frac{1}{2s_W c_W} \left(1 - \frac{4}{3} s_W^2 \right) \delta_{IJ}, \quad R_{u_I \bar{u}_J Z} = \frac{1}{2s_W c_W} \left(-\frac{4}{3} s_W^2 \right) \delta_{IJ}, \quad (\text{A.14})$$

$$L_{d_I \bar{d}_J Z} = -\frac{1}{2s_W c_W} \left(1 - \frac{2}{3} s_W^2 \right) \delta_{IJ}, \quad R_{d_I \bar{d}_J Z} = -\frac{1}{2s_W c_W} \left(-\frac{2}{3} s_W^2 \right) \delta_{IJ}, \quad (\text{A.15})$$

$$L_{u_I \bar{d}_J W} = \frac{1}{\sqrt{2}s_W} K_{IJ}^*, \quad R_{u_I \bar{d}_J W} = 0. \quad (\text{A.16})$$

Squark-antisquark-squark-antisquark coupling

These coupling coefficients can be rather complex and contain parts proportional to the strong coupling g_s , the electromagnetic charge e and the Yukawa couplings Y_q^I . For the associated gaugino-gluino production they only enter the squark self-energy diagrams. However, for non-mixing squarks these contributions get completely canceled after renormalization and hence the explicit expressions are not needed. The interested reader may have a look at Ref. [156].

Propagators

In Fig. A.2 we state the analytical expressions of the used propagators in Feynman-t'Hooft gauge. Momentum flow goes from left to right. Index notation is the same as in Fig. A.1.

$$\begin{aligned}
 & \begin{array}{ccc} \alpha & \longrightarrow & \beta \\ \bullet & & \bullet \end{array} = \frac{i(\not{p}+m)\delta_{\alpha\beta}}{p^2-m^2} \\
 & \begin{array}{ccc} \mu, a & \text{---} & \nu, b \\ \bullet & & \bullet \end{array} = \frac{-ig_{\mu\nu}\delta_{ab}}{p^2} \\
 & \begin{array}{ccc} \alpha & \text{---} & \beta \\ \bullet & & \bullet \end{array} = \frac{i\delta_{\alpha\beta}}{p^2-m^2} \\
 & \begin{array}{ccc} a & \text{---} & b \\ \bullet & & \bullet \end{array} = \frac{i(\not{p}+m)\delta_{ab}}{p^2-m^2} \\
 & \begin{array}{ccc} \mu & \text{---} & \nu \\ \bullet & & \bullet \end{array} = \frac{-ig^{\mu\nu}}{p^2-m^2}
 \end{aligned}$$

Figure A.2: Feynman rules for propagators in Feynman-t'Hooft gauge. Momentum flow goes from left to right. Index notation is the same as in Fig. A.1.

Here, m is the mass of the particle, p the four-momentum, α and β are color indices of the fundamental representation and a and b of the adjoint representation.

B Virtual Corrections

In this chapter we present our computations of the self-energies and vertex corrections needed for direct slepton pair and the associated gaugino-gluino production. For the analytical results of the box diagrams we refer to [130].

Due to the fact that the gluinos and gauginos are Majorana fermions, we use for some of the Feynman diagrams an arbitrary fermion flow bearing in mind some additional rules which are given in Ref. [158]. Furthermore, care has to be taken for the definition of γ_5 , since we compute the virtual corrections in $D = 4 - 2\epsilon$ dimensions. It has been shown that in anomaly-free computations it is possible to use the anticommuting property $\{\gamma_5, \gamma_\mu\} = 0$ and the relation $\text{Tr}[\gamma_5 \gamma^\mu \gamma^\nu \gamma^\rho \gamma^\sigma] = -4i\epsilon^{\mu\nu\rho\sigma}$, despite the fact that this scheme is in general inconsistent [44].

All results are stated in terms of tensor or scalar integrals. The former can be reduced to the latter by the so called Passarino-Veltman reduction. For the definition of the scalar and tensor integrals we use LOOPTOOLS' [134] conventions. Before going to the actual computations we address the common prefactor of the scalar loop integrals and show how to match it to LOOPTOOLS' conventions. We define our generic scalar loop integrals as

$$I := \int \frac{d^D q}{(2\pi)^D} \mu^{4-D} \mathcal{I}(q), \quad (\text{B.1})$$

where the factor μ^{4-D} , with μ having the dimension of mass, has been introduced to keep the dimension of the integral fixed in D dimensions and $\mathcal{I}(q)$ denotes the scalar integrand. For the evaluation of the scalar integrals we use the LOOPTOOLS [134] library which uses a slightly different convention:

$$I_{\text{LT}} := \int \frac{d^D q}{i\pi^{D/2} r_\Gamma} \mu^{4-D} \mathcal{I}(q), \quad (\text{B.2})$$

with¹

$$\begin{aligned} r_\Gamma &:= \frac{\Gamma(1-\epsilon)^2 \Gamma(1+\epsilon)}{\Gamma(1-2\epsilon)} \\ &= 1 - \gamma_E \epsilon + \left(\frac{\gamma_E^2}{2} - \frac{\pi^2}{12}\right) \epsilon^2 + \mathcal{O}(\epsilon^3). \end{aligned} \quad (\text{B.3})$$

¹Note that the expansion of $1/\Gamma(1-\epsilon)$ gives the same result up to order $\mathcal{O}(\epsilon^2)$.

For this reason, we need the following conversion factor in order to use the integrals of that library:

$$\begin{aligned}
I &= \left(i(4\pi)^{-2+\epsilon} r_\Gamma \right) I_{\text{LT}} \\
&= \left(\frac{i}{16\pi^2} - \frac{i(\gamma_E - \ln(4\pi))}{16\pi^2} \epsilon \right. \\
&\quad \left. + \frac{i(6\gamma_E^2 - \pi^2 - 12\gamma_E \ln(4\pi) + 6\ln(4\pi)^2)}{192\pi^2} \epsilon^2 \right) I_{\text{LT}} + \mathcal{O}(\epsilon). \tag{B.4}
\end{aligned}$$

Here, we have expanded the prefactors for $\epsilon \rightarrow 0$ up to $\mathcal{O}(\epsilon^2)$. As the maximal power of divergence of the scalar integrals I_{LT} is two, all further terms of the expansion vanish in the limit $\epsilon \rightarrow 0$. Usually, a whole factor $(4\pi)^\epsilon/\Gamma(1-\epsilon)$ can be factorized. Then the expansion of the scalar integrals multiplied by the expansion of this prefactor gives rise to the common finite parts $\ln 4\pi - \gamma_E$ which get subtracted in the $\overline{\text{MS}}$ -scheme. In RESUMMINO we multiply the integrals I_{LT} just by the factor $i/(16\pi^2)$. After adding counterterms in the minimal subtraction scheme we immediately obtain the finite result in the $\overline{\text{MS}}$ -scheme. By following this approach a similar factor should be factored out in the expression of the insertion operator \mathbf{I} in order to obtain the correct finite terms after the cancellation of the IR divergences. However, in this thesis we state the field renormalization counterterms in the $\overline{\text{MS}}$ -scheme and assume for our analytical computations that the prefactor $(4\pi)^\epsilon/\Gamma(1-\epsilon)$ has been absorbed by the scalar integrals I_{LT} .

For the sake of convenience we do not always state the arguments of the scalar integrals explicitly. They are the same as those of the self-energies or vertex corrections, unless stated otherwise.

Self-energies

In this section we present the computations for the self-energy diagrams. We start with the quark self-energy, followed by the squark and gluino self-energies.

To get the field renormalization counterterms in the $\overline{\text{MS}}$ -scheme it is useful to know the $\overline{\text{UV}}$ divergent pieces of the following scalar integrals:

$$\begin{aligned}
\overline{\text{UV}}[B_0] &= \Delta, & \overline{\text{UV}}[B_1] &= -\frac{1}{2}\Delta, \\
\overline{\text{UV}}[B_{00}] &= -\frac{1}{12}\Delta p^2, & \overline{\text{UV}}[DB_{00}] &= -\frac{1}{3}\Delta p^2, \\
\overline{\text{UV}}[B_{11}] &= \frac{1}{3}\Delta.
\end{aligned} \tag{B.5}$$

Self-energies of massless quarks

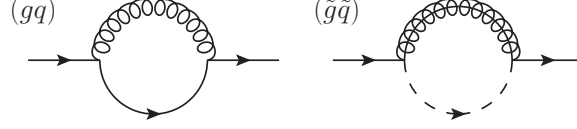


Figure B.1: Quark self-energy diagrams for QCD (left) and SUSY-QCD (right) corrections. The momentum and fermion flows go from left to right.

Gluon-quark contribution:

$$\begin{aligned}
 -i\Sigma^{(gq)}(p^2, 0, 0) &= \mu^{4-D} (-ig_s \gamma^\mu T_{\alpha\beta}^a) \int \frac{d^D q}{(2\pi)^D} \frac{i\not{q}(-ig_{\mu\nu})}{q^2(q-p)^2} (-ig_s \gamma^\nu T_{\beta\gamma}^a) \\
 &= -\mu^{4-D} g_s^2 (T^a T^a)_{\alpha\gamma} (2-D) \int \frac{d^D q}{(2\pi)^D} \frac{\not{q}}{q^2(q-p)^2} \\
 &= -\frac{ig_s^2}{16\pi^2} C_F \delta_{\alpha\gamma} 2(\epsilon-1)(-\not{p}) B_1
 \end{aligned} \tag{B.6}$$

Using the general decomposition in Eq. (3.30) we get

$$\Sigma_V^{(gq)}(p^2, 0, 0) = \frac{g_s^2}{8\pi^2} C_F (1-\epsilon) B_1. \tag{B.7}$$

By employing Eq. (B.5) we obtain the field renormalization counterterm

$$\delta Z_{qI}^{(gq)} = -\frac{g_s^2 C_F}{16\pi^2} \Delta. \tag{B.8}$$

As the quarks are external particles we need to multiply the external spinors by the square root of the propagator's residue $\sqrt{\mathcal{R}} \simeq 1 + 1/2\delta\mathcal{R}$. According to Eq. (3.42) and by using $B_1(0,0,0) \propto (1/\epsilon_{IR} - 1/\epsilon_{UV})$ this yields

$$\delta\mathcal{R}_{qI}^{(gq)} = \frac{g_s^2 C_F}{16\pi^2} \Delta_{IR}. \tag{B.9}$$

We remark that Eq. (B.9) is IR divergent. It is also common to use the fact that $B_1(0,0,0) = 0$, but we prefer to keep the IR and UV divergences separately.

Squark-gluino contribution:

$$\begin{aligned}
 -i\Sigma^{(\tilde{g}\tilde{q}_i)}(p^2, m_{\tilde{g}}^2, m_{\tilde{q}_i}^2) &= \mu^{4-D} g_s^2 C_F \delta_{\alpha\gamma} \int \frac{d^D q}{(2\pi)^D} \frac{(\mathcal{L}_{Ii} P_L + \mathcal{R}_{Ii} P_R)(\not{q} + m_{\tilde{g}})(\mathcal{L}'_{Ii} P_L + \mathcal{R}'_{Ii} P_R)}{(q^2 - m_{\tilde{g}}^2)((q-p)^2 - m_{\tilde{q}_i}^2)} \\
 &= \frac{ig_s^2 C_F \delta_{\alpha\gamma}}{16\pi^2} (\mathcal{L}_{Ii} P_L + \mathcal{R}_{Ii} P_R) (-\not{p} B_1 + m_{\tilde{g}} B_0) (\mathcal{L}'_{Ii} P_L + \mathcal{R}'_{Ii} P_R)
 \end{aligned}$$

$$\begin{aligned}
&= \frac{ig_s^2 C_F \delta_{\alpha\gamma}}{16\pi^2} \left(-\not{p} B_1 (\mathcal{R}_{Ii} \mathcal{L}'_{Ii} P_L + \mathcal{L}_{Ii} \mathcal{R}'_{Ii} P_R) + m_{\tilde{g}} B_0 (\mathcal{L}_{Ii} \mathcal{L}'_{Ii} P_L + \mathcal{R}_{Ii} \mathcal{R}'_{Ii} P_R) \right) \\
&= \frac{ig_s^2 C_F \delta_{\alpha\gamma}}{16\pi^2} \left(-\not{p} B_1 (\mathcal{R}_{Ii} \mathcal{L}'_{Ii} P_L + \mathcal{L}_{Ii} \mathcal{R}'_{Ii} P_R) \right)
\end{aligned} \tag{B.10}$$

Eq. (B.10) only holds for massless quarks because of the zero off-diagonal elements of the squark mixing matrix. For the parts of the decomposition we get

$$\Sigma_V^{L(\tilde{g}\tilde{q}_i)}(p^2, m_{\tilde{g}}^2, m_{\tilde{q}_i}^2) = \frac{g_s^2 C_F}{16\pi^2} B_1 \mathcal{R}_{Ii} \mathcal{L}'_{Ii}, \tag{B.11}$$

$$\Sigma_V^{R(\tilde{g}\tilde{q}_i)}(p^2, m_{\tilde{g}}^2, m_{\tilde{q}_i}^2) = \frac{g_s^2 C_F}{16\pi^2} B_1 \mathcal{L}_{Ii} \mathcal{R}'_{Ii}. \tag{B.12}$$

This leads to the following field renormalization counterterms:

$$\begin{aligned}
\delta Z_{qI}^{L(\tilde{g}\tilde{q}_i)} &= -\frac{g_s^2 C_F}{32\pi^2} \mathcal{R}_{Ii} \mathcal{L}'_{Ii} \Delta, & \delta Z_{qI}^{L(\tilde{g}\tilde{q})} &= \sum_{\tilde{q}_i} \delta Z_{qI}^{L(\tilde{g}\tilde{q}_i)} = -\frac{g_s^2 C_F}{16\pi^2} \Delta, \\
\delta Z_{qI}^{R(\tilde{g}\tilde{q}_i)} &= -\frac{g_s^2 C_F}{32\pi^2} \mathcal{L}_{Ii} \mathcal{R}'_{Ii} \Delta, & \delta Z_{qI}^{R(\tilde{g}\tilde{q})} &= \sum_{\tilde{q}_i} \delta Z_{qI}^{R(\tilde{g}\tilde{q}_i)} = -\frac{g_s^2 C_F}{16\pi^2} \Delta.
\end{aligned} \tag{B.13}$$

Squark self-energy

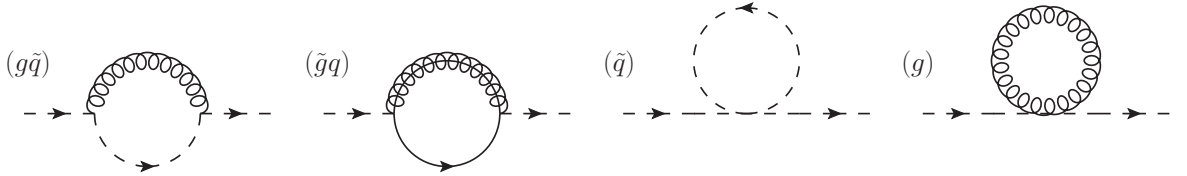


Figure B.2: Squark self-energy diagrams.

Gluon-squark contribution:

$$\begin{aligned}
-i\Sigma_{ij}^{(g\tilde{q}_i)}(p^2, 0, m_{\tilde{q}_i}^2) &= \mu^{4-D} g_s^2 \delta_{ij} \int \frac{d^D q}{(2\pi)^D} \frac{[-g_{\mu\nu}(2p^\mu + q^\mu) T_{\alpha\gamma}^a][(2p^\nu + q^\nu) T_{\gamma\beta}^a]}{q^2((q+p)^2 - m_{\tilde{q}_i}^2)} \\
&= -\mu^{4-D} g_s^2 C_F \delta_{\alpha\beta} \delta_{ij} \int \frac{d^D q}{(2\pi)^D} \frac{q^2 + 4q \cdot p + 4p^2}{q^2((q+p)^2 - m_{\tilde{q}_i}^2)} \\
&= -\frac{ig_s^2 C_F \delta_{\alpha\beta}}{16\pi^2} \delta_{ij} \left(B_\mu^\mu + 4B^\mu p_\mu + 4p^2 B_0 \right) \\
&= -\frac{ig_s^2 C_F \delta_{\alpha\beta}}{16\pi^2} \delta_{ij} \left(p^2 B_{11} + DB_{00} + 4p^2 (B_1 + B_0) \right)
\end{aligned} \tag{B.14}$$

Thereby, we get

$$\Sigma_{ij}^{(g\tilde{q}_i)}(p^2, 0, m_{\tilde{q}_i}^2) = \frac{g_s^2 C_F \delta_{\alpha\beta}}{16\pi^2} \delta_{ij} \left(p^2 B_{11} + DB_{00} + 4p^2(B_1 + B_0) \right) \quad (\text{B.15})$$

which leads to the following counterterms:

$$(\delta Z_m^{(g\tilde{q}_i)})^2 m_{\tilde{q}_i}^2 = - \frac{g_s^2 C_F}{16\pi^2} \text{Re} \left((p^2 B_{11} + DB_{00} + 4m_{\tilde{q}}^2(B_1 + B_0)) \right) \Big|_{p^2=m_{\tilde{q}_i}^2}, \quad (\text{B.16})$$

$$\delta Z_{ii}^{(g\tilde{q}_i)} = \frac{g_s^2 C_F}{8\pi^2} \Delta. \quad (\text{B.17})$$

The counterterms for $i \neq j$ vanish.

Gluino-quark contribution:

$$\begin{aligned} -i\Sigma_{ij}^{(\tilde{g}qI)}(p^2, m_{\tilde{g}}^2, 0) &= \mu^{4-D} g_s^2 \int \frac{d^D q}{(2\pi)^D} \frac{-\text{Tr} \left[(\mathcal{L}'_{Ij} P_L + \mathcal{R}'_{Ij} P_R) T_{\alpha\gamma}^a (\not{q} + m_{\tilde{g}}) (\mathcal{L}_{Ii} P_L + \mathcal{R}_{Ii} P_R) T_{\gamma\beta}^a (\not{q} + \not{p}) \right]}{(q^2 - m_{\tilde{g}}^2)(q+p)^2} \\ &= -\mu^{4-D} g_s^2 C_F \delta_{\alpha\beta} \int \frac{d^D q}{(2\pi)^D} \frac{\text{Tr} \left[(\mathcal{L}_{Ii} P_R + \mathcal{R}_{Ii} P_L) (\mathcal{L}'_{Ij} P_L + \mathcal{R}'_{Ij} P_R) (q^2 + \not{q}\not{p}) \right]}{(q^2 - m_{\tilde{g}}^2)(q+p)^2} \\ &= -\mu^{4-D} g_s^2 C_F \delta_{\alpha\beta} \int \frac{d^D q}{(2\pi)^D} \frac{\text{Tr} \left[(\mathcal{R}_{Ii} \mathcal{L}'_{Ij} P_L + \mathcal{L}_{Ii} \mathcal{R}'_{Ij} P_R) (q^2 + \not{q}\not{p}) \right]}{(q^2 - m_{\tilde{g}}^2)(q+p)^2} \\ &= -\mu^{4-D} g_s^2 C_F \delta_{\alpha\beta} \int \frac{d^D q}{(2\pi)^D} \frac{\frac{1}{2}(\mathcal{R}_{Ii} \mathcal{L}'_{Ij} + \mathcal{L}_{Ii} \mathcal{R}'_{Ij})(4q^2 + 4q \cdot p)}{(q^2 - m_{\tilde{g}}^2)(q+p)^2} \\ &= -\frac{ig_s^2 C_F \delta_{\alpha\beta}}{8\pi^2} (\mathcal{R}_{Ii} \mathcal{L}'_{Ij} + \mathcal{L}_{Ii} \mathcal{R}'_{Ij}) (p^2(B_{11} + B_1) + DB_{00}). \end{aligned} \quad (\text{B.18})$$

This leads to

$$\Sigma_{ij}^{(\tilde{g}q)}(p^2, m_{\tilde{g}}^2, 0) = \sum_{qI} \frac{g_s^2 C_F \delta_{\alpha\beta}}{8\pi^2} (\mathcal{R}_{Ii} \mathcal{L}'_{Ij} + \mathcal{L}_{Ii} \mathcal{R}'_{Ij}) (p^2(B_{11} + B_1) + DB_{00}). \quad (\text{B.19})$$

The counterterms for $i = j$ are

$$\begin{aligned} (\delta Z_m^{(\tilde{g}q)})^2 m_{\tilde{q}_i}^2 &= - \sum_{qI} \frac{g_s^2 C_F \delta_{ij}}{8\pi^2} \text{Re} \left((\mathcal{R}_{Ii} \mathcal{L}'_{Ij} + \mathcal{L}_{Ii} \mathcal{R}'_{Ij}) (p^2(B_{11} + B_1) + DB_{00}) \right) \Big|_{p^2=m_{\tilde{q}_i}^2} \\ &= -\frac{g_s^2 C_F \delta_{ij}}{4\pi^2} \text{Re} \left((p^2(B_{11} + B_1) + DB_{00}) \right) \Big|_{p^2=m_{\tilde{q}_i}^2}, \end{aligned} \quad (\text{B.20})$$

$$\delta Z_{ii}^{(\tilde{g}q)} = -\frac{g_s^2 C_F}{8\pi^2} \Delta. \quad (\text{B.21})$$

For $i \neq j$ we get

$$\begin{aligned} \delta Z_{ij}^{(\tilde{g}q)} &= -\frac{g_s^2 C_F}{8\pi^2 (m_{\tilde{q}_i}^2 - m_{\tilde{q}_j}^2)} \sum_{q_I} (\mathcal{R}_{Ii} \mathcal{L}'_{Ij} + \mathcal{L}_{Ii} \mathcal{R}'_{Ij}) \Delta = 0 \\ &= -\delta Z_{ji}^{(\tilde{g}q)*}. \end{aligned} \quad (\text{B.22})$$

This counterterm is only zero for zero off-diagonal elements of the squark mixing matrix.

Squark and gluon tadpoles: The remaining two self-energy contributions are the squark and the gluon tadpole. The former gets completely canceled by the mass renormalization counterterm and the latter is proportional to $A_0(0) = 0$ and hence vanishes as well [128].

Gluino self-energy

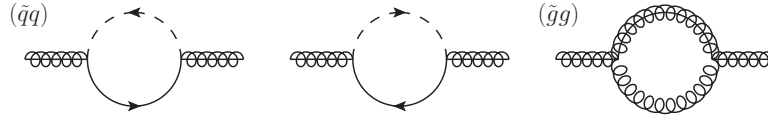


Figure B.3: Gluino self-energy diagrams. Fermion flow goes from left to right.

Squark-quark contribution: The first two contributions only differ in the charge flow. For both contributions we fix the fermion flow going from left to right. The sum of both contributions yields

$$\begin{aligned} -i\Sigma^{(\tilde{q}_i q_I)}(p^2, m_{q_I}^2, m_{\tilde{q}_i}^2) &= \mu^{4-D} \int \frac{d^D q}{(2\pi)^D} \left[\frac{g_s^2 (\mathcal{L}'_{Ii} P_L + \mathcal{R}'_{Ii} P_R) T_{\alpha\beta}^a (\not{q} + m_{q_I}) (\mathcal{L}_{Ii} P_L + \mathcal{R}_{Ii} P_R) T_{\beta\alpha}^b}{(q^2 - m_{q_I}^2) ((q-p)^2 - m_{\tilde{q}_i}^2)} \right. \\ &\quad \left. + \frac{g_s^2 (\mathcal{L}_{Ii} P_L + \mathcal{R}_{Ii} P_R) T_{\beta\alpha}^a (\not{q} + m_{q_I}) (\mathcal{L}'_{Ii} P_L + \mathcal{R}'_{Ii} P_R) T_{\alpha\beta}^b}{(q^2 - m_{q_I}^2) ((q-p)^2 - m_{\tilde{q}_i}^2)} \right] \\ &= \frac{ig_s^2 \delta^{ab}}{32\pi^2} \left[(\mathcal{L}'_{Ii} P_L + \mathcal{R}'_{Ii} P_R) (-\not{p} B_1 + m_{q_I} B_0) (\mathcal{L}_{Ii} P_L + \mathcal{R}_{Ii} P_R) \right. \\ &\quad \left. + (\mathcal{L}_{Ii} P_L + \mathcal{R}_{Ii} P_R) (-\not{p} B_1 + m_{q_I} B_0) (\mathcal{L}'_{Ii} P_L + \mathcal{R}'_{Ii} P_R) \right] \\ &= \frac{-ig_s^2 \delta^{ab}}{32\pi^2} \left[\not{p} B_1 [(\mathcal{R}'_{Ii} \mathcal{L}_{Ii} + \mathcal{R}_{Ii} \mathcal{L}'_{Ii}) P_L + (\mathcal{L}'_{Ii} \mathcal{R}_{Ii} + \mathcal{L}_{Ii} \mathcal{R}'_{Ii}) P_R] \right. \\ &\quad \left. - 2m_{q_I} B_0 (\mathcal{L}'_{Ii} \mathcal{L}_{Ii} P_L + \mathcal{R}'_{Ii} \mathcal{R}_{Ii} P_R) \right]. \end{aligned} \quad (\text{B.23})$$

This gives the following vector and scalar parts of the self-energy decomposition:

$$\Sigma_V^{L(\tilde{q}_i q_I)} = \frac{g_s^2}{32\pi^2} (\mathcal{R}'_{Ii} \mathcal{L}_{Ii} + \mathcal{R}_{Ii} \mathcal{L}'_{Ii}) B_1, \quad (\text{B.24})$$

$$\Sigma_V^{R(\tilde{q}_i q_I)} = \frac{g_s^2}{32\pi^2} (\mathcal{L}'_{Ii} \mathcal{R}_{Ii} + \mathcal{L}_{Ii} \mathcal{R}'_{Ii}) B_1, \quad (\text{B.25})$$

$$\Sigma_S^{L(\tilde{q}_i q_I)} = -\frac{g_s^2}{16\pi^2} m_{q_I} \mathcal{L}'_{Ii} \mathcal{L}_{Ii} B_0, \quad (\text{B.26})$$

$$\Sigma_S^{R(\tilde{q}_i q_I)} = -\frac{g_s^2}{16\pi^2} m_{q_I} \mathcal{R}'_{Ii} \mathcal{R}_{Ii} B_0. \quad (\text{B.27})$$

The mass and field counterterms are

$$\begin{aligned} \delta Z_m^{(\tilde{q}q)} = & - \sum_{\tilde{q}_i, q_I} \frac{g_s^2}{64\pi^2} \text{Re} \left[B_1 (\mathcal{R}'_{Ii} \mathcal{L}_{Ii} + \mathcal{R}_{Ii} \mathcal{L}'_{Ii} + \mathcal{L}'_{Ii} \mathcal{R}_{Ii} + \mathcal{L}_{Ii} \mathcal{R}'_{Ii}) \right. \\ & \left. - 2B_0 \frac{m_{q_I}}{m_{\tilde{g}}} (\mathcal{L}'_{Ii} \mathcal{L}_{Ii} + \mathcal{R}'_{Ii} \mathcal{R}_{Ii}) \right]_{p^2=m_{\tilde{g}}^2}, \end{aligned} \quad (\text{B.28})$$

$$\delta Z_{\tilde{g}}^{L(\tilde{q}_i q_I)} = -\frac{g_s^2}{64\pi^2} (\mathcal{R}'_{Ii} \mathcal{L}_{Ii} + \mathcal{R}_{Ii} \mathcal{L}'_{Ii}) \Delta, \quad (\text{B.29})$$

$$\delta Z_{\tilde{g}}^{R(\tilde{q}_i q_I)} = -\frac{g_s^2}{64\pi^2} (\mathcal{L}'_{Ii} \mathcal{R}_{Ii} + \mathcal{L}_{Ii} \mathcal{R}'_{Ii}) \Delta. \quad (\text{B.30})$$

Summing over the internal quarks q_I and left- and right-handed squarks \tilde{q}_i yields

$$\delta Z_{\tilde{g}}^{L(\tilde{q}q)} = \sum_{\tilde{q}_i, q_I} \delta Z_{\tilde{g}}^{L(\tilde{q}_i q_I)} = -\frac{g_s^2}{16\pi^2} (n_f + 1) \Delta, \quad (\text{B.31})$$

$$\delta Z_{\tilde{g}}^{R(\tilde{q}q)} = \sum_{\tilde{q}_i, q_I} \delta Z_{\tilde{g}}^{R(\tilde{q}_i q_I)} = -\frac{g_s^2}{16\pi^2} (n_f + 1) \Delta. \quad (\text{B.32})$$

Gluino-gluon contribution:

$$\begin{aligned} -i\Sigma^{(\tilde{g}g)}(p^2, m_{\tilde{g}}^2, 0) &= \mu^{4-D} \int \frac{d^D q}{(2\pi)^D} \frac{(g_s f_{bdc} \gamma^\mu) (-ig_{\mu\nu}) i(\not{q} + m_{\tilde{g}}) (g_s f_{dac} \gamma^\nu)}{(q^2 - m_{\tilde{g}}^2)(q-p)^2} \\ &= \frac{ig_s^2 (-C_A \delta^{ab})}{16\pi^2} \left[(2-D)(-\not{p}) B_1 + D m_{\tilde{g}} B_0 \right] \\ &= \frac{ig_s^2 C_A \delta^{ab}}{16\pi^2} \left[2(\epsilon-1) \not{p} B_1 - 2(2-\epsilon) m_{\tilde{g}} B_0 \right] \end{aligned} \quad (\text{B.33})$$

We get the following parts of the self-energy decomposition:

$$\Sigma_V^{(\tilde{g}g)} = -\frac{g_s^2 C_A}{8\pi^2} (\epsilon - 1) B_1, \quad (\text{B.34})$$

$$\Sigma_S^{(\tilde{g}g)} = \frac{g_s^2 C_A}{8\pi^2} (2 - \epsilon) m_{\tilde{g}} B_0. \quad (\text{B.35})$$

The mass and field counterterms are

$$\delta Z_m^{(\tilde{g}g)} = \frac{g_s^2 C_A}{8\pi^2} \text{Re}((\epsilon - 1) B_1 + (\epsilon - 2) B_0)_{p^2 = m_{\tilde{g}}^2}, \quad (\text{B.36})$$

$$\delta Z_{\tilde{g}}^{(\tilde{g}g)} = -\frac{g_s^2 C_A}{16\pi^2} \Delta. \quad (\text{B.37})$$

Vertex corrections

In this section we present the results of the vertex corrections. The momentum configuration is defined in the left Feynman diagram of Fig. B.4. The argument set of the resulting scalar and tensor integrals is $a = p_1^2, p_2^2, (p_1 + p_2)^2, m_1^2, m_2^2, m_3^2$. Different contributions to a vertex correction are labeled by the particles appearing in the loop. We remark that a sum over all particles inside the loop is implied and hence not written explicitly. No top quark can appear in the loop correction due to flavor conservation. Therefore, we set the quark masses to zero. For the sake of convenience we do not show the indices of the coupling coefficients. They can be inserted by using the Feynman rules of Fig. A.1.

Antisquark-quark-gaugino vertex

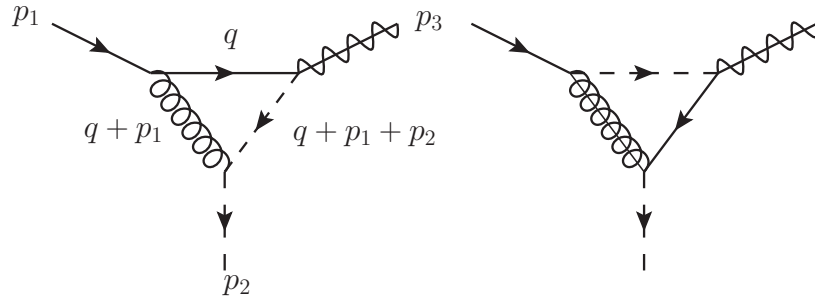


Figure B.4: Virtual correction diagrams for the antisquark-quark-gaugino vertex. All external momenta are directed into the loop. The argument set of the resulting scalar and tensor integrals is $a = p_1^2, p_2^2, (p_1 + p_2)^2, m_1^2, m_2^2, m_3^2$. For the diagram on the left this leads to $a = p_q^2, p_{\bar{q}}^2, (p_q + p_{\bar{q}})^2, m_q^2, 0, m_{\tilde{g}}^2$.

Quark-gluon-squark contribution:

$$\begin{aligned}
\Lambda &= \mu^{4-D} \int \frac{d^D q}{(2\pi)^D} g_s^2 (T_{\beta\alpha'} T_{\alpha'\alpha}) \frac{(L' P_L + R' P_R)(-\not{q})(g_s \gamma^\mu)(-q - 2p_2 - p_1)_\mu}{q^2(q+p_1)^2 \left((q+p_1+p_2)^2 - m_{\tilde{q}}^2 \right)} \\
&= C_F \delta_{\beta\alpha} g_s^2 \mu^{4-D} \int \frac{d^D q}{(2\pi)^D} \frac{\left(q^2 + \not{q}(2\not{p}_2 + \not{p}_1) \right) (L' P_L + R' P_R)}{q^2(q+p_1)^2 \left((q+p_1+p_2)^2 - m_{\tilde{q}}^2 \right)} \\
&= \frac{i}{16\pi^2} g_s^2 C_F \delta_{\beta\alpha} \left(C^{\mu\mu} + \gamma_\mu C^\mu (2\not{p}_2 + \not{p}_1) \right) (L' P_L + R' P_R) \\
&=: \frac{g_s^2}{16\pi^2} C_F \left(C^{\mu\mu} + \gamma_\mu C^\mu (2\not{p}_2 + \not{p}_1) \right) \Lambda^{(0)}. \tag{B.38}
\end{aligned}$$

Here, $\Lambda^{(0)} = i(L' P_L + R' P_R) \delta_{\beta\alpha}$ denotes the LO vertex (see Fig. A.1). We remark that this contribution is IR divergent and contains $1/\epsilon_{IR}$ poles.

Squark-gluino-quark contribution: For the sake of convenience we use the abbreviation $\Gamma_i = C_L^i P_L + C_R^i P_R$ for the vertices, where i denotes the external particle going into the loop. In addition, we define $\Gamma'_i := C_R^i P_L + C_L^i P_R$ and fix the fermion flow in such a way that it is aligned with the charge flow of the external quark.

$$\begin{aligned}
\Lambda &= \mu^{4-D} \int \frac{d^D q}{(2\pi)^D} g_s^2 C_F \delta_{\beta\alpha} \frac{(i\Gamma_{\tilde{\chi}})i(\not{q} + \not{p}_1 + \not{p}_2)(i\Gamma_{\tilde{q}})i(\not{q} + \not{p}_1 + m_{\tilde{g}})(i\Gamma_q)i}{(q^2 - m_{\tilde{q}}^2) \left((q+p_1)^2 - m_{\tilde{g}}^2 \right) (q+p_1+p_2)^2} \\
&= -\mu^{4-D} \int \frac{d^D q}{(2\pi)^D} g_s^2 C_F \delta_{\beta\alpha} \frac{\Gamma_{\tilde{\chi}} \Gamma'_q (\not{q} + \not{p}_1 + \not{p}_2)(\not{q} + \not{p}_1 + m_{\tilde{g}}) \Gamma_q}{(q^2 - m_{\tilde{q}}^2) \left((q+p_1)^2 - m_{\tilde{g}}^2 \right) (q+p_1+p_2)^2} \\
&= \frac{-i}{16\pi^2} g_s^2 C_F \delta_{\beta\alpha} \Gamma_{\tilde{\chi}} \Gamma'_q \left[C^{\mu\mu} + C^\mu \left(\{\gamma_\mu, \not{p}_1\} + (\not{p}_2 + m_{\tilde{g}}) \gamma_\mu \right) \right. \\
&\quad \left. + C^0 \left(p_1^2 + \not{p}_2 \not{p}_1 + m_{\tilde{g}} (\not{p}_1 + \not{p}_2) \right) \right] \Gamma_q \\
&= \frac{-g_s^2}{16\pi^2} C_F \Lambda^{(0)} (\mathcal{R}' P_L + \mathcal{L}' P_R) \left[C^{\mu\mu} + C^\mu \left(2p_{1\mu} + (\not{p}_2 + m_{\tilde{g}}) \gamma_\mu \right) \right. \\
&\quad \left. + C^0 \left(p_1^2 + \not{p}_2 \not{p}_1 + m_{\tilde{g}} (\not{p}_1 + \not{p}_2) \right) \right] (\mathcal{L}' P_L + \mathcal{R}' P_R). \tag{B.39}
\end{aligned}$$

Here, $\{\gamma_\mu, \not{p}_1\} = 2p_{1\mu}$ is the anticommutator and $\Lambda^{(0)}$ is the LO coupling. This diagram is IR finite.

Antisquark-quark-gluino vertex

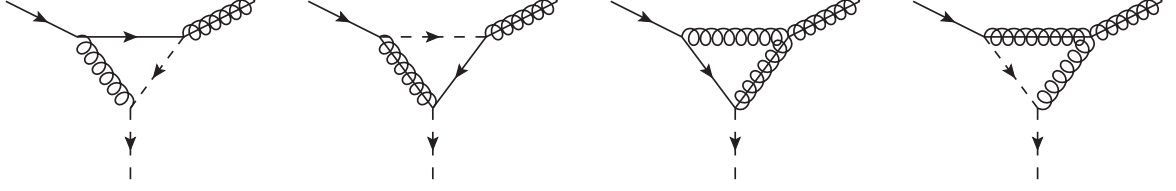


Figure B.5: Virtual correction diagrams for the antisquark-quark-gluino vertex.

Quark-gluon-squark contribution: This vertex correction is similar to the result in Eq. (B.38). We only have to adapt the color factor and the coupling coefficients. This yields

$$\begin{aligned}
 \Lambda &= \frac{i}{16\pi^2} g_s^2 [T^a T^b T^a]_{\beta\alpha} \left(C^{\mu\mu} + \gamma_\mu C^\mu (2\not{p}_2 + \not{p}_1) \right) (\mathcal{L}' P_L + \mathcal{R}' P_R) \\
 &= \frac{i}{16\pi^2} g_s^2 \frac{-T_{\beta\alpha}^b}{2C_A} \left(C^{\mu\mu} + \gamma_\mu C^\mu (2\not{p}_2 + \not{p}_1) \right) (\mathcal{L}' P_L + \mathcal{R}' P_R) \\
 &=: \frac{-g_s^2}{16\pi^2} \frac{1}{2C_A} \left(C^{\mu\mu} + \gamma_\mu C^\mu (2\not{p}_2 + \not{p}_1) \right) \Lambda^{(0)}. \tag{B.40}
 \end{aligned}$$

Squark-gluino-quark contribution: By adapting the color factor we can reuse the result in Eq. (B.39). This yields

$$\begin{aligned}
 \Lambda &= \frac{g_s^2}{16\pi^2} \frac{1}{2C_A} \Lambda^{(0)} (\mathcal{R}' P_L + \mathcal{L}' P_R) \left[C^{\mu\mu} + C^\mu (2p_{1\mu} + (\not{p}_2 + m_{\tilde{g}}) \gamma_\mu) \right. \\
 &\quad \left. + C^0 (p_1^2 + \not{p}_2 \not{p}_1 + m_{\tilde{g}} (\not{p}_1 + \not{p}_2)) \right] (\mathcal{L}' P_L + \mathcal{R}' P_R). \tag{B.41}
 \end{aligned}$$

Gluon-quark-gluino contribution:

$$\begin{aligned}
 \Lambda &= \mu^{4-D} \int \frac{d^D q}{(2\pi)^D} g_s^2 g_s (-i) [f^{bb'a} T_{\beta\alpha'}^{b'} T_{\alpha'\alpha}^a] \frac{\gamma^\mu (\not{q} + \not{p}_1 + \not{p}_2 + m_{\tilde{g}}) (\mathcal{L}' P_L + \mathcal{R}' P_R) (\not{q} + \not{p}_1) \gamma_\mu}{q^2 (q + p_1)^2 ((q + p_1 + p_2)^2 - m_{\tilde{g}}^2)} \\
 &= \mu^{4-D} \int \frac{d^D q}{(2\pi)^D} g_s^2 g_s \frac{T_{\beta\alpha}^b C_A}{2} \frac{\gamma^\mu (\not{q} + \not{p}_1 + \not{p}_2 + m_{\tilde{g}}) (\not{q} + \not{p}_1) \gamma_\mu (\mathcal{L}' P_L + \mathcal{R}' P_R)}{q^2 (q + p_1)^2 ((q + p_1 + p_2)^2 - m_{\tilde{g}}^2)} \\
 &= \frac{i}{16\pi^2} g_s^2 g_s \frac{T_{\beta\alpha}^b C_A}{2} \gamma^\mu \left[C^{\nu\nu} + C^\nu (\{\gamma_\nu, \not{p}_1\} + (\not{p}_2 + m_{\tilde{g}}) \gamma_\nu) + C^0 (p_1^2 + \not{p}_2 \not{p}_1 + \not{p}_1 m_{\tilde{g}}) \right] \\
 &\quad \times \gamma_\mu (\mathcal{L}' P_L + \mathcal{R}' P_R)
 \end{aligned}$$

$$=: \frac{1}{16\pi^2} g_s^2 \frac{C_A}{2} \gamma^\mu \left[C^{\nu\nu} + C^\nu (2p_{1\nu} + \not{p}_2 \gamma_\nu + \gamma_\nu m_{\tilde{g}}) + C^0 (p_1^2 + \not{p}_2 \not{p}_1 + \not{p}_1 m_{\tilde{g}}) \right] \gamma_\mu \Lambda^{(0)}. \quad (\text{B.42})$$

This diagram is IR divergent and contains $1/\epsilon_{IR}$ and $1/\epsilon_{IR}^2$ poles.

Gluino-squark-gluon contribution:

$$\begin{aligned} \Lambda &= \mu^{4-D} \int \frac{d^D q}{(2\pi)^D} g_s^2 g_s [f^{bb'a} T_{\beta\alpha'}^a T_{\alpha'\alpha}^{b'}] \frac{(-\gamma^\mu) i(-\not{q} + m_{\tilde{g}}) i(\mathcal{L}' P_L + \mathcal{R}' P_R) (-i)(q + p_1 - p_2)_\mu (-i)i}{(q^2 - m_{\tilde{g}}^2) \left((q + p_1)^2 - m_{\tilde{q}}^2 \right) (q + p_1 + p_2)^2} \\ &= \mu^{4-D} \int \frac{d^D q}{(2\pi)^D} g_s^2 g_s \frac{T_{\beta\alpha}^b}{2C_A} \frac{(\not{q} + \not{p}_1 - \not{p}_2)(\not{q} - m_{\tilde{g}})(\mathcal{L}' P_L + \mathcal{R}' P_R)}{(q^2 - m_{\tilde{g}}^2) \left((q + p_1)^2 - m_{\tilde{q}}^2 \right) (q + p_1 + p_2)^2} \\ &= \frac{i}{16\pi^2} \frac{C_A}{2} T_{\beta\alpha}^b g_s^2 g_s \left(C^{\mu\mu} + C^\mu (\not{p}_1 - \not{p}_2 - m_{\tilde{g}}) \gamma_\mu + C_0 m_{\tilde{g}} (\not{p}_1 - \not{p}_2) \right) (\mathcal{L}' P_L + \mathcal{R}' P_R) \\ &=: \frac{g_s^2 C_A}{32\pi^2} \left(C^{\mu\mu} + C^\mu (\not{p}_1 - \not{p}_2 - m_{\tilde{g}}) \gamma_\mu + C_0 m_{\tilde{g}} (\not{p}_1 - \not{p}_2) \right) \Lambda^{(0)}. \quad (\text{B.43}) \end{aligned}$$

This diagram is IR finite.

Quark-antiquark-electroweak vector boson vertex

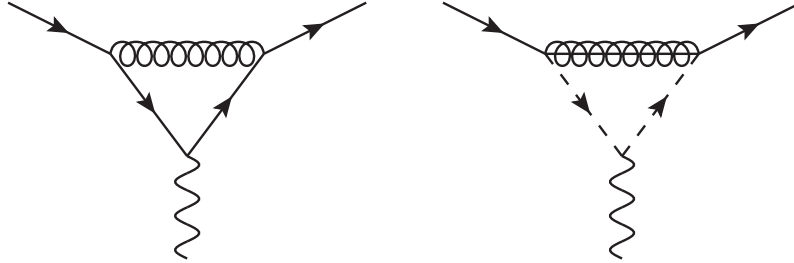


Figure B.6: Virtual correction diagrams for the quark-antiquark-electroweak vector boson vertex.

Gluon-quark-quark contribution:

$$\begin{aligned} \Lambda^\mu &= -\mu^{4-D} \int \frac{d^D q}{(2\pi)^D} e g_s^2 C_F \delta_{\beta\alpha} \frac{\gamma_\nu (\not{q} + \not{p}_1 + \not{p}_2) \gamma^\mu (\mathcal{L} P_L + \mathcal{R} P_R) (\not{q} + \not{p}_1) \gamma^\nu}{q^2 (q + p_1)^2 (q + p_1 + p_2)^2} \\ &= -\mu^{4-D} \int \frac{d^D q}{(2\pi)^D} e g_s^2 C_F \delta_{\beta\alpha} \frac{\gamma_\nu (\not{q} + \not{p}_1 + \not{p}_2) \gamma^\mu (\not{q} + \not{p}_1) \gamma^\nu (\mathcal{L} P_L + \mathcal{R} P_R)}{q^2 (q + p_1)^2 (q + p_1 + p_2)^2} \\ &= -\mu^{4-D} \int \frac{d^D q}{(2\pi)^D} e g_s^2 C_F \delta_{\beta\alpha} \frac{\gamma_\nu \gamma_\rho \gamma^\mu \gamma^{\rho'} \gamma^\nu (q + p_1 + p_2)^\rho (q + p_1)_{\rho'} (\mathcal{L} P_L + \mathcal{R} P_R)}{q^2 (q + p_1)^2 (q + p_1 + p_2)^2} \end{aligned}$$

$$= \frac{g_s^2 C_F}{16\pi^2} \gamma_\nu \gamma_\rho \Lambda^{(0)\mu} \gamma^{\rho'} \gamma^\nu \left[C_{\rho'}^\rho + C_{\rho'} (p_1 + p_2)^\rho + C^\rho p_{1\rho'} + C_0 [(p_1 + p_2)^\rho p_{1\rho'}] \right]. \quad (\text{B.44})$$

This diagram is IR divergent and contains $1/\epsilon_{IR}$ and $1/\epsilon_{IR}^2$ poles.

Gluino-squark-squark contribution:

$$\begin{aligned} \Lambda^\mu &= -\mu^{4-D} g_s^2 e C \delta_{\beta\alpha} C_F \\ &\times \int \frac{d^D q}{(2\pi)^D} (2q^\mu + 2p_1^\mu + p_2^\mu) \frac{(\mathcal{L}P_L + \mathcal{R}P_R)(-\not{q} + m_{\tilde{g}})(\mathcal{L}'P_L + \mathcal{R}'P_R)}{(q^2 - m_{\tilde{g}}^2) \left((q + p_1)^2 - m_{\tilde{q}}^2 \right) \left((q + p_1 + p_2)^2 - m_{\tilde{q}}^2 \right)} \\ &= \frac{ig_s^2 e C}{16\pi^2} C_F \delta_{\beta\alpha} (\mathcal{L}P_L + \mathcal{R}P_R) \left[\gamma_\nu (2C^{\mu\nu} + C^\nu (2p_1^\mu + p_2^\mu)) \right. \\ &\quad \left. - 2m_{\tilde{g}} C^\mu - m_{\tilde{g}} (2p_1^\mu + p_2^\mu) C_0 \right] (\mathcal{L}'P_L + \mathcal{R}'P_R). \end{aligned} \quad (\text{B.45})$$

This diagram is IR finite.

C Plus-Distribution

The plus-distribution is defined by its action on an integrand as

$$\int_0^1 [g(x)]_+ f(x) dx := \int_0^1 g(x) [f(x) - f(1)] dx \quad (\text{C.1})$$

and can be represented as [38, Eq. 4.73]

$$[g(x)]_+ := \lim_{\beta \rightarrow 0} \left(g(x) \theta(1 - \beta - x) - \delta(1 - \beta - x) \int_0^{1-\beta} g(y) dy \right). \quad (\text{C.2})$$

This distribution is often introduced after the cancellation of the IR divergences among the virtual and real corrections (see Sec. 3.2). We encounter it in terms of the collinear remainder, which contain diagonal parton splitting functions. If we have massive final state particles the lower integration boundary will not be zero, but $z = (m_1 + m_2)^2/s$, where m_1 and m_2 are the masses of the final state particles and s is the invariant mass of the initial state. Hence, we have to subtract a finite term in order to make use of the definition of the plus-distribution. This leads to

$$\begin{aligned} \int_z^1 [g(x)]_+ f(x) dx &= \int_0^1 [g(x)]_+ f(x) dx - \int_0^z [g(x)]_+ f(x) dx \\ &= \int_0^1 g(x) [f(x) - f(1)] dx - \int_0^z g(x) f(1) dx. \end{aligned} \quad (\text{C.3})$$

The subtraction term can lead to complicated integrals which often contain the dilogarithmic function Li_2 defined as

$$\text{Li}_2(z) := \int_z^0 dt \ln(1 - t)/t = \sum_{k=1}^{\infty} z^k/k^2. \quad (\text{C.4})$$

For instance, in the insertion operator \mathbf{K} we encounter the integral

$$\int_0^z \frac{2}{1-x} \ln\left(\frac{1-x}{x}\right) dx = \frac{\pi^2}{3} - \ln^2(1-z) - 2\text{Li}_2(1-z). \quad (\text{C.5})$$

D Mellin Transform of the PDFs

In order to use the resummation formula in Eq. (4.17) we need the Mellin transforms of the PDFs. These are obtained by fitting the functional form used by the MSTW [103] collaboration

$$f(x) = A_0 x^{A_1} (1-x)^{A_2} \left(1 + A_3 \sqrt{x} + A_4 x + A_5 x^{\frac{3}{2}} + A_6 x^2 + A_7 x^{\frac{5}{2}} \right), \quad (\text{D.1})$$

to the parameterizations tabulated in x -space. Eq. (D.1) has the advantage that it can be transformed analytically with the result

$$F(x) = A_0 \Gamma(y) \left[B'(A_1 + N, y) + A_3 B' \left(A_1 + N + \frac{1}{2}, y \right) + A_4 B'(A_1 + N + 1, y) \right. \\ \left. + A_5 B' \left(A_1 + N + \frac{3}{2}, y \right) + A_6 B'(A_1 + N + 2, y) + A_7 B' \left(A_1 + N + \frac{5}{2}, y \right) \right], \quad (\text{D.2})$$

where $y = A_2 + 1$ and $B'(x, y) = B(x, y)/\Gamma(y) = \Gamma(x)/\Gamma(x + y)$. Here, B and Γ are the Euler beta and Euler gamma functions, respectively. In Fig. D.1 we present our obtained fits

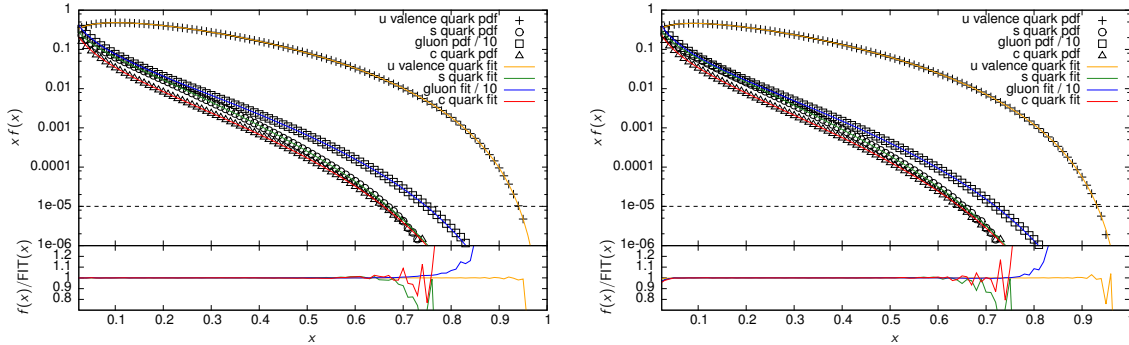


Figure D.1: Upper panel: Momentum distribution of MSTW2008NLO90CL PDF at $\mu_F = 500$ GeV (left) and $\mu_F = 3500$ GeV (right) for the up valence quark, the strange and charm sea quarks and the gluon as points and their corresponding performed fits as solid lines. Lower panel: Ratio of the fits to the PDFs.

for different partons using the MSTW2008NLO90CL PDF and factorization scale values of $\mu_F = 500$ GeV (left) and $\mu_F = 3500$ GeV (right). We observe a very good agreement for x values up to 0.7. The ratio (lower panel) starts to get worse for higher x . However, in this region the momentum distribution has already dropped to a value below 10^{-5} and hence this

discrepancy is negligible. We obtain similar results for CT10NLO fits (see Fig. D.2), even though they use an ansatz including an exponential function. We have also verified that we obtain good fits for the more recent CT14NLO and MMHT2014NLO118 PDFs.

The fits to the NNPDF30 PDFs are depicted in Fig. D.3 and are less stable compared to the previous ones. We find a large discrepancy in the large x -region for lower scales and in the small and large x -region for higher scales. Further investigations are needed to improve these fits. For instance, one could try to scan different weights or use another parameterization. Since our fits for NNPDF-like PDFs are not satisfying yet, we use another approach: we compute only NLO results and scale them with an (approximately PDF-independent) κ -factor, i.e. the ratio of NLL+NLO over NLO cross sections using stable (e.g. CT10NLO) PDFs and then multiply with it the NLO calculation convoluted with NNPDFs directly in x -space.

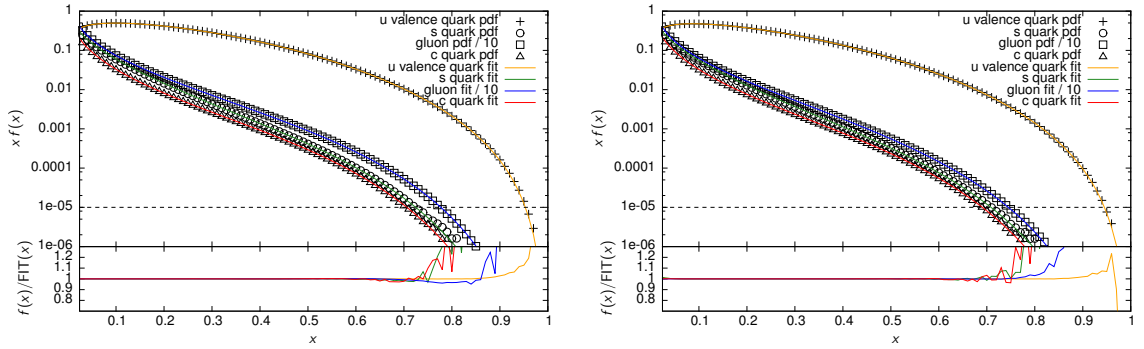


Figure D.2: Same as in Fig. D.1, but using CT10NLO as the PDF.

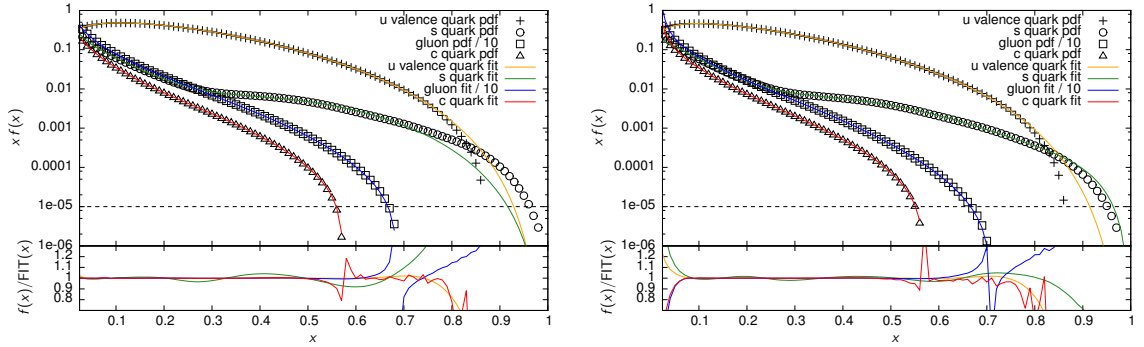


Figure D.3: Same as in Fig. D.1, but using NNPDF30_nlo_as_0118 as the PDF.

There are also other approaches like a numerical Mellin transform of the PDFs which is discussed in Ref. [69]. This method could be used in the future as it has been shown that it also works with NNPDF-like PDFs. However, for the collinear improved resummation formula where the DGLAP-equations are solved in Mellin space it is much more feasible to have an analytical Mellin transform of the PDFs.

Bibliography

- [1] M. K. Gaillard, P. D. Grannis, and F. J. Sciulli, “The Standard model of particle physics,” *Rev. Mod. Phys.*, vol. 71, pp. S96–S111, 1999.
- [2] T. Aoyama, M. Hayakawa, T. Kinoshita, and M. Nio, “Quantum electrodynamics calculation of lepton anomalous magnetic moments: Numerical approach to the perturbation theory of qed,” *Progress of Theoretical and Experimental Physics*, 2012.
- [3] G. Aad *et al.*, “Observation of a new particle in the search for the Standard Model Higgs boson with the ATLAS detector at the LHC,” *Phys. Lett.*, vol. B716, pp. 1–29, 2012.
- [4] G. Altarelli, “The Higgs: so simple yet so unnatural,” *Phys. Scripta*, vol. T158, 2013.
- [5] V. F. Weisskopf, “On the self-energy and the electromagnetic field of the electron,” *Phys. Rev.*, vol. 56, pp. 72–85, Jul 1939.
- [6] S. Weinberg, “Implications of Dynamical Symmetry Breaking,” *Phys. Rev.*, vol. D13, pp. 974–996, 1976.
- [7] M. Drees, R. Godbole, and P. Roy, *Theory and phenomenology of sparticles: An account of four-dimensional N=1 supersymmetry in high energy physics*. 2004.
- [8] S. P. Martin, “A Supersymmetry primer,” 1997. [Adv. Ser. Direct. High Energy Phys.18,1(1998)].
- [9] G. Hinshaw *et al.*, “Nine-Year Wilkinson Microwave Anisotropy Probe (WMAP) Observations: Cosmological Parameter Results,” *Astrophys. J. Suppl.*, vol. 208, p. 19, 2013.
- [10] R. Adam *et al.*, “Planck 2015 results. I. Overview of products and scientific results,” 2015.
- [11] K. Garrett and G. Duda, “Dark Matter: A Primer,” *Adv. Astron.*, vol. 2011, p. 968283, 2011.
- [12] A. D. Sakharov, “Violation of CP Invariance, c Asymmetry, and Baryon Asymmetry of the Universe,” *Pisma Zh. Eksp. Teor. Fiz.*, vol. 5, pp. 32–35, 1967. [Usp. Fiz. Nauk161,61(1991)].
- [13] J. M. Cline, “Baryogenesis,” in *Les Houches Summer School - Session 86: Particle Physics and Cosmology: The Fabric of Spacetime Les Houches, France, July 31-August 25*, 2006.

- [14] M. Carena, G. Nardini, M. Quiros, and C. E. M. Wagner, “MSSM Electroweak Baryogenesis and LHC Data,” *JHEP*, vol. 02, p. 001, 2013.
- [15] W. Buchmüller, “Baryogenesis: 40 Years Later,” in *Proceedings on 13th International Symposium on Particles, strings, and cosmology (PASCOS 2007)*, 2007.
- [16] S. Liebler, S. Profumo, and T. Stefaniak, “Light Stop Mass Limits from Higgs Rate Measurements in the MSSM: Is MSSM Electroweak Baryogenesis Still Alive After All?,” *JHEP*, vol. 04, p. 143, 2016.
- [17] S. Davidson, E. Nardi, and Y. Nir, “Leptogenesis,” *Phys. Rept.*, vol. 466, pp. 105–177, 2008.
- [18] I. Affleck and M. Dine, “A new mechanism for baryogenesis,” *Nuclear Physics B*, vol. 249, no. 2, pp. 361 – 380, 1985.
- [19] S. R. Coleman and J. Mandula, “All Possible Symmetries of the S Matrix,” *Phys. Rev.*, vol. 159, pp. 1251–1256, 1967.
- [20] R. Haag, J. T. Łopuszański, and M. Sohnius, “All possible generators of supersymmetries of the S-matrix,” *Nuclear Physics B*, vol. 88, no. 2, pp. 257 – 274, 1975.
- [21] M. Robinson, *Symmetry and the Standard Model: Mathematics and Particle Physics*. SpringerLink : Bücher, Springer New York, 2011.
- [22] J. Wess and B. Zumino, “Supergauge Transformations in Four-Dimensions,” *Nucl. Phys.*, vol. B70, pp. 39–50, 1974.
- [23] P. Bechtle *et al.*, “Killing the cMSSM softly,” *Eur. Phys. J.*, vol. C76, no. 2, p. 96, 2016.
- [24] P. Z. Skands *et al.*, “SUSY Les Houches accord: Interfacing SUSY spectrum calculators, decay packages, and event generators,” *JHEP*, vol. 07, p. 036, 2004.
- [25] J. Debove, *QCD resummation for gaugino-pair hadroproduction*. PhD thesis, U. Grenoble, 2010.
- [26] B. Fuks, *QCD-resummation and non-minimal-flavour violation for supersymmetric particle productions at hadron colliders*. PhD thesis, U. Grenoble, 2007.
- [27] M. Gell-Mann, “A schematic model of baryons and mesons,” *Physics Letters*, vol. 8, no. 3, pp. 214 – 215, 1964.
- [28] H. Fritzsch, M. Gell-Mann, and H. Leutwyler, “Advantages of the Color Octet Gluon Picture,” *Phys. Lett.*, vol. B47, pp. 365–368, 1973.
- [29] D. J. Gross and F. Wilczek, “Ultraviolet Behavior of Nonabelian Gauge Theories,” *Phys. Rev. Lett.*, vol. 30, pp. 1343–1346, 1973.
- [30] H. D. Politzer, “Reliable Perturbative Results for Strong Interactions?,” *Phys. Rev. Lett.*, vol. 30, pp. 1346–1349, 1973.

- [31] G. Altarelli and G. Parisi, “Asymptotic freedom in parton language,” *Nuclear Physics B*, vol. 126, no. 2, pp. 298–318, 1977.
- [32] V. N. Gribov and L. N. Lipatov, “Deep inelastic e p scattering in perturbation theory,” *Sov. J. Nucl. Phys.*, vol. 15, pp. 438–450, 1972. [*Yad. Fiz.*15,781(1972)].
- [33] Y. L. Dokshitzer, “Calculation of the Structure Functions for Deep Inelastic Scattering and e+ e- Annihilation by Perturbation Theory in Quantum Chromodynamics,” *Sov. Phys. JETP*, vol. 46, pp. 641–653, 1977. [*Zh. Eksp. Teor. Fiz.*73,1216(1977)].
- [34] S. Catani and M. Seymour, “The Dipole formalism for the calculation of QCD jet cross-sections at next-to-leading order,” *Phys.Lett.*, vol. B378, pp. 287–301, 1996.
- [35] S. Catani, S. Dittmaier, M. H. Seymour, and Z. Trocsanyi, “The Dipole formalism for next-to-leading order QCD calculations with massive partons,” *Nucl.Phys.*, vol. B627, pp. 189–265, 2002.
- [36] L. H. Ryder, *Quantum Field Theory*. Cambridge University Press, 2 ed., June 1996.
- [37] R. Brock *et al.*, “Handbook of perturbative QCD: Version 1.0,” *Rev. Mod. Phys.*, vol. 67, pp. 157–248, 1995.
- [38] R. Ellis, W. Stirling, and B. Webber, *QCD and Collider Physics*. Cambridge Monographs on Particle Physics, Nuclear Physics and Cosmology, Cambridge University Press, 2003.
- [39] S. Bethke, “The 2009 World Average of $\alpha(s)$,” *Eur. Phys. J.*, vol. C64, pp. 689–703, 2009.
- [40] B. Delamotte, “A Hint of renormalization,” *Am. J. Phys.*, vol. 72, pp. 170–184, 2004.
- [41] R. P. Feynman, “Very high-energy collisions of hadrons,” *Phys. Rev. Lett.*, vol. 23, pp. 1415–1417, 1969.
- [42] T. Kinoshita, “Mass singularities of Feynman amplitudes,” *J. Math. Phys.*, vol. 3, pp. 650–677, 1962.
- [43] T. Plehn, “Lectures on LHC Physics,” *Lect. Notes Phys.*, vol. 844, pp. 1–193, 2012.
- [44] M. Böhm, A. Denner, and H. Joos, *Gauge theories of strong and electroweak interactions; 3rd ed.* Stuttgart: B. G. Teubner, 2001. Trans. of 3rd ed.: Eichtheorien der starken und elektroschwachen Wechselwirkung. Stuttgart, Teubner, 2001.
- [45] J. Collins, *Foundations of perturbative QCD*. Cambridge monographs on particle physics, nuclear physics, and cosmology, New York, NY: Cambridge Univ. Press, 2011.
- [46] J. C. Collins, D. E. Soper, and G. F. Sterman, “Factorization of Hard Processes in QCD,” *Adv. Ser. Direct. High Energy Phys.*, vol. 5, pp. 1–91, 1989.
- [47] A. Martin, W. Stirling, R. Thorne, and G. Watt, “Parton distributions for the LHC,” *Eur. Phys. J.*, vol. C63, pp. 189–285, 2009.

- [48] A. Denner, “Techniques for calculation of electroweak radiative corrections at the one loop level and results for W physics at LEP-200,” *Fortsch.Phys.*, vol. 41, pp. 307–420, 1993.
- [49] S. Heinemeyer, H. Rzehak, and C. Schappacher, “Proposals for Bottom Quark/Squark Renormalization in the Complex MSSM,” *Phys.Rev.*, vol. D82, p. 075010, 2010.
- [50] H. Lehmann, K. Symanzik, and W. Zimmermann, “Zur formulierung quantisierter feldtheorien,” *Il Nuovo Cimento (1955-1965)*, vol. 1, no. 1, pp. 205–225, 1955.
- [51] M. Srednicki, *Quantum Field Theory*. Cambridge University Press, 2007.
- [52] S. Catani and L. Trentadue, “Resummation of the QCD Perturbative Series for Hard Processes,” *Nucl. Phys.*, vol. B327, p. 323, 1989.
- [53] M. Kramer, E. Laenen, and M. Spira, “Soft gluon radiation in Higgs boson production at the LHC,” *Nucl. Phys.*, vol. B511, pp. 523–549, 1998.
- [54] B. Fuks, M. Klasen, D. R. Lamprea, and M. Rothering, “Revisiting slepton pair production at the Large Hadron Collider,” *JHEP*, vol. 01, p. 168, 2014.
- [55] B. Fuks, M. Klasen, D. R. Lamprea, and M. Rothering, “Gaugino production in proton-proton collisions at a center-of-mass energy of 8 TeV,” *JHEP*, vol. 10, p. 081, 2012.
- [56] W. Beenakker, C. Borschensky, M. Krämer, A. Kulesza, E. Laenen, V. Theeuwes, and S. Thewes, “NNLL resummation for squark and gluino production at the LHC,” *JHEP*, vol. 12, p. 023, 2014.
- [57] W. Beenakker, C. Borschensky, M. Krämer, A. Kulesza, E. Laenen, S. Marzani, and J. Rojo, “NLO+NLL squark and gluino production cross-sections with threshold-improved parton distributions,” *Eur. Phys. J.*, vol. C76, no. 2, p. 53, 2016.
- [58] W. Beenakker, C. Borschensky, R. Heger, M. Krämer, A. Kulesza, and E. Laenen, “NNLL resummation for stop pair-production at the LHC,” *JHEP*, vol. 05, p. 153, 2016.
- [59] B. Fuks, M. Klasen, F. Ledroit, Q. Li, and J. Morel, “Precision predictions for Z' - production at the CERN LHC: QCD matrix elements, parton showers, and joint resummation,” *Nucl. Phys.*, vol. B797, pp. 322–339, 2008.
- [60] T. Jezo, M. Klasen, D. R. Lamprea, F. Lyonnet, and I. Schienbein, “NLO+NLL limits on W' and Z' gauge boson masses in general extensions of the Standard Model,” *JHEP*, vol. 12, p. 092, 2014.
- [61] R. V. Harlander, A. Kulesza, V. Theeuwes, and T. Zirke, “Soft gluon resummation for gluon-induced Higgs Strahlung,” *JHEP*, vol. 11, p. 082, 2014.
- [62] T. Sjostrand, S. Mrenna, and P. Z. Skands, “PYTHIA 6.4 Physics and Manual,” *JHEP*, vol. 05, p. 026, 2006.
- [63] B. Jager, A. von Manteuffel, and S. Thier, “Slepton pair production in the POWHEG BOX,” *JHEP*, vol. 10, p. 130, 2012.

- [64] B. Jäger, A. von Manteuffel, and S. Thier, “Slepton pair production in association with a jet: NLO-QCD corrections and parton-shower effects,” *JHEP*, vol. 02, p. 041, 2015.
- [65] A. Broggio, M. Neubert, and L. Vernazza, “Soft Gluon Resummation for Slepton Pair-Production,” *PoS*, vol. EPS-HEP2011, p. 269, 2011.
- [66] T. Becher, M. Neubert, and G. Xu, “Dynamical Threshold Enhancement and Resummation in Drell-Yan Production,” *JHEP*, vol. 07, p. 030, 2008.
- [67] G. F. Sterman, “Partons, factorization and resummation, TASI 95,” in *QCD and beyond. Proceedings, Theoretical Advanced Study Institute in Elementary Particle Physics, TASI-95, Boulder, USA, June 4-30, 1995*, 1995.
- [68] S. Catani, M. L. Mangano, P. Nason, and L. Trentadue, “The Resummation of soft gluons in hadronic collisions,” *Nucl. Phys.*, vol. B478, pp. 273–310, 1996.
- [69] C. J. Borschensky, *Precision Calculations for Coloured Supersymmetric Particle Production at the Large Hadron Collider*. PhD thesis, Westfälische Wilhelms-Universität Münster, Münster, 2016.
- [70] S. C. Brensing, *Resummation for supersymmetric particle production at hadron colliders*. PhD thesis, RWTH Aachen University, Aachen, 2011.
- [71] H. Contopanagos, E. Laenen, and G. F. Sterman, “Sudakov factorization and resummation,” *Nucl. Phys.*, vol. B484, pp. 303–330, 1997.
- [72] V. M. Theeuwes, *Soft Gluon Resummation for Heavy Particle Production at the Large Hadron Collider*. PhD thesis, Westfälische Wilhelms-Universität Münster, Münster, 2015.
- [73] G. Curci, W. Furmanski, and R. Petronzio, “Evolution of Parton Densities Beyond Leading Order: The Nonsinglet Case,” *Nucl. Phys.*, vol. B175, pp. 27–92, 1980.
- [74] G. F. Sterman, “Summation of Large Corrections to Short Distance Hadronic Cross-Sections,” *Nucl. Phys.*, vol. B281, p. 310, 1987.
- [75] J. C. Collins and D. E. Soper, “Back-To-Back Jets in QCD,” *Nucl. Phys.*, vol. B193, p. 381, 1981. [Erratum: *Nucl. Phys.*B213,545(1983)].
- [76] J. Botts and G. F. Sterman, “Hard Elastic Scattering in QCD: Leading Behavior,” *Nucl. Phys.*, vol. B325, pp. 62–100, 1989.
- [77] A. Kulesza and L. Motyka, “Soft gluon resummation for the production of gluino-gluino and squark-antisquark pairs at the LHC,” *Phys. Rev.*, vol. D80, p. 095004, 2009.
- [78] N. Kidonakis and G. F. Sterman, “Resummation for QCD hard scattering,” *Nucl. Phys.*, vol. B505, pp. 321–348, 1997.
- [79] W. Beenakker, S. Brensing, M. Kramer, A. Kulesza, E. Laenen, and I. Niessen, “Soft-gluon resummation for squark and gluino hadroproduction,” *JHEP*, vol. 12, p. 041, 2009.

- [80] N. Kidonakis and J. F. Owens, “Soft gluon resummation and NNLO corrections for direct photon production,” *Phys. Rev.*, vol. D61, p. 094004, 2000.
- [81] W. Beenakker, S. Brensing, M. Kramer, A. Kulesza, E. Laenen, and I. Niessen, “NNLL resummation for squark-antisquark pair production at the LHC,” *JHEP*, vol. 01, p. 076, 2012.
- [82] S. Catani, D. de Florian, M. Grazzini, and P. Nason, “Soft gluon resummation for Higgs boson production at hadron colliders,” *JHEP*, vol. 07, p. 028, 2003.
- [83] I. Niessen, *Improving Predictions for SUSY Cross Sections - Soft-Gluon Resummation for SUSY-QCD*. PhD thesis, Nijmegen, 2012.
- [84] H. Contopanagos and G. F. Sterman, “Principal value resummation,” *Nucl. Phys.*, vol. B419, pp. 77–104, 1994.
- [85] B. Fuks, M. Klasen, D. R. Lamprea, and M. Rothering, “Precision predictions for electroweak superpartner production at hadron colliders with Resummino,” *Eur. Phys. J.*, vol. C73, p. 2480, 2013.
- [86] S. Catani, D. de Florian, and M. Grazzini, “Higgs production in hadron collisions: Soft and virtual QCD corrections at NNLO,” *JHEP*, vol. 05, p. 025, 2001.
- [87] A. Kulesza, G. F. Sterman, and W. Vogelsang, “Joint resummation in electroweak boson production,” *Phys. Rev.*, vol. D66, p. 014011, 2002.
- [88] W. R. Frazer and J. F. Gunion, “Scale Breaking for Quark and Gluon Distributions in QCD: A Diagrammatic Analysis,” *Phys. Rev.*, vol. D19, p. 2447, 1979.
- [89] S. Dawson, E. Eichten, and C. Quigg, “Search for Supersymmetric Particles in Hadron - Hadron Collisions,” *Phys. Rev.*, vol. D31, p. 1581, 1985.
- [90] H. Baer, C.-h. Chen, F. Paige, and X. Tata, “Detecting Stopped at Hadron Colliders and Supercolliders,” *Phys. Rev.*, vol. D49, pp. 3283–3290, 1994.
- [91] G. Bozzi, B. Fuks, and M. Klasen, “Stopped production in polarized hadron collisions,” *Phys. Lett.*, vol. B609, pp. 339–350, 2005.
- [92] W. Beenakker, M. Klasen, M. Kramer, T. Plehn, M. Spira, and P. M. Zerwas, “The Production of charginos / neutralinos and sleptons at hadron colliders,” *Phys. Rev. Lett.*, vol. 83, pp. 3780–3783, 1999. [Erratum: *Phys. Rev. Lett.*100,029901(2008)].
- [93] G. Bozzi, B. Fuks, and M. Klasen, “Threshold Resummation for Stopped-Pair Production at Hadron Colliders,” *Nucl. Phys.*, vol. B777, pp. 157–181, 2007.
- [94] G. Bozzi, B. Fuks, and M. Klasen, “Joint resummation for stopped pair production at hadron colliders,” *Nucl. Phys.*, vol. B794, pp. 46–60, 2008.
- [95] E. Byckling and K. Kajantie, *Particle kinematics*. A Wiley-Interscience publication, Wiley, 1973.

- [96] J. Pumplin, D. R. Stump, J. Huston, H. L. Lai, P. M. Nadolsky, and W. K. Tung, “New generation of parton distributions with uncertainties from global QCD analysis,” *JHEP*, vol. 07, p. 012, 2002.
- [97] H.-L. Lai, M. Guzzi, J. Huston, Z. Li, P. M. Nadolsky, J. Pumplin, and C. P. Yuan, “New parton distributions for collider physics,” *Phys. Rev.*, vol. D82, p. 074024, 2010.
- [98] W. Beenakker, R. Hopker, M. Spira, and P. Zerwas, “Squark and gluino production at hadron colliders,” *Nucl. Phys.*, vol. B492, pp. 51–103, 1997.
- [99] T. Plehn, “Measuring the MSSM Lagrangean,” *Czech. J. Phys.*, vol. 55, pp. B213–B220, 2005.
- [100] J. Kuipers, T. Ueda, J. A. M. Vermaseren, and J. Vollinga, “FORM version 4.0,” *Comput. Phys. Commun.*, vol. 184, pp. 1453–1467, 2013.
- [101] A. Buckley, J. Ferrando, S. Lloyd, K. Nordström, B. Page, M. Rüfenacht, M. Schönherr, and G. Watt, “LHAPDF6: parton density access in the LHC precision era,” *Eur. Phys. J.*, vol. C75, p. 132, 2015.
- [102] J. M. Lindert, F. D. Steffen, and M. K. Trenkel, “Direct stau production at hadron colliders in cosmologically motivated scenarios,” *JHEP*, vol. 08, p. 151, 2011.
- [103] A. D. Martin, W. J. Stirling, R. S. Thorne, and G. Watt, “Parton distributions for the LHC,” *Eur. Phys. J.*, vol. C63, pp. 189–285, 2009.
- [104] R. D. Ball, L. Del Debbio, S. Forte, A. Guffanti, J. I. Latorre, A. Piccione, J. Rojo, and M. Ubiali, “A Determination of parton distributions with faithful uncertainty estimation,” *Nucl. Phys.*, vol. B809, pp. 1–63, 2009. [Erratum: *Nucl. Phys.*B816,293(2009)].
- [105] R. D. Ball *et al.*, “Parton distributions for the LHC Run II,” *JHEP*, vol. 04, p. 040, 2015.
- [106] J. Butterworth *et al.*, “PDF4LHC recommendations for LHC Run II,” *J. Phys.*, vol. G43, p. 023001, 2016.
- [107] S. Dulat, T.-J. Hou, J. Gao, M. Guzzi, J. Huston, P. Nadolsky, J. Pumplin, C. Schmidt, D. Stump, and C. P. Yuan, “New parton distribution functions from a global analysis of quantum chromodynamics,” *Phys. Rev.*, vol. D93, no. 3, p. 033006, 2016.
- [108] G. Aad *et al.*, “Search for direct slepton and gaugino production in final states with two leptons and missing transverse momentum with the ATLAS detector in pp collisions at $\sqrt{s} = 7$ TeV,” *Phys. Lett.*, vol. B718, pp. 879–901, 2013.
- [109] C. Collaboration, “Search for direct EWK production of SUSY particles in multilepton modes with 8TeV data,” 2013.
- [110] J. Alwall, M. Herquet, F. Maltoni, O. Mattelaer, and T. Stelzer, “MadGraph 5 : Going Beyond,” *JHEP*, vol. 06, p. 128, 2011.

- [111] S. Jadach, Z. Was, R. Decker, and J. H. Kuhn, “The tau decay library TAUOLA: Version 2.4,” *Comput. Phys. Commun.*, vol. 76, pp. 361–380, 1993.
- [112] S. Ovin, X. Rouby, and V. Lemaitre, “DELPHES, a framework for fast simulation of a generic collider experiment,” 2009.
- [113] J.-L. Agram, J. Andrea, E. Conte, B. Fuks, D. Gelé, and P. Lansonneur, “Probing top anomalous couplings at the LHC with trilepton signatures in the single top mode,” *Phys. Lett.*, vol. B725, pp. 123–126, 2013.
- [114] N. D. Christensen and C. Duhr, “FeynRules - Feynman rules made easy,” *Comput. Phys. Commun.*, vol. 180, pp. 1614–1641, 2009.
- [115] C. Degrande, C. Duhr, B. Fuks, D. Grellscheid, O. Mattelaer, and T. Reiter, “UFO - The Universal FeynRules Output,” *Comput. Phys. Commun.*, vol. 183, pp. 1201–1214, 2012.
- [116] E. Conte, B. Fuks, and G. Serret, “MadAnalysis 5, A User-Friendly Framework for Collider Phenomenology,” *Comput. Phys. Commun.*, vol. 184, pp. 222–256, 2013.
- [117] M. Cacciari, G. P. Salam, and G. Soyez, “FastJet User Manual,” *Eur. Phys. J.*, vol. C72, p. 1896, 2012.
- [118] A. Robichaud-Véronneau, “Searches for electroweak production of supersymmetric charginos, neutralinos and sleptons with the ATLAS detector,” *Nucl. Part. Phys. Proc.*, vol. 273-275, pp. 570–576, 2016.
- [119] C. Collaboration, “Search for electroweak production of charginos in final states with two tau leptons in pp collisions at $\sqrt{s} = 8$ TeV,” 2016.
- [120] G. Aad *et al.*, “Search for the electroweak production of supersymmetric particles in $\sqrt{s}=8$ TeV pp collisions with the ATLAS detector,” *Phys. Rev.*, vol. D93, no. 5, p. 052002, 2016.
- [121] A. Barr, C. Lester, and P. Stephens, “m(T2): The Truth behind the glamour,” *J. Phys.*, vol. G29, pp. 2343–2363, 2003.
- [122] K. T. Matchev and M. Park, “A General method for determining the masses of semi-invisibly decaying particles at hadron colliders,” *Phys. Rev. Lett.*, vol. 107, p. 061801, 2011.
- [123] G. Aad *et al.*, “Search for direct production of charginos, neutralinos and sleptons in final states with two leptons and missing transverse momentum in pp collisions at $\sqrt{s} = 8$ TeV with the ATLAS detector,” *JHEP*, vol. 05, p. 071, 2014.
- [124] G. Aad *et al.*, “Summary of the searches for squarks and gluinos using $\sqrt{s} = 8$ TeV pp collisions with the ATLAS experiment at the LHC,” *JHEP*, vol. 10, p. 054, 2015.
- [125] “Search for squarks and gluinos in final states with jets and missing transverse momentum at $\sqrt{s} = 13$ TeV with the ATLAS detector,” Tech. Rep. ATLAS-CONF-2015-062, CERN, Geneva, Dec 2015.

- [126] G. Aad *et al.*, “Search for direct production of charginos and neutralinos in events with three leptons and missing transverse momentum in $\sqrt{s} = 8\text{TeV}$ pp collisions with the ATLAS detector,” *JHEP*, vol. 04, p. 169, 2014.
- [127] M. Spira, “Higgs and SUSY particle production at hadron colliders,” in *Supersymmetry and unification of fundamental interactions. Proceedings, 10th International Conference, SUSY’02, Hamburg, Germany, June 17-23, 2002*, pp. 217–226, 2002.
- [128] E. L. Berger, M. Klasen, and T. M. P. Tait, “Associated production of gauginos and gluinos at hadron colliders in next-to-leading order SUSY QCD,” *Phys. Lett.*, vol. B459, pp. 165–170, 1999.
- [129] E. L. Berger, M. Klasen, and T. M. P. Tait, “Erratum: Next-to-leading order supersymmetric QCD predictions for associated production of gauginos and gluinos (Phys.Rev.D62:095014,2000),” *Phys. Rev.*, vol. D67, p. 099901, 2003.
- [130] E. L. Berger, M. Klasen, and T. M. P. Tait, “Next-to-leading order SUSY QCD predictions for associated production of gauginos and gluinos,” *Phys. Rev.*, vol. D62, p. 095014, 2000.
- [131] B. Fuks, M. Klasen, and M. Rothering, “Soft gluon resummation for associated gluino-gaugino production at the LHC,” *JHEP*, vol. 07, p. 053, 2016.
- [132] P. Achard *et al.*, “Measurement of the running of the electromagnetic coupling at large momentum-transfer at LEP,” *Phys. Lett.*, vol. B623, pp. 26–36, 2005.
- [133] K. Hasegawa, “Super AutoDipole,” *Eur. Phys. J.*, vol. C70, pp. 285–293, 2010.
- [134] T. Hahn and M. Perez-Victoria, “Automatized one loop calculations in four-dimensions and D-dimensions,” *Comput.Phys.Commun.*, vol. 118, pp. 153–165, 1999.
- [135] W. Hollik, E. Kraus, M. Roth, C. Rupp, K. Sibold, and D. Stockinger, “Renormalization of the minimal supersymmetric standard model,” *Nucl. Phys.*, vol. B639, pp. 3–65, 2002.
- [136] D. Stockinger, “Regularization by dimensional reduction: consistency, quantum action principle, and supersymmetry,” *JHEP*, vol. 03, p. 076, 2005.
- [137] W. Beenakker, R. Hopker, M. Spira, and P. M. Zerwas, “Squark and gluino production at hadron colliders,” *Nucl. Phys.*, vol. B492, pp. 51–103, 1997.
- [138] J. A. Aguilar-Saavedra *et al.*, “Supersymmetry parameter analysis: SPA convention and project,” *Eur. Phys. J.*, vol. C46, pp. 43–60, 2006.
- [139] R. Gavin, C. Hangst, M. Krämer, M. Mühlleitner, M. Pellen, E. Popena, and M. Spira, “Matching Squark Pair Production at NLO with Parton Showers,” *JHEP*, vol. 10, p. 187, 2013.
- [140] N. Kidonakis, “Single top production at the Tevatron: Threshold resummation and finite-order soft gluon corrections,” *Phys. Rev.*, vol. D74, p. 114012, 2006.

- [141] J. Debove, B. Fuks, and M. Klasen, “Threshold resummation for gaugino pair production at hadron colliders,” *Nucl. Phys.*, vol. B842, pp. 51–85, 2011.
- [142] K. A. Olive *et al.*, “Review of Particle Physics,” *Chin. Phys.*, vol. C38, p. 090001, 2014.
- [143] K. De Causmaecker, B. Fuks, B. Herrmann, F. Mahmoudi, B. O’Leary, W. Porod, S. Sekmen, and N. Strobbe, “General squark flavour mixing: constraints, phenomenology and benchmarks,” *JHEP*, vol. 11, p. 125, 2015.
- [144] W. Porod and F. Staub, “SPheno 3.1: Extensions including flavour, CP-phases and models beyond the MSSM,” *Comput. Phys. Commun.*, vol. 183, pp. 2458–2469, 2012.
- [145] M. Klasen, M. Pohl, and G. Sigl, “Indirect and direct search for dark matter,” *Prog. Part. Nucl. Phys.*, vol. 85, pp. 1–32, 2015.
- [146] J. Harz, B. Herrmann, M. Klasen, K. Kovařík, and Q. L. Boulc’h, “Neutralino-stop coannihilation into electroweak gauge and Higgs bosons at one loop,” *Phys. Rev.*, vol. D87, no. 5, p. 054031, 2013.
- [147] J. Harz, B. Herrmann, M. Klasen, and K. Kovařík, “One-loop corrections to neutralino-stop coannihilation revisited,” *Phys. Rev.*, vol. D91, no. 3, p. 034028, 2015.
- [148] J. Harz, B. Herrmann, M. Klasen, K. Kovařík, and P. Steppeler, “Theoretical uncertainty of the supersymmetric dark matter relic density from scheme and scale variations,” *Phys. Rev.*, vol. D93, no. 11, p. 114023, 2016.
- [149] G. Aad *et al.*, “Search for new phenomena in final states with large jet multiplicities and missing transverse momentum with ATLAS using $\sqrt{s} = 13$ TeV proton-proton collisions,” *Phys. Lett.*, vol. B757, pp. 334–355, 2016.
- [150] C. Collaboration, “Search for SUSY in same-sign dilepton events at $\sqrt{s}=13$ TeV,” 2015.
- [151] V. Khachatryan *et al.*, “Searches for electroweak production of charginos, neutralinos, and sleptons decaying to leptons and W, Z, and Higgs bosons in pp collisions at 8 TeV,” *Eur. Phys. J.*, vol. C74, no. 9, p. 3036, 2014.
- [152] W. Beenakker, R. Hopker, and M. Spira, “PROSPINO: A Program for the production of supersymmetric particles in next-to-leading order QCD,” 1996.
- [153] P. M. Nadolsky, H.-L. Lai, Q.-H. Cao, J. Huston, J. Pumplin, D. Stump, W.-K. Tung, and C. P. Yuan, “Implications of CTEQ global analysis for collider observables,” *Phys. Rev.*, vol. D78, p. 013004, 2008.
- [154] M. Bonvini, S. Marzani, J. Rojo, L. Rottoli, M. Ubiali, R. D. Ball, V. Bertone, S. Carrazza, and N. P. Hartland, “Parton distributions with threshold resummation,” *JHEP*, vol. 09, p. 191, 2015.
- [155] L. A. Harland-Lang, A. D. Martin, P. Motylinski, and R. S. Thorne, “Parton distributions in the LHC era: MMHT 2014 PDFs,” *Eur. Phys. J.*, vol. C75, no. 5, p. 204, 2015.

- [156] J. Rosiek, “Complete set of Feynman rules for the MSSM: Erratum,” 1995.
- [157] B. C. Allanach *et al.*, “SUSY Les Houches Accord 2,” *Comput. Phys. Commun.*, vol. 180, pp. 8–25, 2009.
- [158] A. Denner, H. Eck, O. Hahn, and J. Kublbeck, “Compact Feynman rules for Majorana fermions,” *Phys.Lett.*, vol. B291, pp. 278–280, 1992.

Acknowledgments

The final words of my thesis are dedicated to the people who helped and supported me during my PhD in Münster.

First of all I would like to thank my supervisor Michael Klasen for giving me the opportunity to work on my PhD thesis in his research group. He gave me the freedom to develop some of the objectives of this work on my own and guided me whenever I got stuck. His doors were always open for useful discussions and even when I had issues apart from my work. So, thank you very much, Michael!

Furthermore, I want to express my gratitude to my collaborator Benjamin Fuks. He took the time to answer all of my questions via e-mail in detail and had always valuable ideas, e.g. for cross-checking my real emission diagrams and the dipoles. Besides, his optimistic attitude and his great sense of humor helped me during my work. It was a pleasure to work with him! Thank you, Benjamin!

Next, I want to thank Anna Kulesza for being my second examiner and for her very useful work and references related to resummation including colored final state particles. Thanks, Anna!

Many thanks go to all the current and former members of Michael's and Anna's research team. In particular to David Regalado Lamprea who taught me a lot about programming. It was great fun to work with him. Also, when I had private issues he listened to me and had good ideas. I want to thank Christoph Borschensky for the useful discussions about resummation, for explaining to me most of the things in detail and for checking parts of my thesis. I hope I have not bothered you too much at the end of my work, Christoph? Moreover, I would like to thank Vincent Theeuwes. Especially for cross-checking some of my analytical results needed for resummation and for useful comments about resummation and about my thesis. Furthermore, I would like to thank Florian König who listened and answered to my questions concerning my NLO computations, even when I was sometimes bothering him. Also, I want to thank Karol Kovařík who had always an open door and who was very good in explaining things. In addition, I would like to thank Daniel Schwartländer who cross-checked some of my real corrections. Once again, I would like to thank my former office mates Matthias Brandt, Florian and David for being very nice and funny office partners. So, thank you guys of the institute!

Of course, I would like to thank my parents and my brother for giving me the best family background and helping me with many things. Special thanks goes also to Marcel Pollmann. Thanks for trying to distract me from work in my free time. Thanks to all the people who could stand me during my PhD. I hope I did not get to much on your nerves!

Last, but definitely not least, I want to thank my girlfriend Rebecca Hagen for her mental support and cheering me up when I was in a bad mood. Certainly, it was not always a pleasure having me around when I was always talking about my work and thesis. Therefore, I dedicate the final words of my thesis to you, Rebecca. Thanks for everything. You were really the greatest support and you always believed in me. Thanks for being the best! I love you!

Marcel Rothering

Lebenslauf

Zur Person

Geburtsdatum 22/10/1987
Geburtsort Vreden
Staatsangehörigkeit Deutsch
Status Ledig
Geschlecht Männlich

Wissenschaftlicher Mitarbeiter & Doktorand

Seit 12/2012 Wissenschaftlicher Mitarbeiter für theoretische Physik in der AG Klasen an der Westfälischen Wilhelms-Universität Münster

Aufgaben

- Programmentwicklung für Resummationvorhersagen für Teilchenproduktion am Large Hadron Collider (www.resummino.org)
- Übungsgruppenleiter für theoretische Physik (Mechanik, Thermodynamik, Elektrodynamik, Quantenmechanik und Quantentheorie)
- Betreuung von Bachelor- und Masterarbeiten
- Betreuung eines Praktikanten: DAAD RISE (Research Internships in Science and Engineering)

Vorträge

- 04/2014 Vortrag auf der DPG-Konferenz in Mainz
- 03/2013 Vortrag auf der DPG-Konferenz in Dresden
- 01/2013 Vortrag und Tutorial am CERN (Conseil Européen pour la Recherche Nucléaire) für Experimentalphysiker

Veröffentlichungen

1. B. Fuks, M. Klasen, M. Rothering, *Soft gluon resummation for associated gluino-gaugino production at the LHC*, JHEP 07:053, 2016.
1. B. Fuks, M. Klasen, David R. Lamprea, M. Rothering, *Revisiting slepton pair production at the Large Hadron Collider*, JHEP 01:168, 2014.
3. B. Fuks, M. Klasen, David R. Lamprea, M. Rothering, *Precision predictions for electroweak superpartner production at hadron colliders with Resummino*, Eur. Phys. J. C 73, 2480, 2013.
4. B. Fuks, M. Klasen, David R. Lamprea, M. Rothering, *Gaugino production in proton-proton collisions at a center-of-mass energy of 8 TeV*, JHEP 10:081, 2012.

Hochschulstudium

Masterstudium in Physik

10/2010 - 12/2012 Masterstudium in Physik an der Westfälischen Wilhelms-Universität Münster

21.11.2012 Masterarbeit

Titel *Resummation predictions for slepton pair-production and implications for dark matter*

Schwerpunkt Theoretische Teilchenphysik

Betreuer Prof. Dr. Klasen

08/28 - 09/08/2012 Internationale Sommerschule und Konferenz für Hochenergiephysik: *Standard Model and Beyond* (ISSCSMB '12)

Bachelorstudium in Physik

8/2007 - 8/2010 Bachelorstudium in Physik an der Westfälischen Wilhelms-Universität Münster

19.07.2010 Bachelorarbeit

Titel *Optically induced dynamics in coupled two-level-systems*

Schwerpunkt Theoretische Festkörperphysik

Betreuer Prof. Dr. Kuhn

Schulausbildung

8/2003 - 7/2007 Städtisches Heriburg-Gymnasium in Coesfeld

8/1998 - 7/2003 Städtisches Gymnasium Nepomucenum in Coesfeld

8/1994 - 7/1998 Pankratius-Grundschule in Gescher

Sprachkenntnisse

Deutsch Muttersprache

Englisch Fließend in Wort und Schrift

Französisch Grundkenntnisse

Technische Fähigkeiten

Programmiersprachen C++, Python, R und Shell

Software-Tools Mathematica, \LaTeX , Gnuplot und MS-Office

Betriebssysteme Windows und Unix-basierende Systeme

Münster, 2. Oktober 2016